Effects of configuration and operating conditions on turbidity removal of jet clarifier

Ploypailin Romphophak

THÈSE

En vue de l'obtention du
DOCTORAT DE L'UNIVERSITÉ DE TOULOUSE

Délivré par l'Institut National des Sciences Appliquées de Toulouse

Cotutelle internationale: Chulalongkorn University

Présentée et soutenue par
Ploypailin ROMPHOPHAK

Le 16 novembre 2021

Effets de configuration et de conditions opératoires sur la réduction de turbidité dans un clarificateur à jet

Ecole doctorale : **MEGEP - Mécanique, Energétique, Génie civil, Procédés**

Spécialité : **Génie des Procédés et de l'Environnement**

Unité de recherche :
TBI - Toulouse Biotechnology Institute, Bio & Chemical Engineering

Thèse dirigée par
Alain LINE et Pisut PAINMANAKUL

Jury

M. Julien LAURENT, Rapporteur
M. Seoktae KANG, Rapporteur
Mme Carole COUFORT-SAUDEJAUD, Examinatrice
M. Sutha KHAODHIAR, Examinateur
M. Arnaud COCKX, Examinateur
Patiparn PUNYAPALAKUL, Examinateur
M. Alain LINE, Directeur de thèse
M. Pisut PAINMANAKUL, Co-directeur de thèse

ACKNOWLEDGEMENT

I gained a lot of precious experiences throughout my student life; particularly, conducting research and writing this thesis, the greatest challenge, turned my dream into reality and shaped my life. Without the help from supportive people, I could not have done it and been where I am today. Thus, I would like to take this opportunity to express my deepest appreciation to those experts who have never given up on me and tirelessly supported me throughout my journey.

First of all, Professor Dr. Pisut Painmanakul and Professor Dr. Alain Liné, my supervisors who always trust and believe in me. The opportunities and advice they gave me were priceless. I would also like to thank Professor Arnaud Cockx and Associate Professor Carole Coufort-Saudejaud, who always generously supported and passionately taught me to achieve my research goals. Without their help, guidance, and encouragement, I could not have come to this far-further than I have ever dreamed of. I am very thankful for the things they all gave to me; they will be my lifelong inspiration in my academic life either as a learner or a teacher. I really appreciate all the hard work they have done to help me.

I am also grateful to my co-workers and friends from both Chulalongkorn University and the Toulouse Biotechnology Institute, Bio and Chemical Engineering (TBI), National Institute of Applied Sciences Toulouse (INSA-Toulouse), especially colleagues in team 7, for sharing their precious experiences and perspectives with me. Thank Kritchart Wongwailikhit, Claude Le Men, and Arezki Chekroun for their valuable comments, constructive remarks, useful guidance, and work advice and other people who made up my years during my study.

Moreover, I would like to express my gratitude for the Royal Golden Jubilee Ph.D. Program, under Thailand Research Fund (TRF), the French Embassy in Thailand, and the team Transfer-Interface-Mixing from Toulouse Biotechnology Institute in France for providing my tuition and research grants during my research program.

ABSTRACT

In water treatment, flocculation creates large and weighty flocs enough to be removed by the downstream processes of sedimentation and filtration. Among the various existing technologies, the jet clarifier is considered as an effective and compact system as it couples flocculation and clarification in a single unit. For the design of jet mixing, much experimental work has been done and many correlations have been proposed. However, these correlations are case specifics, and, to date, there is no comprehensive view for the flocculation aspect.

In order to evaluate the performance of the jet clarifier for turbidity removal and understand hydrodynamics to propose the optimal operating conditions and design criteria, two different configurations of the continuous jet clarifiers are figured out. The first one is a prototype of a 3D jet clarifier studied at two scales and implemented at Samsen Water Treatment Plant, Thailand; these two reactors were designed to investigate the performance and mean Residence Time Distribution (RTD) for various injected flow rates. The results indicated no effect of reactor sizes, and a reduction of the initial turbidity (50 NTU) was achieved with an efficiency of approximately 80% under optimal conditions.

Moreover, the second jet clarifier configuration was designed as a Quasi-2Dimensional (Q2D) jet clarifier at the TBI-INSA-Toulouse, France allowing the application of optical metrological methods used to understand better local phenomena controlling the efficiency of the jet clarifier. Hence, measurements of instantaneous velocity field were performed by means of Particle Image Velocimetry (PIV). The processing of experimental PIV data highlighted a strong circulation induced by the jet in the flocculation zone. At this location, the range of velocity gradient (G) is 3 to 13 s^{-1} whereas the residence time decreases from 4 to 1 hour. Based on the hydrodynamic analysis, the Camp number (*Gt*) in the flocculation zone is shown to be constant at around 7,000 for different jet flow rates (from 11L/hr to 49L/hr). The efficiency of such the jet clarifier can thus be foreseen. Plus, measurements of the number of flocs and their size distributions were performed by means of shadowgraphy and image analysis. Thanks to a

coupling between the different experimental results obtained in the Q2D jet clarifier, it was possible to relate the evolution of the number of flocs along the jet to the recirculation loop present in the flocculation zone. The relative independence of the floc size distributions on the flow rate is discussed in light of the Camp number, which can explain the efficiency of the jet clarifier in terms of flocculation.

Finally, due to reactor design, the simulations using CFD code showing encouraging results were presented at the end of the manuscript. Here as well, characteristic time scales and velocity gradient were used to perform the first comparisons.

Keywords

    1. Jet clarifier

    2. Hydrodynamics

    3. Camp number

    4. Floc size distribution

    5. Turbidity removal

RÉSUMÉ

Dans le cas du traitement des eaux, l'étape de flocculation consiste à agglomérer de fines particules solides en agrégats suffisaments grands pour pouvoir ensuite les éliminer par sédimentation ou filtration. Parmi les différentes technologies existantes, le clarificateur à jet est considéré comme un système efficace et compact car il couple floculation et clarification en une seule unité. Pour la conception du mélange par jets, de nombreux travaux expérimentaux ont été réalisés et de nombreuses corrélations ont été proposées. Cependant, ces corrélations sont spécifiques à des cas particuliers, et, à ce jour, il n'y a pas de compréhension globale des phénomènes controlant la floculation.

Afin d'évaluer les performances du clarificateur à jet pour l'élimination de la turbidité des eaux à potabiliser et afin de mieux comprendre en particulier l'hydrodynamique et la floculation, deux configurations différentes des clarificateurs à jet continu sont étudiées pour proposer les conditions de fonctionnement optimales et les critères de conception. La première configuration est un prototype de clarificateur à jet tridimensionnel étudié à deux échelles et mis en œuvre à l'usine de traitement d'eau de Samsen, en Thaïlande ; ces deux réacteurs ont été conçus pour étudier les performances et la distribution moyenne du temps de séjour (DTS) pour différents débits injectés. Les résultats n'ont indiqué aucun effet de la taille des réacteurs, et une réduction de la turbidité initiale (50 NTU) a été obtenue avec une efficacité d'environ 80% dans des conditions optimales.

La la deuxième configuration du clarificateur à jet a été conçue comme un clarificateur à jet Quasi-2Dimensional (Q2D) au laboratoire TBI de l'INSA de Toulouse, France, permettant l'application de méthodes métrologiques optiques pour mieux comprendre les phénomènes locaux contrôlant l'efficacité du clarificateur à jet. Dans cette étude, les mesures du champ de vitesse instantanée ont été effectuées au moyen de la vélocimétrie par image de particules (PIV). Le traitement des données expérimentales de PIV a mis en évidence une forte circulation induite par le jet dans la zone de floculation. Dans cette zone et pour diférents débits injectés, la plage de gradient de vitesse (G)

augmente de 3 à 13 s^{-1} alors que le temps de séjour diminue de 4 à 1 heure. Sur la base de l'analyse hydrodynamique, le nombre de Camp (*Gt*) dans la zone de floculation est constant de l'ordre de 7,000 pour différents débits de jet (de 11L/h à 49L/h). De plus, les mesures du nombre de flocs et de leurs distributions granulométriques ont été effectuées par ombroscopie suivie d'analyse d'images. Grâce à un couplage entre les différents résultats expérimentaux obtenus dans le clarificateur à jet Q2D, il a été possible d'expliquer l'évolution du nombre de flocs dans la zone de floculation. L'indépendance relative des distributions de taille des flocs au débit est discutée en considérant le nombre de Camp, ce qui permet d'expliquer l'efficacité du clarificateur à jet en termes de floculation.

Finalement, des simulations numériques du pilote 3D utilisant le code Fluent de CFD ont montré des résultats encourageants qui sont présentés en fin de manuscript. Là encore, les échelles de temps caractéristiques et les gradients de vitesse ont été estimés et comparés aux données expérimentales.

Mots-clés

1. Clarificateur à jet

2. Hydrodynamique

3. Nombre de Camp

4. Distribution de la taille des flocs

5. Élimination de la turbidité

CONTENTS

LIST OF FIGURES

LIST OF TABLES

NOMENCLATURES

Abbreviations	Definitions
BOD	Biological Oxygen Demand
CCC	Critical Coagulation Concentration
CFD	Computational Fluid Dynamics
COD	Chemical Oxygen Demand
CSTR	Continuous Stirred Tank Reactor
HRT	Hydraulic Retention Time
LDS	Laser Diffraction Scattering
LSP	Large Scale Prototype
NOM	Natural Organic Matter
NTU	Nephelometric Turbidity Units
O&M	Cost Operation and Maintenance Cost
PFR	Plug Flow Reactor
PIV	Particle Image Velocimetry
Q2D	Quasi-2 Dimensional
RTD	Residence Time Distribution
SS	Suspended Solids
SSP	Small Scale Prototype
WHO	World Health Organization

SYMBOL LIST

Latin letters	Unit	Definitions
A	[m^2]	Projected two-dimensional area
A$_{HC}$	[J]	Hamaker constant
A$_p$	[m^2]	Cross section area of pipe
A$_s$	[m^2]	Surface area
a, b, c, d	[-]	Constant
a$_P$	[m^2]	Area of pixel
B	[s^{-1}]	Frequency of breakup
C$_1$, C$_2$	[-]	Constants value
C$_D$	[-]	Drag coefficient
C$_\mu$	[-]	Model constant
c	[mg/L]	Concentration
ccc.	[mol/L]	Critical coagulation concentration
D$_{ef}$	[m^2/s]	Effective diffusivity
D$_h$	[m]	Value of the hydraulic diameter
D$_{pi}$	[m]	Particle diameter
D$_t$	[m^2/s]	Turbulent diffusivity
D_{ij}	[m^2/s]	Mutual diffusion coefficient of particle i and j
D_i , D_i	[m^2/s]	Stokes diffusion coefficient of particle i or j
D$_{im}$	[m]	Impeller diameter
d_{eq}	[m]	Circular equivalent diameter
d_{floc}	[m^2]	Projected area of an aggregate on a 2D plane
d_i , d_j, d_p	[m]	Particle diameter
e	[C]	Electron charge
F$_B$	[N]	Buoyancy force
F$_c$	[N]	Cohesion force
F$_D$	[N]	Drag force

F_G	[N]	Gravitational force
F_h	[N]	Hydrodynamic forces
f	[-]	Fanning friction factor
f_i	[-]	Number fraction of particles of the ith class
G	[s^{-1}]	Global velocity gradient or Mean velocity gradient
Gt_{cont}	[-]	Camp number
g	[m/s^2]	Gravitational acceleration
H_c	[m]	Distance between the center of two particles
H_s	[m]	Distance between the surfaces of the plates
h_f	[m]	Frictional head loss
J	[m^3/s]	Flux of particle
κ	[m]	Reciprocal Debye length
k	[m^2/s^2]	Turbulent kinetic energy (per unit mass)
k_B	[J/K]	Boltzmann constant
l	[m]	Size
m_g	[kg]	Mass of displaced medium
c	[mg/L]	Concentration
ccc.	[mol/L]	Critical coagulation concentration
N	[rpm.]	Impeller rotation frequency
N_p	[-]	The power number of the impeller
n_i , n_j	[-]	Number of particles of size i or j
P	[Watt]	Power dissipated in the flocculation tank
Pe	[-]	Peclet number
P_k	[m^2/s^3]	Production rate of turbulence
P_w	[m]	Wetted perimeter of pipe
p	[Pa]	Mean pressure
Q	[m^3/s]	Flow rate
Qc	[m^3/s]	Circulation flow rates
R	[m]	Radius of the aggregate

Re	[-]	Reynolds number
r_i , r_j	[m]	Radius of the particle i or j
Sc	[-]	Schmidt number
T_{in}	[NTU]	Turbidity of initial water
T_{out}	[NTU]	Turbidity of effluent water
t	[m]	Time
t_c	[s]	Circulation time
t_{cont}	[min]	Contact time
t_m	[min]	Mean residence time
t_n	[m]	Thickness of the clay platelet
t_{RF}	[m]	Residence time in flocculation zone
T_{temp}	[K]	Absolute temperature
U	[m/s]	Relative speed between the two phases
$\vec{U}$	[m/s]	Mean velocity vector
U_t	[m/s]	Terminal settling velocity
U_{total}	[m/s]	Average velocity
u	[m/s]	The flow velocity
$\bar{u}$	[m/s]	Mean velocity
u_i	[m/s]	Velocity of the ith acquisition
$\overline{u_i'}$, $\overline{u_j'}$	[m/s]	Fluctuating of velocity components
$\overline{u'^2}$	[m²/s²]	Mean value of the square of turbulent velocity fluctuations
u_{pi} , u_{pj}	[m/s]	Velocity of particle i or j
V	[m³]	Volume
V_A	[mV]	Attractive potential
V_{eq}	[m³]	Spherical equivalent volume
V_m	[mV]	Occurrence of maximum energy
V_{Net}	[mV]	Total or net interaction energy
V_p	[m³]	Particle volume

V_R	[mV]	Repulsive potential
w	[m]	Width of the impeller
y	[-]	Adjustable parameter in the expression of collision efficiency
z	[-]	Valence of the ion

Greek letters	Unit	Definitions
ζ	[mV]	Zeta potential
ε	[m²/s³]	Dissipation rate of turbulent kinetic energy
$<\varepsilon>$	[m²/s³]	Dissipation rate of the turbulent kinetic energy
ε_0	[F/m]	Dielectric constant of a medium
ε_c	[m²/s³]	Rate of dissipation of the critical turbulent kinetic energy
ϵ	[m]	Roughness of a pipe
η	[m]	Kolmogrov scale
Λ	[m]	Taylor macroscale
λ	[m]	Taylor microscale
μ	[Pa·s]	Dynamic viscosity
μ_t	[m²/s]	Dynamic turbulent viscosity
ν	[m²/s]	Kinematic viscosity
ρ	[kg/m³]	Density
γ	[N/m³]	Specific weight
ρ_i, ρ_p	[kg/m³]	Particle density
ρ_l	[kg/m³]	Liquid density
σ^2	[min²]	Variance
σ_h	[N/m²]	Hydrodynamic stress exerted on the floc
σ_I	[Pa]	Local stress in the inertial domain

σ_v	[Pa]	Local stress in the viscous domain
τ	[N/m²]	Mean viscous stress tensor
Ψ	[m/s]	Electrophoretic mobility
Ψ_s	[mV]	Stern layer potential
$\beta_{i,j}$	[m³/s]	Collision rate
$\beta_{i,j}^{agitation}$	[m³/s]	Collision rate in regime
$\beta_{i,j}^{brownian}$	[m³/s]	Collision rate generated by the Brownian motion
$\beta_{i,j}^{sedimentation}$	[m³/s]	Collision rate generated by differential sedimentation
$\beta_{i,j}^{laminar\ flow}$	[m³/s]	Collision rate in laminar regime
$\beta_{i,j}^{turbulent\ flow}$	[m³/s]	Collision rate in turbulent regime
δ	[-]	Size ratio between two particles
α_c	[-]	Collision efficiency
$\alpha_c^{agitation}$	[-]	Efficiency of collisions in agitated system
$\alpha_c^{brownian}$	[-]	Efficiency of collisions in Brownian motion
$\alpha_c^{sedimentation}$	[-]	Efficiency of collisions in differential sedimentation

INTRODUCTION

Among the various existing technologies for water treatment, the jet clarifier, that couples flocculation and clarification in a single device, is considered an effective and compact system. Even though it is economical and robust to operate, since the jet clarifier has no mechanical moving part, thus requiring less cost of operation and maintenance (O&M cost) (Pani and Patil, 2007), the guidelines for the preliminary design of a jet clarifier are not available.

In a previous study, the average turbidity removal efficiency of the jet clarifier was shown to be approximately 80% (Romphophak et al., 2016) while flocculators fitted with mechanical stirrers have an average turbidity removal efficiency of approximately 70% (Pani and Patil, 2007). Thus, the jet clarifier is a high-performance reactor. Hence, the present thesis is directed to study and understand the phenomena taking place in the jet clarifier to further be able to improve and/or scale-up such reactor.

The primary objective of the jet clarifier is to remove the suspended particles which cause turbidity. The turbidity indicates the presence of total suspended solids (TSS) such as clay, silt, organic matter which can be very harmful to humankind, biologically as well as chemically. The solids can be classified by their size and state as settleable, suspended, colloidal, or dissolved. The solid phase transported by rivers and streams usually consists of about 85% suspended matter, 10-15% settleable detritus, and some floating material. Thus suspended matter predominates with about 80% inorganic components and 20% organic substance (Eppler et al., 1975; Hariganesh et al., 2020; Hassanien, 2004). Turbidity removal has been identified as the major problem in community water supply plants to produce clean and safe drinking water, in industries, and whenever water of high quality is required. Consequently, turbidity set as one of the main indicators of the quality of tap water and it has been set a maximum value on the guidelines for drinking water quality by World Health Organization (WHO) at 1 nephelometric turbidity units (NTU) for acceptable turbidity in treated water (WHO, 2017).

Coagulation and flocculation processes that are usually included in conventional water treatment are well-known techniques of solid-liquid separation. They are characterized by several advantages, including cost-saving, easy to operate, and high performance for turbidity removal, which will in turn effectively minimize the risk of water-borne diseases and prevent the clogging of filters to produce large amounts of water (Aboubaraka et al., 2017). Suspended particles are first destabilized using hydrolyzed metals/salts (such as Al or Fe) and further gathered to form large aggregates, called flocs, during flocculation. After that, the agglomerates can be separated via setling, filtration, centrifugation or other separation techniques.

The design of coagulation-flocculation process is generally based on the concept of global velocity gradient (G), which was first developed by Camp and Stein (1943) and the contact time, t_{cont}, that is the second important parameter. Together, velocity gradient and contact time control the probability of aggregation and break-up of flocs (Clark, 1985; Cleasby, 1984; Garland et al., 2017; T. Kramer and Clark, 1997a; Marques and Ferreira, 2017; Mohammed and Shakir, 2018). The Camp and Stein criteria (G·t_{cont}) recommended achieving efficient flocculation is usually in the range of $10^4 < Gt_{cont} < 10^5$.

For the design of the jet clarifier, the mixing zone is controlled by the velocity gradient (G) that is occurred by liquid flow, liquid velocity with turbulent shear force (hydrodynamic), and flow phenomena, and residence time (τ) in each section play an important role to control the mixing mechanisms. Besides the velocity magnitude, the residence time in each section is also essential since large residence time is required to increase the contact opportunity among coagulated particles to form large flocs, that are more easily separated in the sedimentation zone. Consequently, the performance of jet clarifier not only depends on physicochemical conditions, including coagulant type and dosage, solution temperature and pH, but also on hydrodynamic phenomena because it is the main conditions to be designed and controlled the system (He et al., 2018; Huang et al., 2016; Yang et al., 2016; T. Zhou et al., 2014). Moreover, few studies have focused on local key parameters of each part that affect turbidity removal efficiency and also the existing

hydrodynamic models have not been assessed and evaluated yet in order to revise the design guideline.

Thus, this work intends to fulfill the gap by investigation concerning the performance of the jet clarifier into two distinct phases. In the first phase, experiments were conducted to arrive at an appropriate configuration of the reactor. Two sizes of 3D jet clarifiers are operated and sensitivity analysis of turbidity removal efficiency to geometrical parameters are investigated. In order to have a more in-depth assessment of the performance of the jet clarifier, a third pilot, called Quasi-2D pilot, was designed, in order to investigate velocity fields by using particle image velocimetry (PIV) and size distribution of flocs formed in the flocculation zone. The objective is to understand the link between floc size distribution (which controls turbidity removal efficiency) and hydrodynamics.

Finally, the flow in the 3D jet clarifier is simulated using a CFD software package, FLUENT version 16.2.

Research objectives

- To investigate the effect of liquid flow rate and reactor configuration on hydrodynamics in the jet clarifier
- To investigate the effect of flow rate on the properties of flocs and turbidity removal efficiency
- To propose the key variables for scale-up/scale-down of the jet clarifier
- To determine the optimal operating condition and design criteria for jet clarifier for effective turbidity removal

Research hypothesis

- Increasing the liquid flow rate decreases the turbidity removal efficiency by increasing the velocity gradient in the flocculation zone where smaller flocs are produced

- Enlarging the truncated cone base diameter in a jet clarifier can generate bigger flocs due to increasing the floc recirculation rate resulting in higher turbidity removal efficiency.
- Decreasing the size of the jet clarifier decreases the turbidity removal efficiency by reducing length dimension resulting in smaller Re number that directly corresponds to the velocity gradient of the reactor

Expected Outcome

- Understanding liquid flow (hydrodynamics) and its relation to turbidity removal efficiency
- Obtain appropriate key parameters in order to achieve the optimum design criteria and operation conditions of jet clarifier

Thesis Structure

The document is divided into 6 chapters along with references and an appendix. Details of each chapter can be expressed as follow:

Chapter 1 (Overview on Turbidity Removal in Water Treatment Plant and Reactor Design) contains a review of the scientific and technical literature about turbidity removal efficiency, including physicochemical effects. In the first part, the general information of water treatment and raw water characteristics are introduced. The second one presents the as mechanical and physical phenomena arising in coagulation and flocculation. The third part presents the property of flocs (size, distribution…) and how to monitor them by in-situ techniques. Then, the sedimentation related to turbidity removal efficiency is explained. The last part of this chapter deals with the basics of hydrodynamics and reactor design.

Chapter 2 (Experimental Methods and Analysis) outlines the experimental set ups, as well as the different kinds of suspensions. The strategy of the experimentation plan consists in coupling of global and local analysis. The global analysis includes turbidity removal efficiency and mean residence time distribution are discussed. The local analysis

aims at measuring local velocity gradient and floc size distribution in flocculation zone by particle image velocimetry (PIV) and shadowgraphy technique.

Chapter 3 (Experimental Analysis of Small Scale and Large Scale Prototype: Turbidity Removal and Residence Time Distribution) is dedicated to evaluation of the performance for two different protypes (Small Scale and Large Scale). Furthermore, Residence Time Distribution (RTD) methods is used to connect the results among the different experiments and scales for a better understanding of the global hydrodynamic condition in the jet clarifier.

Chapter 4 (Experimental Analysis of the Q2D Pilot: Particle Image Velocimetry (PIV) and Floc Size Distribution) consists of two parts. The first part utilizes Particle Image Velocimetry (PIV) to determine the local parameters, especially the velocity gradient that is one of the crucial parameters that affect flocs aggregation. The latter part uses the shadowgraphy technique to observe the floc size distribution. The effect of hydrodynamics on the flocs aggregation is depicted in this part.

Chapter 5 (Computational Fluid Dynamic (CFD)) presents the simulation results of the hydrodynamics and the RTD in the Small Scale Prototype (SSP) and consider upscaling based on CFD.

Finally, Chapter 6 presents the overall research conclusion of the study conducted in this thesis, highlighting the novel findings and concluding with recommendations for further work, along with bibliographies and appendixes.

CHAPTER 1

OVERVIEW ON TURBIDITY REMOVAL IN WATER TREATMENT PLANT AND REACTOR DESIGN

The information in this chapter is intended to introduce water systems that treat surface water resources. These systems have to deal with complicated processes, which consist of coagulation, flocculation, sedimentation, filtration, and disinfection processes. In this thesis, the field of flocculation process was considered as the main subject. Thus, the study especially focuses on this process and parameters and factors which affect the process.

1.1 Introduction to Water Treatment

1.1.1 The Conventional Water Treatment Process

The practical objective of water treatment process is to obtain sanitary water by extracting pollutants, removing toxicants, eliminating particles, and killing pathogens. This system concept is also used to treat water for specific applications, such as an industrial plant, boiler water and cooling water. Despite the same design concept, the water treatment processes depend on raw water quality, technology, and quality of effluent water. The conventional process of water treatment consists of two steps: water clarification and disinfection. Clarification refers to the sequence of operations used to remove suspended matter which consists of large solid particles be able to settle by gravity without any external aid and non-settleable material, often colloidal in nature. Colloidal particles are generally eliminated by coagulation, flocculation, and sedimentation. The combination of these three processes is referred to as conventional clarification. Disinfection is the final stage in water treatment before its distribution; it is developed to remove pathogenic micro-organisms and also all the dissolved pollution from the water. An example of the water treatment plant can be seen in Figure 1.1.
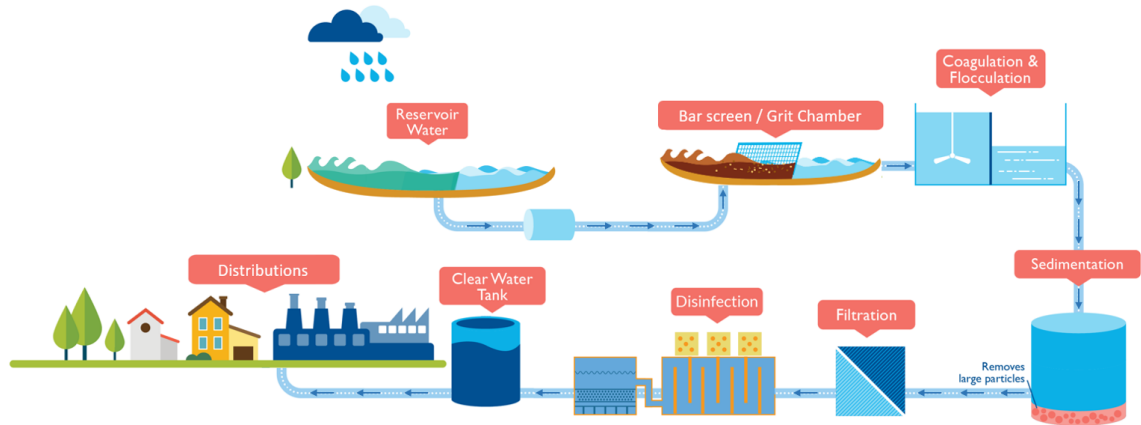
Figure 1.1 Conventional water treatment process schematic (adapted from PUB®)

In coagulation, coagulant is added to raw water and mixed in the rapid mixing in order to be homogeneously dispersed in the whole vessel. The coagulant destabilizes negatively charged particles, colloidal contaminants. During flocculation, slower mixing promotes the rate of particle collision; the destabilized particles are further aggregated into larger particles, known as flocs. Flocculation is affected by several parameters, including the effective coagulant, dosage rates, pH, velocity gradient (G) and contact time (t_{cont}) (Mohammed and Shakir, 2018; Moran, 2018; Ramphal and Sibiya, 2014). Following flocculation, agglomerated particles enter the clarification unit where they are removed by sedimentation or by flotation. In the sedimentation process, the flocs are removed by settling; particles that cannot settle are removed during the next filtration process.

Nowadays, a combination of coagulation, flocculation, sedimentation, and sludge removal is the most widely applied water treatment technology, usually called as solid contact clarifier (Ghawi and Abudi, 2012; Qasim et al., 2000b; T. Zhou et al., 2014). Moreover, there are two parameters frequently used to describe the clarification process: the overflow rate and the detention time that are related to the contact time and velocity gradient due to hydrodynamics inside the reactors (EPA, 2019; Kawamura, 2000). Typical detention times range from 1 to 2 hours, although many units require up to 4 hours for full-scale surface water treatment (Degremont, 2007; Qasim et al., 2000b).

1.1.2 Solids Contact Clarifier

Solids contact clarifier is generally used to remove solid particulates or suspended solids from liquid for clarification and/or thickening. It usually works continuously. The settled flocs at the bottom of the tank, are known as sludge, while the particles that float to the surface of the liquid are called scum. Solids contact clarifier is a combination reactor that gathers in one single unit: a mixing zone for coagulation and flocculation, solids-water-separation, and continuous removal of sludge it. The steric hindrance is thus greatly reduced compared to conventional equipment. To design a mixing zone, the mean velocity gradient (G) and contact time (t_{cont}) are the key factors (Degremont, 2007; Kawamura, 2000; Qasim et al., 2000b) whereas the velocity of water related to resident time is the key factor for the settling zone (Degremont, 2007; Svarovsky, 2000). To accomplish the sedimentation, the resident time should be larger than the settling time of flocs, that related to the gravity and buoyancy force acting on the flocs.

Two main types of clarifiers are the sludge blanket and sludge recirculation clarifier as shown in Figure 1.2 (a and b). The existing sludge in the clarifiers is used to make different actions for the system; for the sludge blanket, the sludge blanket acts as a filter since the small-suspended particles and flocs enter the reactor through the sludge blanket, then flocs stick with the blanket. On Figure 1.2. (a), number 9 is the coagulated water distribution pipe, and number 4 is the sludge blanket. In the sludge recirculation clarifiers, coagulated water is injected through the flocculation zone mixed with flocs recirculated to promote agglomeration. Moreover, on the Figure 1.2. (b), the sludge deposited in the settling zone (n°2) returns to the central mixing zone (n°1) by the induced flow. The previous resulting recirculated flocs can be a target to allow the rapid flocculation and the formation of a dense precipitate. The jet clarifier used in this research is a sludge recirculation unit with a static mixer for destabilization (coagulation). The details are presented in Chapter 2.

1. Raw water inlet	7. Vacuum pump or fan
2. Clarified water outlet	8. Automatic vacuum breaker valve
3. Sludge removal	9. Raw water distribution perforated pipes
4. Stilling baffles	10. Sludge concentrators
5. Top layer of sludge blanket	11. Reagent injection
6. Vacuum pump chamber	12. Float switch

Zone 1 : flocculation   zone 2 : sedimentation

a) Sludge blanket clarifiers   b) Sludge recirculation clarifiers

Figure 1.2 A schematic of (a) sludge blanket clarifiers and (b) sludge recirculation clarifiers (Degremont, 2007)

1.2 Raw Water Characteristics

The natural water is obtained from 4 major reservoirs, i.e., ground water, surface water, brackish water, and seawater. Surface water thus constitutes approximately 80 percent of the water used on a daily basis (Mullen, 2020). Thus, nowadays, the primary resources of raw water for water treatment plants are surface water.

The chemical composition of surface water depends on the nature of the terrain surrounding the reservoir. Along its path, the water stream dissolves the various elements that constitute the terrains, especially soil erosion and leaching. Therefore, three main characteristics of raw water are described in this content: pH, alkalinity and turbidity.

1.2.1 pH

The definition of pH is a measure of hydrogen ion concentration or a measure of the acidity or basicity of a solution. The pH value is also a key factor of coagulation and flocculation process; not only does it impact the form and surface charge of coagulants utilized, but also the selfsame parameters for the impurities that are to be removed. In the

literature, "coagulation" usually stands for the destabilization of particles while "flocculation" denotes to aggregate (floc) formation (Naceradska et al., 2019). In relation to aluminium-based salt that is the most frequently utilized coagulants, pH values influence hydrolysis, polymerization and the resultant species. In brief, at low pH values, < 4.5, (see Figure 1.12) Al^{3+} ions occur as hexaaqua complexes $[Al(H2O)6]^{3+}$ in an aqueous medium (Duan and Gregory, 2003). Hydrolysis takes place alongside the increase in pH, forming species with an ever greater reduction in charge. Besides hydrolysis, formation of amorphous precipitates of $Al(OH)_3$ occurs. The pH value is calculated using the Equation 1.1.

$$pH = -\log[H^+] \qquad\qquad \text{Equation 1.1}$$

The pH value has a significant effect on the stabilization of colloidal suspensions because the surface charge of the colloids and the predominance of a particular hydrolysis species of coagulant are largely dependent on pH (Bratby, 2016). The optimal pH range for coagulation is 6 – 7 for aluminium sulfate (alum) coagulant, and for ferric coagulants the optimum pH range is 5.5 – 6.5 (Cao et al., 2010; Saxena et al., 2018; Sohrabi et al., 2018). Normally, the pH of natural water varies from 6 – 8.5 and it is related to alkalinity as well (Alshikh, 2007). For this reason, finding optimal dosage of coagulant by Jar test technique is required to optimize turbidity removal.

1.2.2 Alkalinity

The definition of alkalinity is a chemical measurement of a water's buffering ability. In the water, the significant contributions to alkalinity are the carbonate species, which are bicarbonate (HCO_3^-) and carbonate (CO_3^{2-}), and any free ion, which is hydroxide (OH^-), and hydrogen ion (H^+) as shows in Equation 1.2. (Mackenzie L. Davis, 2010; Patel and Vashi, 2015; Singh and Dara, 2004) and it is reported as mg/L as $CaCO_3$ since most alkalinity is derived from the decaying of carbonate minerals (Snoeyink and Jenkins, 1980).

$$\text{Alkalinity} = [\text{HCO}_3^-] + 2[\text{CO}_3^{2-}] + [\text{OH}^-] + [\text{H}^+] \qquad \text{Equation 1.2}$$

where [ ] refers to concentrations in moles/L.

Moreover, in most natural water characteristic (pH 6 to 8), the hydroxide (OH^-), and hydrogen ion (H^+) are negligible (Mackenzie L. Davis, 2010), so that it can be express as Equation 1.3.

$$\text{Alkalinity} = [\text{HCO}_3^-] + 2[\text{CO}_3^{2-}] \qquad \text{Equation 1.3}$$

Alkalinity is also directly related to water hardness, which is determined by the concentration of multivalent cations (primarily Ca^{2+} and Mg^{2+}) in the water. Alkalinity is essential to make the reaction with coagulant occur and let the coagulation mechanisms proceed. During the process, alkalinity is consumed by added coagulant (Ogedengbe, 1984; Sahu and Chaudhari, 2013). Since most kinds of coagulants are acidic so that alkalinity is consumed, and pH value is decreased for two reasons: bicarbonate consumption and carbonic acid formation. For instance, the reaction between alum (coagulant) and alkalinity is shown by Equation 1.4 (Ravina, 1993).

$$\text{Al}_2(\text{SO}_4)_3 + 3\text{Ca}(\text{HCO}_3)_2 + 6\text{H}_2\text{O} \rightarrow 3\text{CaSO}_4 + 2\text{Al}(\text{OH})_3 + 6\text{H}_2\text{CO}_3 \qquad \text{Equation 1.4}$$

Therefore, alkalinity plays an important role in the enhanced coagulation to remove turbidity and natural organic matter (NOM) from water (Ye et al., 2007).

1.2.3 Turbidity

Turbidity is not a kind of contaminant in water, but its property represents the summation of other contaminants, with the advantage of cheaper and easier measurement than biological oxygen demand (BOD), chemical oxygen demand (COD), suspended solids (SS), dissolved solids, among others (Miljojkovic et al., 2019). Moreover, it is an indicator of the cloudiness of water and the level of water quality resulting from clarification

processes (Al-Husseini et al., 2019). It can be reported in NTU (Nephelometric Turbidity Units). Turbidity in water is caused by fine suspended particles, including silt and clay, well-known as colloid (Aboubaraka et al., 2017). For these reasons, turbidity is one of the crucial parameters used to control the quality of water; to meet the WHO's guidelines, the turbidity should ideally be kept below 1 NTU (WHO, 2017). This is achievable in large well-run municipal supplies, which should be able to achieve less than 0.5 NTU before disinfection and an average of 0.2 NTU or less, irrespective of source water type and quality. Sedimentation may remove suspended solids and reduce turbidity by about 50 to 90 percent, depending on the nature of the solids, the level of pretreatment provided, and the design of the clarifiers. Common values are in the range of 60 to 80 % (Hudson, 1981; Oregon Public Health Division, 2021).

In this study, not only natural surface raw waters are used to examine the performance of jet clarifiers but also the turbid synthetic raw water that were synthesized by mixing bentonite with tap water. Among the wide range of applications of clay minerals, bentonite has been used to create synthetic suspensions in coagulation and flocculation studies since it represents natural surface water turbidity appropriately (Barbot et al., 2010; Shaikh et al., 2017; Wilkinson et al., 2018).

1.2.3.1 Colloids in Natural Raw Water

Solids are present in raw water under three main forms: suspended particles, colloids. Suspended particles, such as sand, vegetable matter and silts, range in size from massive particles down to particles with a typical dimension of 10 µm. Figure 1.3 illustrates the size ranges of solids in water. Colloids are very fine particles, generally ranging from 10 nm to 10 µm. There are two types of colloids: hydrophilic and hydrophobic colloids. Hydrophobic colloids, including clay and non-hydrated metal oxides, are unstable and thus are easily destabilized whereas hydrophilic colloids like soap are stable.
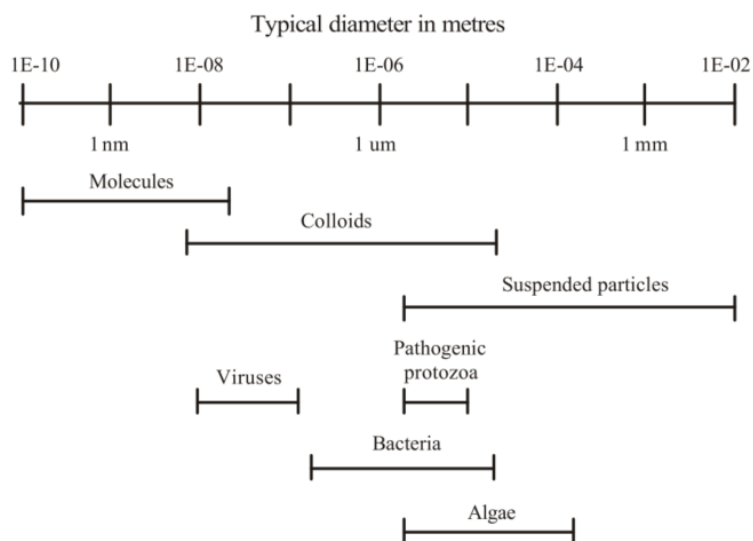
Figure 1.3 Size range of particles of concern in water treatment
(Koohestanian et al., 2008)

1.2.3.2 Bentonite

Bentonite, a montmorillonite based material, is a particularly common colloidal clay contaminant found in natural surface water (Barbot et al., 2010; Shaikh et al., 2017). The bentonite is a hydrated aluminum silicate under the form of rough thin hexanal platelets. Its structure comprises of three layers, which is a central octahedral layer of alumina surrounding with two outer tetrahedral layers of silica (SiO_2) as shown in Figure 1.4. The octahedral Al^{3+} ions in the structure tend to isomorphic substitution with metal ions like Fe^{2+} and Mg^{2+} of a lower valence. Likewise, the tetrahedral Si^{4+} ions can also be used to be instead of by Al^{3+} or Fe^{3+} ions. The result of the substitutions, a net negative charge is over the structure that is balanced usually by exchangeable cations (e.g., Na^+ and Ca^{2+}) along with water molecules that may surround the bentonite structure. In most bentonites, Ca^{2+}, is found to be a sufficient exchangeable ion. Few carry ions like Na^+, H^+, and K^+ (Hunter, 2001).

Bentonite plates have amphoteric properties and the surfaces carry an enduring negatives charge and depending on the pH, and there is a net positive charge on the edges

(Shaikh et al., 2017). The bentonite structure and the rheology of the suspension are solidly affected by a change of the electrolyte and/or pH. Consequently, when plate-like clay particles such as bentonite flocculates, three different modes of particle association may occur: they are face-to-face, edge-to-face, and edge-to-edge. The face-to-face association leads to thicker and larger flakes, while the edge-to-face and the edge-to-edge association lead to three-dimensional voluminous 'house-of-cards' structures (Luckham and Rossi, 1999; Wilkinson et al., 2018). The range of particle size distribution of bentonite is 5 – 105 μm (Baik and Lee, 2010; Karimi and Salem, 2011; Luckham and Rossi, 1999).
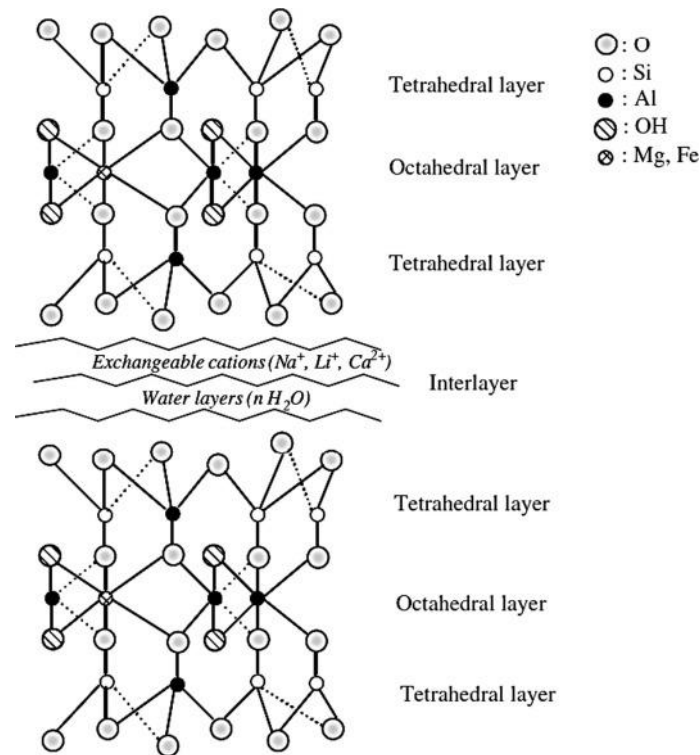
Figure 1.4 Bentonite structure (Luckham and Rossi, 1999)

1.2.3.3 Colloids and Its Dynamic Stability

Colloids present in raw surface water have an equivalent spherical diameter between 10 and 10,000 nm, and usually have very high negative charges (Kretzschmar, 2005; E. Lee, 2019; National Research Council (US) Safe Drinking Water Committee,

1977). Due to the small particle size and their negative surface charge, the suspension of colloids is generally stable. This stability is the result of interparticle forces that consists of van der Waals forces and electrostatic forces (Adair et al., 2001). Such colloidal systems can be described by electric double layer and DLVO theory, which was first introduced by Derjaguin, Landau (1941), Verwey and Overbeek theory (1948) (Ohshima, 2014).

(i) Electric Double Layer

The electric double layer plays a fundamental role in the electrostatic stabilization. As shown in Figure 1.5, a first layer, called Stern layer, includes ions directly adsorbed at the particle surface. In the case of a negatively charged particle, the Stern layer is composed of counter-ions that are positively charged. The second layer, whose limit is the slipping plane, is a diffusive layer made of negative ions. The concentration of ions is high near the surface of the particle and decreases progressively.

The electro kinetic potential of the slipping plane is defined as "zeta potential" (ζ), which is a very important parameter in the theory of interaction of colloidal particles. The higher the ζ value means the greater of the repulsive force between particles. Equation 1.5 is the mathematical equation that can be used to express zeta potential (T. D. Reynolds and Richards, 1996).

$$\zeta = \frac{4\,\pi\,\psi\,\mu}{\varepsilon} \qquad\qquad \text{Equation 1.5}$$

Where Ψ is electrophoretic mobility. Dynamic viscosity (μ) and dielectric constant (ε) are both temperatures dependent. Thus, the seasonal variation of temperature leads to greater zeta potential value in winter.

The zeta potential can be experimentally measured and reflects the effective charge on the particles. For $\zeta < 10$ mV the suspension is unstable whereas for $\zeta > 30$ mV the suspension is stable.
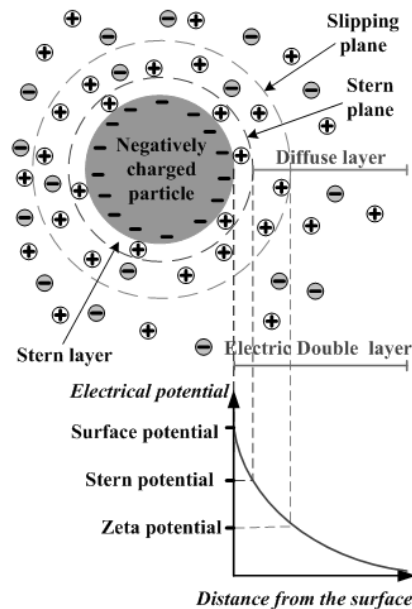
Figure 1.5 Double Layer theory

(Kopeliovich, 2019)
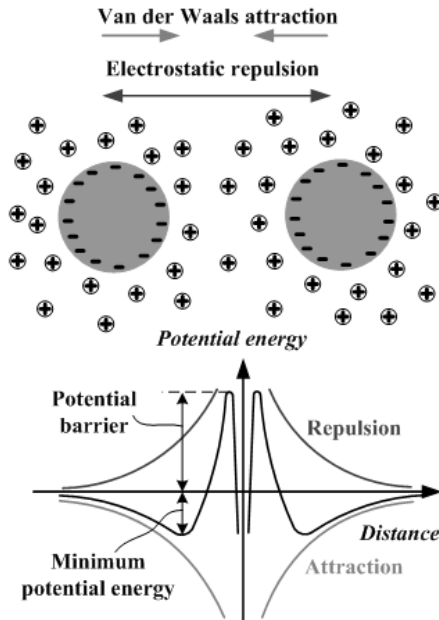
Figure 1.6 DLVO theory

(Kopeliovich, 2019)

In brief, the magnitude of the zeta potential (ζ) is usually used to indicate colloidal stability. The higher the zeta potential, the greater are the repulsion forces between the colloidal particles and, therefore, the more stable is the colloidal suspension. A high zeta potential represents strong forces of separation (via electrostatic repulsion) and a stable system, i.e., particles tend to suspend. Repulsion forces keep them apart from each other, thus the colloids stay in suspension as isolated particles. Low zeta potential indicates relatively unstable systems, i.e., particles tend to aggregate.

(ii) DLVO Theory

As two particles approach each other in suspension, their diffuse double layers begin to interact. Two main forces apply: Van der Waals force and repulsive force. The equilibrium force balance between both forces is the cause of the stability of the suspension of colloids. DLVO theory explain how the interparticle repulsion energy (V_R) and the van der Waals attractive energy (V_A) interact, as shown in Figure 1.6 describing the potential energy of the interaction between two particles.

The repulsive potential or repulsive energy (V_R) between two clay platelets can be computed from the DLVO theory as Equation 1.6 (Luckham and Rossi, 1999).

$$V_R = \frac{64\, \rho\, k_B T_{temp}}{X} \left(\tan H_c \frac{ze\Psi_s}{4k_B T_{temp}} \right)^2 e^{-KH} \qquad \text{Equation 1.6}$$

$$K = \sqrt{\frac{2e^2 \rho z^2}{\varepsilon_0\, k_B\, T_{temp}}} \qquad \text{Equation 1.7}$$

Where ρ is counterion density, k_B is Boltzmann constant, T_{temp} is absolute temperature, H_c is the distance between the center of two particles, Ψ_s is Stern layer potential, e is the electron charge, κ is reciprocal Debye length, z is the valence of the ion, and ε_0 is the dielectric constant of the medium.

The repulsive potential decreases exponentially with increasing the distance between particles, and the range of repulsion is largely reduced with electrolyte concentration.

Whilst intermolecular attraction consists of three type forces that are recognized: dipole-dipole interaction; induced dipole-dipole interaction and attractive forces between non-polar molecules or London dispersion forces, which are due to the polarization of one molecule by fluctuations in the charge distribution in the second molecule, account for nearly all of the van der Waals attraction in colloidal systems. The attractive energy between two semi-infinite flat plates of particles may be expressed by Equation 1.8.

$$V_A = -\frac{A_{HC}}{12\pi} \left(\frac{1}{H_s^2} + \frac{1}{(H_s + 2t_n)^2} - \frac{1}{(H_s - t_n)^2} \right) \qquad \text{Equation 1.8}$$

Where H_s is the distance between the surfaces of the plates and t_n is the thickness of the platelet.

The Hamaker constant (A_{HC}) depends on the nature of the material of the particles. In the case where the liquid is the dispersion medium, rather than a vacuum, this constant must be replaced by an effective Hamaker constant, calculated from Equation 1.9.

$$A_{HC} = \left(\sqrt{A_2 + A_1}\right)^2 \qquad\qquad \text{Equation 1.9}$$

where A_1 refers to the dispersion medium and A_2 to the particles.

The total interaction energy (V_{Net}) is the sum of the repulsive potential and attractive potential as shown in Equation 1.10.

$$V_{Net} = V_R + V_A \qquad\qquad \text{Equation 1.10}$$

A representation of V_{Net}, V_R, and V_A as a function of the interpolate separation for low electrolyte concentrations ($< 10^{-2}$ M) and high surface potentials (> 50 mV) is shown in Figure 1.7 (Luckham and Rossi, 1999).
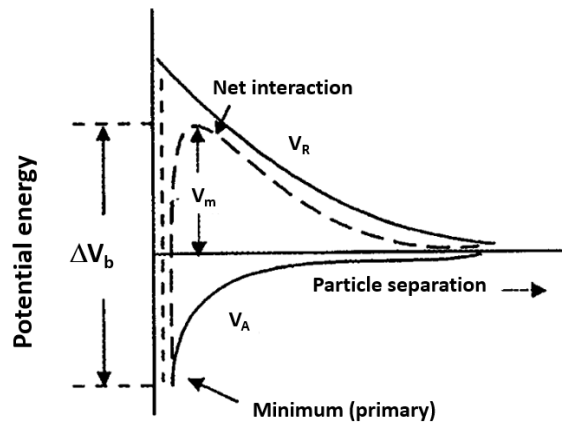
Figure 1.7 Net interaction energy V_{Net} for parallel flat plates
as a function of particle (plate) separation (Luckham and Rossi, 1999)

The significant influence is the occurrence of maximum energy (V_m) at intermediate distances, which is considered as an energy barrier that the particles must overcome to get closer. The height of V_m; therefore, determines the relative stability of the

system. The barrier to redispersion can be represented ΔV_b. At large interparticle separations, a secondary minimum may occur since V_R falls off more rapidly with increasing distances than V_A. Particle coagulation taking place here is relatively reversible since the minimum is quite having only a short distance between particles.

The cations (Na^+) of the montmorillonite particles establish diffuse ionic layers surrounding them and create an electrostatic repulsion between the particles. V_m can be reduced by adding electrolytes in the system or an increase in temperature so that the clay particles can come into contact with one another and agglomerate.

The extent to which the particles become flocculated depends on the degree of compression of the double layer, which is dominated by the concentration and valence of the ions of opposite sign to the particle charge. A low concentration of electrolyte produces slow coagulation, which is retarded by a long-range repulsion. In contrast, high electrolyte concentration attraction predominates at any particle distance except at very close approach. In this case, particle agglomeration occurs at a maximum rate and this process is called rapid coagulation (Luckham and Rossi, 1999).

The minimum of the potential energy determines the distance between two particles corresponding to their stable equilibrium force. The two particles form a loose aggregate, which can be easily re-dispersed. However, strong aggregation is needed as larger particles have higher settling velocity, which enhances turbidity removal efficiency. The strong aggregation may be formed at a shorter distance corresponding to the primary minimum of the potential energy.

In the case of clay colloids, the negative charge is a consequence of imperfection within the interior of the crystal lattice and the negative charge is constant because its surface charge arises from isomorphous substitution. In order to obtain strong aggregation, the particles should be overcome the potential barrier by reducing the negative charge on the surface of particles. This methodology is known as the destabilized of the colloidal dispersion.

1.3 Physico-Chemical Phenomena of Coagulation

To eliminate turbidity in water, colloids and other fine particles are brought together and agglomerated to form larger size particles, called floc that can be afterwards be removed by filtration or sedimentation (Shammas, 2007). Coagulation is the chemical process to decrease or neutralize the negative charge on suspended particles (it corresponds to a diminution of the zeta potential) (Brandt et al., 2017). To that end, a coagulant is injected. This is necessary to ensure the coagulant is thoroughly mixed into the process flow to maximize its effectiveness. Thus, coagulation is often called as rapid mixing and usually has a short detention time in the rapid mixing tank or static mixer. Afterwards, the destabilized colloids or particles gathered into larger aggregates (Suopajärvi, 2015) as shown in Figure 1.8.
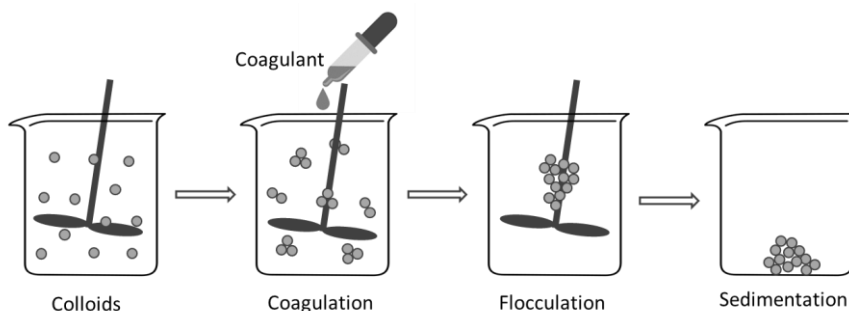
Figure 1.8 Coagulation, Flocculation, and Sedimentation processes

1.3.1 Mechanisms

According to (O'Melia, 1978), four classical mechanisms are used to describe coagulation and flocculation mechanisms:

- Modification of medium characteristics: Compression of the double layer.

- Modification of colloid particle characteristics: Adsorption and charge neutralization.

- Provide bridges with enmeshment in a precipitate (sweep flocculation)

- inter-particle bridging.

The different mechanisms can act at the same time. Moreover, coagulation mechanisms depend on specified pH and coagulant dosage (American Water Works, 1999). Each mechanism is discussed as follow:

1.3.1.1 Double Layer Compression

The mechanism is achieved through the addition of a coagulant (electrolyte) into a suspension of colloids as colloids can be destabilized by coagulants that have the ions, which contain the opposite charge to the suspension. The opposite charges are attracted to the area surrounding the outside of the particle referred to as the diffuse layer (see the topic of 1.2.3.3(ii)). As the counter-ions are pushed closer to the surface so that the diffuse layer becomes compressed then the repulsion force becomes smaller. The coagulating power of ions increases in the ratio of 1:10:1000 as the valence of the ions increased in the ratio from 1 to 2 to 3 as follows the Schulze-Hardy rule. Thus, the efficiency of coagulation increases sharply with increasing ion charges. The minimum concentration of ions, which causes rapid coagulation of colloids known as the critical coagulation concentration (ccc.) (Degremont, 2007; Sano et al., 2000).

1.3.1.2 Adsorption and Charge Neutralization

Some chemical species are capable to adsorb at the surface of colloidal particles. If the adsorbed species carry a charge opposite to that of the colloids, it reduces the surface potential and results in destabilization of the colloidal suspension. Reduction of surface charge by adsorption is different from reduction by double-layer compression because the adsorbed species are capable to destabilize colloids at much lower dosages than double-layer compression. Destabilization by adsorption is stoichiometric; it means that the required dosage of coagulant increases as the concentration of colloids increases. Nevertheless, the coagulant dosages added are possible to overdose, so a system will be able to adsorb species and cause re-stabilization due to a reversal of charge on the colloidal particle.

Practically, to distinguish colloidal particles that have been precipitated in solution between surface precipitation and the attachment of colloidal hydroxide particles is quite tricky. A combination of these effects may be most likely in practice and forms the basis of the precipitation charge neutralization model, which is illustrated schematically in Figure 1.9.
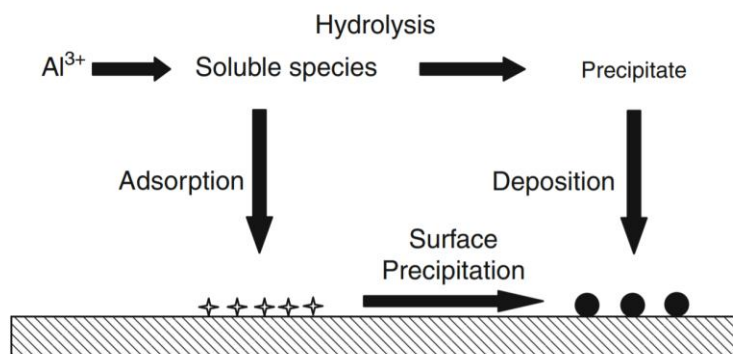
Figure 1.9 Schematic picture showing the precipitation charge neutralization model (John Gregory, 2013)

1.3.1.3 Sweep Flocculation

Sweep flocculation can be described as large aggregates when coagulants are added to water or wastewater in enough amounts and would normally form precipitates. Sweep flocculation almost repeatedly leads to faster aggregation than charge neutralization and gives stronger and larger flocs because the production of a hydroxide precipitate gives a significant increase in the effective particle concentration, hence a greater collision rate, according to Smoluchowski theory, and its formation remains extremely dependent on the operating conditions (pH when a hydrolysable metal salt is used) (Bratby, 2016; J. Gregory, 2016). The flocculant especially cationic hydrolysis form is added, hydroxide ions may adsorb on particles, either as soluble species or precipitate (see Figure 1.9), but under suitable conditions, an amorphous hydroxide precipitate forms, which entangles the particles. A schematic picture of the process is given in Figure 1.10.
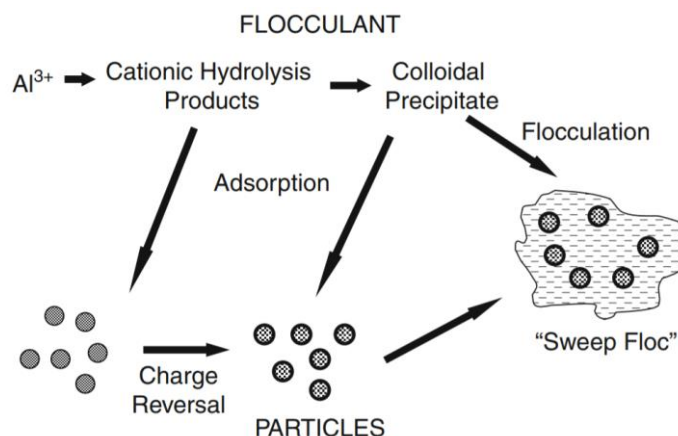
Figure 1.10 "Sweep flocculation" by precipitated hydroxide (John Gregory, 2013)

Figure 1.10 shows that the colloidal particles can be entrapped by the precipitates and settle with them. Removal of colloids in this manner is frequently referred to as sweep-floc coagulation, which is the most crucial mechanism in water treatment (Brandt et al., 2017). Several characteristics that are not similar to sweep-floc coagulation from double-layer compression and adsorption are as follows:

- At low colloid concentrations, a large excess of coagulant is required to produce a large amount of precipitate that can entrain the colloidal particles to settle down. At high colloid concentrations, amount of coagulation required is low because the colloids serve as nuclei to enhance the precipitate.

- Optimum coagulation conditions do not correspond to a minimum zeta potential but depend on pH and solubility-pH relationship for each coagulant.

For instance, sweep flocs in water treatment process are commonly described as large aggregates of aluminium hydroxide ($Al(OH)_3$) or ferric hydroxide ($Fe(OH)_3$) that are formed when the coagulants alum [$Al_2(SO_4)_3$] or ferric chloride ($FeCl_3$) are added in high enough concentration, they will react with water (and hydroxides (OH^-)) to form metal hydroxide precipitates. Previous researchers found that sweep flocs formed in any conventional water treatment process were positively charged (Dentel et al., 1988; Djamel Ghernaout and Ghernaout, 2012). Since the point of zero charge (PZC) of $Al(OH)_3$ and $Fe(OH)_3$ is approximately 8.5; while PZC of silica and kaolin is about 2 and 4, respectively

(Rattanakawin, 2005). Therefore, the colloidal particles in natural surface raw water are electrostatically attached to the sweep flocs in the neutral pH water (Ghernaout and Ghernaout, 2012).

A major advantage of sweep flocculation is that this mechanism does not depend on the character of impurity particles to be removed, whether bacteria, clays, oxides, or others. Moreover, the optimum coagulant dosage is important since it gives the most rapid hydroxide precipitation and is practically independent of the character and concentration of suspended particles (J. Gregory, 2016).

1.3.1.4 Adsorption and Inter-Particle Bridging

Many different natural compounds such as starch, cellulose, polysaccharide gums, protein materials, as well as a wide variety of synthetic polymeric compounds are effective coagulating. These compounds have large and long molecular structures that can attach to colloidal particles at one or more sites due to attractive and van der Waals force (in case of the polymer and particle are opposite charge), ion-exchange, and hydrogen bonding. Thus, that the flocculants of this kind act to bridge dispersed particles. They bind to oppositely charged particles, but the length of the polymer must extend beyond the length of the particle so as to bridge more particles. The process continues with the binding of the next polymer, and until all of the particles have clumped together (Figure 1.11). This bridging action results in the formation of a floc particle having favorable settling characteristics.

| Suspended particles (negatively charged) | Polymer (positively charged) "flocculant" | Particles start to "flock" and second layer of flocculation starts | Bridging of particles to form a "flock" |
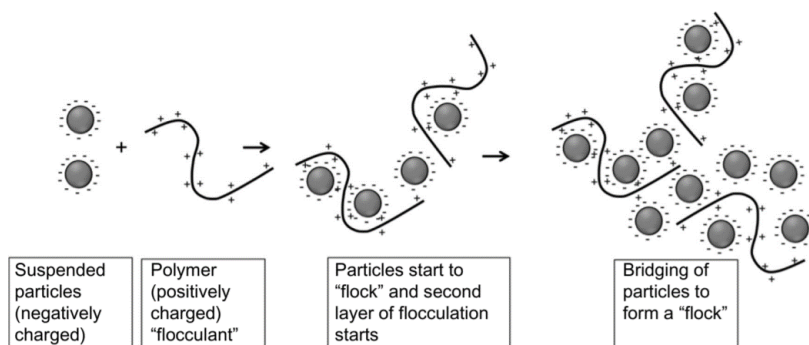
Figure 1.11 Schematic overview of the process of adsorption and inter-particle bridging flocculation (O'Kennedy et al., 2016)

In the case of no other particle available or if there is an overdose of polymer, the free extended portions of the polymer molecule would cover around the same original particle, which could effectively bring about the re-stabilization of the colloids (D. Ghernaout et al., 2011). Re-stabilization can also ensue due to aggressive mixing or extended agitation, which may destroy the interparticle bridging and allow fiber of polymer of fold around the same original particles.

1.3.2 Coagulants

As mention earlier, the coagulants added into water typically destabilize colloids by a single mechanism or a combination of four mechanisms: compression of the double layer, counterion adsorption and charge neutralization, interparticle bridging and enmeshment in a precipitate (Qasim et al., 2000; Suopajärvi, 2015).

Coagulants are mostly metal salts added to the water either to break down the stabilizing forces or enhance the destabilizing forces. The common coagulants are mostly metal salts and are classified into two general categories, which based on aluminium and iron, which is hydrolyzing rapidly in waste to form cationic species when the alkalinity in water is enough to be adsorbed by negatively charged of particles, resulting in simultaneous surface charge reduction (Suopajärvi, 2015). The most common coagulant that is widely used in the water treatment is aluminium sulfate, alum, $(Al_2(SO_4)_3 \cdot nH_2O)$ due to its availability, low cost, and effectiveness in terms of turbidity removal (Bratby, 2016; Sahu and Chaudhari, 2013; Saritha et al., 2019). The form of floc depends on the chemical characteristic of the water, especially its pH, the coagulant type, and dosage.

1.3.2.1 Aluminium Sulfate (Alum)

Aluminium sulfate is widely used as coagulant in water treatment plants for coagulation (Degremont, 2007). Aluminium sulfate has a complex chemistry, and many solid different species are crystallized in aqueous aluminium sulfate environments. This complexity means that alum is also very versatile and conditions can be manipulated to attain different coagulation mechanisms (Sarpola et al., 2007). Indeed, aluminium sulfate

(Al$_2$(SO$_4$)$_3$·nH$_2$O), n is equal to 14 or 18, which is common species, called alum. Alum can be used as a coagulant in water treatment for a large range of turbidity. At low turbidity raw water, high concentration of alum is added to lead to the formation of Al(OH)$_3$. Thus this compound precipitates works in terms of sweep flocculation (Alshikh, 2007; Sahu and Chaudhari, 2013). In the case of high turbidity raw waters, alum positive compounds would be adsorbed on the negatively charged colloids, and destabilization occurs through an adsorption and charge neutralization or coagulation of colloidal particles mechanism. The overlap between those mechanisms depends on the characteristics of raw water and operating conditions (Mackenzie L. Davis, 2010).

1.3.2.2 Coagulant Chemistry in Aqueous Solution

Aluminum sulfate can take different forms in an aqueous solution depending on the pH. They are governed by the equilibrium reactions, as shown in Table 1.1 (John Gregory and Duan, 2001).

Table 1.1 Constant hydrolysis of aluminum

Reaction	pK		Number of reactions
Al(OH)$_{3(s)}$ $\leftrightarrow$ Al^{3+} + 3HO$^-$	pK$_s$	= 31.5	Reaction 1.1
Al^{3+} + 2H$_2$O $\leftrightarrow$ Al(OH)$^{2+}$ + H$_3$O$^+$	pK$_{A1}$	= 4.95	Reaction 1.2
Al(OH)$^{2+}$ + 2H$_2$O $\leftrightarrow$ Al(OH)$_2^+$ + H$_3$O$^+$	pK$_{A2}$	= 5.6	Reaction 1.3
Al(OH)$_2^+$ + 2H$_2$O $\leftrightarrow$ Al(OH)$_3$ + H$_3$O$^+$	pK$_{A3}$	= 6.7	Reaction 1.4
Al(OH)$_3$ + 2H$_2$O $\leftrightarrow$ Al(OH)$^{4-}$ + H$_3$O$^+$	pK$_{A4}$	= 5.6	Reaction 1.5

If both the concentrations of Al$_2$(SO$_4$)$_3$ injected and the pH of the solution are known, it is possible to calculate the concentrations of all the chemical species reported in Table 1.1. For example, for a very low pH (pH < 4), the solution contains almost only Al^{3+} ions and only a few traces of other species, as shown in Figure 1.12. For a higher pH

(pH > 5), $Al(OH)_3$ species is most often predominant; it depends on the concentration of coagulant.
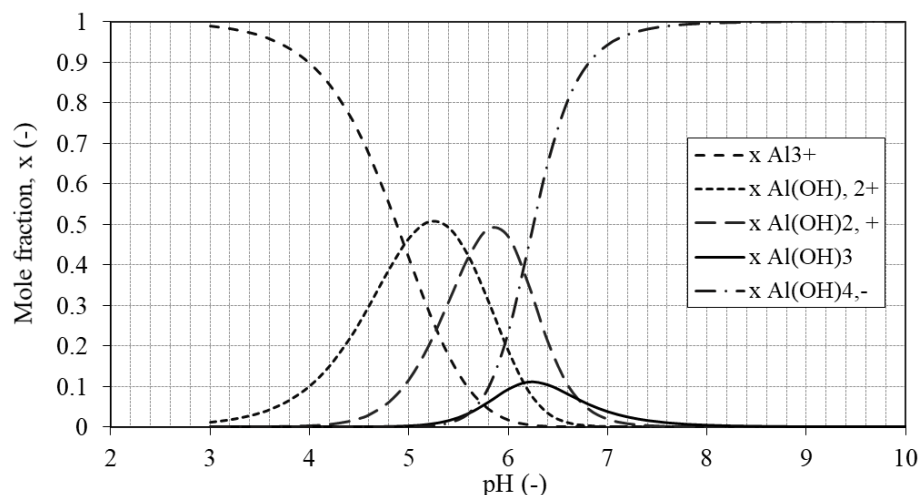
Figure 1.12 Al hydrolysis products as a function of pH (John Gregory, 2013)

1.3.2.3 Reactivity of the Coagulant with Bentonite

The primary reaction when alum is added into the natural water containing alkalinity is shown in Reaction 1.6. During the reaction, a precipitate of aluminium hydroxide is formed, together with releasing of sulfuric acid as a by-product. Then, the sulfuric acid can react with some species in water, especially on the bicarbonate ions resulting in dissolved carbonic acid (Reaction 1.7); excess alkalinity of the solution is required in this step. The dissolved carbonic acid can be dissociated to be a dissolved carbon dioxide (CO_2), which exists in chemical equilibrium with the carbonic acid as displayed in Reaction 1.8. The simplified reaction including all steps of the reactions is shown as Reaction 1.9.

$$Al_2(SO_4)_3 \cdot 18H_2O + 6H_2O \rightarrow 2Al(OH)_3 \downarrow + 3H_2SO_4 + 18H_2O \qquad \text{Reaction 1.6}$$

$$3H_2SO_4 + 6(HCO_3)^- \rightarrow 3SO_4^{2-} + 6H_2CO_3 \qquad \text{Reaction 1.7}$$

$$6H_2CO_3 \leftrightarrow CO_2 + 6H_2O \qquad\qquad \text{Reaction 1.8}$$

$$Al_2(SO_4)_3 \cdot 18H_2O + 6(HCO_3)^- \rightarrow 2Al(OH)_{3(s)} + 3SO_4^{2-} + 6CO_2 + 18H_2O \quad \text{Reaction 1.9}$$
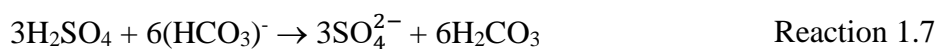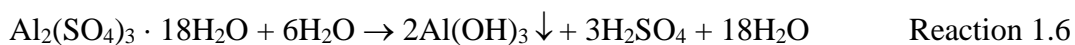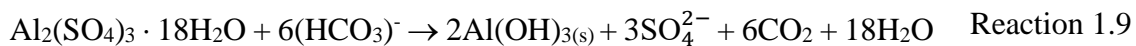
In conclusion, the reaction shifts the carbonate equilibrium (related to alkalinity) and slightly decreases pH because carbonic acid is a weak acid. Nevertheless, as long as alkalinity presents in the water enough to evolve CO_2, the pH is not drastically reduced and is not a general operational problem (Mackenzie L. Davis, 2010). When alkalinity does not present enough to neutralize the sulfuric acid production, the pH may be greatly reduced as expressed in Reaction 1.10. Sulfuric acid is a strong acid that dissociates 100% to the proton, or H^+.

$$Al_2(SO_4)_3 \cdot 18H_2O + 6H_2O \rightarrow 2Al(OH)_{3(s)} + 3H_2SO_4 + 18H_2O \qquad \text{Reaction 1.10}$$
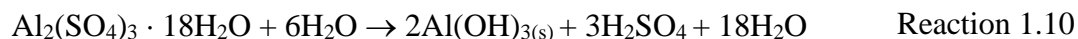
1.4 Physical Phenomena of Flocculation

Flocculation consists in producing interparticle contacts by physical mixing to promote floc formation (American Water Works, 1999; Ratnayaka et al., 2009). The agglomeration can occur as colloids accumulate together to form flocs, which are turned into visible floc masses (Sahu and Chaudhari, 2013), as shown in Figure 1.8. The flocculation depends on the physical mechanisms, aggregation and breakup processes that can limit floc growth, as explained in the next section.

1.4.1 Aggregation Mechanisms

Whatever the mechanism of coagulation and flocculation mentioned above, the collisions between particles are due to different processes, but all have in common the fact that the two particles must have a relative velocity. This later may be due to 3 different mechanisms: Brownian motion, fluid shear, and differential sedimentation (Boadway, 1978; Federico, 2005; Hunt, 1980; Saffman and Turner, 1956a). The collision rate of two

particles i and j in units of m^3s^{-1} is expressed as the sum of the contribution of each mechanism as shown in Equation 1.11.

$$\beta_{i,j} = \beta_{i,j}^{brownian} + \beta_{i,j}^{sedimentation} + \beta_{i,j}^{agitation} \qquad \text{Equation 1.11}$$

1.4.1.1 Brownian Motion (Perikinetic Aggregation)

Brownian motion is the random movement of particles in a fluid. It is related to thermal agitation and corresponds to the disordered movement of colloids.

The collision frequency can be derived by calculating the rate of diffusion (J) of spherical particles (i and j particle) with radius r_i and r_j, respectively. It can be shown that the number of i particles contacting j in unit time is as Equation 1.12 where $r_i + r_j$ is the collision radius since the short-range interactions, the sum radius of the particles can be assumed to be the collision radius.

$$J = 4\,\pi\,D_{ij}\,n_j\big(r_i + r_j\big) \qquad \text{Equation 1.12}$$

Where D_{ij} is the relative diffusion coefficient of the particle i towards j. It can be calculated as $D_{ij} = D_i + D_j$ using the *Stokes* diffusion coefficient of each particle. n_j is the number of particles of size j likely to collide with the particle i. If the medium is diluted, it can be assumed that $n_j = 1$ Moreover, the expression of the diffusion coefficient is given by the relation from Equation 1.13.

$$D_j = \frac{k_B\,T_{temp}}{3\,\pi\,\mu\big(d_p\big)} \qquad \text{Equation 1.13}$$

Where k_B is Boltzmann constant ($k_B = 1.38 \times 10^{-23}$ J/K), d_p is diameter of the particle. The expression of the collision rate generated by the Brownian motion is expressed by Equation 1.14.

$$\beta_{i,j}^{brownian} = \frac{2k_B T_{temp}}{3\mu}(r_i + r_j)\left(\frac{1}{r_i} + \frac{1}{r_j}\right) \qquad \text{Equation 1.14}$$

1.4.1.2 Fluid Motion (Orthokinetic Aggregation)

To induce aggregation of flocs or flocculation, the (flow) shear rate generates a relative velocity between two particles. Great attention has been paid to the influence of shear in flocculation, especially in the case of orthokinetic flocculation. Smoluchowski, in 1917, was the first to propose a theoretic analysis of flocculation due to fluid motion in the case of the laminar regime. Once again, it describes the collision rate between two particles (i and j particle) with radius r_i and r_j, respectively, as being the flow rate of particles entering the sphere of radius $r_i + r_j$ around the particle i. More precisely, for a uniform shear field, Smoluschowski assumed that the particles travel along fluid streamlines flowing with the velocity gradient (G) and collide as they approach each other within a distance of $r_i + r_j$ between their centers. Smoluchowski established the collision rate shown in Equation 1.15.

$$\beta_{i,j}^{laminar\ flow} = \frac{4}{3}G(r_i+r_j)^3 \qquad \text{Equation 1.15}$$

The case of turbulent flows is more complex and has been studied by many authors such as Bouyer et al., (2005), Coufort et al., (2008), and Guérin et al., (2017). It is possible to summarize all the results in Equation 1.16.

$$\beta_{i,j}^{turbulent\ flow} = C_1G(r_i+r_j)^3 \qquad \text{Equation 1.16}$$

Where G is the local velocity gradient or shear rate that can be defined in laminar flow and in turbulent flow, which was described in Equation 1.17 and Equation 1.19, respectively. C_1 is a constant value that can take different values, as shown in Table 1.2.

The local shear rate is defined as:

$$|\dot{\gamma}| = \sqrt{2tr(S^2)} \qquad \text{Equation 1.17}$$

Where S is the symmetric part of the velocity gradient tensor and

$$
\begin{aligned}
tr(S^2) = \ & \left(\frac{\partial U_1}{\partial x_1}\right)^2 + \left(\frac{\partial U_2}{\partial x_2}\right)^2 + \left(\frac{\partial U_3}{\partial x_3}\right)^2 \\
& + \frac{1}{2}\left[\left(\frac{\partial U_1}{\partial x_2} + \frac{\partial U_2}{\partial x_1}\right)^2 + \left(\frac{\partial U_1}{\partial x_3} + \frac{\partial U_3}{\partial x_1}\right)^2 \right. \\
& \left. + \left(\frac{\partial U_2}{\partial x_3} + \frac{\partial U_3}{\partial x_2}\right)^2\right]
\end{aligned}
\qquad \text{Equation 1.18}
$$

In turbulent flow, the local shear rate becomes

$$|\dot{\gamma}| = \sqrt{2tr\left(\overline{s'^2}\right)} \qquad \text{Equation 1.19}$$

Where;

$$
\begin{aligned}
tr\left(\overline{s'^2}\right) = \ & \overline{\left(\frac{\partial u'_1}{\partial x_1}\right)^2} + \overline{\left(\frac{\partial u'_2}{\partial x_2}\right)^2} + \overline{\left(\frac{\partial u'_3}{\partial x_3}\right)^2} \\
& + \frac{1}{2}\left[\overline{\left(\frac{\partial u'_1}{\partial x_2} + \frac{\partial u'_2}{\partial x_1}\right)^2} + \overline{\left(\frac{\partial u'_1}{\partial x_3} + \frac{\partial u'_3}{\partial x_1}\right)^2} \right. \\
& \left. + \overline{\left(\frac{\partial u'_2}{\partial x_3} + \frac{\partial u'_3}{\partial x_2}\right)^2}\right]
\end{aligned}
\qquad \text{Equation 1.20}
$$

Here, $tr(\overline{S^2})$ is an invariant.

Table 1.2 The values of C_1 in Equation 1.16 from different authors.

The constant values of C_1	Bibliographic reference
$\dfrac{4}{3}$	(T. R. Camp and Stein, 1943)
$\sqrt{\dfrac{8\,\pi}{15}}$	(Bałdyga and Bourne, 1999; Saffman and Turner, 1956b)
$\pi\sqrt{\dfrac{1}{15}}$ if the particle is smaller than the micro-scale of Kolmogorov	(Delichatsios and Probstein, 1976)

Moreover, Smoluchowski (1917) defined the orthokinetic collision rate coefficient k_{ij} as Equation 1.21.

$$k_{ij} = \frac{G}{6}\left(d_i + d_j\right)^3$$
Equation 1.21

Where d_i and d_j are the diameters of particles i and j. This expression is one of basic elements to discuss the agglomeration kinetics, through the Population Balance Equation of Equation 1.22.

$$\frac{dn_k}{dt} = \frac{1}{2}\sum_{\substack{i+j\to k \\ i=1}}^{i=k-1} k_{i,j}\, n_i n_j - n_k \sum_{k=1}^{\infty} k_{ij}\, n_i$$
Equation 1.22

The terms on the right hand side of Equation 1.22 deal respectively with the *birth* and the *death* of aggregates of size k. The first term represents the rate of of formation of flocs of size k from the agglomeration of any pair of flocs such that $i + j \to k$. The second term is the rate at which an aggregate of size k collides with any other aggregate.

Given a certain number of assumptions (John Gregory, 2013), it is possible to express from Equation 1.22 the rate of change of total particle concentration n_T under the following form:

$$\frac{dn_T}{dt} = -\frac{4G\phi n_T}{\pi}$$

Equation 1.23

where ϕ corresponds to the total volume of particles.

$$\phi = \frac{\pi d^3 n_T}{6}$$

Equation 1.24

And G stands for a global shear rate or global velocity gradient.

As ϕ can be seen as constant during an aggregation process then Equation 1.29 becomes a first-order rate expression and can be integrated into Equation 1.25.

$$\frac{n_T}{n_0} = exp\left(-\frac{4\phi Gt}{\pi}\right) \ or \ Gt = \frac{\ln\left(\frac{n_T}{n_0}\right)}{\frac{4}{\pi}\phi}$$

Equation 1.25

This simplified model is recalled here to illustrate some important features of flocculation and shows that the extent of flocculation depends on the non-dimensional term *Gt*. The total number of collisions occurring in the suspension is thus related to *Gt*, known as the Camp Number, which is a performance indicator and basic design criteria. For typical water treatment, the recommended values of the Camp Number range between 1×10^4 and 2×10^5 (Thomas R. Camp, 1955). Hence, the specification of the Camp number and either the spatially averaged velocity gradient (G) or residence time (*t*) suffices to determine the total tankage and mixing power required (W. F. Chen and Liew, 2002).

In water treatment, the global velocity gradient (G) is used to predict aggregation kinetics and break-up phenomena; it is defined as Equation 1.26.

$$G = \sqrt{\frac{P}{\mu V}}$$

Equation 1.26

Where V is the volume of liquid in the tank, µ is dynamic viscosity, P is the power corresponds to a volume average of the dissipation rate of kinetic energy $< \varepsilon >$ and its relationships can be determined as Equation 1.27.

$$< \varepsilon > = \frac{P}{\rho V} \qquad \text{Equation 1.27}$$

Where ρ represents the fluid density. Moreover, in a mixing tank, the global power dissipated in the tank is calculated from the power number (N_p) associated with an impeller, as expressed in Equation 1.28. The power number of the impeller, which depends on the mixing device, where D_{im} is impeller diameter, and N is impeller rotation frequency.

$$N_p = \frac{P}{\rho N^3 D_{im}^5} \qquad \text{Equation 1.28}$$

Thus, the global velocity gradient can be written as Equation 1.29 where ν is kinematic viscosity.

$$G = \sqrt{\frac{< \varepsilon >}{\nu}} \qquad \text{Equation 1.29}$$

From a flocculation point of view, numerous studies have proven a direct connection between floc size and hydrodynamics shown that the steady state maximum floc size is related to the average intensity of the turbulent fluid motion, especially ε or G in Equation 1.30 (J. Ducoste and Clark, 1998; J. J. Ducoste et al., 1997; François, 1987; Parker et al., 1972; Thomas, 1964).

$$d_{max} \propto \frac{C}{\varepsilon^n} \text{ or } \propto G^{-\alpha} \qquad \text{Equation 1.30}$$

Where C is linked to the strength of the floc and n or α are coefficients depending on flocculation conditions and hydrodynamics.

1.4.1.3 Differential Sedimentation

When particles of various sizes and densities settle, their different sedimentation velocities could promote their meeting. Indeed, as they fall, larger and denser particles will sediment faster and can thus collide with more slowly settling particles.

If the particles can settle by only gravity force and there is no interaction between them, their path line is linear. The relative velocity is expressed by Equation 1.31, where u_{pi} and u_{pj} are the velocities of particle i and j, respectively.

$$\Delta u = \left| u_{pi} - u_{pj} \right|$$
Equation 1.31

For discrete settling, the sedimentation refers to the separation of particles that have no interaction with each other. The settling velocity of the particle is primarily affected by the size, density, shape of the particle and the density and the viscosity of the continuous phase. The Stokes' law describes the terminal settling velocity (U_t) of discrete spherical particles in a very low Re number regime, called a creeping flow regime, as shown in Equation 1.32.

$$U_t = \frac{g\left(\rho_i - \rho_l\right) d_i^2}{18\mu}$$
Equation 1.32

Where g is the gravitational force constant, d_i is particle diameter, μ is dynamic viscosity, ρ_i is particle density, and ρ_l is liquid density. One can thus estimate the settling velocity of each particle size. Finally, the expression of the collision rate due to differential sedimentation is expressed through the following relation of Equation 1.33.

$$\beta_{i,j}^{sedimentation} = \pi \left(r_i + r_j \right)^2 \left| u_{pi} - u_{pj} \right|$$
Equation 1.33

When the density of flocs is close to that of the water, there is almost no settling.

1.4.1.4 Collision Efficiency

Following an ideal behavior, two particles that come into contact should automatically aggregate. Since this behavior is only rarely observed, a notion of collision efficiency often has to be introduced to take into account this non-ideality. The collision efficiency (α_c), also referred to as attachment efficiency, or striking probability, is a commonly used dimensionless parameter. It depends on the characteristic of the colliding flocs and of the collision mechanism.

In their approach, known as the curvilinear approach, (Han and Lawler, 1992) take into account the fact that clusters mutually influence their trajectory as they come closer to each other. In the case of Brownian motion collisions, the efficiency depends on the size ratio (δ) between the two particles that collide.

$$\delta = \frac{\min (d_i, d_j)}{\max (d_i, d_j)} \qquad\qquad \text{Equation 1.34}$$

The efficiency is then expressed as a function of four constants (*a*, *b*, *c*, and *d*) dependent on the diameter of the larger particle.

$$\alpha_c^{brownien} = a + b\delta + c\delta^2 + d\delta^3 \qquad\qquad \text{Equation 1.35}$$

The resulting collision efficiency is between about 0.4 and 1. It is more significant as the particles that meet have similar and small sizes.

In the case of differential sedimentation, determination of the value of the collision efficiency as a function of the same parameter δ (Han and Lawler, 1992).

$$\alpha_c^{sedimentation} = 10^{a+b\delta+c\delta^2+d\delta^3} \qquad\qquad \text{Equation 1.36}$$

The most effective differential sedimentation collisions are those between small particles. $\alpha_c^{sedimentation}$ decreases as the particles that meet each other have different sizes.

When the collisions are due to the relative velocity generated by the agitation of the fluid, the collision efficiency was determined based on Adler's work which takes into account the hydrodynamic forces as well as the electrostatic forces (Adler, 1981; Han and Lawler, 1992). For a velocity gradient (G) of 20 s^{-1}, the expression of the efficiency is shown as Equation 1.37.

$$\alpha_c^{agitation} = \frac{8}{(1+\delta)^3} 10^{a+b\delta+c\delta^2+d\delta^3}$$

Equation 1.37

The efficiency of collisions related to agitation is much lower than those obtained for Brownian motion and especially in the case of large particles. One of the significant weaknesses of Han and Lawer's (1992) approach is that it does not take into account the porosity of the aggregates and that the trajectory of the fluid can also modify that of the aggregate. Thus, Torres (1991) and later, Kusters (1997) integrated this notion into the computation of the collision efficiency by means of the "core-shell" model in which an aggregate consists of an impermeable solid core surrounded by a permeable envelope (core-shell model) (Kusters et al., 1997; Torres et al., 1991). The values calculated by this model show that the floc porosity significantly increases the collision efficiency. The calculation of efficiency based on the work of Kusters (1997) and using analyzes of trajectories in different cases is not trivial. Thus, Selomulya (2003) suggested a mathematical model to reproduce the trends shown Kusters (1997) (Cordelia Selomulya et al., 2001; C. Selomulya et al., 2003) according to Equation 1.38.

$$\alpha(L,\lambda) = \alpha_{max} . \frac{exp\left(-x\left(1-\frac{n_i}{n_j}\right)^2\right)}{\left(n_i . n_j\right)^y}$$

Equation 1.38

Where n_i (respectively n_j) is the number of primary particles contained in the smallest (respectively, the largest) of the two aggregates. The behavior of the model is governed by three parameters are follow:

- The maximum efficiency α_{max} is reached only during the aggregation of two primary particles $n_i = n_j = 1$.

- The efficiency is all the more important that the aggregates are small. This effect is weighted by the parameter y.

- The efficiency is important as the aggregates are of similar sizes. This effect is weighted by the parameter x.

1.4.2 Breakup

Most of the aggregation processes are carried out in agitated suspensions. Some breakage of aggregates will inevitably occur in these cases. A breakup phenomenon occurs when hydrodynamic forces (external forces) are more significant than floc strength (internal forces of cohesion) as the ratio defined as Equation 1.39; that is if the ratio of hydrodynamic forces and cohesive forces becomes greater than 1 (Denis Bouyer et al., 2005; Carole Coufort et al., 2008).

$$\frac{\text{Hydrodynamic forces}}{\text{Cohesion force}} = \frac{F_h}{F_c} \qquad \text{Equation 1.39}$$

where:

$$F \propto \sigma_h \, d_{floc}^2 \qquad \text{Equation 1.40}$$

Where σ_h is the hydrodynamic stress exerted on the floc and d_{floc} is the projected area of the plane.

The expression of the stress σ_h exerted by the fluid on the aggregate depends on the size of the aggregate relative to the size of the Kolmogorov micro-scale, which is the length scale of the smallest eddies is given as described in the topic of Kolmogorov (η), on Appendix A.

If the floc size is smaller than the Kolmogorov micro-scale ($d_{floc} < \eta$), then the aggregate evolves in the viscous domain. The approximate value of the local stress (σ_V) is then given by Equation 1.41.

$$\sigma_V = \mu \left(\frac{<\varepsilon>}{\nu} \right)^{\frac{1}{2}} = \mu <G> \qquad \text{Equation 1.41}$$

An estimate of the force exerted on the aggregate is given by Equation 1.42

$$F_V = C_1 \mu \, G \, d_{floc}^2 \qquad \text{Equation 1.42}$$

Where the coefficient $C_1 = \frac{5\pi}{8}$ (C. Coufort et al., 2005).

If the size of the floc is greater than the Kolmogorov micro-scale ($d_{floc} > \eta$), then the aggregate evolves in the inertial domain. An approximate value of the local stress is then given by Equation 1.43.

$$\sigma_I = \rho \, \overline{u'^2} \qquad \text{Equation 1.43}$$

Where:

$$\overline{u'^2} = C_2 \left(\varepsilon \, d_{floc} \right)^{\frac{2}{3}} \qquad \text{Equation 1.44}$$

Where the coefficient $C_2 = 0.7$

Finally, the force exerted on the aggregate can be expressed as Equation 1.45.

$$F_I = \rho \, C_2 \, \varepsilon^{\frac{2}{3}} \, d_{floc}^{\frac{8}{3}} \qquad \text{Equation 1.45}$$

Two main break-up mechanisms are currently identified in the literature: erosion and fragmentation. Erosion of an aggregate is related to shear stress while fragmentation is

due to normal stresses (Peter Jarvis et al., 2005). François (1987) showed that erosion phenomena occur in the case of aggregates evolving in the viscous domain, whereas larger aggregates, thus evolving in the inertial domain, are more prone to fragmentation (François, 1987).

Finally, the frequency with which a particle will undergo a breakup phenomenon is generally described according to hydrodynamics. Thus, two forms of rupture kernel are present in the literature: the so-called "exponential" kernel and the "in power law" kernel.

Delichatsios and Probstein (1976) and Kusters (1997) reported that an expression of the breaking frequency involving the overall velocity gradient as well as the rate of dissipation of the turbulent kinetic energy (Delichatsios and Probstein, 1976; Kusters et al., 1997).

$$B(L) = \left(\frac{4}{15\pi}\right)^{1/2} G \exp\left[\frac{-\varepsilon_c}{\varepsilon}\right]$$
<div align="right">Equation 1.46</div>

Where ε_c is the rate of dissipation of the critical turbulent kinetic energy at which the breakup takes place, the value of which is inversely proportional to the radius of the aggregate. Also, Other expressions of the same form have been proposed (L. Marchisio et al., 2003; Wang et al., 2005).

The other form is simpler and is expressed in the form of law can be defined as Equation 1.47.

$$B(L) = C_1 . l^{C_2}$$
<div align="right">Equation 1.47</div>

Where l is a size, C_1 and C_2 constants with $C_1 \propto G^{C_3}$ (Vlieghe et al., 2016; Wang et al., 2005) or $C_1 \propto \varepsilon^{C_4} \nu^{C_5}$ (T. A. Kramer and Clark, 1999; L. Marchisio et al., 2003).

1.5 Sedimentation and Turbidity Removal Efficiency

Sedimentation is the method most frequently used for separating suspended solids. The subject of numerous studies was about sedimentation of isolated floc due to their motion through the fluid in response to the forces acting on them and the difference of density between the particle and the continuous phase. Therefore, this part presents forces that act on the isolated sphere floc in equilibrium and the methodology used to design a sedimentation basin.

1.5.1 The Forces Acting on an Isolated Particle

The general law of sedimentation based on the equilibrium (steady state) of three forces, which is shown in Figure 1.13, that is the gravitational force (F_G), the Buoyancy force (F_B) and the drag force (F_D), is written as follows:

$$F_G - F_B = F_D \qquad\qquad \text{Equation 1.48}$$
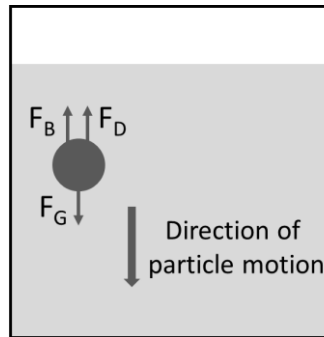
Figure 1.13 Schematic of forces acting on a dispersed particle

The gravity force (weight) causes the mass of the particle to fall. This is expressed as Equation 1.49.

$$F_G = m_p \times g = \rho_p V_p g \qquad\qquad \text{Equation 1.49}$$

Where m_p is particle mass and ρ_p the density of the particle.

A force in the opposite direction of gravity is buoyancy (F_B), which resists gravity, so the greater the buoyancy, the more likely a particle will remain suspended in the continuous phase. This can be expressed as Equation 1.50.

$$F_B = m_g \times g = \rho_l V_p g \qquad \text{Equation 1.50}$$

Where m_g is mass of displaced medium and ρ_l the density of the continuous phase (liquid). As the particle begins to move downward due to F_G, which is induced by the different densities between two phases, it encounters a resistive force that increases with increasing downward velocity. So, this is the third important force acting on a particle, which can be expressed as follow:

$$F_D = \frac{A \rho_l U^2 C_D}{2} \qquad \text{Equation 1.51}$$

Where U is the relative speed between the two phases, A the projected cross section of the particle and C_D is the drag coefficient. This force is opposed to the phenomenon of settling. Replacing each force by its expression in the Equation 1.48, the following relation is obtained.

$$(\rho_p - \rho_l)V_p g = \frac{A \rho_l U^2 C_D}{2} \qquad \text{Equation 1.52}$$

hence:

$$U = \sqrt{\frac{2 (\rho_p - \rho_l)V_p g}{A \rho_l C_D}} \qquad \text{Equation 1.53}$$

The drag coefficient values are related to the flow regime. In the case of the study of solid sphere moving in a fluid, the drag coefficient is defined by Schiller and Naumann correlation (Vallero, 2014):

- The drag coefficient in the creeping flow regime ($0 \leq Re \leq 1$) and the moderate Re numbers regime ($1 < Re < 1000$)

$$C_D = \frac{24}{Re}\,(1 + 0.15 Re^{0.687})$$

Equation 1.54

- The drag coefficient in the high Re numbers regime

$$C_D = \frac{4}{9} = 0.44$$

Equation 1.55

1.5.2 Sedimentation in Settling Tank

The particles, especially colloids have to be pretreated with coagulation and flocculation processes in order to form large and dense particles before throughput into the sedimentation process. Water in the sedimentation process moves slowly and causes the massive flocs to settle to the bottom and form a layer of flocs at the bottom of the tank, known as sludge. The design of the sedimentation basin depends on the concentration, size, and settling velocity of the solids suspension.

In general, there are four types of sedimentation: discrete settling, flocculent settling, hindered settling, and compression settling. The methodology used to design a sedimentation basin depends on the kind of settling encountered in the basin. For discrete settling, sedimentation refers to the separation of particles that have no interaction with others. The settling velocity of particles is primarily affected by the particle size, shape, density, and water viscosity. Stokes' law, as mentioned in Equation 1.32, is used to describe the terminal settling velocity of discrete spherical particles in a laminar flow regime.

In an ideal rectangular settling tank, as shown in Figure 1.14, all particles have a settling velocity greater than the liquid velocity as shown in Equation 1.56.
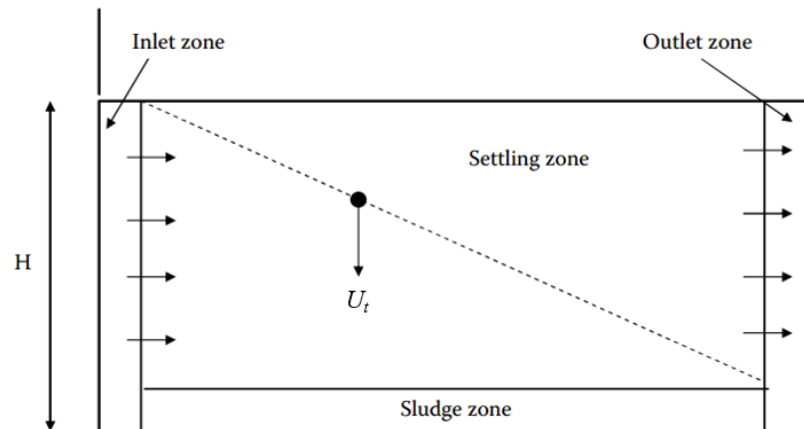
Figure 1.14 An ideal settling basin (John Gregory, 2006b)

$$U_t > \frac{\text{Flow rate}}{\text{Surface Area}} \qquad \text{Equation 1.56}$$

Where U_t is terminal velocity. Equation 1.32 and Equation 1.56 are fundamental to design the conventional horizontal-flow rectangular sedimentation tanks. The term of flow rate (Q)/Surface Area (A_s) is known as the surface loading rate or overflow rate. In other words, the theoretical residence time (τ) of the sedimentation tank, which can be described as Equation 1.57, must longer than the settling time of particles.

$$\tau = \frac{\text{volume}}{\text{Flow rate}} \qquad \text{Equation 1.57}$$

Factors that contribute to non-ideal settling behavior in practice are as follows:

- Nonspherical particles have a higher drag coefficient at a given Reynolds number or flow regime. Consequently, the settling velocity of nonspherical particles is less than a spherical particle with the same volume and density.
- Poor flow distribution and collection, wind, rising bubbles, and density differences caused by either temperature or concentration can cause hydraulic short-circuiting

and bulk mixing; This affects the laminar flow conditions in the basin and reduces its efficiency.

- The settling velocity of a discrete particle is also affected by the presence and concentration of other particles. As the concentration of particles increases and the free area between particles is reduced, settling becomes hindered and the resulting settling velocity of the solid suspension is generally less than for a discrete particle.

As a consequence, the removal turbidity is a delicate and chemically complex phenomenon having three stages: (1) the addition of measured quantities of chemicals to water and their thorough mixing; (2) coagulation and flocculation, or the formation of a precipitate which coalesces and forms a floc; and (3) solid-liquid separation.

1.5.3 Turbidity Removal Efficiency

The effectiveness of turbidity reduction is one of the primary goals of effective water treatment because of potential interference with downstream treatment processes and adverse effects on consumer health and acceptance. Turbidity might interfere with filtration by clogging the filter prematurely. It can interfere with chemical disinfection by creating oxidant demand, blocking light transmission (UV irradiation), and reduce the efficacy of both by providing protection to microbes in aggregates or granules (Soros et al., 2019). Therefore, removing turbidity serves a two-fold purpose in water treatment: it removes some microbes while reducing the levels of organic matter and other particles, increasing the effectiveness of downstream treatment processes.

Turbidity is the most common visible evidence of particles in water that can be measured by detecting light scattering. The value can be affected by the sizes and the numbers of particles as well as the wavelength of the incident light, the angle of observation, the optical properties of the particles, and the refractive index of the suspending medium (Bratby, 2016; John Gregory, 2006b). The nephelometric method is generally used for measuring turbidity by providing the wavelength of the incident light. The amount of the scattered light at a 90º angle from the light source is measured. The detected light is then reported in the unit of NTU (Nephelometric Turbidity Unit).
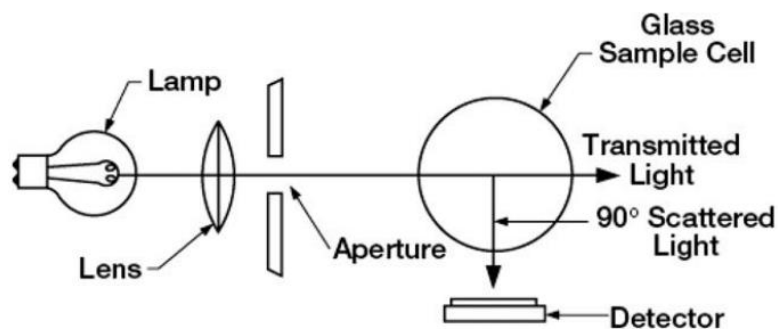
Figure 1.15 Schematic of a nephelometric turbidimeter (Bratby, 2016).

Considering the efficiency of turbidity removal from water by calculating the difference value between initial raw water and effluent water, clear water after the turbidity has been eliminated, as shown in Equation 1.58.

$$\text{Turbidity Removal Efficiency (\%)} = \left(\frac{T_{in} - T_{out}}{T_{in}}\right) \times 100 \qquad \text{Equation 1.58}$$

Where T_{in} and T_{out} are respectively the turbidity of initial raw water and effluent water.

The World Health Organization (WHO) suggested the value of turbidity standard as one of the treated water quality control parameters. For water treatment systems that use conventional or direct filtration, the turbidity of treated water should be less than 1 NTU, and systems that use filtration other than conventional or direct filtration must follow state limits, including turbidity not exceeding 5 NTU (WHO, 2017).

As discussed, the turbidity can be eliminated by physico-chemical technique, and its efficiency is about 50 to 90 percent, depending on the characteristic of the suspended particles causing the turbidity and the treatment system. Thus, the reactor design peculiarly for the coagulation and flocculation, which would be described in the next topic, is essential to clarify the water of the water treatment system.

1.6 Hydrodynamics and Reactor Analysis

The flocculation process involves agglomeration and breakup of aggregates that may be related to fluid motion. These are conditioned by the hydrodynamics generated within the tank. As discussed on the coagulation and flocculation topic, flocculation is required the mixing process. For this research, the flocculation was conducted in a jar-test (standard 1-liter beaker) and the jet clarifier, which is a mechanical technique, and mixing induced by hydrodynamic, respectively. Thus, in the first part of the introduction, the concept of hydrodynamic will be devoted to the physical description of the different flow regimes. The global and local analysis are both focus on a particular description of hydrodynamics in reactors. The determination of velocity gradient (G) and contact time (t_{cont}) will be focused on this part since it is the hydrodynamic parameter of reference in the jet clarifier used in this work.

1.6.1 Global Analysis of Hydrodynamics

The global analysis focuses on defining hydrodynamic quantities for characterizing an agitation system, through the type of mixture it generates. The main objective of this type of approach is to guide a user in choosing the most appropriate mixing system, according to the mixing operation that must be performed, which consists of Reynolds number (Re), power number, and global velocity gradient (G).

1.6.1.1 Reynolds Number

The first of the global quantities is the Reynolds number, established in 1883 by Osborne Reynolds, which allows the characterization of the flow regime (O. Reynolds, 1883). The Reynolds number, which is dimensionless as any number, is the ratio of inertial forces to viscous forces. It is used to categorize the flow. Mathematically, the Reynolds number, Re, is defined as Equation 1.59.

$$Re = \frac{\rho u L}{\mu} = \frac{u L}{\nu} \qquad \text{Equation 1.59}$$

Where u is a characteristic velocity scale, μ is dynamic viscosity, and L is a characteristic length scale.

In the case of the agitated tank, the Reynolds number is expressed Equation 1.60, which is defined the velocity scale and the length scale as N and D_{im}, respectively.

$$Re = \frac{N D_{im}^2}{\nu} \qquad \text{Equation 1.60}$$

Where N is impeller rotation frequency, D_{im} is impeller diameter, and ν is kinematic viscosity. The different values adopted by the Reynolds number make it possible to distinguish 3 flow regimes. For the low values of the Reynolds number, the viscous forces are predominant, thus the flow is laminar. For intermediate Reynolds values, the inertial forces become significant. Whereas the Reynolds number is high values, the predominance of inertial forces causes the flow to become turbulent. The Reynolds values correspond to the different regimes (O. Reynolds, 1883). They are recalled in Table 1.3 in the case of pipe flow and a stirred tank.

Table 1.3 Reynolds numbers associated with different flow regimes in pipes, stirred tanks, and jet flow

Regime	Pipe	Stirred tank	Jet flow
Laminar	$Re < 2000$	$Re < 10$	$Re < 100$
Transition	$2000 < Re < 4000$	$10 < Re < 10^4$	$100 < Re < 2000$
Turbulent	$Re > 4000$	$Re > 10^4$	$Re > 2000$

1.6.1.2 Power Number

The power number N_p is a dimensionless parameter, is similar to the drag coefficient, used for estimating the power consumed by the mixing device. It is expressed under the following form, where D_{im} is impeller diameter.

$$N_p = \frac{P}{\rho N^3 D_{im}^5}$$
Equation 1.61

The power supplied to the shaft is transferred to the liquid by the power of stress along the impeller blades in terms of pressure distributions and viscous stress distributions. It is analogous to a drag coefficient.
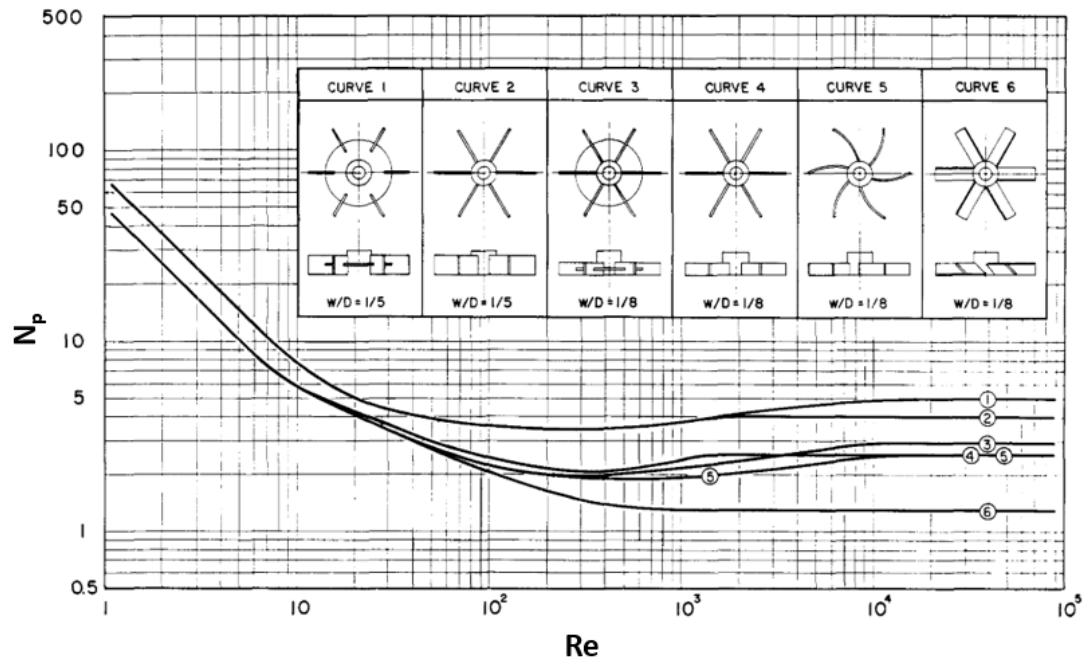
Figure 1.16 Power number-Reynolds number correlation in Newtonian fluids for various turbine impeller designs (Bates et al., 1963)

In the laminar regime, the number of power is inversely proportional to the Reynolds number. In the turbulent regime, the number of power no longer depends on the

Reynolds number, but it depends on only two parameters: the type of agitator and the presence or not of the baffles in the tank. For example, Bates et al. (1963) proposed the correlation of power number for four flat baffles tanks of standard geometry with Newtonian fluids for various turbine impeller designs against Reynolds number of various impellers as shown in Figure 1.16. It can be seen that the power number becomes constant at high Re values, turbulent regime.

The Reynolds number and power number discussed above usually are used to identify the fluid flow phenomena of the agitator reactor, while the fluid flow of the jet clarifier used in this study is induced by the jet flow. Therefore, the power supply of the jet is transferred to the bulk liquid by the dissipation along the plume. Thus, that the details of jet flow were expressed in the next section.

1.6.1.3 Mean Velocity Gradient

Since all the supplied power is dissipated, one can introduce a velocity gradient G and express the equilibrium between power supplied and dissipated power (by viscosity) as:

$$P = \mu \, V \, G^2 \qquad\qquad \text{Equation 1.62}$$

The global or mean velocity gradient (G) is very commonly used in water treatment to characterize the mixing during the flocculation process. It is thus related directly to the total power dissipated (P) by the following expression:

$$G = \sqrt{\frac{P}{\mu V}} \qquad\qquad \text{Equation 1.63}$$

Where V is the volume of liquid in the tank, P is the power corresponds to a volume average of the dissipation rate of kinetic energy $< \varepsilon >$. Moreover, the average rate of viscous dissipation of the kinetic energy ($< \varepsilon >$) is related to the power dissipated by the relation in Equation 1.64. Therefore, the relation can be rewritten in Equation 1.65.

$$< \varepsilon > = \frac{P}{\rho V} \qquad \text{Equation 1.64}$$

$$G = \sqrt{\frac{< \varepsilon >}{\nu}} \qquad \text{Equation 1.65}$$

Equation 1.65 corresponds to the expression conventionally used to define the mean velocity gradient. It represents a global quantity because it involves the average rate of viscous dissipation of kinetic energy (ε). As such, the relation Equation 1.65 does not concern the non-uniformity of the spatial distribution of ε.

1.6.1.4 Residence Time Distribution

Residence time distribution (RTD) theory was originally developed from continuous fluid systems (Levenspiel, 1999) and defined as the probability distribution of time that solid or fluid materials stay inside one or more unit operations in a continuous flow system. Residence time distribution is represented as the probability distribution of time that fluid spent through a reactor in a continuous flow system. It is a general tool and a crucial indicator in understanding the fluid flow profile inside a reactor and is used for two main purposes: (1) to diagnose problems of the operating reactor and (2) to predict effluent concentrations from a reactor if reactions are known (Fogler, 2006). Typically, the most common ideal models of reactor can be divided into two models such as plug flow reactor (PFR) and completely stirred tank reactor (CSTR). For the ideal of PFR, all compounds leave the tracer after spending exactly the same amount of time in the reactor. The time that atoms spend inside a system is called residence time. For CSRT, partly atoms spend time inside the reactor lesser than the residence time, while some atoms stay longer. In fact, the conditions inside the reactor are quite different from the ideal one. Lastly, the flow pattern that occurred in a reactor is essential information to describe the behavior of a non-ideal reactor e.g., non-uniform, dead zones, or short-circuit flows.

Consequently, residence time distribution is represented as a probability distribution of time that fluid spends through the reactor in a continuous flow system. It is a general tool and a crucial index for understanding the fluid flow profile that uses for two leading purposes: to diagnose the problem of the operating reactor and to predict effluent concentrations from the existing reactor if a reaction is ensured in the reactor (Fogler, 2006).

The residence time information is usually compared with the time necessary to complete the reaction or process within the same unit operation. To evaluate the residence time distributions, mean residence time (t_m) and variance (σ^2) calculations are often used as shown in Equation 1.66 and Equation 1.67, respectively.

$$t_m = \frac{\int_0^\infty tc\ dt}{\int_0^\infty c\ dt}$$

Equation 1.66

$$\sigma^2 = \frac{\int_0^\infty (t - t_m)^2\ dt}{\int_0^\infty c\ dt}$$

Equation 1.67

Where t is time, and c is the concentration. The advantage of RTD analysis was reported that it can detect fluid dynamic problems in continuously operating such as dead zones or short-circuiting flow can be detected (Fogler, 2006; Metcalf et al., 2002; Pant et al., 2015). For example, if the actual residence time of fluid/solid stays in the system is shorter than the time required for local mixing, the process cannot provide a complete mixture, and it fails its designed purpose (Gao et al., 2012). Most studies that investigated continuous unit operations by using the RTD have focused on the influence of operation conditions, materials, and the unit geometry on the RTD profile, the improvement of measurement methods (Gao et al., 2012; Minye Liu, 2012). Besides, the RTD analysis can be determined by numerical analysis to predict the reactor behavior, estimation of effluent properties, reactor design and scale-up, and the improvement of predictive modeling on different processes and units (Fazli-Abukheyli and Darvishi, 2019).

In this study, a basic concept of the RTD model has been applied for investigation time since contact time in the flocculation affects aggregation. Thus, the fundamental idea of RTD investigated by experimental and numerical summarized in Chapter 5.

(i) Experimental Determination of the RTD

The experimental determination of the RTD, also called the tracing method, is sufficiently general and can be implemented on a wide variety of industrial systems or at the laboratory scale in micro-structured reactors (El Korchi et al., 2019). The injection of tracers can be realized by various means: immediately injection (a pulse input), injection at a constant rate (a step input), and with diverse physical forms: gas, liquid and powder. A pulse input, the tracer, which is an inert chemical, needs to be injected as fast as possible so that the recorded response at the selected position can be considered as RTD of the marked positions. The response signal shape can be used for figuring of important parameters such as the mean residence time (t_m) of the system's hydrodynamics, the presence of dead volume, recirculation, short-circuiting, bypassing and even help calculate the flow rate where flow meters are not available (Fogler, 2006; Levenspiel, 2013; Metcalf et al., 2002). For more details to analysis RTD can be follow up in the chapter of methodology (see section 2.2.1.1(iv)).

(ii) Numerical Determination of the RTD

Computational Fluid Dynamics (CFD) is a numerical approach for simulating fluid flow. The CFD is based on the basic conservation laws of fluid mechanics, i.e., the laws of conservation of mass, momentum and energy, more details can be found in Chapter 5. Computational Fluid Dynamic (CFD). As mentioned above, the RTD analysis can be determined by numerical analysis technique. Theoretically, the velocity and concentration fields of a tracer, which could be obtained from the solution of the transport phenomena equations, constitute all the information that was needed to determine RTD in a continuous flow system (Fu et al., 2018). Thus, species transport, or tracking method is the most classical method to determine the RTD-numerical and internal age distribution simulation

(Minye Liu, 2012). The numerical simulation is done by CFD and the results are validated by the experiments, so experiments are still necessary in order to validate simulations. Indeed, simulations require the detailed knowledge of the process itself and of fluid dynamics to decide on the suitable CFD model and to analyze results (Fu et al., 2018; Furman and Stegowski, 2011). The use of experimental techniques (tracer experiments) combined with numerical tools as the CFD, which is a powerful approach that provides a detailed spatial distribution of flow fields provide two or three dimensional visualization of the system (Plascencia-Jatomea et al., 2015).

Previously CFD research were focused on hydrodynamic and was applied to quantify the mixing behavior. Several publications have applied CFD to studying the hydrodynamics within settling reactors. However, the reactors with complex geometries and boundary conditions are challenging to apply and develop efficient numerical solution techniques and the ability to implement these techniques on computers (López-Jiménez et al., 2015; T. Zhou et al., 2014).

1.6.1.5 Contact Time and Camp Number

The contact time (t_{cont}), also known as the mixing time, is the length of time a substance is held in direct contact with the coagulant in the coagulation while the contact time for flocculation is the length of time under slow mixing to lead the flocs contact to each other to form larger aggregates. Typically, the amount of seconds unit of time spent in the coagulation process and flocculation process is several minutes. A flocculation test or jar test method can be used to determine the optimum value of G or t_{cont}. The optimum of G and t_{cont} values from several authors were suggested as design criteria for turbidity removal as summarized in Table 1.4.

Table 1.4 Design criteria of reactors to removal turbidity

Type of process	Parameters		Remark	Bibliographic reference
	G (s^{-1})	t_{cont} (min)		
Coagulation	700 - 1000	20 - 60	-	(T. D. Reynolds and Richards, 1996)
	700 - 1000	0.17 - 5	-	(Qasim et al., 2000b)
	250 - 1000	1 - 3	-	(Degremont, 2007)
	2000 - 30000	-	For static mixer	(Degremont, 2007)
Flocculation	< 10	-	-	(T. D. Reynolds and Richards, 1996)
	15 - 60	20 - 60	-	(Qasim et al., 2000b)
	30 - 40	-	For hydraulic flocculator	(Kawamura, 2000)
	< 5	20 - 30	For fluidize bad clarifier	(Svarovsky, 2000)

Commonly, the hydraulic flocculators have been designed based on a global parameter G, t_{cont} and Camp number. The Camp number is the product of the global parameter (G×t_{cont}), which is the dimensionless parameter. It can be said that the Camp number reflects the combined contribution of the turbulent intensity and the aggregation time is frequently used to easily quantify coagulation phenomena and design coagulation processes such as stirred tanks and clarifiers (T. R. Camp and Stein, 1943; Garland et al., 2017; John Gregory, 2013; Marques and Ferreira, 2017; Pedocchi and Piedra-Cueva, 2005; D. Zhou et al., 2012).

1.6.2 Hydrodynamic of Jet

Jet mixing is widely used for several purposes such as mixing liquid to get homogeneous fluid in the tank, to prevent deposition of suspended particles, or prevention of stratification. Thus, that the jet mixer process has been applied to use in the flocculation process in the water treatment plant. In the jet mixing reactor, in general, some part of liquid is circulated at high velocities by the induced jet that through nozzles, which is the cause of circulatory pattern creating in the vessel and leads to mixing in the tank. So, the

hydraulic of jet flocculators depends on the jet flow, which directly affects the velocity gradient, controlled by the turbulent kinetic energy dissipation rate in the region from the jet entrance and mixing time. The principal parameters that are used to determine the hydrodynamics of jet are Reynolds number in the inlet tube and the power number at the inlet tube were described.

(i) Reynolds Number in Tube

The fundamental of Reynolds number was described in section 1.6.1.1, but the term of the length scale of the tube is the hydraulic diameter. The hydraulic diameter (D_h) can be calculated using Equation 1.68. So, Reynolds in tube, jet Reynolds number, can be calculated by using Equation 1.69.

$$D_h = \frac{4 \times A_p}{P_w} \qquad\qquad \text{Equation 1.68}$$

Where A_p is cross-section area of pipe and P_w is the wetted perimeter of pipe.

$$Re = \frac{\rho u D_h}{\mu} = \frac{u D_h}{\nu} \qquad\qquad \text{Equation 1.69}$$

The Reynolds in tube can be interpreted that when the viscous forces are dominant (slow flow, low Re) they are sufficient enough to keep all the fluid particles in line, then the flow is laminar. Even very low Re indicates viscous creeping motion, where inertia effects are negligible. When the inertial forces dominate over the viscous forces (when the fluid is flowing faster and Re is larger) then the flow is turbulent.

In the past, jet flow hydrodynamics was addressed theoretically, experimentally and numerically. (Schlichting, 1979) was the pioneer to study jets. (Bickley, 1937) derived analytical solutions of jet flows; he demonstrated that the developing jet flow entrains external fluid, increasing the flow rate and decreasing the axial velocity, thus preserving constant momentum. Based on experiments, (Miller and Comings, 1957) showed that the

jet decreases axially as the square root of the axial position along the jet (the origin being at the orifice outlet) and the jet size enlargement was shown to increase linearly with the axial position. These hydrodynamic phenomena will be investigated in our jet clarifier. A jet is usually characterized by the Reynolds number at the injection. The Reynolds number is classically defined as Equation 1.70, which was derived from Equation 1.59.

$$Re = \frac{\langle U \rangle \, d}{\nu} \hspace{3cm} \text{Equation 1.70}$$

Where $\langle U \rangle$ is the cross-averaged discharge velocity from the nozzle (m/s), d is the circular orifice nozzle internal diameter (m) and ν is the kinematic viscosity of the fluid (m²/s). Referring to (Pearce, 1965) conclusion, there is no turbulence below 500 and fully turbulent jet starts at 3000. Since in our study, the Reynolds number vary between 1000 and 4000, it corresponds to the transition from laminar to turbulent jet flow. Both jet structure and stability aspects of transition flows have also been reviewed by (Mollendorf and Gebhart, 1973). A submerged liquid jet from a circular orifice nozzle into a similar liquid exhibits three characteristics regions: (1) a developing flow region: about 10 nozzle diameters long; this region is called potential conic region; (2) a developed flow region: up to 100 nozzle diameters from the orifice; (3) a terminal region: above 100 nozzle diameters from the orifice.

It was reported that instabilities appear in the sheared layers induced by the submerged liquid jet. Downstream, mixing is controlled by the entrainment of surrounding liquid in the decelerating jet velocity region. In the developed flow region, the jet structure weakly depends on inlet conditions, in particular on discharge velocity profile. In our study, the discharge flow corresponds to laminar to turbulent flow pattern in the circular nozzle. In the developed flow region, the liquid flow induced by the jet exhibits radial enlargement. This was first addressed by (Chu and Lee, 1996), who assumed that the jet radial size increase was proportional to the discharge jet velocity. This gradual enlargement is related to a decrease of the mean velocity in the jet and to the entrainment of external fluid; thus, the analysis of the axial evolution of the jet radial size would be investigated.

(ii) Power in Tube

Power in tube can be described by the function of energy in the hydraulic power system while the main components for a fluid power system are pumps, motors, control valves, actuators, heat exchange, accumulators, filters and connecting line. In the literature review, the influence of flow in tube can be derived from energy equation.

For the flow in tube, power required to overcome friction is related to the pressure drop which can be expressed as Equation 1.71, which was derived from the energy equation.

$$P = \Delta p \times Q \qquad\qquad \text{Equation 1.71}$$

Where Δp is related to the loss in the Engineering Bernoulli Equation, or equivalently, the frictional head loss (h_f), through

$$\Delta p = \rho \times \text{loss} = \gamma h_f \qquad\qquad \text{Equation 1.72}$$

Here, the specific weight $\gamma = \rho g$, where g is the magnitude of the acceleration due to gravity. The head loss (h_f) is related to the Fanning friction factor f that can be describe as Equation 1.73 or alternatively can be written as Equation 1.74.

$$h_f = 2f \left(\frac{L}{D}\right)\left(\frac{V^2}{g}\right) \qquad\qquad \text{Equation 1.73}$$

$$\Delta p = 2f \left(\frac{L}{D}\right)(\rho V^2) \qquad\qquad \text{Equation 1.74}$$

Where D is the hydraulic diameter of the pipe [m] where L is the pipe length [m].

For the laminar flow, the friction factor can be calculated by Equation 1.75 while to determine the friction factor of high Re numbers regime can be used the Equation 1.76,

which was developed from both the Colebrook or the Zigrang-Sylvester Equation by Colebrook (1939) (White, 2011).

$$f = \frac{16}{Re}$$ Equation 1.75

$$\frac{1}{f^{1/2}} = -2.0 \, log \left(\frac{\varepsilon/d}{3.7} + \frac{2.51}{Re \, f^{1/2}} \right)$$ Equation 1.76

Where ϵ is the average roughness of the interior surface of the pipe. Then the formula was used to plot the chart in 1994 by Moody, which can be called the Moody chart for pipe friction. Moreover, the table of roughness values recommended for commercial pipes given in a textbook on Fluid Mechanics by F.M. White (2011).
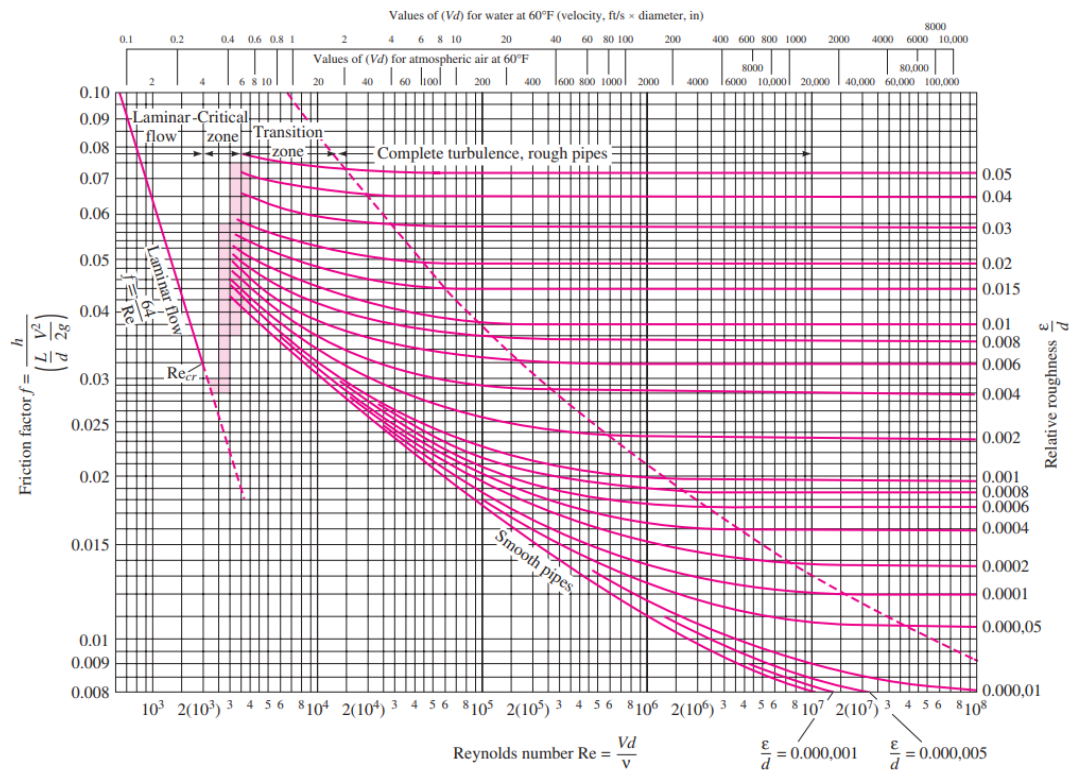
Figure 1.17 The Moody chart for pipe friction with smooth and rough walls.

(White, 2011)

The Moody chart is identical to Equation 1.76 for the high Re numbers regime. It could be seen that the power input relates to the Reynolds number that influences the flow regime. Considering the jet flow, based on the Reynolds number at the outlet of the injection tube or nozzle.

1.6.3 Mixing and Flocculation in Jet Clarifier

As described in the section 1.1.2, it could be noticed that clarification is related to flocculation. Indeed, flocculation efficiency is related to mixing in the jet clarifier. The bibliographic analysis must thus focus on mixing induced by jets, in different geometries. In terms of mixing, an inclined side-entry jet mixing of free turbulent jets in cylindrical tanks have been reported by (H. Fossett and Prosser, 1949) and (H. Fossett, 1951).

(Fox and Gex, 1956) investigated both laminar and turbulent inclined side-entry jet regimes and concluded that the main phenomena controlling the mixing time was the momentum source injected by the jet in the tank. In terms of vertical jet mixer, studies were reported by (Hiby and Modigell, 1978) and by (Lane and Rice, 1981) and (Lane and Rice, 1982) a hemi-spherical base, reporting shorter mixing times compared to flat base cylindrical tank. (Toshiro. Maruyama et al., 1981) found that the mixing time in jet flow tank depended on the liquid depth, nozzle height, and nozzle angle, and the mixing time is a consequence of jet axis length. (T. Maruyama et al., 1984) reviewed mixing induced in different geometries using horizontal, inclined and vertical jets. However, although global circulation was presented and global mixing time were determined, there was neither data nor information on the local phenomena controlling mixing.

(R. K. Grenville and Tilton, 1996) studied the free jet mixing time of the tank with H/D ≤ 1 where H is the fluid depth and D is the vessel diameter. They proposed that the mixing time had been correlated by turbulent kinetic energy dissipation rate (or power per unit mass). The turbulent kinetic energy dissipation rate at the end of the jet's free path can be used to estimate the mixing rate and it controlled the mixing rate for the whole vessel. Then, in 1997, they proffered the correlation based on the jet nozzle angle and compared their model with the circulation time model. They found that both models can be used to

predict accurate mixing time in the tank and their previous model presented in 1996 (R. K. Grenville and Tilton, 1997). Further, in 2001, they continued their work by studying the mixing time in various tank geometries and found that their jet turbulence model fitted in the range of $0.2 < H/D < 3$ and the ratio of mixing time to circulation time is not constant but rather depending on the ratio of fluid depth to diameter of the vessel (R. K. Grenville and Tilton, 2011).

(Jayanti, 2001) reported that the position of the "eye" of the circulation pattern induced by a jet is a key parameter for mixing and it depends on the tank geometry. Jayanti compared hemi-spherical base, ellipsoidal base, conical base with a half cone angle of 31° and conical base with a half cone angle of 58°. The best shape was found to be conical base with a half cone angle of 31°. In this case, the "eye" of the recirculation pattern is half the overall height, the recirculation is quite strong and there is no low velocity region. This conclusion probably contributes to explain the efficiency of the present jet clarifier since flocculation zone corresponds to a divergent (2D cone). (Wasewar, 2006) investigated design of jet mixing tank. His review summarizes different studies of jet mixed tank parameters (tank geometry, jet configuration, jet velocity, jet diameter, jet flow rate and fluid properties) to get an optimum design. He pointed out that mixing time is an important parameter to design jet tank devices.

(Perumal and Saravanan, 2012) and (Randive et al., 2018) investigated jet mixing; they pointed out that the difference between jet and bulk liquid velocity creates a turbulent mixing zone along the jet boundary. In this mixing zone, some part of the surrounding fluid is circulated at high velocity and create a circulation loop, thus leading to mix the bulk of the liquid. This kind of circulation loop induced by the jet will be investigated in this paper. Moreover, Randive et al. (2018) reviewed the jet mixing in the flocculation process and summarized several models to estimate the mixing time in terms of other parameters such as jet velocity, jet diameter, jet path length, and tank diameter and height.

(Kennedy et al., 2018) studied the effect of the distance between injection and suction ports on the control mixing time of submerged recirculation jets. They found that the distance between the ports can be used to control mixing time at the same value of

injection velocity and an empirical correlation to predict the mixing time under short-circuiting conditions of the flow is dominant, which retains the same dependence of mixing time on the injection velocity and the tank diameter.

(Garland et al., 2017) analysed the effects of Gt on turbidity removal by hydraulic flocculator, indicating better performance when a floc blanket had been formed. They concluded that appropriate mixing time is a factor that can be used to limit the size of the clarifier. In our paper, since only clear water hydrodynamics is investigated, floc blanket will not be accounted for.

To our present knowledge, the literature about the floc size, either in terms of average size or size distribution, is rather scarce in the case of jet flocculators. The main available data are generally presented in terms of turbidity removal and their conclusions do not converge on all points. Romphophak et al. (2016) studied the effect of flow rate used on the jet clarifier to reduce the turbid synthetic water: it was concluded that efficiency of about 80% can be achieved at the flow rates of $40 - 180$ L/h ($60000 < Gt < 90000$). Kumar et al. (2009) showed that, for square and circular flocculators ($37000 < Gt < 60000$), the turbidity removal was maximum when the nozzle was located 50% of the height of the tank and that when the detention time increases the residual turbidity sharply falls. In the case of higher Camp numbers ($90000 < Gt < 216000$), Randive et al. (2020) showed that tank geometry is crucial in determining the effective turbidity removal rate and circular basins should be privileged. They also found that (1) in circular tank, turbidity removal was in the range of 80% to 90% whatever the nozzle diameter; (2) increasing the retention time definitely promotes maximum turbidity removal and (3) whatever the tank geometry, jets positioned at bottom of the flocculation chamber provide better turbidity removal. In their study, citing the work of List and Imberger (1973), Sobrinho et al. (1996) mentioned that when the expanding jet collides the wall, the flocs are entrained in the bottom part of the chamber resulting in the formation of a recirculation loop leading to an increase of the concentration of flocs promoting thus their collisions. Sobrinho et al. (1996) also mentioned that the effluent residual turbidity was essentially independent of the flow rate and associated this result to a nearly constant value of *Gt* without being able to prove it.

1.7 Conclusion

This chapter introduced an overview of factors that affect turbidity removal. The aim is to introduce the basic theories and numerous works dealing with flocculation. From this chapter, it can be seen that the effective solid-liquid separation is necessary to eliminate the water turbidity. A good separation can reduce the water pollution due to colloidal particles, which is mandatory for the water treatment field. According to the review, hydrodynamics affects floc formation, which in turn affects turbidity removal. Indeed, mechanisms of coagulation and flocculation affect the properties of floc especially floc size, which is directly related to the solid-liquid separation and turbidity removal efficiency so that turbidity removal efficiency is used to estimate the effectiveness of coagulation and flocculation. For these reasons, the properties of flocs are investigated to enhance, or check, or control the process. Furthermore, a large amount of literature on the topic of flocculation have been published over many years such as floc size distribution obtained in different kinds of reactors and with various impellers. However, mixing mechanisms in the jet clarifier, are not yet fully understood since this compact and complex reactor was designed to induce aggregation in the flocculation zone with jet flow and a sedimentation zone where the flocs settle to the bottom tank. The respective roles of global circulation, and local hydrodynamic are not so clear. Hence, this study aims to determine the main parameters affected to flocs formation as well as hydrodynamics inside the jet clarifier. The obtained knowledge would be useful for dealing with flocculation by optimizing these processes to achieve effective separation performance.

CHAPTER 2

EXPERIMENTAL METHODS AND ANALYSIS

The jet clarifier is a type of solid contact clarifier considered as an effective and compact system for water treatment (Degremont, 2007; Pani and Patil, 2007). This system consists of two sections including mixing and settling zones. In the mixing zone, raw water is mixed with coagulants and injected through the center of the reactor. Flocculation occurs as destabilized particles aggregate into flocs during their ascent in the jet. Flocs can be separated in a settling zone and deposit forming a sludge blanket. Afterwards, sludge is separated from the clarified water in a settling zone where sludge is deposited and recirculated through the central zone by the induced zone. According from this process, the enrichment can induce the rapid flocculation and the formation of dense precipitates. Moreover, the jet clarifier is also comprised of a sludge hopper in order to eliminate the excess sludge (Pani and Patil, 2007; Qasim et al., 2000a; Tse et al., 2011). Consequently, hydrodynamics of the jet clarifier is highly important, at least from the following two perspectives: because of its influence on the performance of a given plant and because of its role in scaling-up from pilot tests.

The present investigation was mainly experimental. This chapter presents the materials and experimental methods that have been employed for the study of flocculation and hydrodynamics in different configurations. Indeed, experiments were performed in three different configurations of the jet clarifier. In the first part, two prototypes were developed (67 Liters: Small Scale Prototype and 243 Liters: Large Scale Prototype) to study turbidity removal efficiency with real raw waters, which was situated in Metropolitan Waterworks Authority, Thailand. It was thus possible to estimate the sensitivity of turbidity removal to different parameters. In the second part, in order to understand the local phenomena, a quasi 2D jet clarified was designed to investigate local hydrodynamics and floc size distributions with synthetic water, which was located at TBI-INSA-Toulouse, France; this pilot was designed with the same volume of flocculation zone as the Small

Scale Prototype (SSP) to keep as much as possible the same hydrodynamics to investigate in-situ floc size distribution and local hydrodynamics. In parallel, computational fluid dynamic (CFD) was developed to reproduce hydrodynamic phenomena of SSP and after validation to consider upscaling based on CFD. In details of all of this study were explained in Chapter 5.

2.1 Pilot Reactors

As explained briefly above, in this section, three different configurations of the continuous jet clarifiers are described.

2.1.1 Jet Clarifiers

This experiment focuses only on flocculation and sedimentation respectively, that took place in mixing and settling zones of the reactor since coagulation occurred in the static mixer equipped before the prototype. In addition, the jet clarifier also comprises a sludge hopper in order to drain the excess sludge for controlling the height of the sludge blanket.

a) Large scale prototype (LSP)   b) Small scale prototype (SSP)
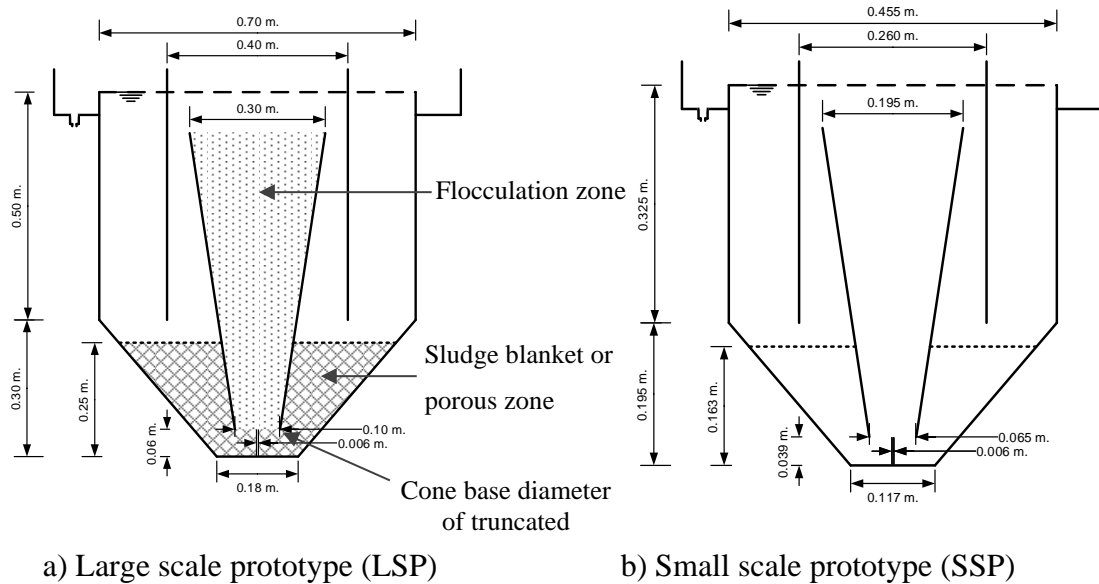
Figure 2.1 Scheme hydrodynamic diagram of jet clarifiers

The jet clarifier reactor was designed based on the design criteria of the conventional solid contact tank (see Figure 1.2) to study the efficiency and the global mean residence time of the reactor to eliminate turbidity for synthetic and surface raw waters. Two sizes of prototype jet clarifier were first applied in this work as in Figure 2.1: (a) large scale prototype (LSP) and (b) small scale prototype (SSP). Their dimensions are shown in Table 2.1. Both reactors were made with transparent acrylic plastic. The SSP was geometrically scaled down from the LSP with 0.65 scale factor (see Equation B.1, Appendix B). As a result, the volumes of LSP and SSP were 243 liters and 67 liters, respectively. Moreover, different base diameters of the flocculation zone were investigated 5 cm., 10 cm., and 15 cm for the LSP and 3.25 cm., 6.5 cm., and 9.75 cm for the SSP. In this study, polyoxymethylene (POM) solid particles with a density of 1250 kg/m^3 and a diameter of 2.82 mm. were used to simulate sludge blanket characteristics (e.g., size, density, and porosity of floc) throughout the studies.

It would notice that there were two sizes of prototype jet clarifier that would be used to examine the performance of them to investigate scale affect the performance of the reactors. Moreover, the configuration of prototype jet clarifiers (base diameter of truncated of the flocculation zone) and characteristics' sludge blanket (simulated and actual sludge), which were sensitivity parameters on reactors' performance, would also be examined for each size.

Table 2.1 Dimensions of prototype jet clarifiers

Dimensions	Units	LSP Value	SSP Value
Volume			
• Total volume	L	243	67
• Flocculation volume	L	22	6
Nozzle injection tube			
• Diameter	mm.	6	4
Flocculation zone: Conical shape			
• Truncated cone height	m.	0.65	0.4225
• Diameter of the truncated cone base	m.	0.05, 0.10, 0.15	0.033, 0.065, 0.98
• Diameter of truncated cone top	m.	0.30	0.195
Transitional zone: Cylindrical shape			
• Height	m.	0.80	0.52
• Diameter	m.	0.40	0.26
Sedimentation zone			
• Truncated cone height	m.	0.30	0.195
• Diameter of the truncated cone base	m.	0.18	0.117
• Diameter of truncated cone top	m.	0.70	0.455
• Cylindrical height	m.	0.50	0.325
• Cylindrical diameter	m.	0.70	0.455

2.1.2 A Quasi-bidimensional Jet Clarifier (Q2D Jet Clarifier)

The pseudo-two-dimensional jet clarifier, named as a quasi-bidimensional (Q2D) jet clarifier, was designed in order to perform visualization of both velocity field (PIV) and floc size distributions (shadowgraphy). The configuration of the Q2D jet clarifier was kept the same volume as the SSP. The dimensions of the Q2D jet clarifier were 56 cm. high, 95 cm. long, and 10 cm. thickness, and 42 liters total volume, which was constructed using

Plexiglass (PMMA) (1 cm thick) to be enabled to utilize the optical methods. The jet clarifier is made of two main zones: a flocculation one (mainly downstream of the jet inlet is discharged by a nozzle of 4 mm diameter within the vertical divergent) and a settling one (downflow & upflow towards the outlet). The two zones are separated by inclined baffles with an angle of 40°. The tank dimensions are shown in Figure 2.2.

Figure 2.2 The diagram of the Q2D jet clarifier

The coagulation was achieved by a 144 liters mixing tank with the 16 cm diameter of Rushton impeller that was fixed rotation speed at 170 rpm ($G = 300$ s^{-1}) for rapid mixing upstream the Q2D jet clarifier that coupled flocculation and sedimentation. The main hydrodynamic of the Q2D jet clarifier has a center-feed for the inlet and an overflow weir for the outlet as same as the jet clarifier prototypes. Thus, symmetrical flow is induced and there is equality repartition of flow into both outlet weirs (left and right).

2.2 Metrological Methods

In this study, the jet clarifier 3D prototypes were used to study the global parameters, including turbidity removal efficiency and mean residence time distribution while the Q2D jet clarifier was used to study hydrodynamic structures as well as floc size distribution through the flocculation.

Turbidity meter and conductivity probes were used to analyze the global inlet parameters. PIV measurement was used to analyze the local hydrodynamics of the liquid phase in the reactor. The floc size distribution was examined by using shadowgraphy. The metrological method details are derived below.

2.2.1 To Investigate Global Parameter

The 3D jet clarifier prototypes, small scale prototype (SSP), and large scale prototype (LSP) were operated continuously. The objectives of this work were to determine the performance of jet clarifier for turbidity removal in the aspect of water treatment and also the effects of flow rates, sizes of the jet clarifier, the diameter of the base truncated cone of flocculation, and two water characteristics, surface raw water, and synthetic water were investigated. The flow behavior in the reactor was also analyzed with RTD experiments.

2.2.1.1 Turbidity Removal Efficiency

(i) Experimental Setup

The jet clarifiers were constructed for investigating turbidity removal efficiency. Both sizes of jet clarifier prototypes were operated continuously until the system reached the steady state that can be stated by the stable turbidity values of effluent. At the beginning of the experiments, the pilot only contained clear tap water at rest. The treated water was collected at the outlet to check turbidity every 30 minutes until the turbidity was constant. The schematic diagram of the experiment setup was shown in Figure 2.3. The system can be divided into 3 parts including the rapid mixing by the static mixer and the slow mixing

followed by the sedimentation in the jet clarifier. These reactors have a center-feed for inlet by a centrifugal pump and an overflow weir for the outlet. The direction of expected flow was shown as the arrows in the tank. The solid line arrows represent the direct flow, and the dashed line arrows represent the recirculation flow by the suction force in the sludge blanket near the inlet tube. The synthetic or surface raw water was fed from the water preparation tank to mix with the coagulant injected by a diaphragm pump and flow through the reactor. The effects of liquid flow rates and configurations of each tank on the removal efficiency at the steady state were examined. Various flow rates studied and the Reynolds number (rec. Equation 1.69) at the inlet for each prototype size was shown in Table 2.2. The theoretical retention time (τ) from each part at different flow rates is compared with those from the conventional processes for turbidity removal as shown in Table 2.3. In order to keep the same hydrodynamics for the different reactor scales, the flow rates of the small scale prototype (SSP) were reduced. The operating conditions were selected to obtain the same theoretical retention times (τ) calculated with Equation 2.1 in the reactors with different sizes as listed in Table 2.2. The designed retention time of the jet clarifier was in the same range as the criteria.

$$\tau = \frac{\text{Total volume}}{\text{Inlet flow rate (Q)}} = t_m \qquad \text{Equation 2.1}$$

Table 2.2 Details of the experimental set-up: inlet conditions and residence time

LSP		SSP		Theoretical residence time (min)	
Flow rate (L/hr.)	Re number	Flow rate (L/hr.)	Re number	Without sludge	With sludge
40	2358	11	997	365	318
70	4126	19	1743	209	182
180	10610	49	4483	81	71

It can be seen that the theoretical residence time (τ) of the reactor with sludge is less than without sludge due to the volume occupied by the sludge inside the reactors.
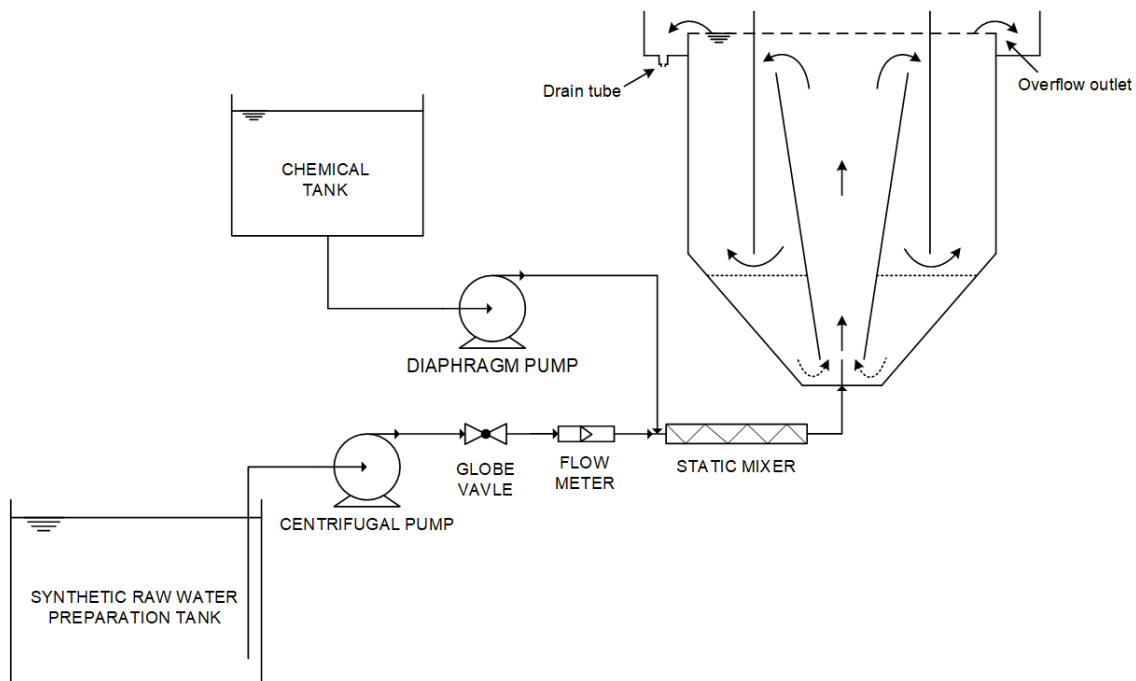
Figure 2.3 Schematic diagram of jet clarifier process

Table 2.3 Comparison of contact or theoretical retention time of the jet clarifier to the design criteria

Category	Flow rate (LPH)		Coagulation time (s)	Flocculation time (min)	Sedimentation time (hr.)	Reference
	Large scale	Small scale				
Design criteria	-	-	$1 < t < 5$	$20 - 40$	$1 - 3$	(Denis Bouyer et al., 2005; Degremont, 2007; Kawamura, 2000; T. D. Reynolds and Richards, 1996)
Jet clarifier	40	11	5.55	33	4.73	
	70	19	3.16	19	2.70	Using Equation 2.1
	180	49	1.23	7	1.05	

<u>(ii) Liquid Phases</u>

The liquid phases were the synthetic raw water and the natural surface water that was taken from/issued from the Samsen Water Treatment Plant, the Metropolitan Waterworks Authority of Thailand. More details were explained separately in the next paragraph.

a) Natural Surface Raw Water

The natural surface raw water was collected from the sampling pipe located in the laboratory of the Water Quality Controlled Department of Samsen Water Treatment Plant, Thailand. It is connected the sampling pipe with the tunnel junction of the Prapa Canal that is used to convey the natural surface water through into the water treatment plant. The pH and alkalinity of the natural raw water were variable parameters due to the climate and season during the experiment period. Characterization of the raw water was carried out immediately after the raw water sampling. The standard method 2320B was used to analyze alkalinity and the pH meter used was microprocessor pH-meter pH 539 (WTW, Germany). The turbidity of the water was 55 – 60 Nephelometric Turbidity Units (NTU). The values of pH and alkalinity were about 7.16 – 7.36 and 80.20 – 90.10 mg/L as $CaCO_3$, respectively. All the experiments were carried out at room temperature ranged from 30 to 35^oC. A Mastersizer (Malvern 2000, USA) gives a volume-weighed mean diameter (d_{50}) of primary particles about 10 µm and the mode of the volume distribution was also about 10 µm as can be seen in Figure 2.4. The characteristic of the sample water determined in accordance with the Standard Method was summarized in Table 2.4.
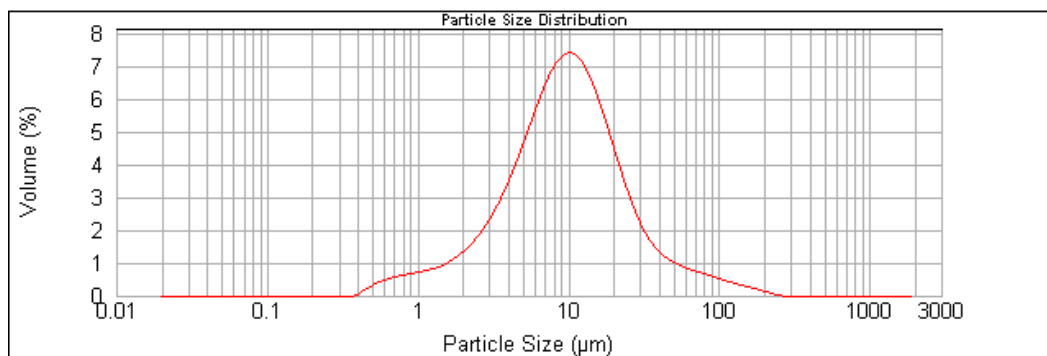
Figure 2.4 Size distribution (volume) of particles in natural raw water

b) *Synthesis Natural Surface Water*

The particles of bentonite (P.P.M. Chemical, Thailand) were used to simulate those present in natural waters as they are negatively charged. The chemical composition of the bentonite is 68.5% SiO_2, 14% Al_2O_3, and 1.2% Fe_2O_3 (%w). The experiments were done at a fixed bentonite mass concentration of 220 mg/L in tap water to synthesize the turbid raw water 50±0.2 NTU that it equals to the average raw water turbidity that fed into the Samsen Water Treatment Plant (MWA., 2019). To avoid any disruption due to the swelling ability of bentonite, the suspension has to be prepared 24 hours before experiments. The synthetic natural surface water was stirred continuously with a Rushton turbine to ensure that the bentonite particles were dispersed thoroughly. The pH and alkalinity of the resulting suspension were variable parameters due to the tap water during the experiment period. The values of pH and alkalinity were about 7.5, and 79.20 – 92.00 mg/L as $CaCO_3$, respectively. All the experiments were carried out at room temperature ranged from 30 to $35^{\circ}C$. A Mastersizer (Malvern 2000, USA) gives a volume-weighed mean diameter (d_{50}) of primary particles of 15 μm and the mode of the volume distribution was about 20 μm as can be seen in Figure 2.5, and the zeta potential value of bentonite was -8.09 mV by a Zetasizer (Nano-zs, USA) device.
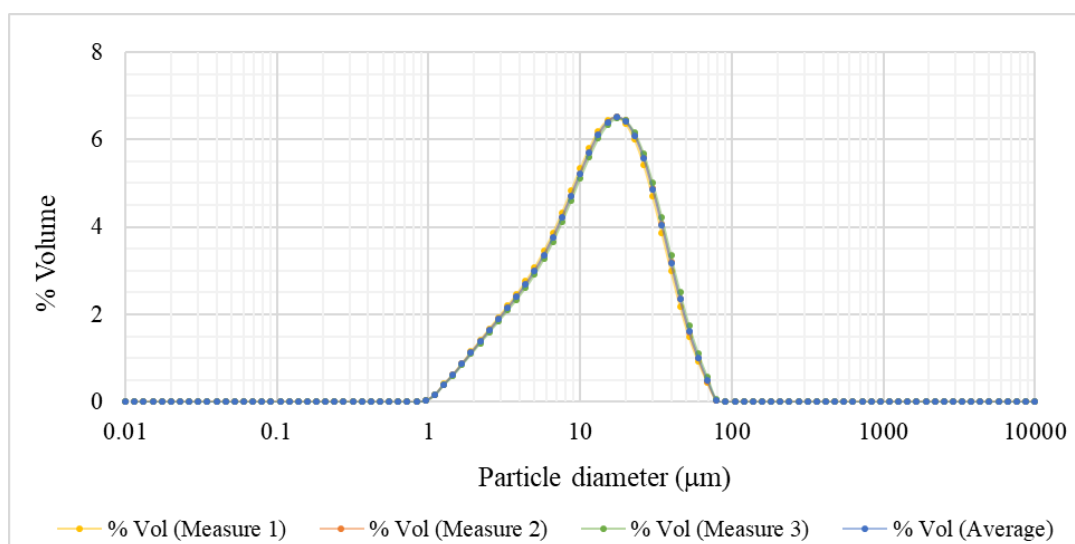
Figure 2.5 Size distribution (volume) of bentonite particles

Table 2.4 Characteristic of suspension liquid

Parameters	Natural surface raw water		Synthetic natural surface water	
	Range	Mean*	Range	Mean*
Turbidity (NTU)	55 – 60	58	49.8 – 50.2	50
pH	7.16 – 7.36	7.25	7.45 – 7.85	7.69
Alkalinity (mg/L as $CaCo_3$)	80.20 – 90.10	80.20	79.2 – 92.0	84.25
Temperature (ºC)	30 – 35	33	30 – 35	33

* Average of the sample taken from May to July 2018

The mode of both distributions (natural and synthetic raw waters) are quite similar. Nevertheless, it can be noticed that the size distribution of the natural raw water is wider. Indeed, the smaller particles are about 0.4µm whereas synthetic raw water is about 1 µm. At the same time, there was the largest size of 300 μm. of the particle in natural surface raw water, while the maximum size of bentonite is 80 μm. Moreover, the alkalinity and pH values of natural surface raw water and synthesis surface water were in the same range. The synthesis surface water thus could be used as the representative of the natural surface raw water.

c) Coagulant

Aluminum Sulfate, $(Al_2(SO_4)_3 \cdot 14H_2O)$, provided by Siam Chemical Public, Thailand, commonly used in water treatment, was chosen as a coagulant and prepared at 1% w/v. concentration. The optimum doses of the Aluminum Sulfate needed for removal of the suspended matter were evaluated via a jar test that are explained in the next paragraph.

(iii) Jar Test Apparatus

The appropriate implementation of this method depends on how precisely coagulant dosage and characteristics of water. Therefore, trial and error has been conventionally practiced to optimize these variables. These studies were conducted using "changing one factor at a time" method, i.e., a single factor is varied while all other factors are kept unchanged for a particular set of experiments. Likewise, other variables would be individually optimized through the single-dimensional searches which are time-consuming and incapable of reaching the true optimum as interaction among variables is not taken into consideration (Ghafari et al., 2009).

Jar testing was performed using the 1-liter cylindrical beakers of water is stirred with a 7.4 cm. × 2.5 cm. flat blade. The blade is mounted at the end of a vertical shaft, which divided the blade into two identical paddles, each with a continuous blade of 3.7 cm. × 2.5 cm. and a Flocculateur 11196 conventional jar test apparatus (Bioblock Scientific, France) equipped with adjustable mixing time and speed. In this study, a rapid mixing (coagulation) of about 1 min at 200 rpm. was followed by 20 min of slow mixing (flocculation) at 60 rpm. to promote the aggregation of flocculated particles. The suspension was then allowed to settle undisturbedly in 10 min. Samples of the supernatant were drawn with a pipette from 2 cm below the surface for residual turbidity measurements by using a 2100N IS Turbidimeter (HACH, USA).

(iv) Analytical Methods

The turbidity and pH were measured by the TL2350 model of turbidity meter (Hach, USA) and the F-73 model of pH meter (Horiba, USA), respectively. The accuracy of turbidity measured by the device is ±2% for the range 0.01 NTU – 1000 NTU. The turbidity removal efficiency was evaluated by Equation 1.58. To evaluate the turbidity removal efficiency, the treated water was collected at the outlet every 15 minutes from the beginning until the system reached steady state. The standard methods of 2540D and 2320B were applied to analyze suspended solid and alkalinity (Eaton et al., 2005).

2.2.1.2 Experimental Residence Time Distribution (RTD-Experiment)

In this study, again, the pilot plant was conducted to determine the mean residence time distribution (RTD). The RTD of the reactor was studied by using a pulse injection method. This study aims to investigate the mean residence time of the jet clarifier. Then, the curve of RTD-experiment (*E*-curve) would be used to validate the mean residence time by solving species transport for RTD-numerical (RTD-numerical in order to validate the model and evaluate the local time), which would describe in heading 5.2. Furthermore, the local residence time from the internal age distribution function was demonstrated. Details about RTD-numerical are given in Chapter 5 on Computational Fluid Dynamic (CFD).

(i) Experimental Setup

The jet clarifiers were constructed to be the pilot plant and were designed explicitly for investigating residence time distribution and a process flow diagram of the experimental set-up and scheme hydrodynamic diagram of jet clarifier are shown in Figure 2.6. Note that the static mixer was removed to avoid the flow phenomena effect of the static mixer. However, the static mixer used in this work was also evaluated the mean residence time; the details and results of the experiment can be seen in Appendix C.

The jet clarifiers have a center-feed for inlet by a centrifugal pump and an overflow weir for the outlet and also a drained tube. Prior to the inlet, a Y-type connector was

installed for tracer injection. In order to obtain the signal of the tracer, a conductivity probe with the accuracy of ±0.5% of reading (Hach, USA) was placed in the reactor at the drain tube on overflow outlet (see Figure 2.7, position ④) every 3 minutes to detect the amount of tracer concentration, which could be represented by conductivity.

The experiments were carried out under three different flow rates for each size, which were 40, 70, and 180 L/hr., and 11, 19, and 49 L/hr. for the LSP and the SSP, respectively, with two other conditions that were the blank reactor (without sludge) and the reactor with the sludge layer conditions of each reactor sizes. 2.82 mm diameter Polyoxymethylene (POM) solid particles with a density of 1,250 kg /m^3 were used instead of actual sludge blanket to maintain sludge blanket characteristics (e.g., size, density, and porosity of floc) throughout the study as well as avoid interference in RTD analysis due to tracer adsorption.
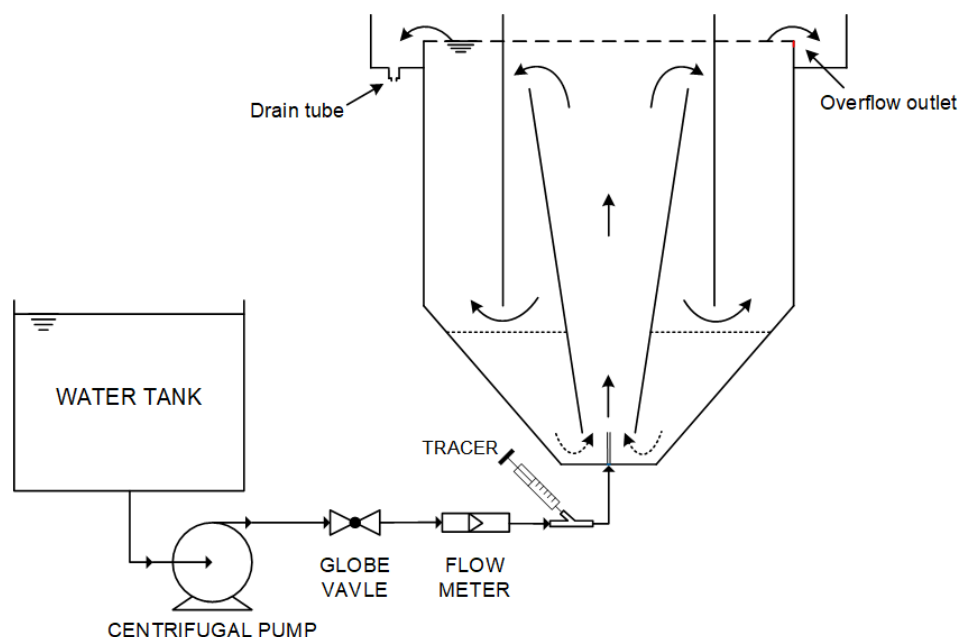
Figure 2.6 A process flow diagram of the experiment and scheme hydrodynamic diagram of a jet clarifier

(ii) Liquid Phases

The analytical chemical-grade from KemAus, Australia, was used to mix as the tracer solution. Sodium chloride (NaCl) mixed with potassium permanganate ($KMnO_4$) with a concentration of 200 g/L and 20g/L, respectively, mixed with demineralized water. The volume of tracer solution used in the experiments was different due to the size of the reactor, which was 50 ml and 13 ml for large and small sizes, respectively.

(iii) Tracer Monitoring and Data Acquisition

The concentration of NaCl in the exit stream of a system can be determined by conductivity detector with the accuracy of ±0.5% of reading, CDC401, (Hach, USA.) was installed at the exit streams, position ④ as shown in Figure 2.7, of each tank to monitor tracer concentration directly. In addition, other conductivity detectors were taken place inside the jet clarifier in positions ① to ③ each reactor to detect the tracer signal along with the jet clarifier. Each detector was connected to conductivity meter model HQ14d (Hach, USA.) set at a detecting time of continued.
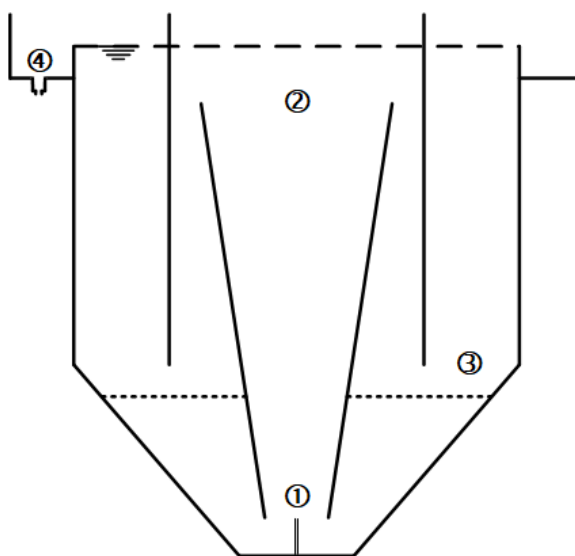
Figure 2.7 The positions of conductivity detectors inside jet clarifier and exit of reactor

(iv) Analytical Methods

The residence time distribution (RTD) was conducted for analyzing the behavior of non-ideal reactors. Two single parameter flow models were used to characterize the RTD results. Although other analysis methods are available, the compartment model and the dispersion model were chosen due to their simplicity and applicability (Fogler, 2006). The method of moments and non-ideal device techniques were used to calculate the parameters from the experimental data, including mean residence time (t_m), variance (σ^2), and skewness (s^3), which were defined as the first, the second, and the third moments, respectively (Alkhaddar et al., 2001; Levenspiel, 1999). In this study, for each sample, the tracer concentration (or conductivity) was determined. The tracer (NaCl) pulse input data are presented using the exit-age distribution function $E(t)$ defined as the fraction of material, which has left the device between time t and $t+dt$. The function $E(t)$ with the unit of min^{-1} can be expressed as Equation 2.2.

$$E(t) = \frac{C_{(t)}}{\int_0^\infty C_{(t)} dt}$$

Equation 2.2

Where C(t) is the concentration of the tracer at time t.

Integrating C(t)dt from 0 to ∞ yields the entire area under the C(t) curve. Mathematically, this value is constant. Therefore, $E(t)$ could be rewritten in Equation 2.3, below, with *Area* representing the area under the entire curve.

$$E(t) = \frac{C_{(t)}}{Area}$$

Equation 2.3

$$\int_0^\infty E(t) dt = \frac{\int_0^\infty C_{(t)} dt}{\int_0^\infty C_{(t)} dt} = 1$$

Equation 2.4

By taking the integral of the *E(t)* curve on the bounds t_1 to t_2, the function can be interpreted as the fraction of material leaving the reactor that has resided in the reactor during the bounded time (Fogler, 2006). For example, integrating from time 0 to 3 min in the *E(t)* function can be seen visually in Figure 2.8. The shaded region represents the fraction of material that spends 3 minutes or less in the reactor.
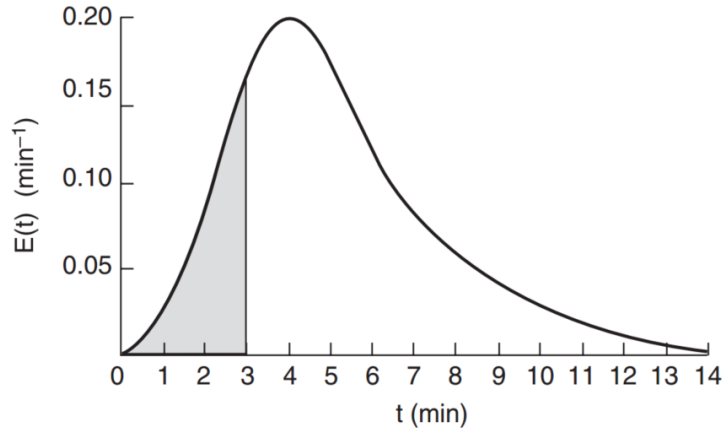
Figure 2.8 *E(t)* vs t integration schematic showing bounds from 0 to 3 minutes (Fogler, 2006)

From the concept, the characteristic flow patterns of the reactor could be different, that depend on flow rate and tank configuration, and could provide different *E(t)*, which can be used for determining the mean residence time (t_m), the first moment, as Equation 2.5.

$$t_m = \frac{\int_0^\infty t E_{(t)}\, dt}{\int_0^\infty E_{(t)}\, dt} = \int_0^\infty t\, E_{(t)}\, dt \qquad \text{Equation 2.5}$$

If the actual residence time spent inside the reactor is shorter than the time required for local mixing, the process cannot provide a complete mixture, and it fails its designed purpose (Gao et al., 2012). If there are no dead, or stagnant zones within the reactor, t_m is equal to the ideal residence time (τ = Volume/Flow rate). The data are also presented in

terms of normalized time, the dimensionless function, and it can be described by Equation 2.6.

$$\theta = \frac{t}{\tau}$$

<div align="right">Equation 2.6</div>

Where τ is the theoretical retention time.

A dimensionless function termed the normalized exit-age distribution function, $E(\theta)$, can be defined as $E(\theta) = \tau\, E(t)$. A plot of $E(\theta)$ is a function of the normalized time, θ. The quantity θ represents the number of reactor volumes of fluid that have flowed through the reactor in time t. The normalized RTD enables to compare directly data for different flow rates and different sizes of reactors. The experiments were stopped at approximately $4 - 5$ theoretical mean residence times, which is greater than the recommended RTD experiment duration when using the methods of moments. The recommended experiment duration is approximately $3 - 4$ times the theoretical mean residence time (Nauman and Buffham, 1983). The second moment of RTD function, σ^2, gives the variances of resident time. It quantifies the width or scatters of the distribution: the greater value of this moment means the greater the distribution spread. This moment is defined as Equation 2.7.

$$\sigma^2 = \int_0^\infty (t - t_m)^2 \, E(t) \, dt$$

<div align="right">Equation 2.7</div>

The concept of skewness, s^3, the third moment of RTD function, was proposed to evaluate the deviation from a symmetrical distribution (Ham and Platzer, 2004). The third moment is defined as Equation 2.8. A left-skew distribution of RTD curve exists when $s^3 < 0$ and a right-skew distribution exists when $s^3 > 0$.

$$s^3 = \frac{1}{\sigma^3} \int_0^\infty (t - t_m)^3 \, E_{(t)} \, dt$$

<div align="right">Equation 2.8</div>

The last component to the reactor analysis is dispersion, which is a parameter used to model reactor flow patterns. The axial dispersion model can be used to represent the time dependent *E*-curve. This model is used to fit the RTD measurement assuming open-open boundary condition. In dimensionless form, the model is given as Equation 2.9 (Levenspiel, 1999).

$$E(\theta) = \frac{1}{2\sqrt{\pi\theta\left(\frac{D}{uL}\right)}} \exp\left[-\frac{(1-\theta)^2}{4\theta\left(\frac{D}{uL}\right)}\right] \qquad \text{Equation 2.9}$$

Where D = dispersion coefficient (m²/s), u = velocity gradient (m/s) and L = Flow distance (m).

The corresponding variance is

$$\sigma^2_{\theta,\,0\text{pen-open vessel}} = \frac{\sigma^2}{t_m^2} = 2\left(\frac{D}{uL}\right) + 8\left(\frac{D}{uL}\right)^2 \qquad \text{Equation 2.10}$$

Defining the exact axial dispersion is difficult. To provide an estimate of dispersion, the following unitless dispersion number, Peclet number, has been defined:

$$Pe = \frac{uL}{D} \qquad \text{Equation 2.11}$$

Where the Peclet number is the dimensionless, *Pe*, L is the characteristic length term, which is the reactor length, u is the local flow velocity, and D is the effective dispersion coefficient.

The *Pe* represents the ratio of the mass transport brought about advection and dispersion. If the *Pe* values are largely greater than 1, advection will be the dominant factor in mass transport. Moreover, *Pe* values greater than 10 indicates plug flow. In this case, the tracer residence time tends to have a narrower distribution, which results in a low value of σ_θ^2 (Minye Liu, 2012).

As briefly mentioned at the beginning of this part, there were two methods used to analyze RTD function as a global parameter in order to examine the mean residence time in the jet clarifier by RTD-experiment. Besides these, the mean residence time of reactors can be determined by several numerical methods, which depend on the purposes to examine. In this study, the RTD-numerical and species transport for internal age distribution simulation were selected. More details about the numerical technique can be found in the next topic.

2.2.2 To Investigate Local Parameter in the Q2D Pilot

Numerous studies on hydrodynamics-flocculation interactions have been conducted in several geometries and with various methods (Denis Bouyer et al., 2005; Coufort - Saudejaud et al., 2005; Carole Coufort et al., 2008; Kinoshita et al., 2017; Ren et al., 2017); it has been confirmed that hydrodynamics conditions play an important role in physico-chemical floc characteristics, which affect turbidity removal efficiency. Aggregation of flocs is directly related to collision rate since the density of flocs is close to the density of the water. The fluid motion leads following flocs, and then the collisions are induced by the local velocity gradient. Consequently, the local velocity gradient and the floc size distribution would be examined by Particle Image Velocimetry (PIV) and shadowgraphy technique, respectively. The metrological method details are described as the following for each topic.

2.2.2.1 Particle Image Velocimetry (PIV) Experiment

PIV has become a trendy non-intrusive tool for measuring various types of flows. Although flows in nature are three-dimensional, 2D PIV is still broadly used due to its simple setup and high reliability (Adrian, 1991; H. Lee and Hwang, 2019; Scharnowski et al., 2017). The principle of the 2D PIV technique consists in acquiring two-dimensional instantaneous velocity component of the velocity field in a plan. Fluorescent seeding particles are used to follow fluid flow. The fluid velocimetry can be calculated by estimating the displacement of particles from images analysis.

(i) PIV Principle

The main principle consists in recording two successive images of particles illuminated by a laser plane. The most probable local displacement of a small number of seeding particles gives an instantaneous velocity vector, which can be calculated by capturing the comparative displacements of these particles within a known interval of time (Δt). Considering the displacement of all the particles, the instantaneous velocity field can be calculated. In this way, the main base of the PIV method is very simple: the fluid instantaneous velocity is measured by the determination of all the displacements of the seeding particles, which are lighted by a laser plan. The Particle Image Velocimetry (PIV) is a powerful tool to find a complete flow field. The main condition is that, during the two instants measure, the particle must remain inside the thickness of the lightning plane. Generally, the laser source used is an impulsion laser which delivers two impulsions separated by a time interval Δt (adjustable depending on the velocity you want to measure). All the images are taken by a video camera.
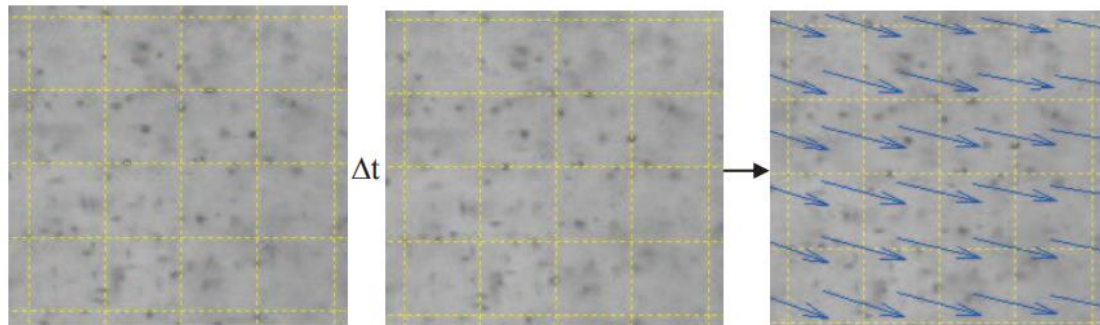
Figure 2.9 Principle of the Particle Image Velocimetry: Record of two successive in time images (Palacios, 2010)

(ii) 2D PIV Technique

The 2D PIV system used in this study is the commercial system acquired from Dantec Dynamic Co (Denmark). This technique enables the acquisition of an instantaneous two-dimensional velocity field in a plan, which has been used at TBI to examine the

velocity flow field in the agitated tanks (D. Bouyer et al., 2005; Escudié and Liné, 2003; Fernandes del Pozo et al., 2020; Gabelle et al., 2013; Laupsien et al., 2021). The 2D PIV setup consists of three main components including seeding particles, illumination, and recording systems. While the PIV technique can be described briefly as followed:

1) Feeding the fluid flow volume under investigation with fluorescent polymer particles in aqueous suspension called Rhodamine B suspensions (PMMA-Rhodamine B-Particles, Dantac Dynamics). The Rhodamine B suspensions have homogeneous distribution and good ability to represent the flow motion, which particle size range is 10 to 20 μm and a density of 1190 kg/m^3;

2) Illuminating the located slice selected of the flow field with a double-pulsed light sheet to visualize the target plane and the fluorescent particles;

3) Taking the images of fluid flow by the CCD camera located perpendicular to the laser sheet with the interval time between double-pulsed, then recording them;

4) Processing these images to get the instantaneous velocity field.

For the jet clarifier, the hydrodynamics were studied in four fields to measure the velocity field in the whole flocculation zone, illustrated in Figure 2.10, but the hydrodynamic study was focused on fields 1 and 2, and partially on field 3 since these fields corresponded to the jet mixing, flocculation zone.
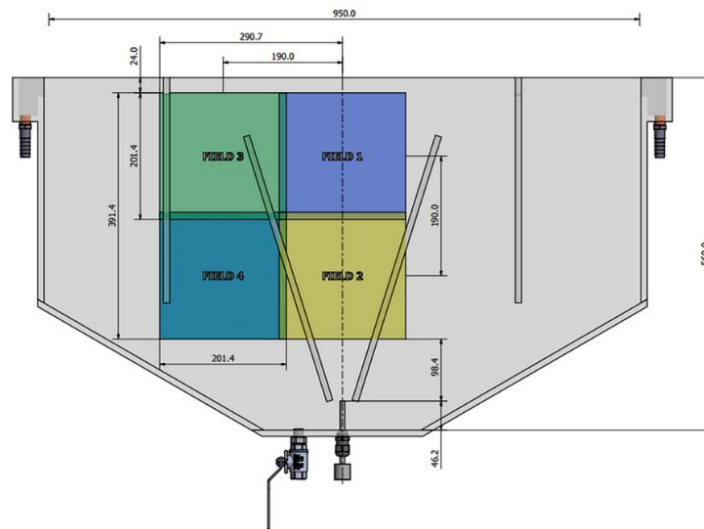
Figure 2.10 PIV windows in the vertical plane of symmetry of the jet clarifier

(iii) Experimental Setup

The Q2D jet clarifier was designed to investigate the local hydrodynamics of the jet clarifier. The laboratory pilot was shown in Figure 2.11 illustrates the schematic PIV experimental, the inlet flow was regulated and measured by a micro gear pump (WT3000-1JA, Longer Precision Pump Co.). The water exited the Q2D jet clarifier over weirs (outlet). In this work, the Rhodamine B suspensions are well mixed in the water preparation tank by an agitator with the motor before feeding into the Q2D jet clarifier.

The PIV system used was the commercial system from Dantec Dynamics Co. (Denmark). The required basic elements include a double-pulsed Nd: YAG laser (big sky laser of 30 mJ.) operated at a trigger rate of 10 Hz. Each pulsation was controlled by the trigger rate between 3 – 25 ms depending on the flow velocity and the projection field. The details of the acquisition parameters of the time interval between consecutive images can be found in Table 2.5. The CCD camera (Flow sense EO, Dantec Dynamic) was used to record the flow at each flash laser. This technique enables the acquisition of an instantaneous two-dimensional velocity field in a vertical plane. The vertical plane investigated in this study was fixed in the plane of symmetry of the pilot (at a position $Z = 5$ cm, half the depth of the Q2D pilot). The size of the developed flow region is supposed to be up to 100 nozzle diameters from the orifice, corresponding to 400 mm. The size of each PIV image was fixed to 200 mm. Each velocity field measured over a square 200×200 mm² with a scale close to 0.1 mm/pixels (2048×2048 pixels^2), is composed of the two components (U horizontal and V vertical) of the instantaneous velocity on 127×127 squared matrixes. Thus, the distance between two vectors, called the PIV filter, is 1.57 mm (16 pixels). The number of image pairs is 3000.
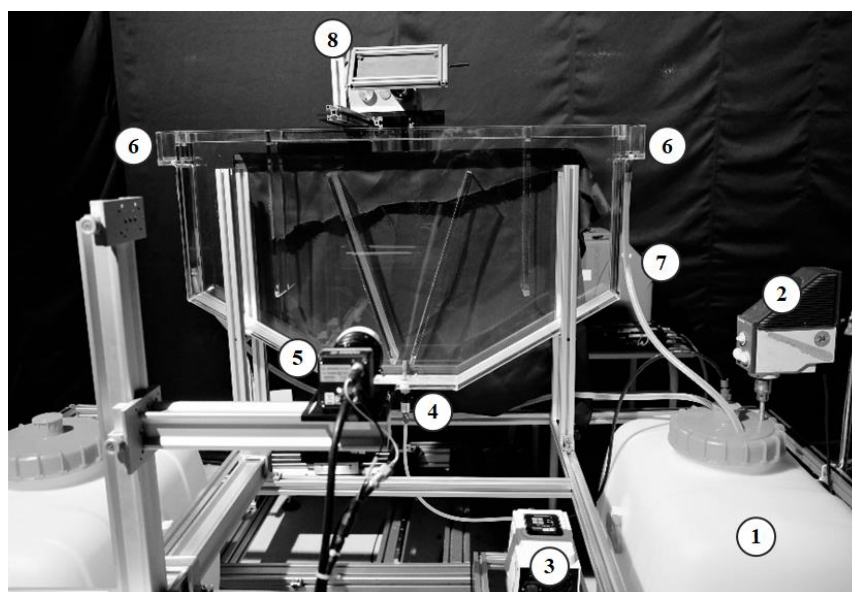
1. Water
   preparation tank
2. Agitator with
   motor
3. Micro gear
   pump
4. Inlet
5. CCD camera
6. Outlet
7. Laser generator
8. Light source

Figure 2.11 PIV experimental setup

Table 2.5 The details of acquisition parameters of the time interval between consecutive
images

| Flow rate (L/hr.) | Time interval between consecutive images (msec) | |
	Projection field 1	Projection field 2
11	25	20
19	12	10
49	5	3

(iv) Analytical Methods

a) *Statistical Analysis: Convergence*

The proper amount of images, represented as events, on the flow statistics (mean values and standard deviation) was investigated by plotting the cumulative average of velocity, in order to determine and check the statistical convergence of the data. The reliability and stability of velocity fields were verified to determine to the required minimum number of image pairs. The cumulative mean average of U (velocity in x-direction) and V (velocity in y-direction) mean velocity components, as well as u'^2 and v'^2 variances, are plotted in Figure 2.12 (a and b). The ordinate represents the mean values averaged over a number of events (instantaneous measurements) given in abscissa.
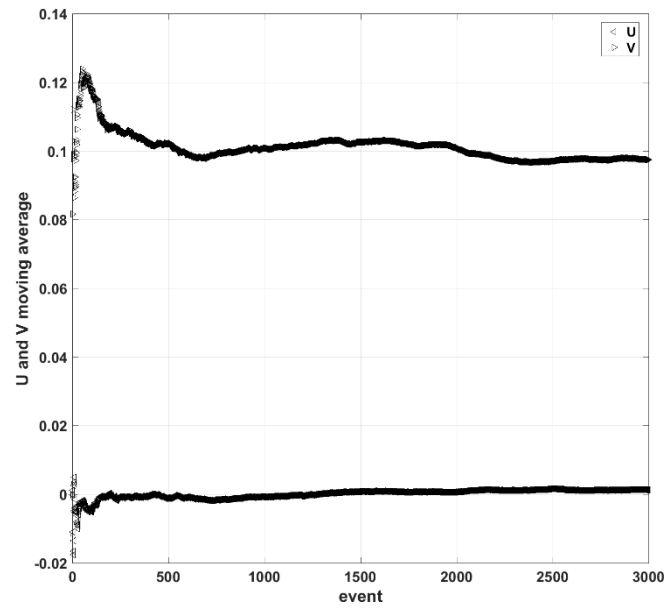
a) cumulative average of mean velocity components
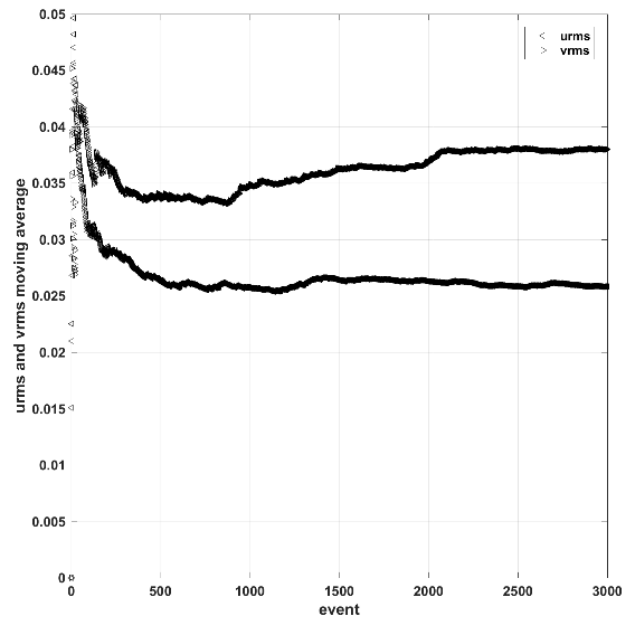
b) cumulative average of root mean square of fluctuating velocity components

Figure 2.12 Cumulative averaged of a) mean velocity components and
b) root mean square of fluctuating velocity components. Operating condition: 49 L/hr.,
Field 2, time interval between consecutive images 5 msec.

Figure 2.12 shows that the number of images should be larger than 2000 images (event) to reach statistical convergence. Statistical convergence was also verified on fluctuating speeds (rms, "root mean square"). Thus, 3000 instantaneous velocity fields were sufficient to derive statistically converged mean and rms. velocity components.

b) *Preliminary Considerations*

Before performing a local analysis of the hydrodynamic based on PIV, it is necessary to investigate global parameters. Three flow rates were investigated in this study. They are given in Table 2.6, as well as the Reynolds number at the outlet of the orifice nozzle. The flow pattern in the 4 mm internal diameter circular orifice nozzle is laminar for the two lower flow rates and slightly turbulent for the larger one. Considering the downstream liquid jet, based on the Reynolds number at the outlet of the injection tube, and referring to (Pearce, 1965) the flow pattern of the liquid jet is laminar for Re smaller than 500 and fully turbulent for Re larger than 3000.

Two characteristic inlet parameters can be quantified. The flux of momentum flow rate at the injection is defined as Equation 2.12.

$$J_0 = \iint \rho \, U(r)^2 \, r \, dr \, d\theta = \rho \, S \, \langle U^2 \rangle = \rho \, S \, C_2 \, \langle U \rangle^2 \qquad \text{Equation 2.12}$$

Where S is the cross-section area of the circular orifice nozzle. Since the discharge velocity profile is not uniform, C_2 has been introduced to relate the average of the square of the velocity to the square of the mean discharge velocity $\langle U \rangle$.

The supplied power can be derived from the flux of kinetic energy at the injection:

$$P = \iint \rho \, U(r)^3 \, r \, dr \, d\theta = \rho \, S \, \langle U^3 \rangle = \rho \, S \, C_3 \, \langle \overline{U} \rangle^3 \qquad \text{Equation 2.13}$$

Here again, C_3 has been introduced to relate the average of the cubic of the velocity to the cubic of the mean discharge velocity $\langle U \rangle$.

Assuming laminar flow in the injection tube, one can express the radial discharge velocity profile in terms of parabolic profile:

$$\frac{U(r)}{U_{max}} = 1 - \left(\frac{r}{R}\right)^2 \qquad \text{Equation 2.14}$$

One can thus handily derive analytically the two coefficients C_2 and C_3 in laminar flow as Equation 2.15 and Equation 2.16, respectively.

$$C_2 = \frac{\langle U^2 \rangle}{\langle U \rangle^2} = \frac{4}{3} \qquad \text{Equation 2.15}$$

$$C_3 = \frac{\langle U^3 \rangle}{\langle U \rangle^3} = 2 \qquad \text{Equation 2.16}$$

For the turbulent flow, the velocity profile in turbulent flow is flatter in the central part of the pipe (i.e., in the turbulent core) than in laminar flow. The flow velocity drops rapidly extremely close to the walls. This is due to the diffusivity of the turbulent flow.

In the case of turbulent pipe flow, there are many empirical velocity profiles. The simplest and the best known is the power-law velocity profile assumed as described in Equation 2.17.

$$\frac{\overline{U}(r)}{\overline{U}_{max}} = \left(1 - \frac{r}{R}\right)^{\frac{1}{6}} \qquad \text{Equation 2.17}$$

Where the power 1/6 depends on the Reynolds number (close to 4300), following Schlichting book. One can thus easily derive analytically the two coefficients C_2 and C_3 in turbulent flow by Equation 2.18 and Equation 2.19, respectively.

$$C_2 = \frac{\langle U^2 \rangle}{\langle U \rangle^2} = 1.03 \qquad\qquad \text{Equation 2.18}$$

$$C_3 = \frac{\langle U^3 \rangle}{\langle U \rangle^3} = 1.077 \qquad\qquad \text{Equation 2.19}$$

The numerical values of C_2 and C_3 are also reported in Table 2.6for the three flow rates. The averaged dissipated power per unit mass is defined as described in Equation 2.20.

$$\langle \varepsilon \rangle = \frac{P}{m} = \frac{S}{V} C_3 \langle \bar{U} \rangle^3 \qquad\qquad \text{Equation 2.20}$$

Where m is the mass of liquid (kg) in the pilot and V is the volume of water in the pilot. For the PIV experiments were done with the Q2D jet clarifier that has 42 liters total volume.

Assuming turbulent flow induced by the jet in the pilot, a global Kolmogorov scale can be estimated by Equation 2.21.

$$\langle \eta \rangle = \left(\frac{\nu^3}{\langle \varepsilon \rangle} \right)^{\frac{1}{4}} = \left(\frac{V}{S} \frac{\nu^3}{C_3 \langle \bar{U} \rangle^3} \right)^{\frac{1}{4}} \qquad\qquad \text{Equation 2.21}$$

One can relate the Kolmogorov scale to the Reynolds number in the orifice nozzle diameter as:

$$\frac{\langle \eta \rangle}{d} = \left(\frac{1}{C_3} \frac{V}{S\,d} \right)^{\frac{1}{4}} Re^{-\frac{3}{4}} \qquad\qquad \text{Equation 2.22}$$

In this study case, $\left(\frac{V}{S\,d}\right)^{\frac{1}{4}} = 30$ and thus $\left(\frac{1}{C_3}\frac{V}{S\,d}\right)^{\frac{1}{4}}$ ranges between 25 in laminar flow and 30 in turbulent flow in the tube. The ratio $\frac{\langle\eta\rangle}{d}$ varies thus between 15% and 5%, as far as the flow induced by the jet is turbulent.

One can also derive the volume averaged velocity gradient G or volume averaged shear rate:

$$G = \sqrt{\frac{\langle\varepsilon\rangle}{\nu}} \qquad\qquad \text{Equation 2.23}$$

The residence time is simply given by the volume of liquid in the pilot divided by the discharge flow rate Q.

$$t = \frac{V}{Q} \qquad\qquad \text{Equation 2.24}$$

From the velocity gradient (G) and the residence time (t), one can estimate the Camp and Stein criteria $G\,t$:

$$G\,t = \sqrt{\frac{V}{S\,d}}\,C_3\,\sqrt{Re} \qquad\qquad \text{Equation 2.25}$$

Where, as previously, $\sqrt{\frac{V}{S\,d}}\,C_3$ ranges between 1850 and 1350. t is thus between 25,000 and 45,000; recall that in flocculation, $G\,t$ is usually in the following range:

$$10^4 < G\,t < 10^5$$

Table 2.6 Global hydrodynamic characteristics for the 3 flow rates

Parameters	Flow rate (Q) (L/hr.)		
	11	19	49
$U_{injection}$ (m/s)	0.24	0.42	1.08
Re tube	970	1680	4330
Coeff $<U^3>/<U>^3$	2	2	1.077
Supplied power (mW)	0.36	1.86	17.2
$\langle \varepsilon \rangle$ (W/kg)	4.3 e-6	2.2 e-5	2 e-4
$\langle \eta \rangle$ (μm)	700	460	260
$\langle G \rangle$ (s^{-1})	2.1	4.7	14.3
J_0 (kg m/s²)	0.001	0.004	0.020
Residence time (hr.)	3.82	2.21	0.86
Gt	28,500	37,500	44,150

The present study focuses on hydrodynamics, in terms of the local and instantaneous velocity field, induced by the jet in the flocculation zone of a jet clarifier (Field 1 and 2, see Figure 2.10). In order to investigate the hydrodynamics of the new jet clarifier, PIV experiments would be presented and discussed, both in terms of jet characteristics and in terms of flow structure leading to the estimation of Gt criteria.

2.2.2.2 Floc Size Distribution

Hydrodynamically-induced turbulent shear is an essential driver of the flocculation process, especially in the case of orthokinetic aggregation of particles. The floc growth and stability in any flocculation process have been suggested to be a function of the collision of particles to agglomerate to larger ones (Oyegbile et al., 2016). In the case of hydrodynamic flocculation, velocity gradient promotes the aggregation process but might also be responsible for floc breakage as a result of increased viscous shear stress. Consequently, in the case of shear-induced collisions, the effect of hydrodynamics can be very significant (John Gregory, 2006a).

To understand flocculation in the jet clarifier, which is a free jet flow and complex system due to a combination of flocculation and settling process in a single unit, the focus has be made on the results of the flocculation of bentonite. The mean floc size diameter, the number of flocs, and floc size distribution have been measured for different flow rates. In order to study the influence of hydrodynamics on floc size, the coagulant dosage was optimized based on the experiment conducted in the jar test. Although the coagulation will not be studied here in detail, the size of the flocs of a continuous process from coagulation will be checked before feeding into the reactor.

<u>(i) Experimental Setup</u>

The same laboratory pilot that those of the PIV experiment was used, but in this work, the bentonite suspension was directly prepared and destabilized with aluminium sulphate in the coagulation tank of 144 L, the tank ①, see Figure 2.13. The suspension was stirred with a 16 cm diameter Rushton turbine at a rotation speed of 170 rpm corresponding to a velocity gradient of 300 s^{-1}, which was calculated by the global power dissipated in the tank that is related to the power number (N_p) associated with an impeller as express in Equation 1.28. The suspension was routed to the Q2D jet clarifier thanks to a gear pump. Experiments also have been realized with 3 different flow rates (Q) that are recapitulated in Table 2.7. The theoretical residence time (τ_{Q2D}) shown in the table was calculated by Equation 2.1. Note that the total volume of the Q2D jet clarifier is 42 liters.

Table 2.7 Operating Conditions of Floc Size Distribution Experiments

Flow rate (Q)	Value (L/hr.)	Residence Time (τ_{Q2D}) (hr.)
Low Flow Rate (LFR)	11	3.8
Medium Flow Rate (MFR)	19	2.2
High Flow Rate (HFR)	49	0.9
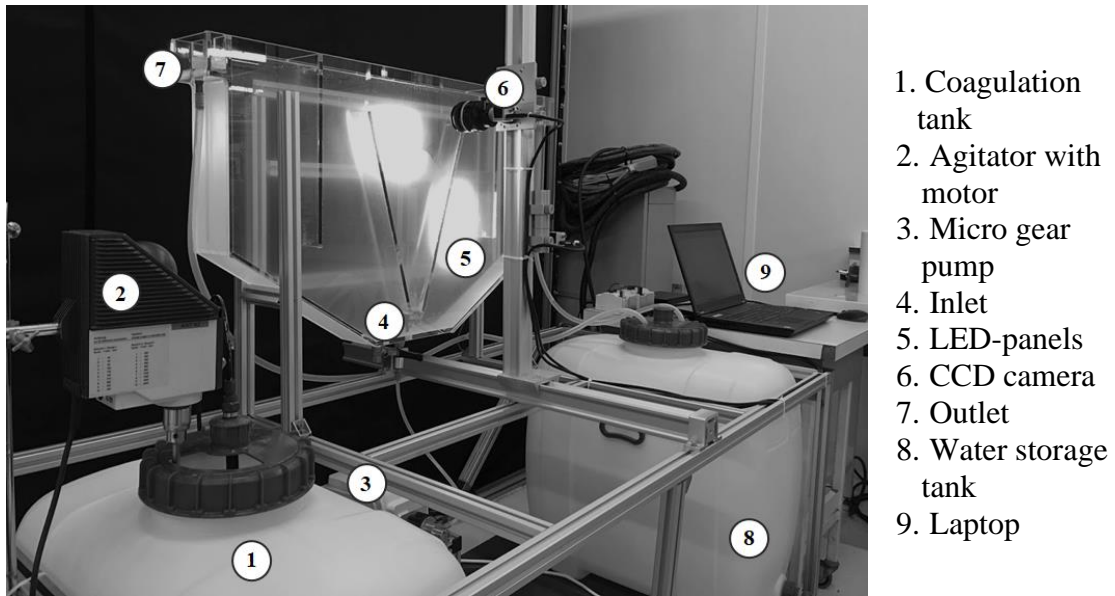
Figure 2.13 Floc size distribution experimental setup

1. Coagulation tank
2. Agitator with motor
3. Micro gear pump
4. Inlet
5. LED-panels
6. CCD camera
7. Outlet
8. Water storage tank
9. Laptop

The flocculation experiments took place in a Q2D jet clarifier whose dimensions and the positions of cameras are noticed in Figure 2.14.
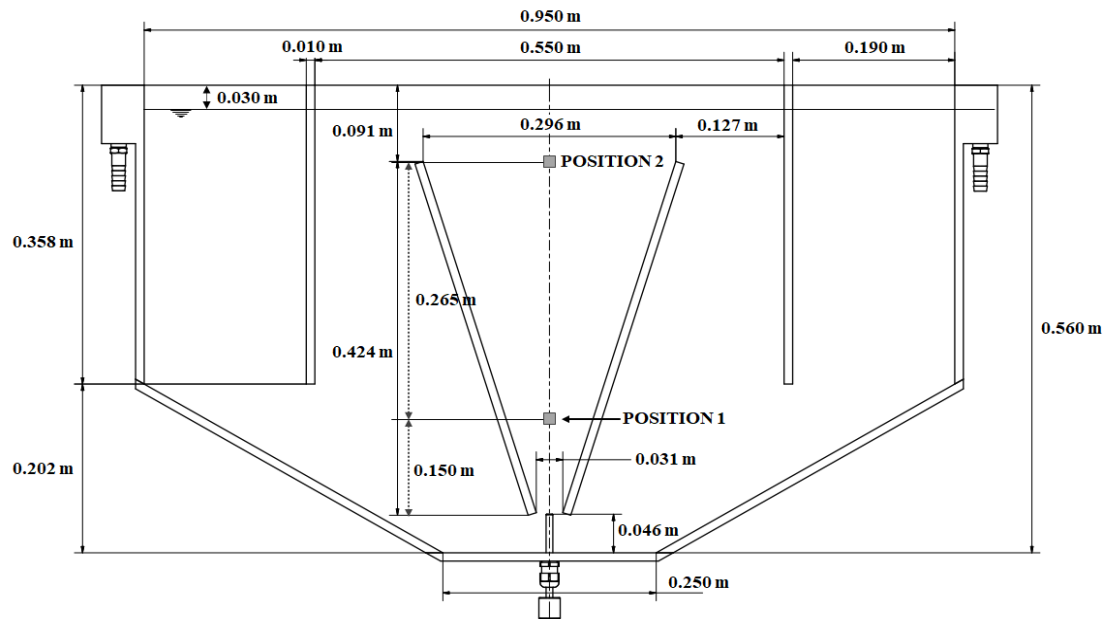
Figure 2.14 Schematic of the Q2D jet clarifier to show the positions of cameras

Recall that the total volume is 42 liters and the volume of the flocculation zone (V_F) corresponding to the cone, is 7 liters. The residence time (τ) calculated with Equation 2.1, leading to the residence times indicated in Table 2.7. This work focused on flocculation in the zone of the cone: floc size distributions have been measured by shadowgraphy methods near the inlet (Position 1) and outlet (Position 2) of the cone as shown in Figure 2.14. Indeed, the Position 1 was 15 cm above the injection and the Position 2 at the top of the flocculation zone.

(ii) Liquid phase

The characteristics of liquid phases used in this experiment were roughly the same as the liquid used in the experiment on the topic of turbidity removal efficiency, but their details were quite different due to the fact that experiments have been realized in France; their properties were summarized as follow:

a) Suspension

Bentonite (P.P.M. Chemical, Thailand) was used to simulate the behavior of particles naturally present in raw water as same as turbidity removal experiment (see 2.2.1.1(ii)). The experiments were done for two concentrations of 220 mg/L and 1100 mg/L in the tap water of Toulouse (France) corresponding to turbidity equal to respectively 50±0.2 NTU and 250±1 NTU. The standard method 2320B was used to analyze alkalinity and the pH meter used was microprocessor pH-meter pH 539 (WTW, Germany). The values of pH and alkalinity were 7.84 – 8.12, and 87.73 – 130.66 mg/L as $CaCO_3$, respectively. The pH and alkalinity of the resulting suspension were variable parameters due to the tap water during the experiment period. All the experiments were carried out at room temperature between 10 and 20 ºC. The size distribution of the primary bentonite particles has been measured by laser diffraction with a Mastersizer (Malvern 2000). The volume-weighted mean diameter (d_{50}) of primary particles of 15 μm and the mode of the volume distribution is about 20 μm as can be seen in Figure 2.5 and the zeta potential value was measured with a Zetasizer (Nano-zs) device and was equal to -8.09 mV.

b) Coagulant and Optimum Dose

Aluminum Sulfate ($Al_2(SO_4)_3 \cdot 14H_2O$) was chosen as a coagulant and prepared at 1% w/v. concentration stock. The optimum dose that was evaluated by the jar test apparatus (with the condition explained in 2.2.1.1(iii)) would be applied for the in-situ floc size distribution investigation in the jet clarifier. The results revealed the optimum dose varies in the fairly wide range, which was 15 – 25 mg/L for the 50 NTU synthesis raw water, and 45 – 55 mg/L for the 250 NTU synthesis raw water. It can be observed that the required appropriate doses were slightly different in the different range of water turbidity as shown in Table 2.8.

Table 2.8 Characteristic the synthetic raw water and optimum dose of alum

| Parameters | Bentonite concentration | | | |
| | 220 mg/L | | 1100 mg/L | |
	Range	Mean*	Range	Mean*
Turbidity (NTU)	49.8 – 50.2	50	249 – 251	250
pH	7.84 – 8.12	7.95	7.6 – 8.12	7.93
Alkalinity (mg/L as $CaCo_3$)	87.73 – 94.00	87.73	123.34 – 130.66	127.42
Temperature (ºC)	17 – 20	18	17 – 20	18
Optimum dose of alum (mg/L)	15 – 25	20	45 – 55	50

* Average of the sample taken from September 2019 to January 2020

(iii) Monitoring Floc Size Distribution

The most common methods applied to examine floc size are based on two techniques that have been used for measuring particle sizes, including laser diffraction scattering (LDS) and image analysis. The brief details on the apparatus based on two different techniques used for measuring sizes are provided in the next section.

§ *Laser Diffraction Technique*

The laser diffraction scattering (LDS) technique is widely used to measure the distribution of particle size based on the analysis of the diffraction pattern produced when particles are exposed to a beam of monochromatic light (see Equation 2.15). The intensity of the detected signal is determined by three processes: scattering, diffraction and absorption (Bohren and Huffman, 1983). Scattered light consists of reflected and refracted waves, and is influenced by the form, size, and composition of the particles. Diffracted light arises from edge phenomena, and is dependent only on the geometric cross-section. of the particle; thus diffraction is independent of the composition and refractive properties. Absorption occurs when light is converted to other forms of energy by interaction with the particles, thereby attenuating the intensity. Absorption is influenced by both particle size and composition. LDS is sensitive to all three of these phenomena, but is often limited to light detected at the forward (low) scattering angles. More recently, instruments have incorporated wide angle and backscatter detection to aid in the analysis of finer size particles. For non-spherical particles, an equivalent sphere-size distribution is obtained because the technique assumes spherical particles in its optical model. The resulting particle-size distribution may differ from those obtained by methods based on other physical principles (e.g., sedimentation, sieving) (Boer et al., 1987; Kerker, 1969).
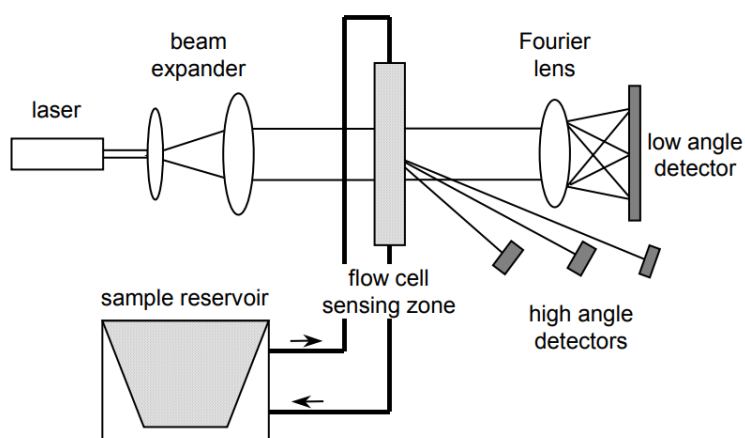
Figure 2.15 Schematic of the optical system for a typical laser diffraction spectrometer with a liquid flow cell (Hackley et al., 2004)

▪ *Image Analysis*

The image analysis was applied to investigate the in-situ methods to measure the floc characterization, such as floc size, flocs size distribution, and morphology of floc. Taking images to reveal and observe the morphology of floc, which has been established and continued development (Denis Bouyer et al., 2005; Carole Coufort et al., 2008; Eisma and Kalf, 1996; Kinoshita et al., 2017; Maggi et al., 2006; Shen and Maa, 2016; Syvitski and Hutton, 1996). Optical imaging has an advantage over other techniques because of its high spatial resolution, moderate temporal resolution, and wide range of applicability together with robust image processing techniques. The disadvantage of optical imaging techniques is their need for undisturbed visibility to the measurement. (Honkanen et al., 2010).

The shadowgraphy is a useful tool for the direct measurement of the geometrical properties of flocs. A camera is used to record highlighted aggregates. A homogeneous LED-panel, is installed behind the transparent column as shown in Figure 2.13, and the located positions are shown in Figure 2.14. The camera records projected shadows of each floc. Flocs appear as dark shadows on images, as illustrated in Figure 2.16. The images are converted from greyscale to black-and-white, to measure several floc parameters. This configuration is a technique to visualize clearly the outlines of shapes objects.
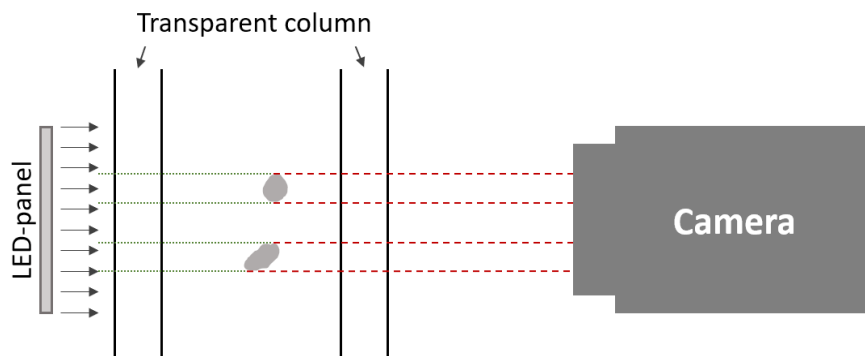
Figure 2.16 Schematic of shadowgraphy experimental setup

a) Image Acquisition and Data Processing

Acquisition windows width were fixed with a resolution of 1024×1024 pixels corresponding to 10×10 mm^2 (1 pixel = 10.1 μm). Piles of the image included 1000 images were acquired instantaneous two-dimensions (2D) fields and recorded every 15 minutes from start to steady state, and the camera speed was 5 images per second.

The image processing technique was applied by D. Laupsien (Laupsien et al., 2019). The principle of this technique consists in (1) homogeneity from the inhomogeneities background light by applying a so-called flat on every image. The flat is nothing else than a shadowgraphy picture of the same acquisition window without any flocs (2) determination of the particle size by the intensity of the grey level gradient, which is corresponding to projected interfaces, are then identified by searching the highest light intensity gradients and (3) image binarization. In this experiment, a threshold of 0.5 was applied, which corresponds to 1024 levels of grey in the case of a 10-bit image. Due to the high contrast on the images, the maximum of the grey level intensity gradient could be identified easily, and the resulting contours match the actual interface position well.
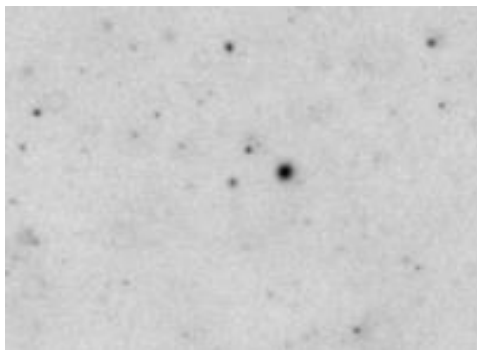
Figure 2.17 Raw image   Figure 2.18 Binarized image
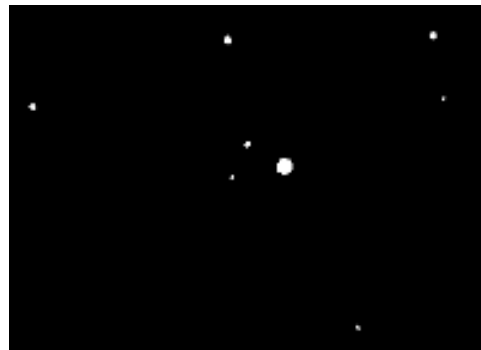
The characteristic floc scales can be estimated by image analysis; nonetheless, it gives only 2D information on the floc size, such as floc area, from which a circular equivalent diameter (CED) can be calculated using Equation 2.27.

In this study, the floc size distribution would be analyzed in terms of the number and size; however, the first class of any particle progression (Arithmetic and geometric progression) must be carefully analyzed since the floc size was determined by an image analysis technique, the smallest particle detached has the same size as the pixel of the camera (10.1 μm).

b) *The Properties of Particles*

Recently, the particle can be characterized in terms of the size of the individual particle. These parameters are important factors since they are directly influent the separation mechanism of particles from the fluid (DeCarlo et al., 2004). Moreover, many parameters have been developed to determine the properties of particles in this study as follow:

▪ *Projected Area*

Since most of the instruments are optical equipment, the first measurement is the projected two-dimensional area (A). The area of the particle is calculated from the summation of the areas of each individual pixel (a_P) within the borders of the particle, which can be analyzed by the image processing technique. The processes including non-homogeneities background light removal and binary image conversion were applied to the raw images prior to statistical analysis as shown in Figure 2.19. The projected area can be calculated by Equation 2.26.

$$A= \sum a_p \qquad\qquad \text{Equation 2.26}$$
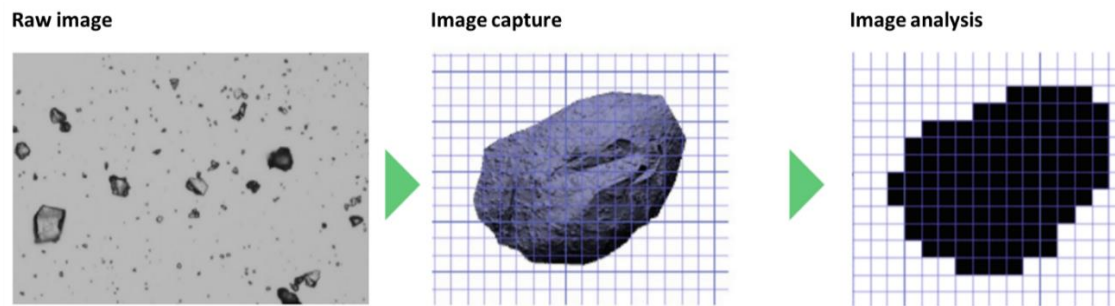
Figure 2.19 Image processing process (adapted from Malvern®)

- *Circular Equivalent Diameter*

The circular equivalent diameter, or area-equivalent diameter, is defined as the diameter of a circle with the same area as the particle. Thus, once the area of the particle (A) is known, the circular equivalent diameter (d_{CED}) can be calculated by Equation 2.27. Note that A in this study represents the cumulative pixel area of each floc on the image.

$$d_{CED} = \sqrt{\frac{4A}{\pi}}$$

Equation 2.27

- *Spherical Equivalent Volume*

Like the circular equivalent diameter, the spherical equivalent volume (V_{eq}) is defined as the volume of a sphere whose diameter is a function of the measured area:

$$V_{eq} = \frac{1}{6}\pi \left(\sqrt{\frac{4A}{\pi}}\right)^3 = \frac{1}{6}\pi\left(d_{eq}^3\right)$$

Equation 2.28

- *Number, Area and Volume-based Distributions*

Populations of particles can be arranged in terms of classes. The size class (Cs) is the most common technique to organize particles as it is illustrated in Table 2.9. The data is shown in each class; it means that they are the result of the range of the class. For instance, in the first size class, a number of particles (N_1) with particle size between d_{eq1} and d_{eq2}, which together regathers an area A_1 and a volume V_1. The same interpretation can be extended until the last class ($d_{eq(n-1)} - d_{eq(n)}$). This type of classification essentially enables to observe the correspondent number, area, or volume fraction of a group of particles inside the whole particle population (N_T, A_T, V_T).

Table 2.9 Size classes and their correspondent number, area, and volume of particles.

Size class	Number	Area	Volume
$d_{eq1} - d_{eq2}$	N_1	A_1	V_1
$d_{eq2} - d_{eq3}$	N_2	A_2	V_2
$\vdots$	$\vdots$	$\vdots$	$\vdots$
$d_{eq(n-1)} - d_{eq(n)}$	N_n	A_n	V_n
Total	$\mathbf{N_T}$	$\mathbf{A_T}$	$\mathbf{V_T}$

Thus, the procedure to calculate the number, area, and volume fraction for the first class is expressed as follows:

$$Nb_1 \ (\%) = \frac{N_1}{N_T} \qquad \text{Equation 2.29}$$

$$A_1 \ (\%) = \frac{A_1}{A_T} \qquad \text{Equation 2.30}$$

$$Vol_1 \ (\%) = \frac{V_1}{V_T} \qquad \text{Equation 2.31}$$

Once the defined fractions regard to each class, it is possible to represent them by frequency distributions of size in number, area, or volume. The best basis to represent each distribution will depend on the analysis purpose. An illustrative X-population of particles under the three resolution bases can be shown in Figure 2.20.
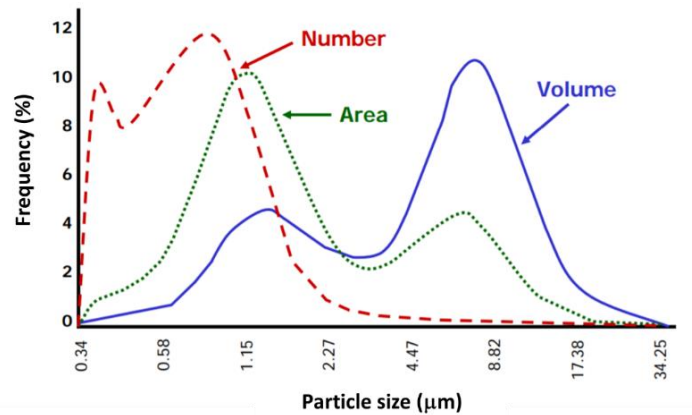
Figure 2.20 Representation of a particle size distribution on number,

area, and volume basis (adapted from HORIBA®)

The rough red dashed line represents a number-based distribution. In this resolution, a tiny particle has precisely the same weighting as a larger particle. This means that the contribution made by each particle to the distribution is the same.

The solid blue line, in turn, is a volume-based distribution. On this basis, the contribution of each particle is proportional to its volume. As a result, the large particles dominate the distribution and the sensitivity to small particles are reduced as their volume is considerably smaller in comparison to the larger ones.

Likewise, volume-based distributions, the area-based distributions, which represent by a dotted green line, capture the most information about the large particles, nevertheless, if porous particles are being analyzed, this distribution will shift even more towards the right since they present a more significant surface area.

2.3 Turbidity and Floc Size Distribution of the Synthetic Suspension in the Coagulation Tank

The floc size distribution in the coagulation tank (shown as n°2 in Figure 2.13) was examined to make sure that the sizes of flocs in the synthetic suspension, injected into the Q2D jet clarifier through the nozzle were constant over time. To that end, the synthetic suspension has been prepared in the tank. 3 minutes after the coagulant injection, samples of 300 mL have been taken every 15 minutes at the outlet of the gear pump (between ③ and ④ in Figure 2.13) until the tank was empty. Thus, for the highest flow, the experiment lasted 150 minutes while for the lowest flow it lasted 480 minutes. The samples have then been analyzed by light scattering with a Mastersizer (Malvern 2000, USA). This data is then analyzed to calculate the size of the particles that created the scattering pattern. In this study, the refractive index was set at 1.55 for bentonite.

2.3.1 Turbidity

The turbidity of the synthetic suspension over time, for the three flow rates, is shown in Figure 2.21.
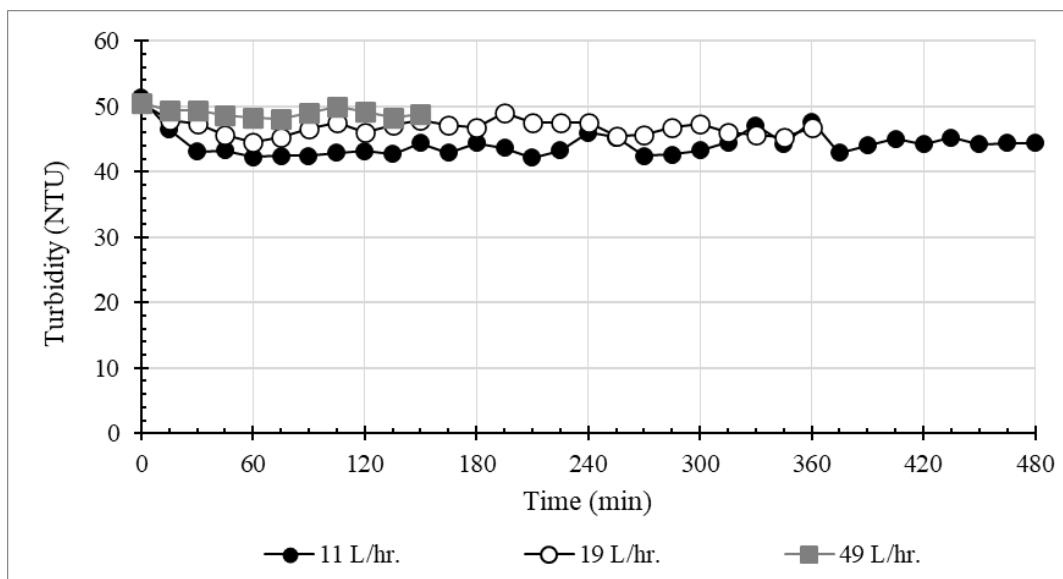
Figure 2.21 Turbidity of suspension in coagulation tank

The turbidity values of the solution were relatively stable along with whole the operation time and depended on the flow rate as shown in Figure 2.21.

2.3.2 Mean Volume Diameter

Results are presented in terms of mean volume diameter (d_{50}), and floc size distributions. The beginning of this experiment ($t = 0$) means that the suspension was collect after allowed mixing in the coagulation tank for 3 minutes. Figure 2.22 shows the mean volume diameter of flocs; it can be seen that the range of floc was a narrow range which was varied in 20 – 28 μm except at the beginning of experiments since aggregation of flocs required time (see next paragraph)
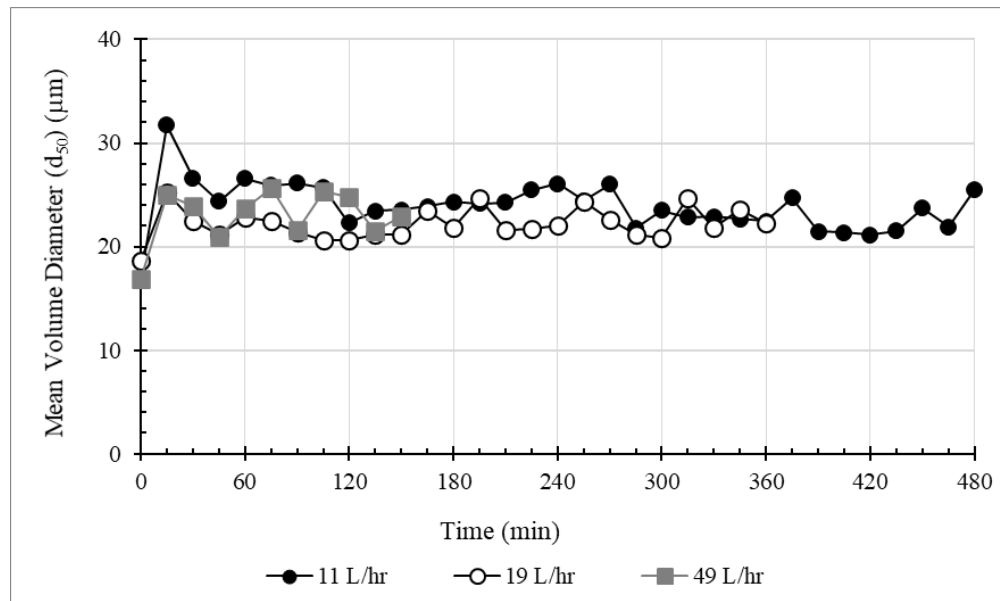
Figure 2.22 Mean volume diameter of flocs from the coagulation tank

2.3.3 Floc Size Distributions

In Figure 2.23 (a-b) are presented for each flow rate, the size distributions of bentonite particles, floc size distribution 3 minutes after the injection of the coagulant (t = 0), and at various times during the emptying of the tank. The results show that at the beginning of the experiment (t = 0), flocs have been aggregated already; accordingly, both the mean volume diameter and the floc size distribution were also larger than the primary particles, bentonite. The floc size and floc size distribution at t = 15 min of all flow rates were the largest because this was the first aggregation period. In the meantime, the formed flocs became denser and smaller particles and passably constant. For times greater than 15 min, the distributions are quite close and stable.
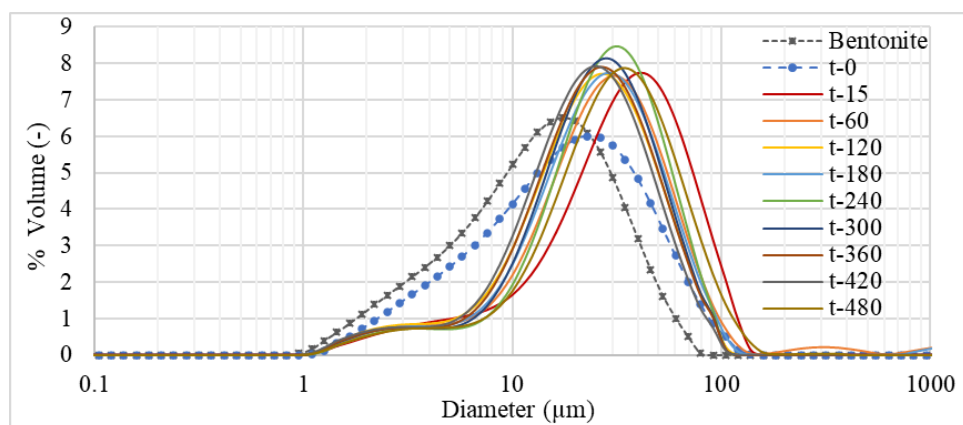
a) 11 L/hr.
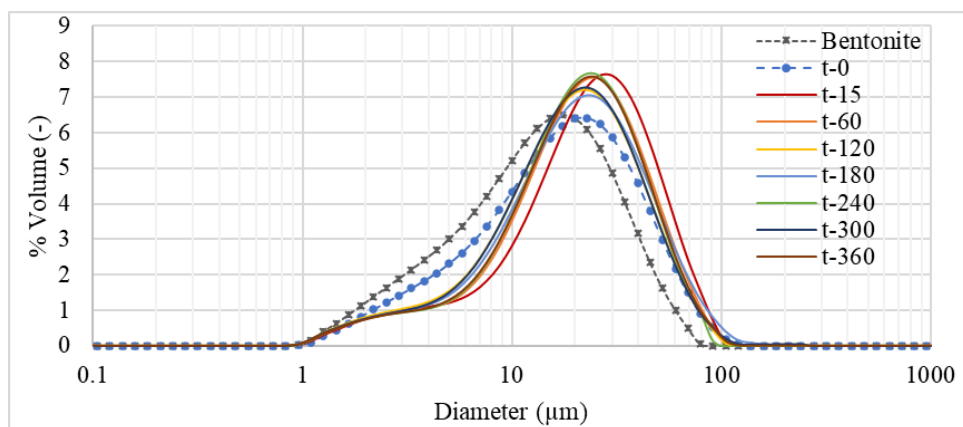
b) 19 L/hr.
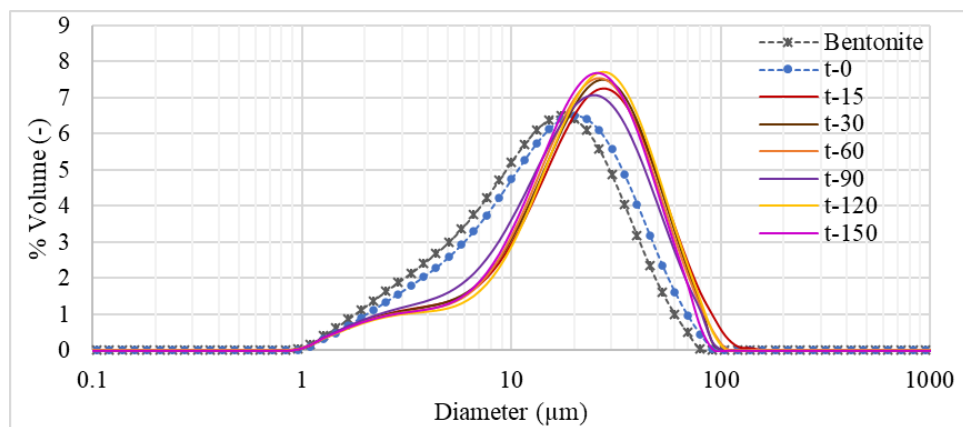
c) 49 L/hr.

Figure 2.23 Floc size distribution of flocs from the coagulation tank of flow rate
a) 11 L/hr, b) 19 L/hr., and c) 49 L/hr.

Figure 2.24 show the floc size distributions for t = 120 min for the injection 3 flow rates. It can be seen that the 3 distributions are superimposed. Their mode was situated around 25 µm and the maximal size around 100 µm. The size distribution of the flocs injected in the Q2D was thus stable against time and totally independent of the injection flowrate.
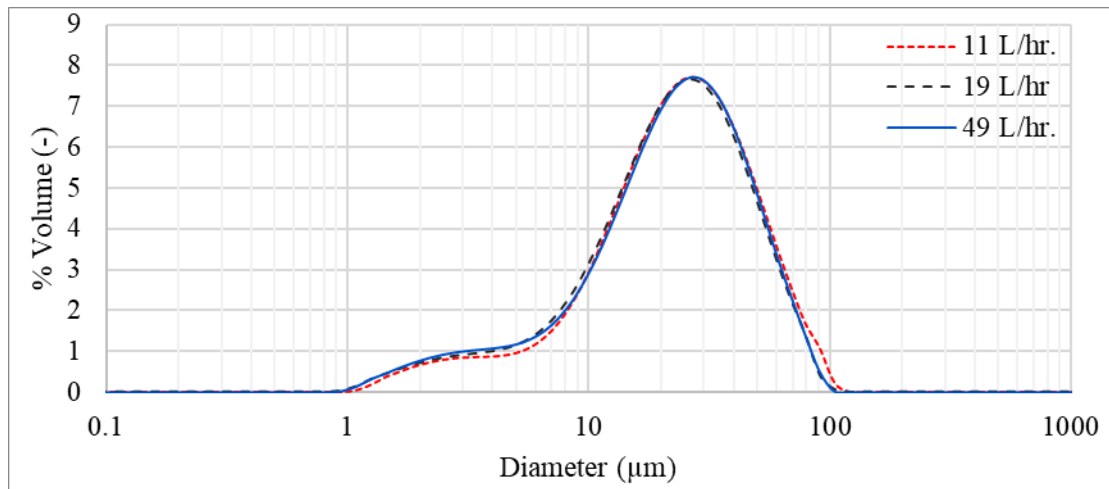
Figure 2.24 Floc size distribution of flocs from the coagulation tank at t = 120 minutes

The population of flocs has been analyzed in terms of mean surface diameter (D_{mean}) and floc size distribution weighted by surface thus focusing on larger aggregates (Coufort et al. (2005)). In order to check the statistical convergence of the data, the cumulative average of D_{mean} is plotted in Figure 2.25. The ordinate represents the mean values averaged over a number of analyzed images (abscissa). It can be concluded the statistic is reliable.
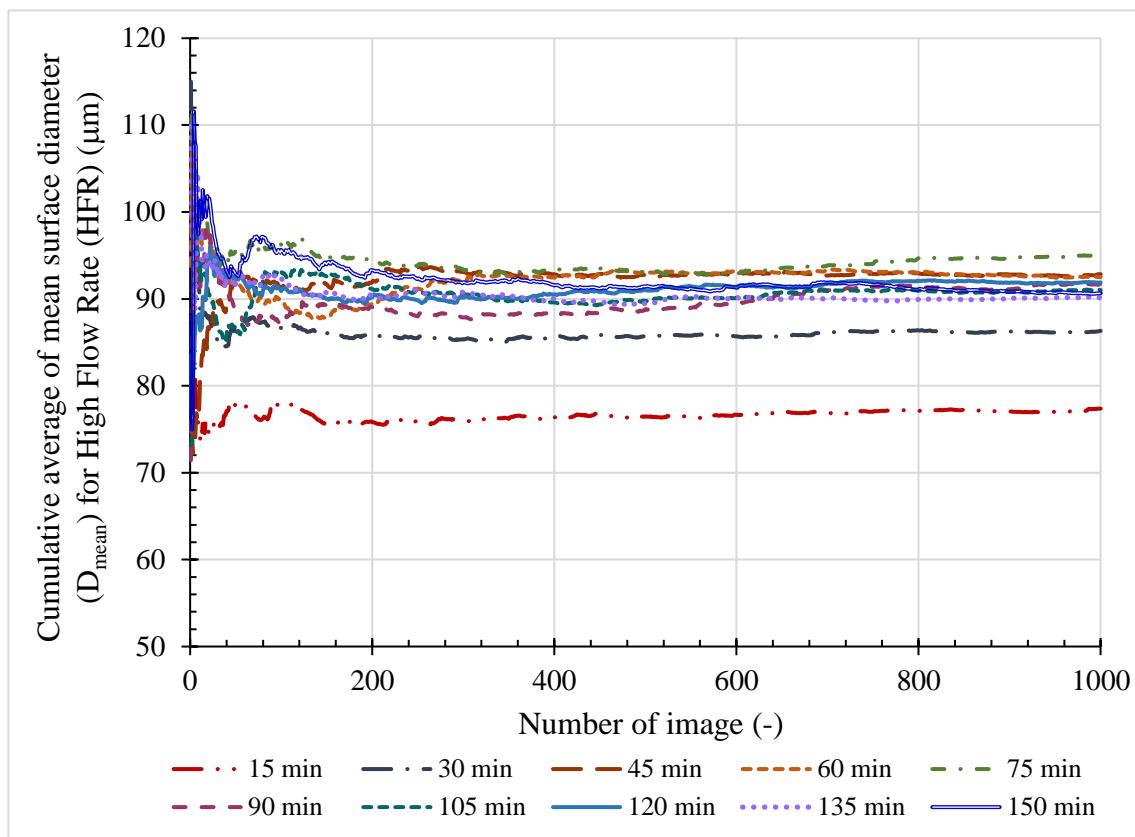
Figure 2.25 Cumulative average of mean surface diameter (D_{mean})

for High Flow Rate (HFR) – Position 1

In short, the small scale prototype (SSP) and the large scale prototype (LSP) of jet clarifiers were performed to examine the parameter that might affect the performance of the reactor such as the effect of the reactor's configuration and the appearance of sludge. At the same time, the mean residence time distribution (RTD) was used to investigate the global fluid flow pattern. Then, the Q2D jet clarifier was conducted to examine the local hydrodynamic and its effects on the floc size distributions. To the accompaniment of upscaling based on computational fluid dynamic (CFD), the Fluent code was used to develop to reproduce hydrodynamic phenomena of SSP and, after validation, to consider upscaling based on CFD, which could be seen in Chapter 5.

CHAPTER 3

EXPERIMENTAL ANALYSIS OF SMALL SCALE AND LARGE SCALE PROTOTYPE: TURBIDITY REMOVAL AND RESIDENCE TIME DISTRIBUTION

This chapter deals with twofold: performance and the residence time distribution of the reactors, a global analysis of the jet clarifiers. Effects of liquid flow rate and reactor configuration were examined to determine the performance of jet clarifier for turbidity removal in the aspect of water treatment. To answer to scientific questions (see Introduction), the turbidity removal efficiency has been evaluated by performing experiments in different scale reactors with the various configuration of the flocculation zone and flow rates under the jet (eddies) flow in the reactor. Afterwards, tracer methods are used to determine the residence time distribution for a better understanding of the global hydrodynamic condition in the reactor. The information obtained from this work could be utilized for designing the reactor as well as scale-up and suggesting the appropriate operation for a jet clarifier.

3.1 Turbidity Removal Efficiency

Regarding the clarifying process of the water treatment plant, Coagulation and flocculation are the main processes selected to use. The jet clarifier is a free jet flow and complex system due to a combination of flocculation and settling processes in a single unit to eliminate turbidity from the raw water. Until now, design and operation have rarely been studied directly. One of the simplest ways of tackling this problem is to design experiments assuming that hydrodynamic is a parameter that affects the reactor performance. The SSP and LSP were thus conducted to determine the appropriate reactors' configuration to examine the turbidity removal performance of the reactors.

Hydrodynamic could control various phenomena occurring during the flocculation process. It also causes the collision of particles to agglomerate to larger ones, which will

be easy to remove from the water. Whereas flow rate and reactor configuration directly affect the hydrodynamics of the reactor. Thus, this investigation addresses the jet clarifier's effectiveness at optimized coagulant dose for turbidity removal at two size reactors with various inlet diameter of the flocculation zone. The focus will be made on the results of the flocculation of synthetic turbid water and surface raw water performed under the jet flow in the jet clarifier of the continuous system from start to a steady state. Synthetic turbid water was prepared using bentonite particles. Solutions were treated using the static mixer as the coagulation process then the flocculation and settling processes were done before the outlet of the jet clarifier. The details of the experiment could be seen in section 2.2.1.1.

3.1.1 Results and Discussions

The appropriate implementation of the coagulation and flocculation technique depends on how precisely the operating variables are selected. Therefore, trial and error have been traditionally practiced optimizing. These available directly depend on water characteristics and coagulant dosage. Even though, water characteristic is not a variable parameter of this study since the characteristic of raw water and tap water could not be controlled, which were dependent on season and climate. For instance, in the rainy season, the turbidity of surface raw water fed into the Samsen Water Treatment Plant, Thailand was about 80 NTU while in the dry season was approximately 20 NTU. The average turbidity of raw water that fed into the water treatment plant was 50 NTU. Therefore, the synthetic raw water was set at 50±0.2 NTU without adjustable pH. Consequently, the dosage of coagulant is the primary variable optimized in coagulation and flocculation studies. Furthermore, the operational conditions such as duration and speed of mixing were fixed. In this study, jar test apparatus was implemented to optimize the only dosage of coagulant (Aluminium Sulfate; alum) based on the highest turbidity removal percentage of the water.

3.1.1.1 Optimum Coagulant Dose

Conventionally in a water treatment plant fine suspended matter is made to agglomerate into larger size flocs by adding chemicals that neutralize the inherent negative charges on colloidal impurities that repel them from each other and interfere with their settling mechanism. It is crucial that the exact dosage of the coagulant (chemical) is determined prior to add into the water because if the dosage is low then the negative charge on all the particles shall not be neutralized, and if the dosage becomes more than the particles acquire net positive charge resulting in their repulsion from each other and non-settlement (John Gregory, 2013; Kim et al., 1982; Zhao et al., 2021).

In the absence of any basis for an approximate coagulant dose, a preliminary study-initiated experiments in order to determine an approximate alum dosage, where the optimum value would be included, and as a result, a narrow range of 15 – 40 mg/L was selected to the optimum dosage test. Jar test experiments were carried out and the result disclosed that the optimum doses of alum, coagulant, for synthetic surface raw water and natural surface raw water at 50 NTU were 20 mg/L and 30 mg/L, respectively, as shown in Figure 3.1. Moreover, the investigation of appropriate alum was done prior to all experiments of turbidity removal efficiency of jet clarifier determination and the floc size distribution also since the liquid phase varied with the period of time as it was explained in section 2.2.1.1(ii). The results revealed the optimum dose various in the same range was 15 – 25 mg/L for the synthetic water, while for the natural surface raw water, the optimum dose was 30 – 40 mg/L for the water characteristic during the experiment period. The optimum dose of alum for natural surface raw water was slightly higher than the optimum dose required for the synthesis water. It can be explained that the required appropriate doses were slightly different in the same range of water characteristics shown in Table 3.1 since the size of particles affects the critical coagulation concentration (CCC). The larger particles were less probable to coagulate than small particles since the greater the primary maximum of the total interaction energy. On the other hand, the smaller are the particles, the higher is the critical coagulation concentration (Hsu and Liu, 1998).

Therefore, it can be said that alum concentration was examined at the neutral pH for every experiment done, and the optimum dosages for treating the 220 mg/L suspending in tap water (50 NTU) in the coagulation-flocculation process were in a narrow range. These conditions were then applied in the performance of the jet clarifier investigation experiments as presented in the following section.
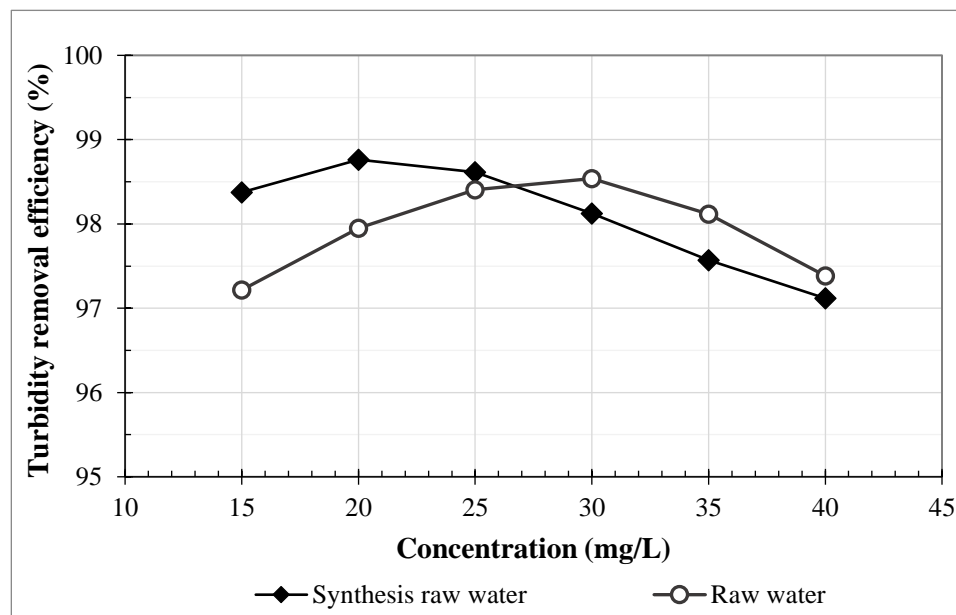
Figure 3.1 Efficiency of the coagulation with varied alum dosages
at different water types in a jar test

Table 3.1 Characteristic of the raw water and the synthetic water

Parameters	Natural surface raw water		Synthetic natural surface water	
	Range	Mean*	Range	Mean*
Particles mean diameter (d_{50}) (μm.)	0.4 – 250	9.64	1 – 80	14.67
Turbidity (NTU)	55 – 62	58	49.8 – 50.2	50
pH	7.16 – 7.36	7.25	7.45 – 7.85	7.69
Alkalinity (mg/L as $CaCo_3$)	80.20 – 90.10	80.20	79.2 – 92.0	84.25
Temperature (°C)	30 – 35	33	30 – 35	33

* Average of the sample taken from May to July 2018

3.1.1.2 Turbidity Removal Efficiency of Jet Clarifier

The turbidity removal efficiency of the jet clarifier part would be split into four parts to precisely investigate turbidity removal efficiency, which would be directly on each purpose. Moreover, the natural surface raw water would be used to verify that the system could be used to treat the water as a conventional water treatment system. Both sizes of jet clarifier prototypes (LSP and SSP) were used to investigate the performance of jet clarifiers. The installation of the LSP and SSP were simply removable to adjust whatever configuration of the reactors. In this experiment, the diameters of the truncated cone base of the flocculation part were varied in length of 5, 10, and 15 cm, and 3.25, 6.5, and 9.75 cm for the LSP and SSP, respectively; on the other hand, the gaps between partitions were fixed as shown in Figure 2.1. At the beginning of the experiments, the pilot only contained clear tap water at rest except for the cases of sludge blanket or porous zone existence. The sludge blanket or porous zone was prepared before the experiment was started 12 hr. to allow the small particles/flocs or granular plastic to settle and rest at the sludge blanket or porous zone as shown in Figure 2.1. These studies were conducted using the "changing one factor at a time" method, i.e., a single factor is varied while all other factors are kept unchanged for a particular set of experiments. The system thus was operated on each condition and the treated water was collected at the overflow outlet to check turbidity every 30 minutes until the turbidity was constant, which can be inferred that the system reached to steady state.

(i) Impact of Flow Rates on Operating Time to Reach Steady State

The flow rate affected theoretical mean residence time that could be calculated by the total volume of the reactor divided by flow rate (τ = Total volume/flow rate), which could be proved by the experimental results shown in Figure 3.3. The results of the SSP have been representative of the experiments were shown in various flow rates with different sludge blanket conditions. The experiment results were plotted the effluent turbidity over the time (Figure 3.2) and the dimensionless time (θ) defined as the ratio of t and the

theoretical residence time (τ) (Figure 3.3) through experiments to demonstrate the effect of flow rate in terms of the operation time along with the flocculation process.
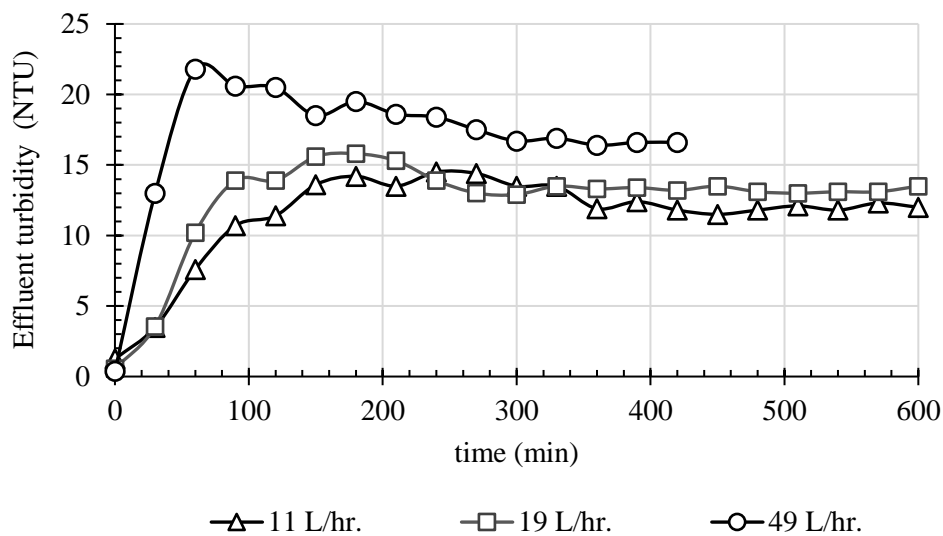
a) without sludge blanket
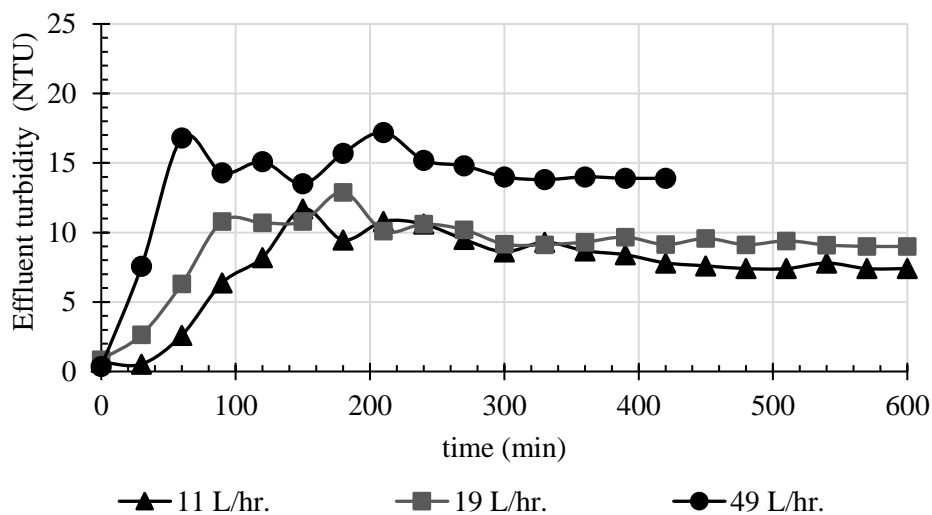
b) with sludge blanket

Figure 3.2 Effluent turbidity over time through experiments of SSP in different flow rates with a) without sludge blanket, and b) with sludge blanket conditions
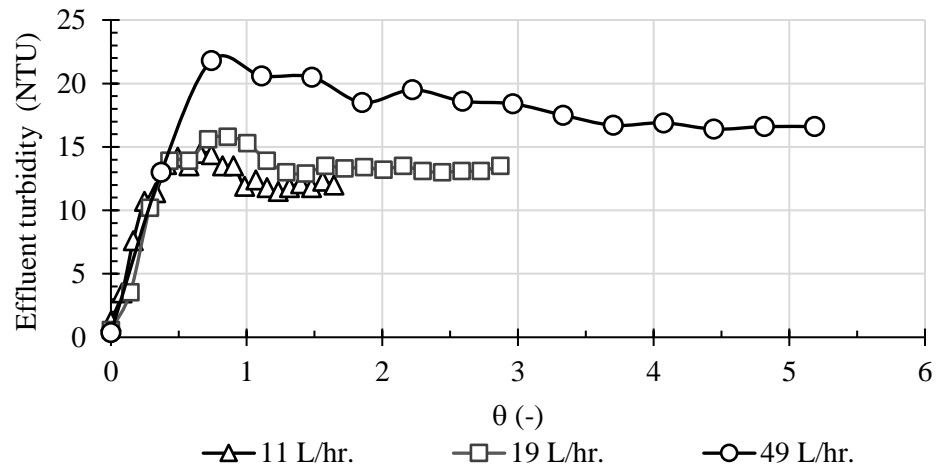
a) without sludge blanket
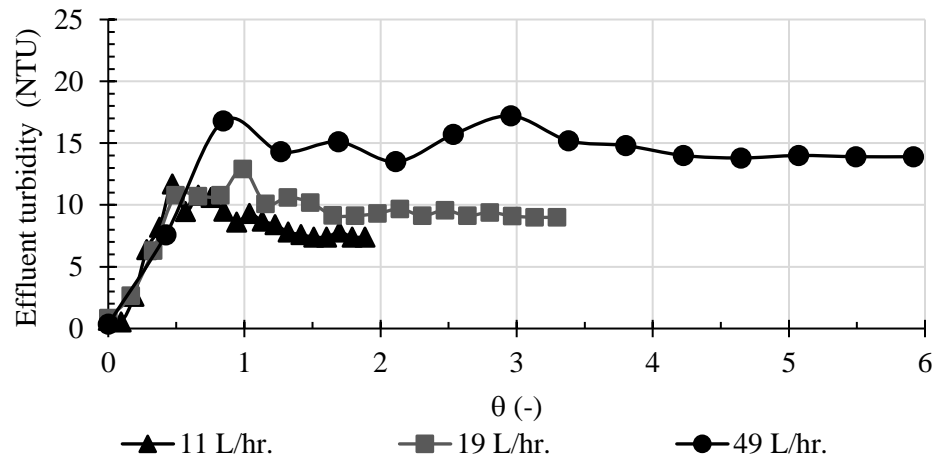
b) with sludge blanket

Figure 3.3 Effluent turbidity versus non-dimensional time of SSP in different flow rates with a) without sludge blanket, b) with sludge blanket conditions

At the beginning of the experiments, the lowest turbidity of the water could be detected because of filled tap water and settled sludge blanket. Thus, the turbidity of the water had been measured and noted at the starting time (t = 0 min); then the experiment started the treated water was sampled at the overflow outlet every 30 minutes.

The results of the experiments found clear support for the increasing flow rate that providing more time to reach steady state as seen in Figure 3.3 (a and b). Looking at the operating time to reach steady state, it can be seen that operation time required the values of θ more than those of τ (θ = 1). As can be seen, the dimensionless time (θ) was required 1, 1.5, and 3.5 for the flow rate of 14, 19, and 49 L/hr., respectively, for the without sludge blanket cases. Furthermore, the θ was required 1.5, 2, and 4 for the cases that existence sludge blanket from the lowest flow rate to the highest flow rate. The operating time required of the existence sludge blanket in the jet clarifier case was longer than without the sludge blanket case, which might be explained that the settled sludge blanket acted as a barrier to water flow. Thus, there might be no shortcut flow in the reactor and the main streamline might be flow following the direction as shown in Figure 2.3, which was the expected flow field. The operating time thus required more than another case. The assumption could be recognized by comparison the effluent turbidity (see Figure 3.3). In the case of existence sludge blanket, the turbidity could be detected quite a delay than without sludge.

From this standpoint, the flow rate would be considered as the dominant that affects not only turbidity removal but the operation time also. Here again, the operation time would directly affect the mixing time of the flocculation of the reactor. On the other hand, it is difficult to explain such results within the context of mixing time since the results discussed were the overall system effectiveness.

(ii) Impact of Sludge Blanket and Reactor Size on the Treatment Efficiency

To ensure the feasibility of the developed jet clarifier, the experiment was to simulate the clarifier process of the water treatment system. For the determination of the turbidity treatment efficiency, the sludge blanket was produced by flocs formed. While, the cone base diameter of the truncated of the SSP and LSP was specified at the middle range, which was 6.5 and 10 cm., respectively. The three flow rates were varied for each jet clarifier size. At the same time, the theoretical residence time was the same within the same

condition shown in Table 3.2 as well as a summary of turbidity removal at steady state can be found.

It could be explained that the experiments were conducted changing theoretical residence time (τ) that depends on the liquid flow rate. For sludge blanket existence cases, theoretical residence time was decreased since the volume of sludge was disregarded. Moreover, the experiment results could show the effect of flow rate that affects the time to reach steady state, which would be described on the topic of 3.1.1.2(ii). Figure 3.4 presents the turbidity removal efficiency from the representative experiments at steady state with different flow rates and sludge blanket conditions. The turbidity removal efficiency was shown in Table 3.2 for altogether experiments. It could be observed that the efficiency from both LSP and SSP of jet clarifiers was no significant differences and the trend of performance of the reactor with a different size was equal. It could be expected that the hydrodynamic of the reactor in various sizes were the same since the theoretical residence time was fixed by adjusting inlet flow rates.

Table 3.2 Summarize the treatment efficiency at various theoretical mean residence time of jet clarifier

Sludge blanket condition	Theoretical residence time (τ) (min)	Flow rate (L/hr.)		Treatment efficiency at steady state (%)	
		LSP	SSP	LSP	SSP
Without	365	40	11	75.30	76.04
	209	70	19	72.11	73.21
	81	180	49	66.07	66.67
With	318	40	11	83.22	83.68
	182	70	19	80.00	81.03
	71	180	49	71.33	70.32

Besides, the existence of the sludge blanket affected efficiency by about 10% increases. As the residence time increased, the turbidity removal efficiency increased for both size reactors. Given that the lowest theoretical residence time, the highest flow rate,

had the lowest turbidity removal efficiency than other experiments for LSP and SSP, which was about 67% and 70% for without and with sludge blanket case, respectively. Although, the results of the lowest flow rate and intermediate flow rate were rather no different.

Effluent turbidity of the without sludge blanket cases was higher than the conditions that consist of sludge blanket in the jet clarifier for all of the flow rate investigated. The results of this study could be demonstrated that the existence of the sludge noticeably affected reactor performance. The sludge blanket might affect the hydrodynamic and might be suctioned into the flocculation zone as sludge recirculation to increase aggregation targets. It thus increases targets to be aggregated, which were assumptions to be used to explain the effect of sludge blanket on turbidity removal efficiency.
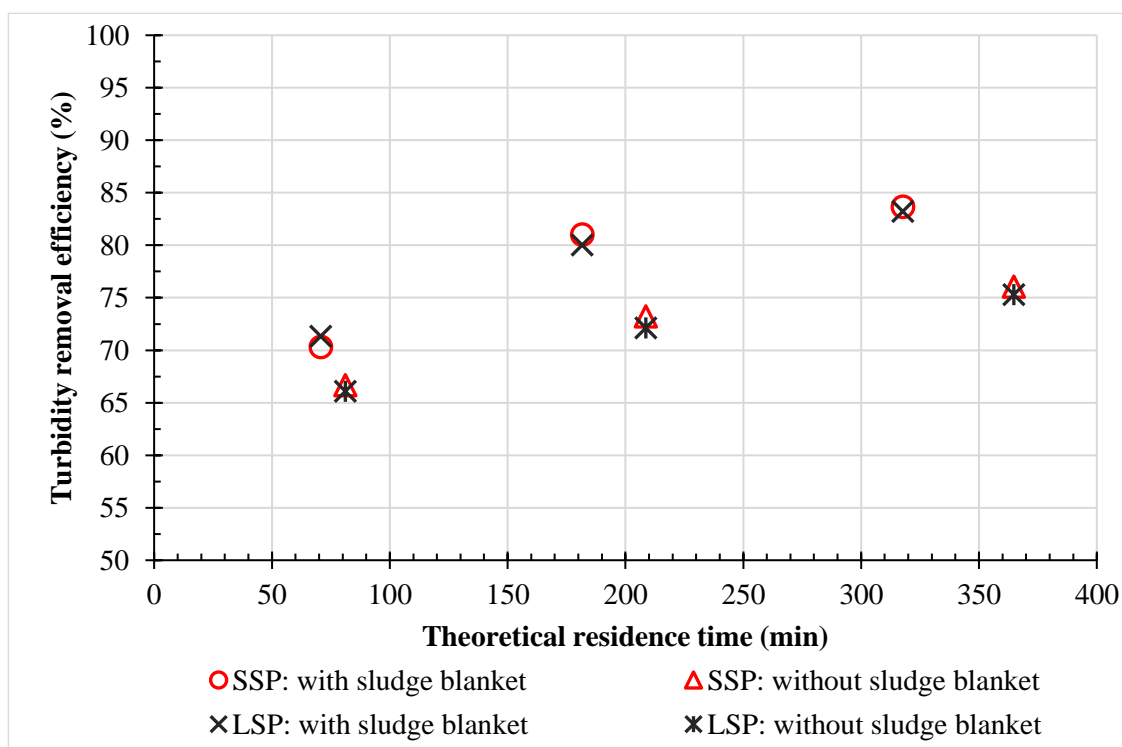
Figure 3.4 Effect of sludge blanket on treatment efficiency of jet clarifier prototypes

(iii) Impact of Different Characteristics of Sludge on the Treatment Efficiency

To study the effect of sludge blanket on the facet of the target particle of flocculation; the higher is the concentration, the more is agglomeration. The granular plastic, polyoxymethylene (POM) solid particles, would replace the sludge blanket named the porous zone to maintain sludge blanket characteristics (e.g., size, density, and porosity of floc) throughout the studies. The conditions examined were in the same manner previous study but only carried out on the SSP.
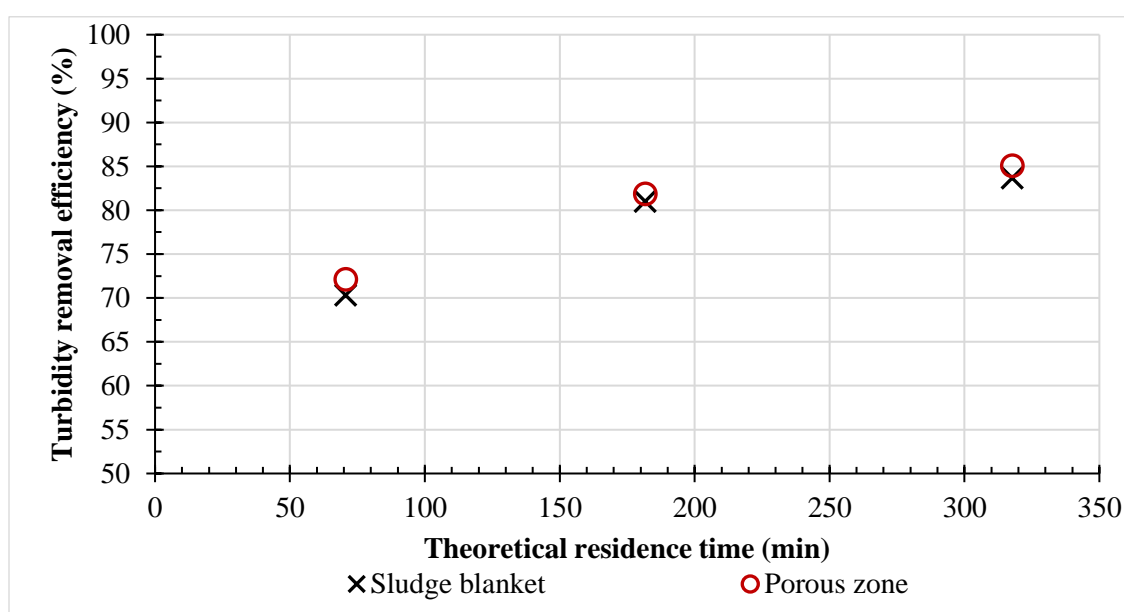
Figure 3.5 Effect of sludge blanket characteristic on treatment efficiency in SSP

The results could be shown in Figure 3.5 with the actual sludge blanket results as reported in Figure 3.4 to compare the treatment efficiency from different kinds of sludge. It can be seen that the treatment efficiency was similar. For the porous zone cases, the turbidity removal efficiency was 85.11, 81.89, and 72.14% from the lowest flow rate (11 L/hr.) to the highest flow rate (49 L/hr.). Consequently, the porous zone would be applied to other experiments due to its advantage on the experimental setup and controlling the characteristic of the sludge blanket.

(iv) Impact of Configuration of Tank on the Treatment Efficiency

As the latest discussion, the flow field and sludge blanket seemed to be the main factor that affects the turbidity removal efficiency, while the kinds of sludge blanket were not affected significantly. As a result, it could be concluded that one of the factors that significantly affect the turbidity removal efficiency was hydrodynamic. It relates to reactor design and thus the tank's configuration would be examined to determine the appropriate geometry. Recently, the jet clarifier has been examined by other installations to figure out appropriate jet clarifier design and operating conditions. For instance, the gap between the flocculation zone and the reactor base is 6 cm., the gap between the partition of sedimentation is 30 cm. and the reactor base, and the height of the sludge blanket is 25 cm. for the LSP that is shown in Figure 2.1 (a) (Romphophak, 2013). Nevertheless, the diameter of the truncated cone's base might be another important factor since it might affect the flocculation zone directly has not still evaluated yet; therefore, it would be evaluated to evaluate its effect on flocculation and fill the research gap. This study was conducted in both sizes of the jet clarifier with 3 different diameters each to ensure that the performance of the reactor of scaled-down by geometric similarity and the prototype were the same. So, all of the flow rates and existing conditions of the porous zone were examined.

Figure 3.6 and Figure 3.7 were singly plotted to show the jet clarifiers' performance in the case of without and with porous zone cases, respectively, and the details of treatment efficiency were presented in Table D.1 and Table D.2 (see Appendix D) It could be seen that the results of all cases of existence porous zone were higher than without porous zone, which was similar to results discussed in 3.1.1.2(ii) section. Furthermore, the effect of the diameter of the truncated cone's base is not significant to turbidity removal efficiency in the range of flow rates studied. It just varied in a narrow range of less than 5% in various flow rates. However, the efficiency of the middle diameter of the truncated cone's base was a little better than others. As the results, the middle diameter, 6.5 cm. and 10 cm. for SSP and LSP, respectively, were chosen to be representative of the appropriate design.
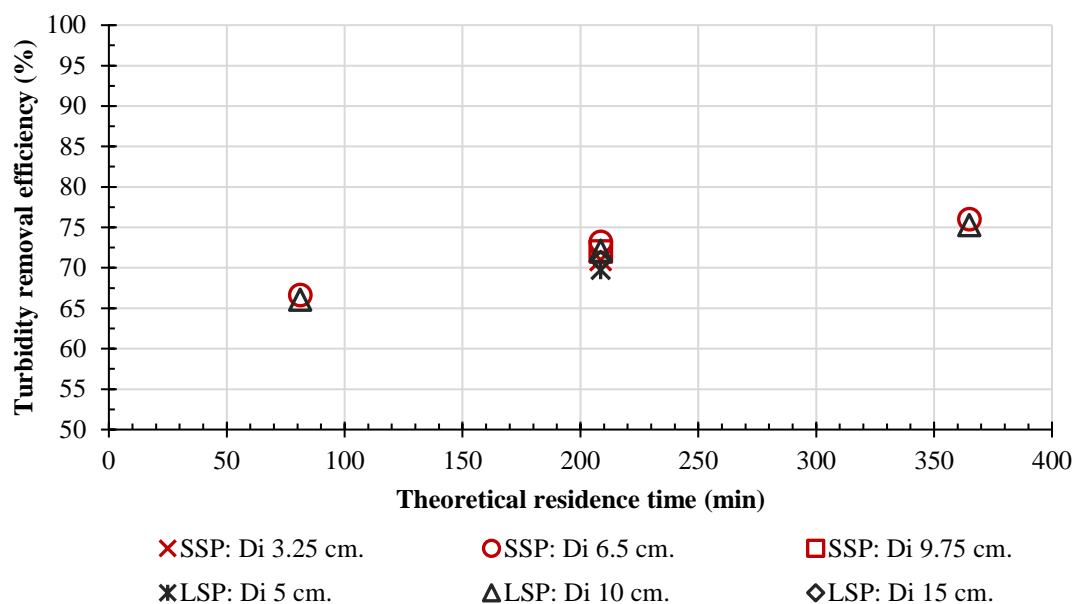
Figure 3.6 Effect of the truncated cone's base on treatment efficiency
of the SSP and LSP without porous zone
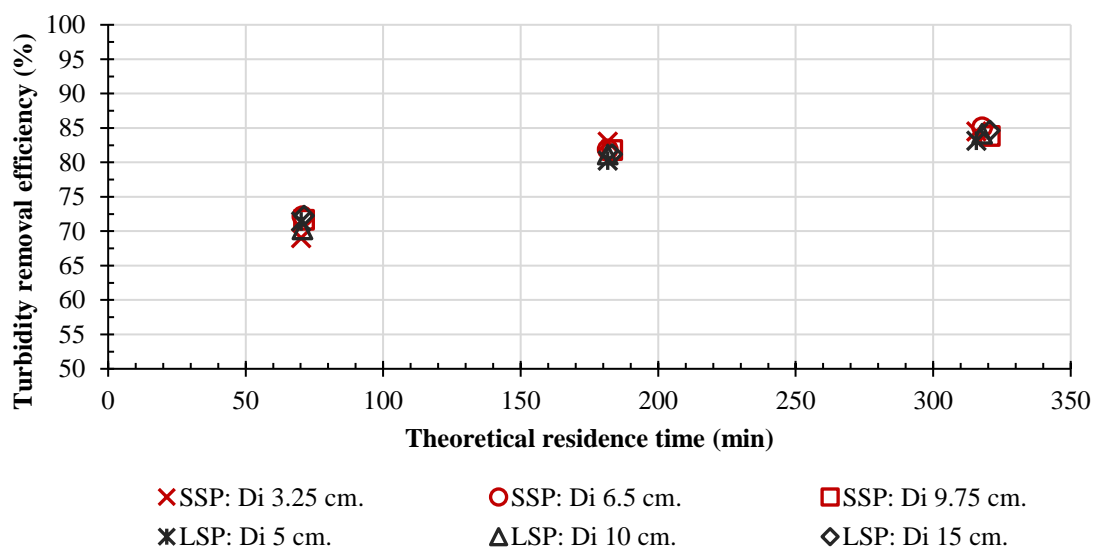
Figure 3.7 Effect of the truncated cone's base on treatment efficiency
of the SSP and LSP with the porous zone

(v) Impact of water characteristic on the Treatment Efficiency

To ensure the feasibility of this developed jet clarifier could be applied to the water treatment system, the experiment planned to examine the reactor's performance if the water characteristic change to natural surface raw water. To ensure the feasibility of this developed jet clarifier could be applied to the water treatment system, the experiment planned to examine the performance of the reactor if the water characteristic change to natural surface raw water. Then, the treatment efficiency would be compared with the synthetic water by adding bentonite into tap water. The summarized water characteristics were presented in Table 3.1. It could be said that the characteristics were in the same range. Focusing on the turbidity, the natural water characteristic was 10 NTU higher than synthesis raw water. The SSP with a 6.5 cm. diameter of the truncated cone base and all flow rates was representative of the experimental condition. The sludge blanket was selected using in the experiment to simulate the water treatment system.

In the following section, the water characteristic effect is in focus. Therefore, comparisons were done between the different sources of water since the water characteristic and particle size distributions were in the same range. Thus, the turbidity removal efficiency was constant for all of them. Like in the previous section, all water characteristics can be seen in Table D.3 (see Appendix D). Furthermore, results were presented in graphical form in Figure 3.8. In the case of natural surface raw water, a clear efficiency was recognized. For all flow rates studied, theoretical residence times were decreasing with increasing velocity flow rates in a range from 11 L/hr. to 49 L/hr.; besides, the turbidity removal efficiency decrease which was the same result as the synthesis of raw water as discussed previously. To comparison the treatment efficiency, there was no effect from the water characteristic on the jet clarifier. The treatment efficiency of the raw water was 82.97, 81.59, and 69.00% for the flow rate 11, 19, and 49 L/hr., respectively. and 83.64, 81.99, 70.74 L/hr. for the synthesis water.
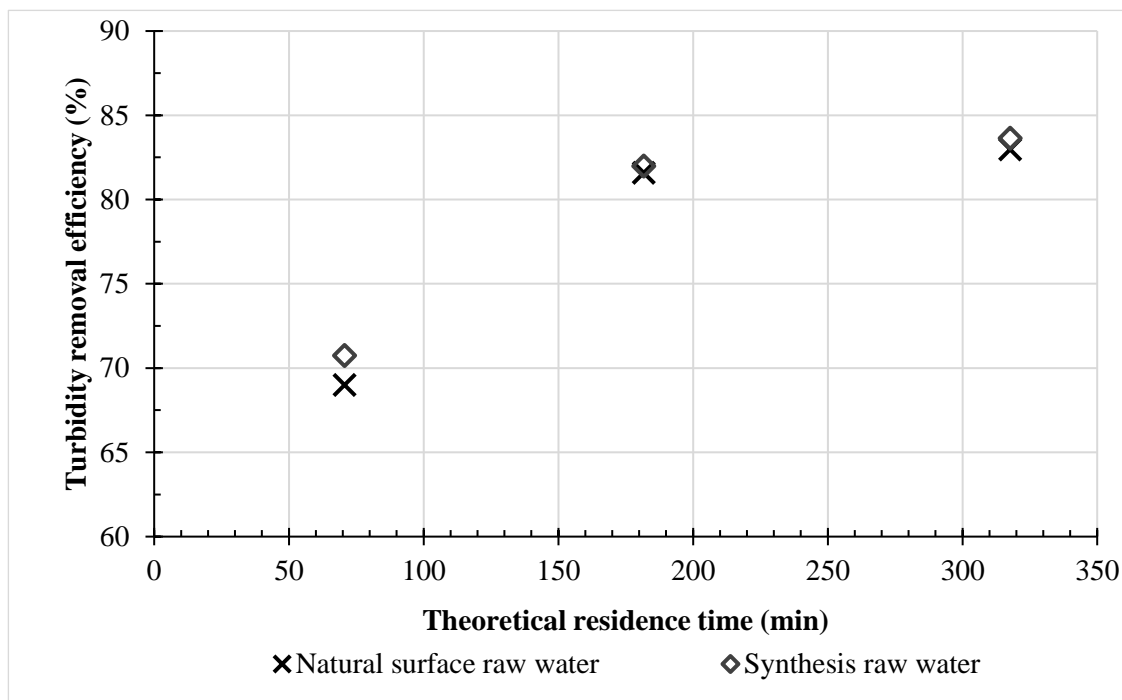
Figure 3.8 Effect of water characteristic on treatment efficiency of SSP

3.1.1.3 Summary

This is an important finding in the understanding of the factors that affect turbidity removal efficiency of jet clarifier. The effect of sludge blanket, sludge blanket's characteristic, liquid flow rate, tank's configuration, and water characteristic were evaluated. The results demonstrate the factors evaluated could be divided into two impact levels. First, the liquid flow rates and the sludge blanket were the high impact factors of the design and operation due to their effects on efficiency. Second, sludge blanket's characteristics, tank's configuration, and water characteristics were the low impact factors because they were not significant to turbidity removal efficiency. Note that the lower efficiency of the jet clarifier compared to the jar test was a result of different operation modes, which are continuous and batch systems, respectively. Moreover, G values in the static mixer and the jet clarifier were controlled by the liquid flow rates, while the gradient used in the jar test (see section 2.2.1.1(iii)) to examine the optimum dose that is used for

each experiment batches were kept constant. Additionally, the details of the static mixer were described in Appendix C.

On a flocculation point of view, numerous studies have proven a direct connection between floc size and hydrodynamics and accordingly, the definition of design and modeling of jet clarifier requires mean or global velocity gradient (G), contact time (t_{cont}) and camp number (Gt_{cont}) (Carole Coufort et al., 2008; Hughes, 2001; Kawamura, 2000; Qasim et al., 2000b; T. D. Reynolds and Richards, 1996; Vlieghe et al., 2014). Moreover, increasing the velocity gradient of the flocculator would be expected to produce smaller flocs as floc size scales inversely with shear (P. Jarvis et al., 2005; Parker et al., 1972; Spicer and Pratsinis, 1996). For this reason, the various parameters that affect turbidity removal efficiency were presented and confirm that the different velocity gradient (G) and mixing time or contact time (t_{cont}) that might affect turbidity removal efficiency, are the consequence of the flow rates and flow fields. The lowest flow rates of 40 L/hr. and 11 L/hr. for the LSP and SSP, respectively, might be come up with low G for mixing in flocculation but might be provided larger retention time and contact time (t_{cont}). This allowed particles to separate from water by settling resulting in good efficiency. On the contrary, the jet clarifier was ineffective in turbidity removal at the high flow rate, 180 L/hr. and 49 L/hr. for the LSP and SSP, respectively, due to their smaller retention time.

Moreover, the sludge blanket also affected the efficiency. It might be assumed that (1) the cumulative sludge volume would be recirculated to the flocculation zone; it can increase the contact probability between particles and enhance the agglomeration of destabilized particles forming to larger flocs (particles to cluster aggregation), therefore, increases the turbidity removal efficiency of the jet clarifier (Garland et al., 2017; John Gregory, 1997) (2) liquid flow field of the reactor; the sludge blanket might change the flow pattern of the reactor such as reducing short-cut flow or dead zone (Degremont, 2007; Kawamura, 2000). While the results as shown in Figure 3.5 could be asserted that the first assumption was not accurate in the range of this study since the overall efficiency was equal in both cases of a sludge blanket and granular plastic.

Because of the lack of evidence studied in this part to prove the details of hydrodynamic which have been anticipated, especially, flow fields, velocity gradient (G) and contact time (t_{cont}), mixing time. The following experiment was performed to not only investigate the mean residence time of the jet clarifiers in order to evaluate the actual residence time distribution of the jet clarifier but also using the results to validate the modeling by Computational Fluid Dynamics (CFD) that would be discussed in heading 5.1.

3.2 Residence Time Distribution (RTD)

The performance of jet clarifier depends on not only physicochemical conditions (i.e., coagulant type and dosage, solution temperature, and pH) but also hydrodynamic phenomena inside the reactor because it is the primary condition to design and control the system (He et al., 2018; Huang et al., 2016; Ma et al., 2017; Yang et al., 2016). The orientation inside the clarifier aims to have a thoroughly mixed flow or a plug flow depending on the requirement. The coagulation process will be efficient when the chemical is added and mixed completely as fast as possible. On the contrary, flocculation will be efficient when all of the destabilized particles in suspension move as a plug flow.

Existing methods, residence time distribution (RTD) have been developed and applied to predict hydrodynamic behaviors of the reactor (S. Chen et al., 2019; Zheng et al., 2012). The measurement is obtained from the tracer experiment that consists of an impulse response method. The injection of a tracer is conducted at the system inlet and a probe is introduced at the outlet to record the concentration-time relation (Essadki et al., 2011). The relationship can be used to construct the exit age distribution in the reactor, which indicates the flow pattern in the reactor. The different regions of a reactor can be modelled as mix flow or plug flow reactor having dead spaces with bypassing between zones (Zheng et al., 2012). The determination of RTD is frequently combined with the modeling of the system using one, two or three-parameter models, either based on mass balance or in statistical analysis (Bittante et al., 2014; Gao et al., 2012). Therefore, RTD measurement can be an efficient tool for better understanding the hydrodynamic conditions

in the reactor. This information can be applied for designing reactor as well as scale-up, operation, and optimization (Gao et al., 2012; Harris et al., 2003).

In this part, the results of the RTD experiment were deal with both LSP and SSP with the same configuration ratio in order to check the effect of reactor size on global hydrodynamics, especially on the mean residence time, which could be used to imply roughly that if the jet clarifier is scaled down and the flow rate is reduced to control the hydraulic residence time (HRT), the hydrodynamics of both sizes is identical.

3.2.1 Results and Discussions

3.2.1.1 Accurately Data Acquisition

Commonly, the RTD is determined experimentally by injecting an inert chemical, tracer, into the reactors at some time ($t = 0$) and then measuring the tracer concentration in the effluent stream as a function of time. The tracer's behavior will directly reflect the liquid flowing through the reactors (Fogler, 2006). Based on the jet clarifier design as shown in Figure 3.9, the outlet of the jet clarifier was an overflow outlet the tracer detection thus was installed at the drain tube, main exit streams, representing as ④ in Figure 3.9 (a). Moreover, the tracer was monitored at the overflow outlet with the other 4 checkpoints that can be presented by the top-view of the reactor (see Figure 3.9 (b), $O_1 - O_4$) at the overflow outlet area in order to evaluate the non-axisymmetry effect of the liquid flow due to the jet clarifier constructed. The experiments were done in the SSP with 3 inlet flow rates in the condition of without sludge. Figure 3.10 is the plot of the RTD curves, $E(t)$ versus sampling time (t), for $O_1 - O_4$ position compared with the RTD curve of the drain tube.

In addition, the tracer detectors were taken place to detect tracer signals in different positions inside the jet clarifier, representing as ① - ③ as shown in Figure 3.9 (a), even so, the results have not been used to analyze the behavior of fluid flow to limit analysis error since those positions do not cover the whole section area. The error would be caused by somehow the signal through the section, but it could not be detected. Nevertheless, the signal could be reasonably detected since the shape and the peak of each position varying

with time and flow patterns. For instance, the order over the time of the peak of the curves each position arranges from inlet to outlet (position ① to ④) as would be seen in Figure D.1 on Appendix D, which were the results of small jet clarifier in the case of without porous zone with various inlet flow rate.

a)   b)
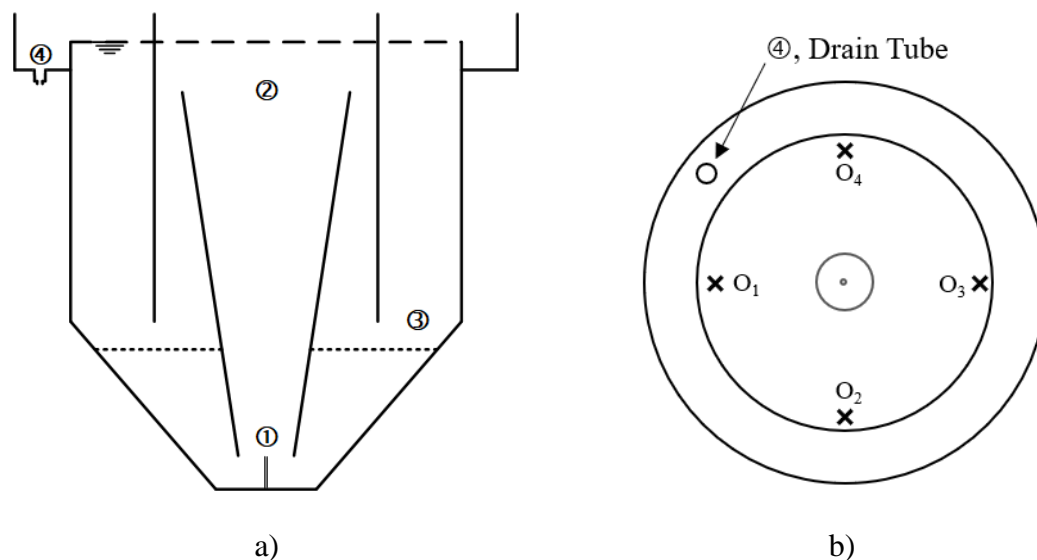
Figure 3.9 The positions of conductivity detectors of (a) inside jet clarifier prototypes and (b) at the overflow area of jet clarifier prototypes

Figure D.1 (see Appendix D) could be seen that the very sharp peak exhibited of overflow outlet checkpoints 2 and 3 by each flow rate indicated initial high concentration and the almost instantaneous subsequent decay, especially, on 19 L/hr. and 49 L/hr. flow rates. However, the curve clearly to be seen that the tracer signal detected at various positions quite consistently, and the RTD curves at the drain tube represent the mean values average the fraction of tracer concentration from 4 other checkpoints at the overflow outlet. Furthermore, the RTD experiment results were focused on the beginning of the experiment until 10% of conductivity signal leaving the reactor that has resided in the jet clarifier, which was named as t_{10} were shown in Table 3.3.

Table 3.3 Mean residence time analysis at 10% of conductivity signal (t_{10})

Checkpoints	t_{10} (min)		
	Flow rate (L/hr.)		
	11	19	49
Overflow outlet 1	69	39	21
Overflow outlet 2	66	39	18
Overflow outlet 3	69	36	15
Overflow outlet 4	75	42	18
Outlet	69	40	18

It can be seen that the RTD experimental data reported the t_{10} of each overflow outlet position and the average t_{10} that represents the result of the outlet were reasonably close for each flow rate. The mean values of t_{10} at the overflow outlet were 69.75, 39, and 18 minutes while the t_{10} of the outlet was 69, 40, and 18 minutes for flow rate 11, 19, and 49 L/hr., respectively. The maximum different value of t_{10} between overflow outlet and inlet checkpoints was less than 2.5%. In contrast, the results from the outlet position of each flow rate can be considered the velocity of the fluid. For the highest flow rate, the t_{10} is smaller than the lowest flow rate and moderate flow rate about 4 and 2.5 times, respectively, which is relatively close to the ratio of flow rates.

To consider the non-asymmetry effect of the liquid flow due to the jet clarifier constructed, the characteristics of the *E(t)* curve and t_{10} were used to assess the accurate data acquisition. It could be concluded that the data detected at the outlet was reliable to be used to represent the overflow outlet.
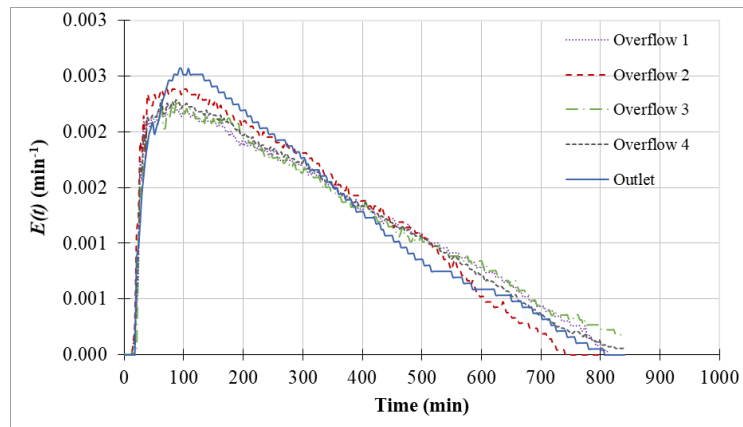
a) 11 L/hr.
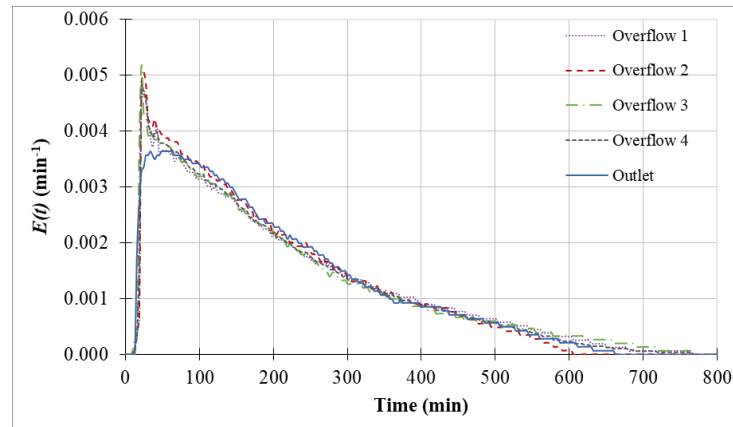
b) 19 L/hr.
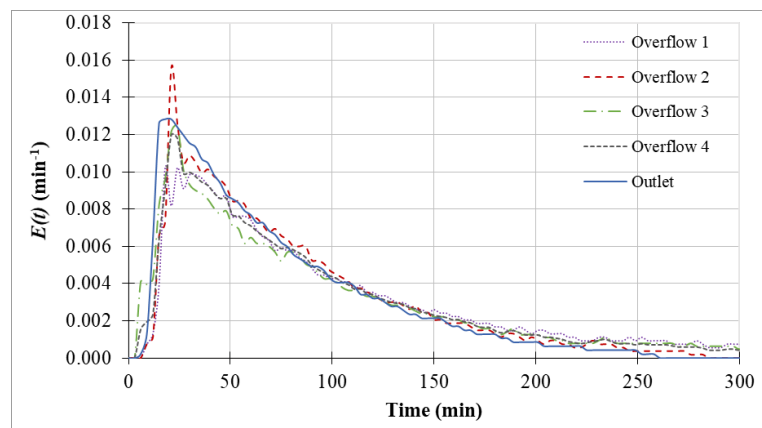
c) 49 L/hr.

Figure 3.10 *E(t)* experimental data curve for overflow and mainstream outlet of
(a) 11 L/hr., (b) 19 L/hr., and (c) 49 L/hr.

3.2.1.2 Effect of Jet clarifier's Size and Flow Rate on RTD Responses Curve and the Mean Residence Time

The main objective of this set of experiments is to characterize the flow behavior of jet clarifiers and to compare flow characteristics in terms of mean residence time (t_m), standard deviation (σ), and skewness (s^3) with results obtained from RTD experiments using two different jet clarifier sizes (LSP and SSP) and three flow rates, as described previously in Chapter 2, section 2.1.1. Several flow rate conditions were tested, and their characteristic parameters including flow rate, theoretical residence time, and Reynolds number (Re number), are shown in Table 2.2 with the cone base diameter of the truncated of the small and large reactor sizes was specified at the middle range, which was 6.5 and 10 cm., respectively.

To determine the effect of different flow rates on the mean residence time (t_m) in various jet clarifier sizes, the t_m of the LSP and SSP was calculated from the experimental data using the method of moments. Plots of the RTD curves, *E(t)* versus sampling time (t), is derived into the dimensionless function that the exit ages distribution (*E(θ)*) can be calculated from tracer output using Equation 2.2 while the sampling time (θ) can be calculated by using the Equation 2.6 in order to determine to mean residence time distribution between both reactor sizes. The total experimental time was conducted at least 3 times their theoretical mean residence time. The *E(θ)* for each tank followed the normal exponential decay curves typical of ideal mixers. However, the curves exhibited a long tail indicating deviation from ideality. The RTD curves were used to compare the mean residence time of each condition e.g., different flow rates, with and without porous zone.

All of the RTD curves are presented in Figure 3.11. There is variance present, but all the curves have nearly identical shapes to their curves with different peak values. The *E(θ)* of different jet clarifier sizes follow the same general flow pattern. The *E(θ)* curve of without porous zone cases, each curve has a sharp peak around 100, 40, and 17 minutes with a downward exponential slope with completion at 840, 700, and 300 minutes for low, medium, and high flow rate, respectively. For the case of porous zone existence, the peaks

were a bit delay than without the porous zone, but the completion time was more minor. The peaks were around 180, 75, and 30 minutes also with a downward exponential slope with completion at 760, 510, and 180 minutes for low, medium, and high flow rates, respectively. It can be said that the porous zone is one of the parameters that affect mean residence time and flow pattern because it is a cause of changing reactor volume and might change hydraulic phenomena inside the reactor.

The mean residence time (t_m), standard deviation (σ), and skewness (s^3) with the theoretical residence time was reported in Table 3.4 and Table 3.5. for the small and large size jet clarifier, respectively. The values of mean residence time (t_m) from the RTD experiment were lower than the theoretical residence time (τ) approximately 16.44%, 4.31%, and 11.11% for low flow rate to high flow rate without porous. In comparison, in the porous cases, the difference values between τ and t_m were 8.81%, 12.64%, and 11.27% for low flow rate to high flow rate due to the limit of the device and it could be explained that the tracer was not detected very well by a conductivity meter at a low concentration region or that some dead zone around 10% of the tank is present (Romphophak et al., 2016).

On figure 3.11, it is important to observe that the peak is displaced closer to *θ=1* with the porous zone whatever the size and the flow rate. It means that the reactor is close to a plug flow with a porous media. Inversely, the whole flow is more like a perfectly mixed reactor without the porous zone.
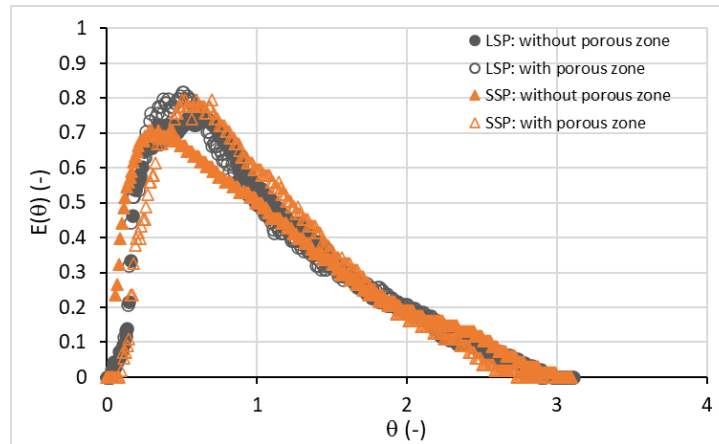
a) Low flow rate
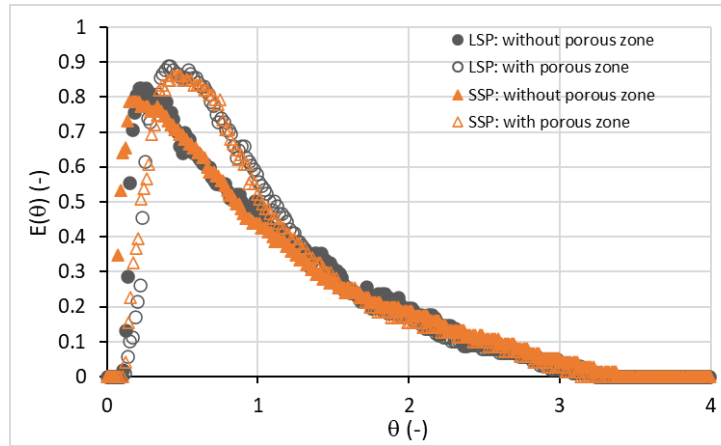
b) Medium flow rate
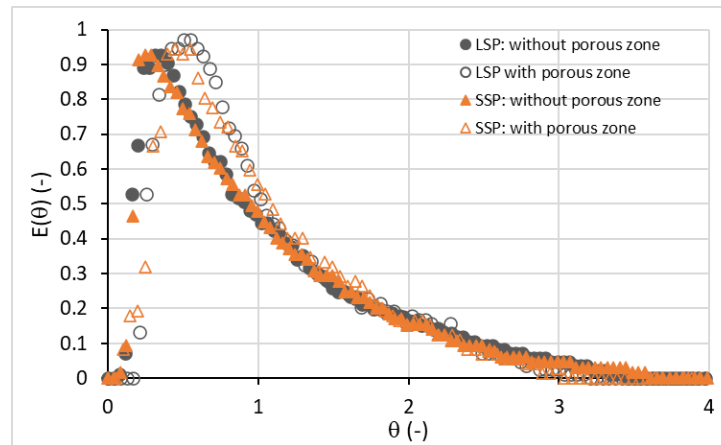
c) High flow rate

Figure 3.11 The effect of reactor size on exit age distribution in the LSP and SSP of

(a) low flow rate, (b) medium flow rate, and (c) high flow rate

Table 3.4 Mean residence time analysis of the SSP

Conditions	Inlet flow rate (Q)	Flow rate (L/hr.)	Theoretical residence time; τ (min)	Mean residence time distribution; t_m (min)	% of τ and t_m difference	Std. deviation; σ (min)	Skewness; s^3 (-)	$\frac{D}{uL}$ (−)	Peclet Number (-)
without porous	Low	11	365	305	16.44	178	0.68	0.1374	7.28
	Medium	19	209	200	4.31	143	0.89	0.1562	6.40
	High	49	81	72	11.11	52	1.04	0.1567	6.38
with porous	Low	11	318	290	8.81	155	0.64	0.1011	9.89
	Medium	19	182	159	12.64	92	0.98	0.1265	7.90
	High	49	71	63	11.27	36	0.94	0.1227	8.15

Table 3.5 Mean residence time analysis of the LSP

Conditions	Inlet flow rate (Q)	Flow rate (L/hr.)	Theoretical residence time; τ (min)	Mean residence time distribution; t_m (min)	% of τ and t_m difference	Std. deviation; σ (min)	Skewness; s^3 (-)	$\frac{D}{uL}$ (−)	Peclet Number (-)
without porous	Low	40	365	315	13.70	190	0.55	0.1330	7.52
	Medium	70	209	197	5.74	137	0.86	0.1511	6.62
	High	180	81	73	9.88	59	0.93	0.1524	6.56
with porous	Low	40	318	286	10.06	181	0.77	0.1316	7.60
	Medium	70	182	161	11.54	102	0.57	0.1157	8.64
	High	180	71	65	8.45	42	0.97	0.1210	8.27

From the results shown in Figure 3.11, Table 3.4, and Table 3.5, it is clear that the RTD of both sizes of the jet clarifier (LSP and SSP) is sensitive to change in flow rate, but not as proportionally sensitively to change in size and the mean residence time is reasonably equal in the same conditions between different sizes due to theoretical residence time controlled of each size. It means that the mean residence time (t_m) is one of the main controlled parameters is the same. So, it can be extrapolated that the velocity field of both jet clarifier sizes is the same in the range of inlet flow rate examined. Thus, for brevity, the next sections focused on hydrodynamic phenomena of the jet clarifier with and without porous zone in only a small size reactor.

3.2.1.3 Effect of Configuration of Tank on the RTD Responses Curve and Function

The RTD curves determined for the SSP with the various conditions, porous zone, and different truncated cone base, were shown in Figure 3.12 and Figure 3.13 for without and with porous zone, respectively. It can be observed in Figure 3.12 and Figure 3.13 that the mean residence time distribution decreases with an increased inlet flow rate. The mean residence time (t_m), standard deviation (σ), and skewness (s^3), and Peclet number have been calculated for the present experimental condition and were presented in Table 3.6.

The shape of $E(\theta)$ curves was as same as the $E(\theta)$ curves discussed in the 3.2.1.2 topic. All of the RTD curves are presented in Figure 3.12, and Figure 3.13 were plotted to compare the effect of flow rate on the same range of different truncated cone bases. In the case of fixed flow rate with the various range of truncated cone bases, there is variance present, but all the curves have nearly identical shapes to their curves. In contrast, the increasing flow rate causes higher peak values of $E(\theta)$ in both cases of with porous and without porous zone. Moreover, the $E(\theta)$ of different truncated cone bases diameter follow the same general flow pattern.
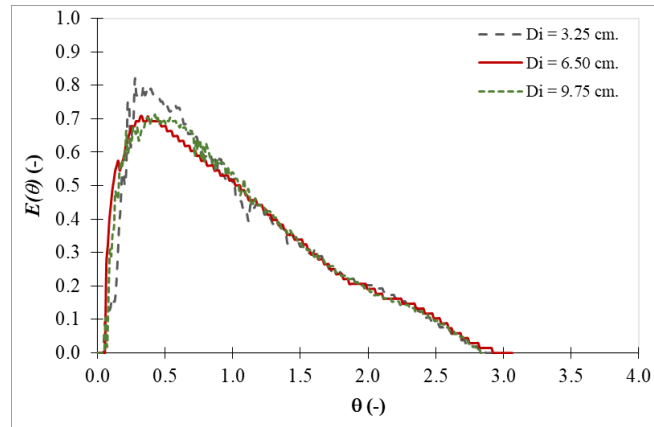
a) 11 L/hr.
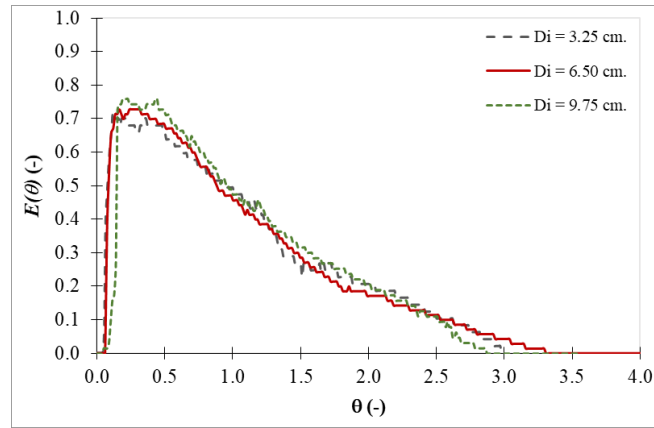
b) 19 L/hr.
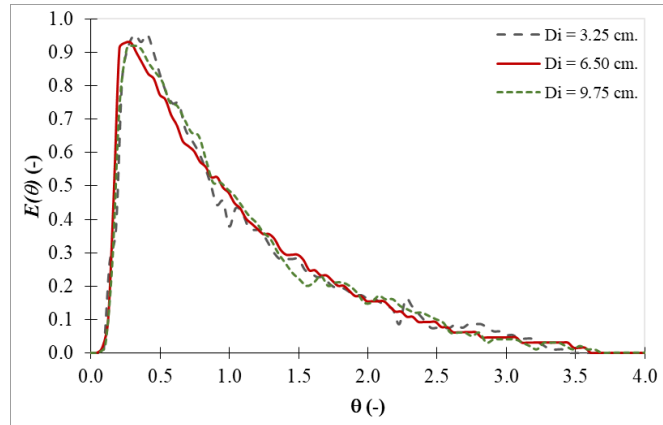
c) 49 L/hr.

Figure 3.12 The effect of diameter of the truncated cone base on exit age distribution
in the SSP of (a) 11 L/hr., (b) 19 L/hr., and (c) 49 L/hr. without porous zone
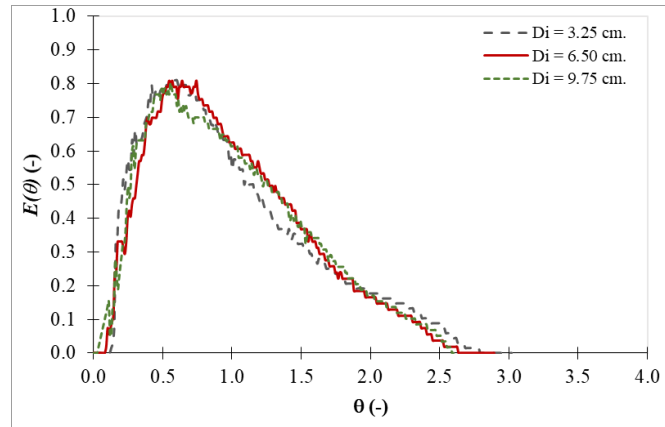
a) 11 L/hr.
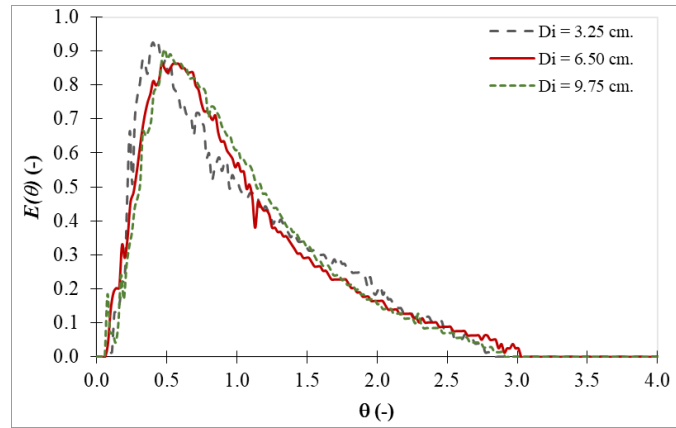
b) 19 L/hr.
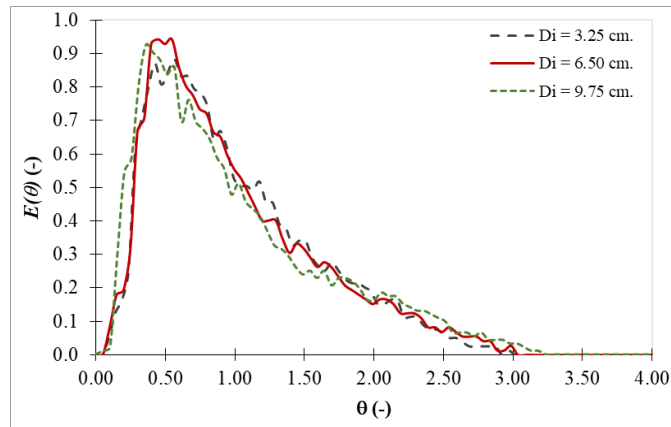
c) 49 L/hr.

Figure 3.13 The effect of diameter of the truncated cone base on exit age distribution
in the SSP of (a) 11 L/hr., (b) 19 L/hr., and (c) 49 L/hr. with porous zone

Table 3.6 Mean residence time analysis of the SSP in with various conditions

Porous	Flow rate (L/hr.)	Diameter (cm.)	Theoretical residence time (min)	t_m (min)	% of τ and t_m difference	σ^2 (min^2)	Std. deviation; σ (min)	Skewness; s^3 (-)	$\dfrac{D}{uL}$ (−)	Peclet Number (-)
without	11	3.25	365	302	17.26	31527	177.56	0.71	0.130	7.68
		6.50	365	305	16.44	31733	178.14	0.68	0.137	7.28
		9.75	365	300	17.81	34891	186.79	0.69	0.131	7.65
	19	3.25	209	198	5.26	38086	155.16	0.74	0.150	6.67
		6.50	209	200	4.31	20367	142.71	0.89	0.156	6.40
		9.75	209	196	6.22	23071	151.89	0.70	0.134	7.47
	49	3.25	81	73	9.88	2220	47.12	1.12	0.157	6.38
		6.50	81	72	11.11	2664	51.62	1.14	0.157	6.38
		9.75	81	76	6.17	1656	40.70	1.15	0.154	6.50
with	11	3.25	318	293	7.86	26206	161.88	0.78	0.116	8.64
		6.50	318	290	8.81	23919	154.66	0.64	0.101	9.89
		9.75	318	287	9.75	31391	177.18	0.60	0.106	9.47
	19	3.25	182	165	9.34	9926	99.63	0.78	0.123	8.13
		6.50	182	159	12.64	8417	91.74	0.98	0.127	7.90
		9.75	182	160	12.09	7790	88.26	0.88	0.113	8.88
	49	3.25	71	64	9.86	1356	36.82	0.86	0.161	6.19
		6.50	71	63	11.27	1328	36.44	0.94	0.123	8.15
		9.75	71	65	8.45	1486	38.55	0.98	0.140	7.16

The $E(\theta)$ curve of without porous zone, each curve has a sharp peak approximately 100, 40, and 17 minutes with a downward exponential slope with completion at 840, 700, and 300 minutes for 11 L/hr., 19 L/hr., and 49 L/hr., respectively. For the case of porous zone existence, the peaks were a bit delay than without the porous zone, but the completion time was more minor. The peaks were around 180, 75, and 30 minutes also with a downward exponential slope with completion at 760, 510, and 180 minutes for 11 L/hr., 19 L/hr., and 49 L/hr., respectively. It could be clearly detected that the shape of $E(\theta)$ which have presented in the previous topic (see Figure 3.11) were as same as Figure 3.12 and Figure 3.13. Moreover, the RTD function was presented in Table 3.6. The mean residence time (t_m) of the reactor for the present conditions also about 15% lower than the theoretical residence time (τ) due to the limit of the device. It could be explained that once the tracer was injected through the jet clarifier it was diluted by the tap water resting in the jet clarifier. Thus, the concentration of tracer was reduced and not detected very well by a conductivity meter at a low concentration region near the outlet due to dilution.

The comparison of global hydrodynamic in the case of various truncated cone base, t_m of each case was not insignificant differences since the t_m was 282, 273, and 296 minutes for 11 L/hr., and 182, 200, and 196 minutes for 19 L/hr., and 66, 72, and 68 minutes for 49 L/hr. of 3.25, 6.5, and 7.25 cm. of truncated cone base diameter in the case of without porous zone, respectively. While the t_m of the case of existence porous zone were 278, 290, and 287 minutes for 11 L/hr., and 165, 149, and 154 minutes for 19 L/hr., and 64, 60, and 58 minutes for 49 L/hr. of 3.25, 6.5, and 7.25 cm. of truncated cone base diameter, respectively. The difference of each experimental set was lower than 5%, which was within the acceptable range. The present study confirmed the findings of the effect of truncated cone base diameter on RTD was no effect neither RTD nor the performance of the jet clarifier as discussed in the 3.2.1.2 section.

3.2.1.4 Differences of RTD Responses Curve for the Porous and Non-Porous Zone in the Jet Clarifier

Figure 3.11 (a) – (c) could be used to investigate the effect of the porous zone on the hydrodynamics in the jet clarifier since those figures were plotted to compare the RTD response curves with the case of the porous zone and non-porous zone in three flow rate and two sizes of the jet clarifier. The figures show that the porous zone affected the RTD response curves and the mean residence time for both sizes of the reactor. The RTD curves of all study cases consisted of the porous zone show the delay of time at the peak of the curve if comparing the shape of $E(\theta)$ between the existing porous case and without the porous case it meant that the hydrodynamics of the jet clarifier was changed due to the porous zone. It could be explained the hydrodynamic assumption by Figure 2.3 the solid arrows show the expected liquid flow field while the dash-line arrows show the short circuit flow fields. While the existing porous zone at the bottom part of the jet clarifier blocked or reduced the short circuit pathway, so the tracer signal would be detected with the delay time since it should follow the main hydrodynamic pathway.

Moreover, the values of dimensionless of the concentration curve ($E(\theta)$) of porous zone existence cases were higher than without porous zone cases if comparing the case of with and without porous zone in Figure 3.11. Also, the values of fractal of the concentration curve ($E(\theta)$) could be compared with and without porous zone in the SSP in various truncated cone base diameters in Figure 3.12 and Figure 3.13, respectively. It could be seen that for all of various truncated cone base diameters cases the $E(\theta)$ values of without porous cases were lower than with porous zone cases. It might be explained that the liquid flow goes through the main direction with less spread (solid arrows in Figure 2.3), so the tracer concentration was detected higher. Furthermore, the tracer spreading explanation could be used as an explanation of the $E(\theta)$ characteristic in the point of view of various flow rates because the shape of the $E(\theta)$ curve of the low flow rate was more spread than the other flow rates. On the other hand, the shape of the $E(\theta)$ curve of the high flow rate was a narrow

and higher peak due to the concentration of tracer detected following the velocity flow field.

For all the above reasons, it could be concluded that the porous zone is one of the parameters that affect mean residence time and flow pattern because it is a cause of changing reactor volume and might change flow map inside the reactor.

3.2.2 Summary

The RTD experiments were done for two main reasons; the first reason was to examine the effect of the liquid flow rate, tank's configuration, and porous zone on the mean residence time of the LSP and SSP, and the second reason was using the RTD curves to validate hydrodynamic models by numerical technique with using Fluent program to simulate the hydrodynamic, which would be explained in the topic of 5.2.

The findings of this study can be understood some behaviors of the liquid flow characteristic of the jet clarifier prototypes, but more details of flow field still required the local parameter investigations. However, the results demonstrate four crucial things. First, considering results from the RTD experiments could be concluded that the mean residence time distributions (t_m) were equal in the same conditions such as inlet flow rate and porous zone conditions between different sizes, as shown in Table 3.4 and Table 3.5 and. It means that one of the main controlled parameters was the same in both LSP and SSP. Second, the truncated cone base diameter of the flocculation part does not affect residence time distribution since the signal of the tracer detected were tend to be the same even if the truncated cone base diameter varied at every flow rate, which could be seen in Figure 3.12 and Figure 3.13 for the case of the non-porous zone and existing porous zone condition, respectively and the RTD functions analyzed shows as Table 3.6; it might be indicated that it does not affect the flow field. Third, the leading cause that affects turbidity removal efficiency is flow rate which also affects mean residence time, which was investigated and described in this part. Forth, the porous zone not only directly affects the liquid flow field but also the mean residence time, which could be detected by the $E(\theta)$ curves as shown in Figure 3.11. Moreover, this evidence could be used to confirm that the assumption of

changing velocity flow field by porous zone inside the jet clarifier was reasonable. These results go beyond previous reports, showing that the presence of the flocs blanket would improve the performance of the system (Garland et al., 2017).

The mean residence time of the LSP and SSP was determined as the kind of global parameter of hydrodynamics because the mean residence time calculated by the tracer signal at the outlet of the reactor, while the contact time or mixing time of flocculation is one of the key parameters that affect the flocculation process could not be examined by this method because of the detecting tracer signal reason. So, the mean residence time of only the flocculation zone inside the jet clarifier still needs to be determined, which could be defined as the local time included in the local parameters. Thus, the local parameter, including velocity gradient (G) and contact time (t_{cont}) would be investigated and discussed in the next chapter.

For all the above reasons, the parameters that did not affect the hydrodynamic would be neglected to the scope of the experiments would focus on in-depth details. Hence, the jet clarifier would be scope only on the SSP with the medium range of the truncated cone base diameter (6.5 cm.). Furthermore, the jet clarifier configuration would be changed to be able to investigate the local parameters e.g., local hydrodynamic and in-situ floc size distributions the flat quasi-bidimensional (Q2D) jet clarifier would be used to examine. Even though the existing porous zone impacts the hydrodynamic as discussed, to investigate the local parameter will be focused only on the jet clarifier without the porous zone since this was the first step of local analysis of the velocity flow field which should be expected to be like a laminar flow in the mixing zone and settling zone, respectively.

CHAPTER 4

EXPERIMENTAL ANALYSIS OF THE Q2D PILOT: HYDRODYNAMICS AND FLOC SIZE DISTRIBUTIONS

Regarding literature, the hydraulic flocculators have been designed based on global velocity gradient (G) and contact time (t_{cont}). Thus, to improve the jet clarifier the velocity gradient (G) and contact time (t_{cont}) must be evaluated. Until now, these essential parameters of the jet clarifier have not been investigated locally.

The experiments discussed in this chapter have all been realized with the Q2D jet clarifier presented in Chapter 2 (see Figure 2.2). This pilot enables the use of the optical method such as Particle Image Velocimetry (PIV) and shadowgraphy. This chapter is divided into two parts: part 1 addresses the local hydrodynamic analysis and whereas part 2 is devoted to the analysis of aggregate size distribution of flocculation zone in the jet clarifier.

4.1 Local Hydrodynamic Analysis by PIV

The results of local hydrodynamics were mainly limited to the flocculation zone, located in the vertical divergent of the jet clarifier, which was estimated to 7 liters volume. Thus, the results in this section were organized as follows:

- Mean velocity field induced by the jet in the flocculation zone
- Velocity profiles
- Jet flow characteristics: vertical distribution of the width of the jet plume
- Circulation time and flowrate
- Viscous dissipation rate of turbulent kinetic energy (ε)
- Kolmogorov scale (η)
- Velocity gradient (G)
- Discussion on hydrodynamics

4.1.1 Mean Velocity Field Induced by the Jet in the Flocculation Zone

An example of the PIV raw image is plotted on Figure 4.1. The structure of the jet can be easily seen, and instabilities appear along the border of the jet. Considering such instantaneous velocity fields, time averaging turns out to be necessary. Averaging procedure as exposed in Chapter 2.
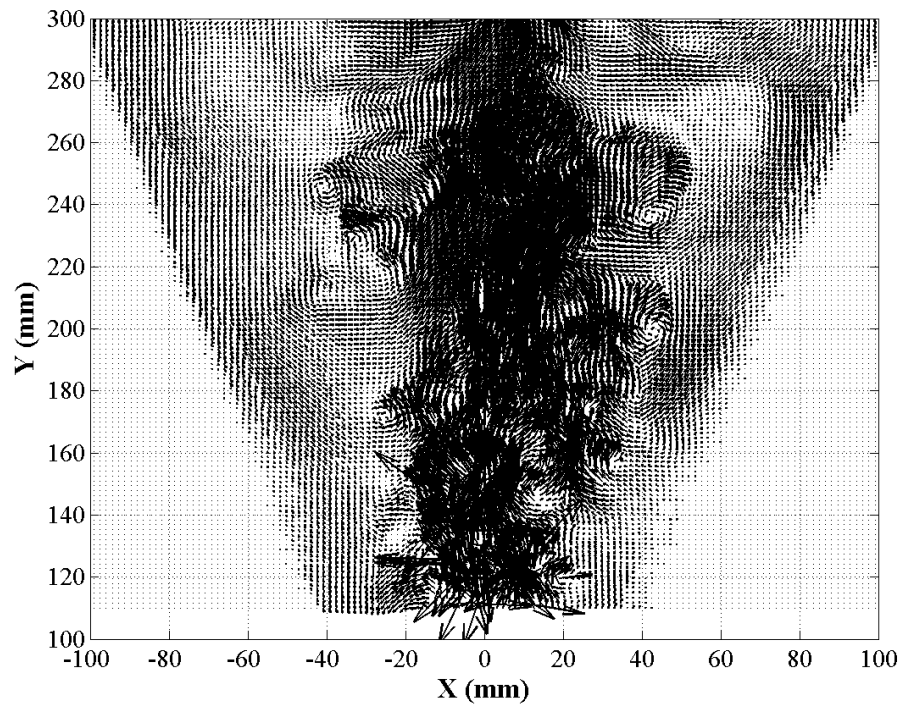
Figure 4.1 Fluctuation of the velocity profile of jet of 11 L/hr. flow rate at field 2

Mean velocity fields are plotted in Figure 4.2 for the 3 flow rates and the 2 measurement fields 1 and 2 as shown in Figure 2.10; only the left-hand side of the PIV fields is plotted. These velocity fields exhibit similar circulation loops generated by the vertical jets. The eyes of circulations are located at vertical positions Y = 340, 360, and 380 mm and horizontal positions X between -80 and -60 mm. for the respective flow rates 11, 19, and 49 L/hr. Clearly, the circulation loop (location and shape) is the same for the three injected flow rates. It means that the jet generates a global circulation with similar patterns.
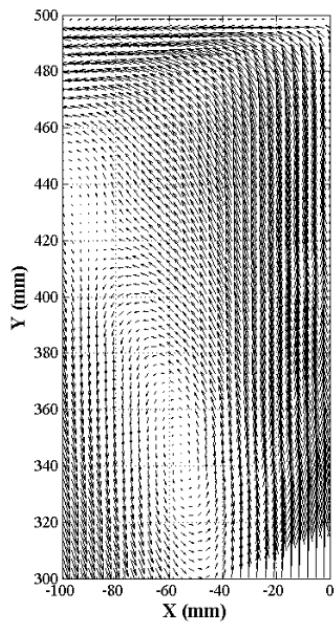
a) Field 1, 11 L/hr.   b) Field 1, 19 L/hr.   c) Field 1, 49 L/hr.
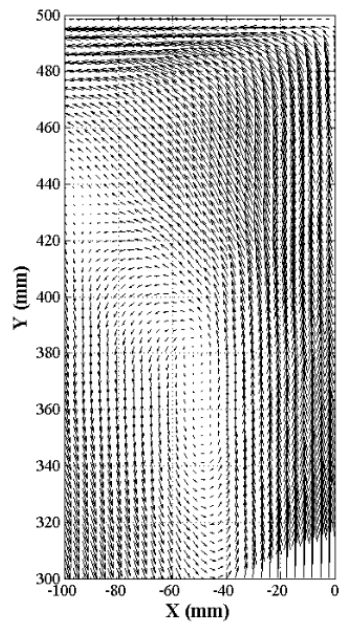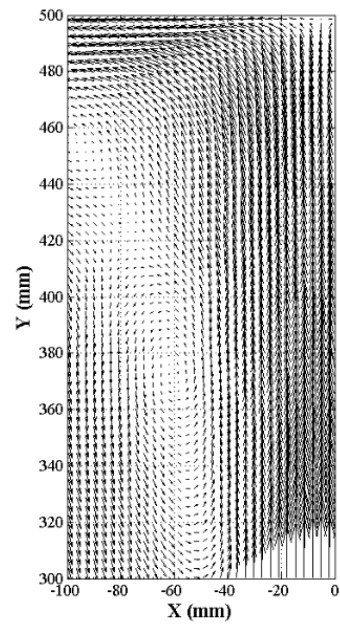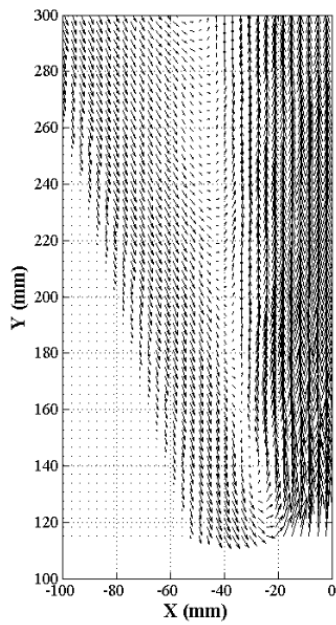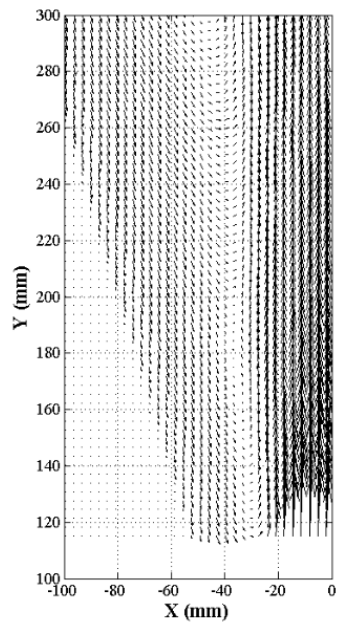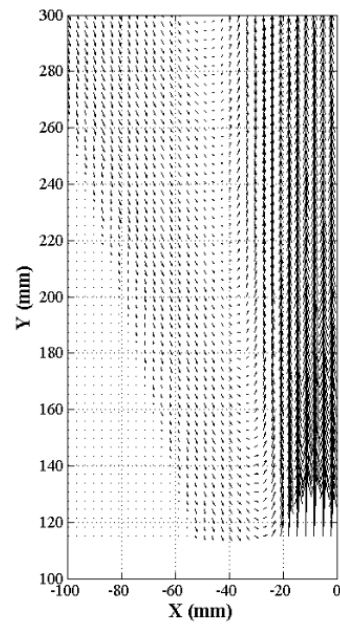
d) Field 2, 11 L/hr.   e) Field 2, 19 L/hr.   f) Field 2, 49 L/hr.

Figure 4.2 Mean velocity field for each injected flow rate

In the lower part of the flocculation zone, Figure 2.2 (d-f), the mean velocity fields exhibit similar circulation loops except for close to the nozzle for the low flow rate (11 L/hr).

4.1.2 Velocity Profiles

4.1.2.1 Vertical Velocity (Velocity Component in the Y-direction; V)

Figure 4.3 represents the vertical profiles of the mean vertical (V) velocity component for the 3 flow rates (Q = 11, 19, and 49 L/hr.). As expected, the velocity magnitude along the axis of the jet decreases with increasing the distance from the nozzle. The 3 plots reveal a similar trend.
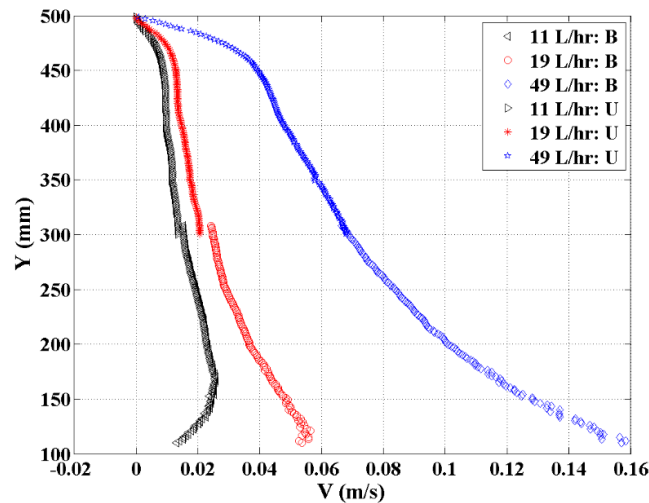
Figure 4.3 The vertical average velocity (V) of
11 L/hr., 19 L/hr., and 49 L/hr. flow rates

In order to better understand the hydrodynamics in this zone, the mean axial (V) velocity component was divided by the injected mean velocity (at the nozzle of the inlet tube) to define a dimensionless velocity. This dimensionless velocity is plotted on Figure 4.4. The three vertical profiles of dimensionless vertical mean velocity are nicely superposed; clearly, the mean axial (V) velocity component depends on inlet velocity, as shown in Figure 4.4.
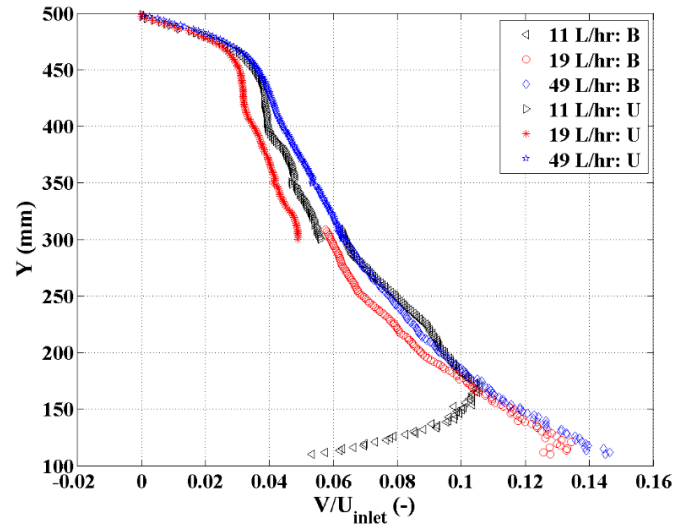
Figure 4.4 The ratio of vertical velocity (V) divided by the injected mean velocity of 11 L/hr., 19 L/hr., and 49 L/hr. flow rates

The first comment is that these ratios are similar for the three flow rates. Then increasing by 3 the distance from the nozzle corresponds to an increase between 2 or 3 of the velocity ratio. There is thus a quasi-linear decrease of vertical velocity with the distance to the inlet nozzle.

Table 4.1 Vertical velocity relating to the vertical plane of 3 flow rates

Flow rate (L/hr.)	Mean vertical velocity at Y = 0 mm. (Inlet velocity) (m/s)	Vertical velocity (m/s)		Ratio of Inlet velocity/Mean vertical velocity	
		Y = 100 mm.	Y = 300 mm.	Y = 100 mm.	Y = 300 mm.
11	0.24	0.035	0.015	7	16
19	0.42	0.055	0.021	7	20
49	1.08	0.160	0.07	7	15

4.1.2.2 Horizontal Profile of Vertical Mean Velocity

The velocity profiles at various Y-axis positions were plotted separately for three flow rates and both window fields, as shown in Figure 4.5.
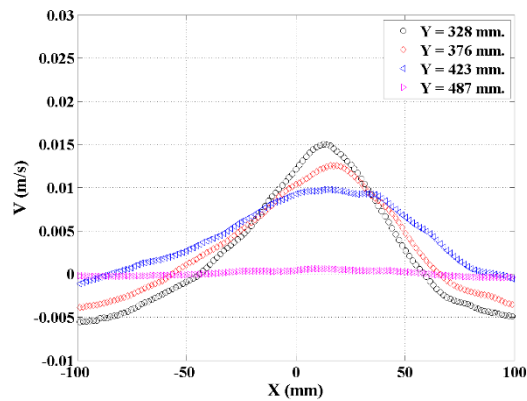
a) Field 1, 11 L/hr.
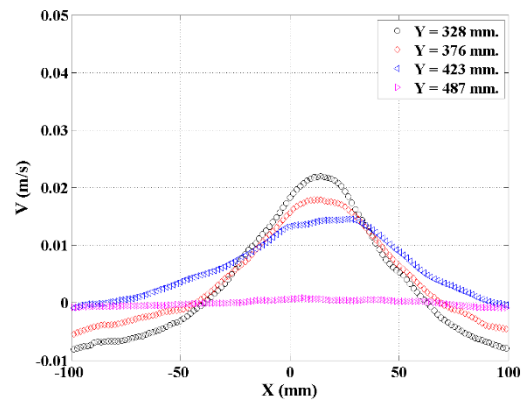
b) Field 1, 19 L/hr.
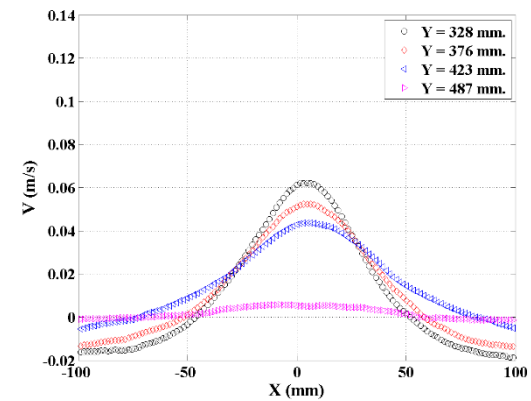
c) Field 1, 49 L/hr.
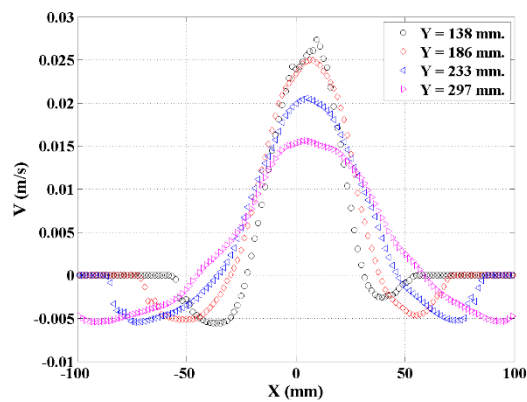
d) Field 2, 11 L/hr.
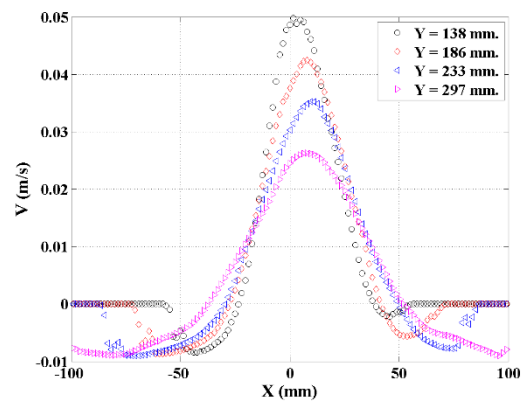
e) Field 2, 19 L/hr.
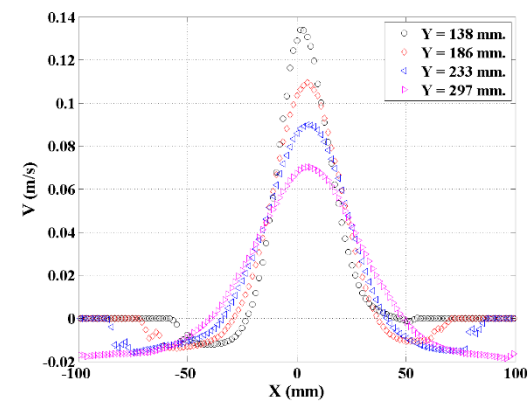
f) Field 2, 49 L/hr.

Figure 4.5 Horizontal profile distribution of vertical velocity (V)

These vertical velocity profiles (field 2) are plotted in the lower part of the flocculation zone, at Y = 138 mm, 186 mm, 233 mm, and 297 mm in Figure 4.5 (d-f) and in the upper part (field 1) at Y = 328 mm, 376 mm, 423 mm in Figure 4.5 (a-c). It can be seen that the peak of the profiles are close to the jet axis (X = 0), which indicates that the vertical velocity flow fields are is nearly symmetrical; symmetry increases with inlet flow rate, highest flow rates inducing more stable flow. There is an apparent affinity of velocity profiles whatever the flow rates.

In order to confirm the similarity of these flow patterns, the vertical profiles of plume width were plotted on Figure 4.6 (b) for the 3 flow rates. The 3 eyes of circulations being located roughly in the same zones (-80 < X < -60 mm. and 340 < Y < 380 mm.) (see Figure 4.2), the horizontal profiles of vertical mean velocity at the location of the eye of circulation have been plotted on Figure 4.6 (a). The vertical velocity profiles were normalized by their maximum velocity, the three profiles could thus be superimposed. Figure 4.6 (a) clearly to be seen that the 3 profiles were similar, indicating that circulation velocity was proportional to the injected flow rate (Q). Since the mixing time was proportional to the circulation length in advection dominated mixing, the flow rate time the mixing is constant.

Moreover, the shape of the horizontal profiles of the vertical velocity is narrow and high which is characteristic of the vertical velocity component in jet flow. Coming back to Figure 4.5, the horizontal profiles of axial velocity exhibit negative values far from the axis of the jet, which confirm that there is a large circulation of the liquid, the liquid flowing upward along the jet axis and downward along the inclined walls.

The jet plume width can be estimated from horizontal profiles of vertical velocity by identifying the position where the mean vertical velocity reaches zero, the vertical velocity being positive in the jet plume (upward flow) and negative outside (downward flow). The horizontal width of the jet is plotted on Figure 4.6 (b); Once again, the gradual enlargement observed is related to the decrease of the mean axial velocity in the jet. The increase of the jet size with axial direction is nearly linear. The evolutions of the jet plume widths for the 3 flow rates are very similar. As reported by (Chu and Lee, 1996), the jet

plume width increases with increasing distance from the nozzle (located at $Y = 0$ mm.). The estimation of the width increase with the distance was around 60 mm for 300 mm from the jet, it gives an angle for the jet development close to 10 degrees, much smaller than the geometrical angle between the two internal baffles.
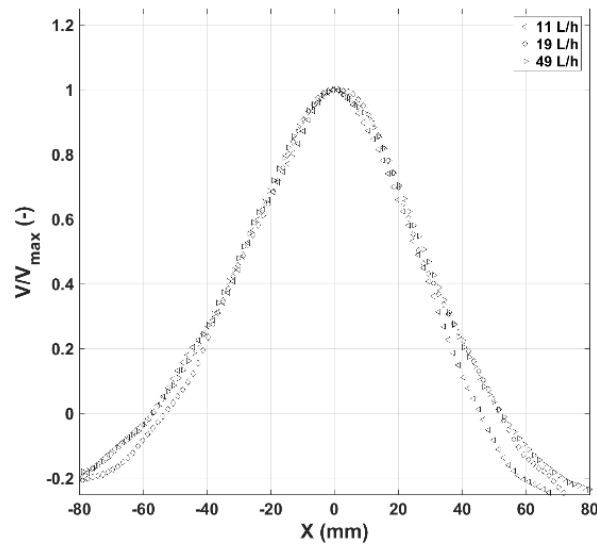
a) Vertical mean velocity profile, at the location of the eye of recirculation
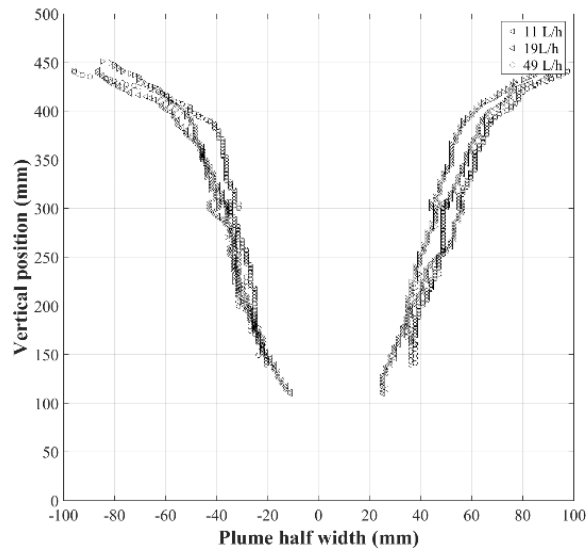
b) Vertical distribution of the width of the jet plume

Figure 4.6 Jet flow characteristics for the three flow rates:
< 11L/h, o 19 L/h, and > 49 L/hr.

4.1.2.3 Velocity Component in the x-direction; U

Figure 4.7 presents vertical profiles of the average horizontal velocity component in the flocculation zone. The horizontal velocity component (U) is much lower than the vertical velocity (main direction of flow).
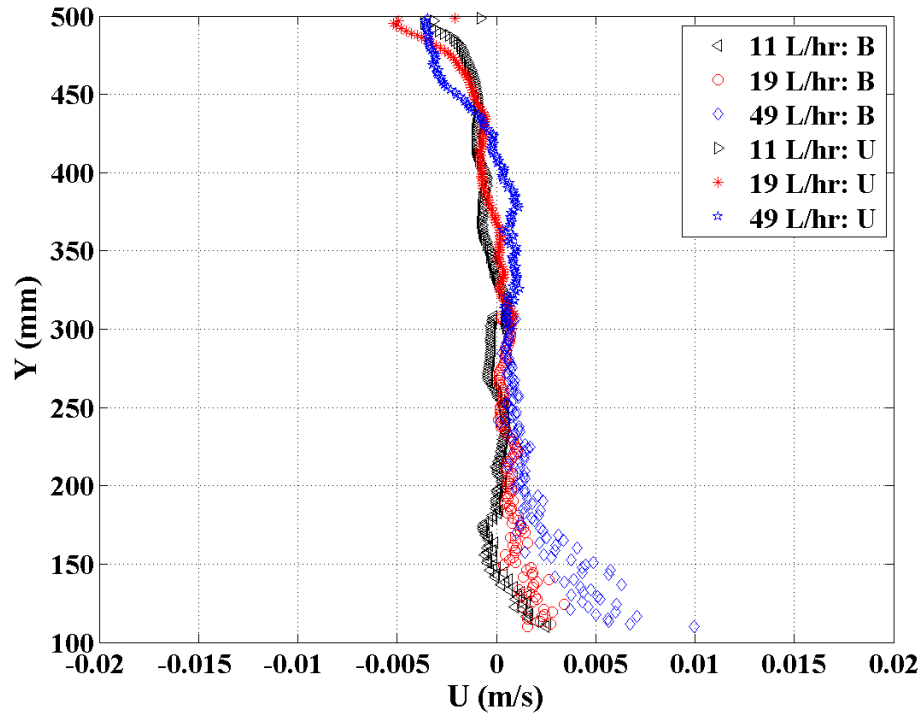
Figure 4.7 The velocity component in the x-direction (U)
of 11 L/hr., 19 L/hr., and 49 L/hr. flow rates

Furthermore, horizontal profiles of horizontal velocity component (U) can be plotted to observe hydrodynamic, especially to highlight the recirculation, as shown in Figure 4.8.

Here again, the first low of Figure 4.8 corresponds to the lower region of the flocculation zone whereas the right column corresponds to the upper zone. The magnitude of the horizontal velocity component increases with the vertical distance to the nozzle.
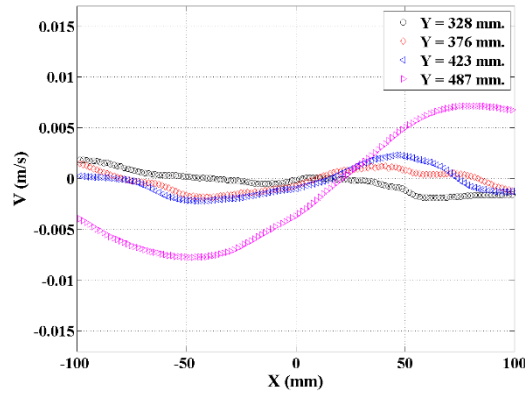
a) Field 1, 11 L/hr.
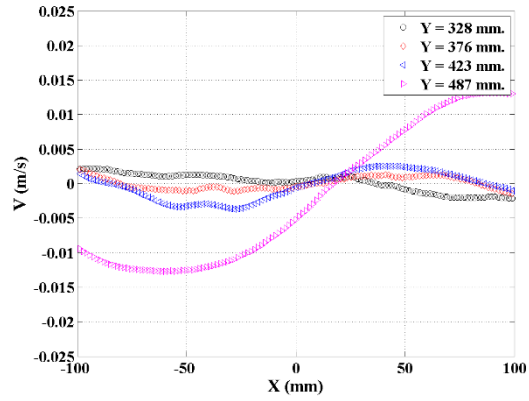
b) Field 1, 19 L/hr.
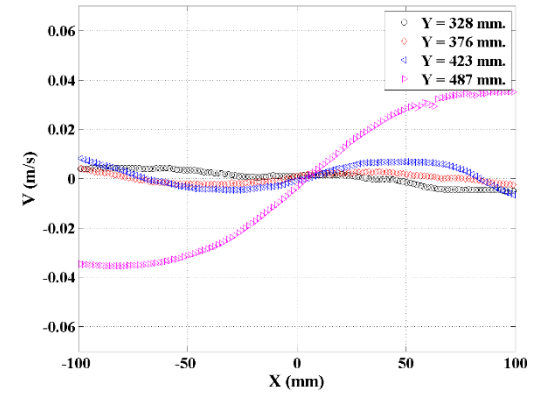
c) Field 1, 49 L/hr.
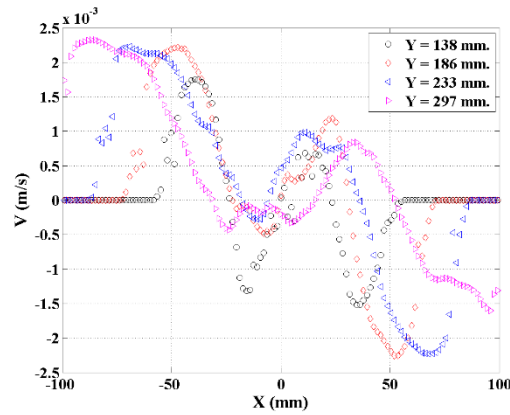
d) Field 2, 11 L/hr.
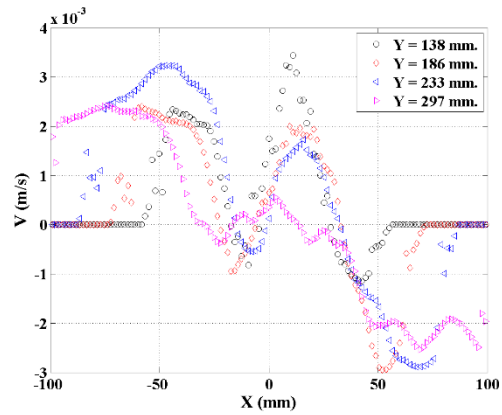
e) Field 2, 19 L/hr.
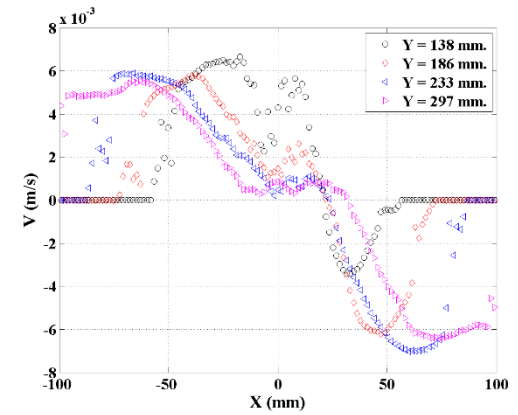
f) Field 2, 49 L/hr.

Figure 4.8 Horizontal profile distribution of horizontal velocity (U)

4.1.2.4 Circulation Time and Flow Rate

From Figure 4.6 (a), it was possible to estimate the vertical flow rate, which will be considered as circulating flow rate Qc, by integrating the horizontal profile vertical velocity between the axis of the pilot and the lateral position of the circulation eye. The width of the half jet plume being close to 50 mm, the thickness of the pilot being 100 mm, an axisymmetric jet could be assumed. Thus, 3 flow rates Qc, called circulation flow rates, have been determined. The values of the circulation flow rate (Qc) were reported in Table 4.2. They range between 12 and 15 times the inlet flow rates, indicating a huge entrainment and a strong recirculation in the flocculation zone.

Clearly, the structure of the flow slightly depends on the injected flow rate, indicating that the circulation loops are similar for the three injected flow rates.

Table 4.2 Processed hydrodynamic characteristics for the 3 flow rates

Abbreviations	Parameters	Injected flow rate (Q) (L/hr.)		
		11	19	49
U (m/s)	Injection velocity	0.24	0.42	1.08
t_{RF} (min)	Residence time in flocculation zone	38.16	22.08	8.58
Q_c (L/hr.)	Circulation flow rate	165	228	637
Q_c/Q	Ratio of circulation flow rate and injected flow rate	15	12	13
t_c (min)	Circulation time	2.55	1.83	0.67

Evidently, the structure of the flow slightly depends on the injected flow rate (Q), indicating that the circulation loops are similar for the 3 injected flow rates. The residence time in the flocculation zone (inside the vertical divergent) was estimated as the ratio of the volume of this zone (estimated to 7 liters) divided by the injected flow rate (Q). The residence times were thus equal to 38.2, 22.1 and 8.6 minutes. Given the circulation flow rates (Q_c), the circulation time (t_c) could be estimated as the ratio of the volume of the

flocculation zone (estimated to 7 liters) divided by the circulation flow rate (Q_c); therefore, circulation time (t_c) depends on flow rate. Certainly, the circulation times were very small compared to the residence time of the flocculation zone. Consequently, the fluid particles will travel along with circulation loops at least 10 times before flowing outward the flocculation zone. This constitutes an efficient macro-mixing zone.

It is however important to evaluate the flow rate outside the flocculation zone. The velocity fields above the left inclined wall were plotted on Figure 4.9 (a) to (c). Vertical profiles of horizontal velocities normalized by the velocity scale (derived as the ratio of the injected flow rate and the section above the wall 65×100 mm²) were plotted on Figure 4.9 (d) for the 3 flow rates. Here again, the flow fields were similar for the 3 jet flow rates.

From Figure 4.9 (d), it was possible to calculate the net flow rate per depth length by integrating the velocity profile above the internal wall. The results were given in Table 4.3. The positive (outward), negative (inward) and total flow rates per unit depth length were estimated. A Reynolds number can be derived based on the average velocity (U_{total}) and the hydraulic diameter of the rectangular cross-section (height 65 mm, depth 100 mm, hydraulic diameter close to 80 mm). The Reynolds numbers ranging between 100 and 150, the flow rate (in cubic meter per second) could be obtained by assuming laminar flow in this region. Since there were two outlets, one on the right side and another one on the left side of the flocculation zone, these estimated outward flow rates were compared to half the inlet flow rate. This ratio varies between 1 and 2.5.

Consequently, one could conclude that the flow rate outside the flocculation zone was close to the injected flow rates, and much smaller than the circulation flow rate inside the flocculation zone (12 to 15 times the inlet flow rate). Therefore, there was a strong internal circulation in the flocculation zone (inside internal walls) but there was almost no circulation around the internal walls. Moreover, the negative flow rate directed inside the flocculation zone increases from 20% to 65% of the positive flow rate and then balances better. It means that the external flow around the inclined baffle was proportionally reduced as confirmed by the decreasing of the ratio between the flow rate above the wall and the inlet flow rate from 2.5 to 1.
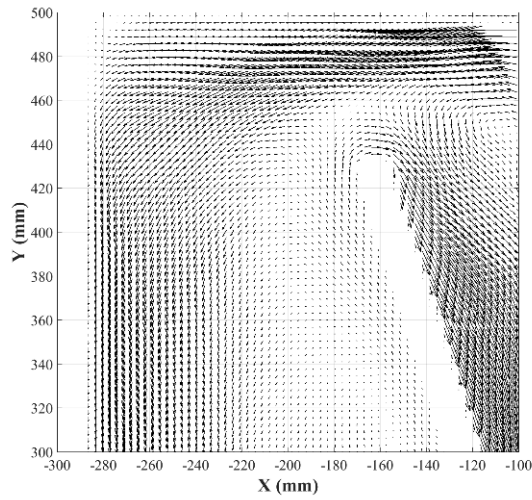
(a) Velocity field 11 L/hr.
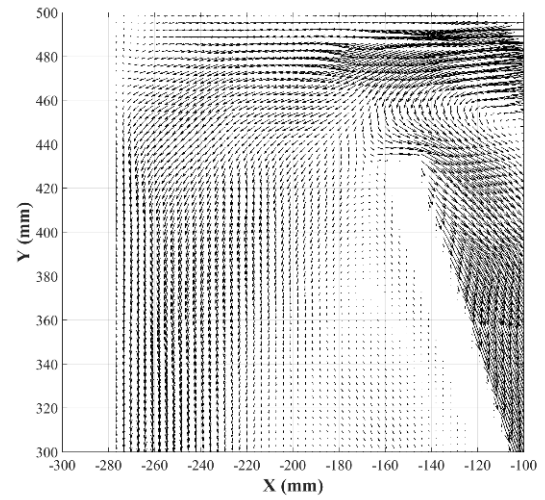
(b) Velocity field 19 L/hr.
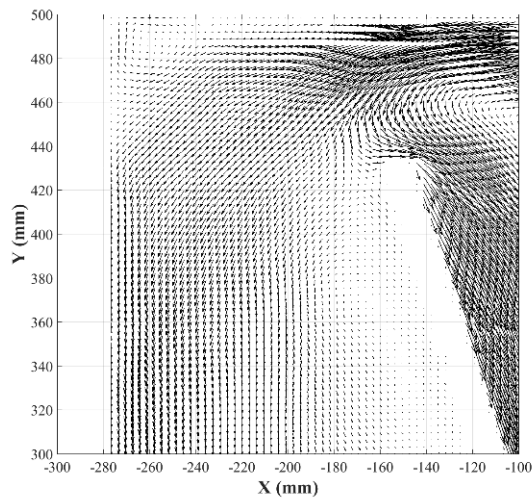
(c) Velocity field 49 L/hr.
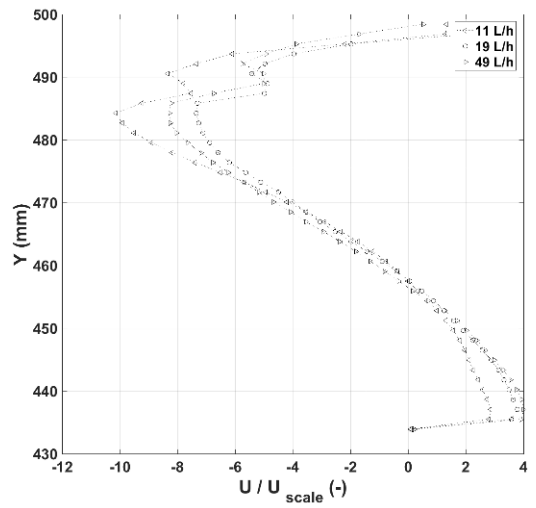
(d) Vertical profile of horizontal and
normalized velocity above
the internal wall

Figure 4.9 Characteristic flow above the internal wall bounding the flocculation zone

Table 4.3 Characteristic data for the flow outside the flocculation zone

Abbreviations	Parameters	Injected flow rate (Q) (L/hr.)		
		11	19	49
Q (m^3/s)	Injected flow rate	3.05×10^{-6}	5.28×10^{-6}	1.3×10^{-5}
Q_{total} (m^3/s/m)	Total flow rate above the wall per width of pilot	8.1×10^{-5}	9×10^{-5}	1.22×10^{-4}
$Q_{outside}$ (m^3/s/m)	Positive flow rate, directed outside the flocculation zone	1.0×10^{-4}	1.34×10^{-4}	3.46×10^{-4}
Q_{inside} (m^3/s/m)	Negative flow rate, directed inside the flocculation zone	-1.9×10^{-5}	-4.22×10^{-5}	-2.25×10^{-4}
U_{total} (m/s)	Total velocity	0.0013	0.0014	0.0019
$U_{outside}$ (m/s)	Positive velocity	0.0025	0.0035	0.0105
U_{inside} (m/s)	Negative velocity	-0.0008	-0.0016	-0.0071
Re	Re	104	112	152
$Q_{total-laminar}$ (m^3/s)	Total flow rate above the wall assuming laminar velocity profile along Z	4.05×10^{-6}	4.5×10^{-6}	6.1×10^{-6}
$Q_{total-laminar} /(Q/2)$	Ratio of total flow rate above the wall and half the injected flow rate	2.6	1.7	0.95

In conclusion, the liquid jet induces a strong circulation loop inside the flocculation zone (vertical divergent). Whatever the flowrate, 30 cm above the nozzle, the angle of the jet development is close to 10°. The presence of the 2 inclined baffles (37°) has clearly an influence on the development of the jet since the circulation patterns are similar for the three flow rates. Characteristic time scales of the circulation have been estimated in Table 4.2. One can now investigate the distributions of velocity gradients.

4.1.3 Viscous Dissipation Rate of Turbulent Kinetic Energy (ε)

The viscous dissipation rate of TKE (Turbulent Kinetic Energy) plays a major role in turbulent flow. Mostly dominated by small scale turbulence, it is a key parameter in the quality and efficiency of flocculation, the one of mixing processes, because it influences a wide range of the flocculation. To understand the effect of injected flow rates on the flow, the viscous dissipation rate of TKE must be estimated. Effectively, the magnitude of viscous dissipation rate of TKE determines the quality and the efficiency of the flow control by the free jet flow within the jet clarifier.

From the instantaneous velocity fields, it was possible to estimate the local viscous dissipation rate of the mean flow kinetic energy (Equation 4.1) and the local viscous dissipation rate of the turbulent kinetic energy (Equation 4.2). These dissipation rates are based on the 2D velocity measurement. Thus, they were estimated following the expressions:

$$
\begin{aligned}
\varepsilon_{mean\,flow} = \nu \left[2 \left(\frac{\partial \bar{U}}{\partial x} \right)^2 + \left(\frac{\partial \bar{U}}{\partial y} \right)^2 + \left(\frac{\partial \bar{V}}{\partial x} \right)^2 + 2 \left(\frac{\partial \bar{V}}{\partial y} \right)^2 \right. \\
\left. + 2 \left(\frac{\partial \bar{W}}{\partial z} \right)^2 + 2 \frac{\partial \bar{U}}{\partial y} \frac{\partial \bar{V}}{\partial x} \right]
\end{aligned}
$$

Equation 4.1

$$
\begin{aligned}
\varepsilon_{turbulent\,flow} = \nu \left[2 \overline{\left(\frac{\partial u'}{\partial x} \right)^2} + \overline{\left(\frac{\partial u'}{\partial y} \right)^2} + \overline{\left(\frac{\partial v'}{\partial x} \right)^2} + 2 \overline{\left(\frac{\partial v'}{\partial y} \right)^2} \right. \\
\left. + 2 \overline{\left(\frac{\partial w'}{\partial z} \right)^2} + 2 \overline{\frac{\partial u'}{\partial y} \frac{\partial v'}{\partial x}} \right]
\end{aligned}
$$

Equation 4.2

In this part, only viscous dissipation of TKE will be reported, the viscous dissipation of mean kinetic energy being negligible.
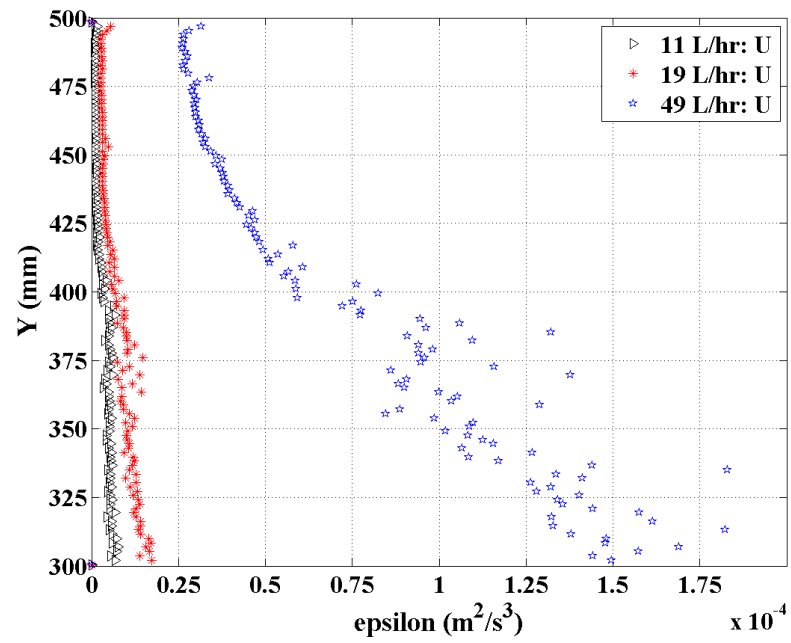
a) Upper part of flocculation zone (field 1)
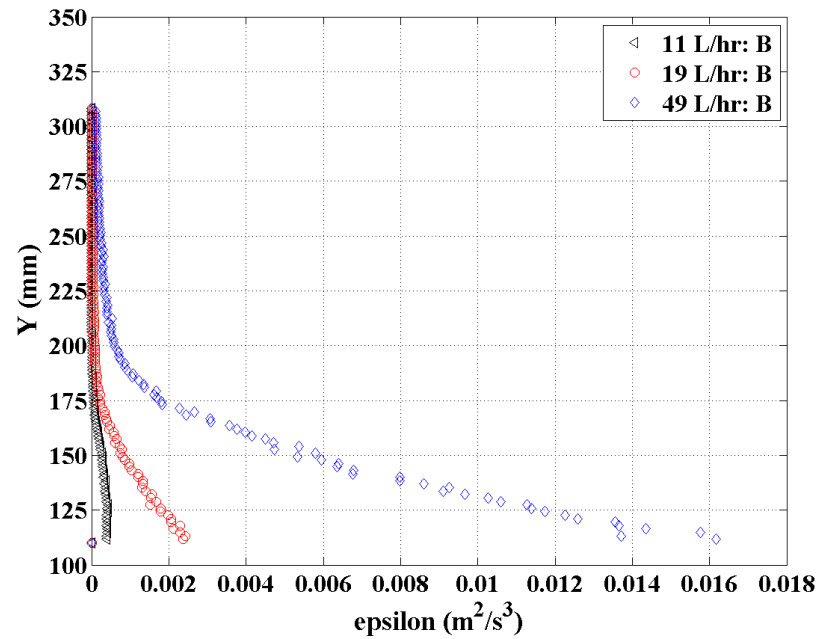
b) Lower part of the flocculation zone (field 2)

Figure 4.10 The dissipation rate estimate for 3 injected flow rates

of (a) field 1 and (b) field 2

Figure 4.10 (a and b) presents the vertical profile of the local viscous dissipation rate of TKE along with the axis of the jet. As expected in jet flow, the viscous dissipation rate of TKE was decreasing along with the jet. Thus, the viscous dissipation rates of TKE were highest close to the injected nozzle.

The local values of the viscous dissipation rate of TKE for Y = 100 mm. and Y = 300 mm. are given in Table 4.4. Two comments: at Y = 300 mm., the viscous dissipation rate of TKE is 100 times lower than the value at Y = 100 mm.; there is thus a huge decrease of dissipation rate (as can be seen on Figure 4.10 (b)). Between Y = 300 mm. and Y = 500 mm. (upper part, Figure 4.10 (a)), the decrease of the dissipation rate of TKE is much smaller; the ratio being between 3 and 4. In addition, in this zone, the local dissipation rate of TKE is close to the global estimation of the dissipation rate of TKE.

Table 4.4 Viscous dissipation rate of TKE of the Q2D jet clarifier

Flow rate (L/hr.)	Global turbulence kinetic energy dissipation rates (m^2/s^3)	The local value of turbulence kinetic energy dissipation rates (m^2/s^3)	
		Y = 100 mm.	Y = 300 mm.
11	4.3×10^{-6}	4.5×10^{-4}	$5\text{-}6 \times 10^{-6}$
19	2.2×10^{-5}	2.5×10^{-3}	1.6×10^{-5}
49	2.0×10^{-4}	2.0×10^{-2}	1.6×10^{-4}

Figure 4.11 shows the horizontal profile of dissipation rate of TKE. The viscous dissipation rate of TKE in the lower part (field 2) is sharp and important near the injection almost null outside the jet, while in the upper part (field 1), the profiles are more spread since the jet width is larger.
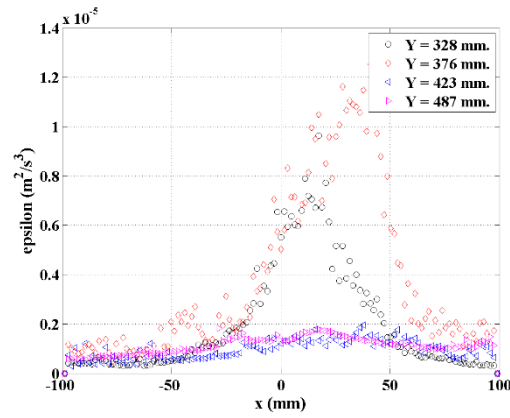
a) Field 1, 11 L/hr.
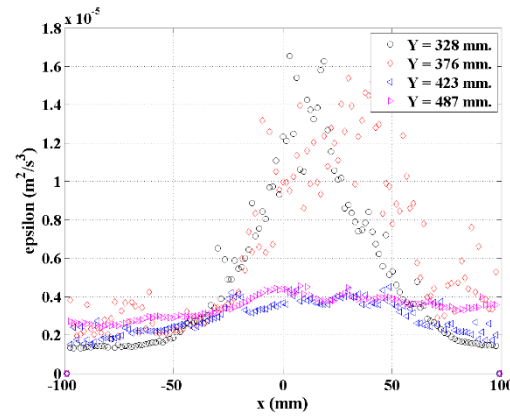
b) Field 1, 19 L/hr.
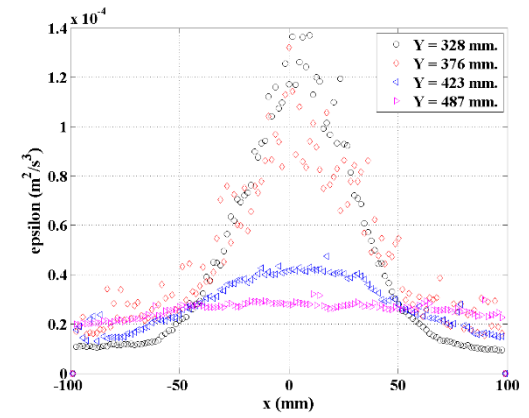
c) Field 1, 49 L/hr.
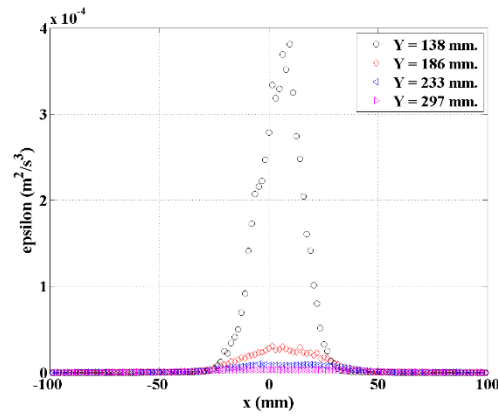
d) Field 2, 11 L/hr.
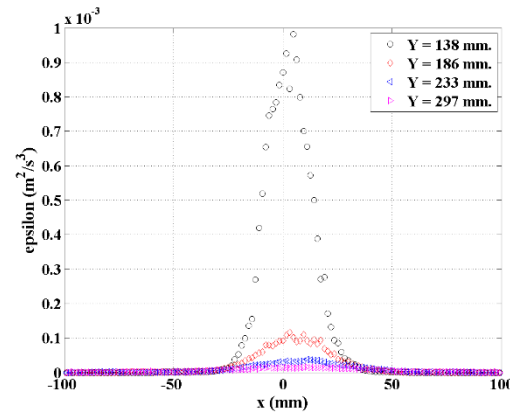
e) Field 2, 19 L/hr.
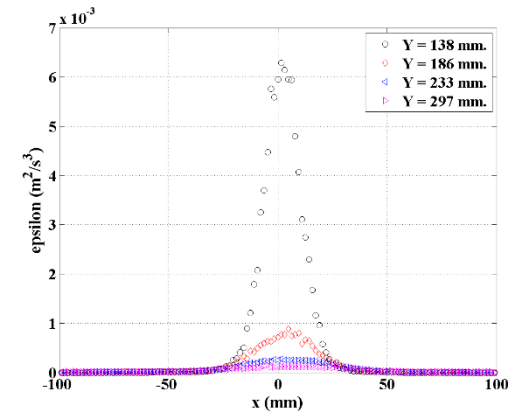
f) Field 2, 49 L/hr.

Figure 4.11 Horizontal profile of turbulence kinetic energy dissipation rate (ε)

It's instructive to compare the horizontal profiles of the dissipation rate of TKE (Figure 4.11) with the horizontal profiles of the mean vertical velocity of the jet flow (Figure 4.5). Clearly, there is no local equilibrium between kinetic energy production (by the gradient of mean velocity). Consequently, the kinetic energy that is dissipated is probably due to its transport by the mean vertical velocity (axial velocity) rather than local production of turbulence kinetic energy (TKE) due to the mean velocity gradients (see 4.1.5).

4.1.4 Kolmogorov Scale (η)

Recall first that many studies have shown that floc size is often close to the Kolmogorov scale. Thus the Kolmogorov scale will be estimated. In addition, the Kolmogorov scale has to be compared to the PIV filter in order to validate its estimation.

Figure 4.12 shows the vertical profiles of the Kolmogorov scale in the lower part (field 2, Figure 4.12 (b)) and in the upper part (field 1, Figure 4.12 (a)) for the 3 injected flow rates (Q = 11, 19, and 49 L/hr.). The Kolmogorov scale increases along with the jet flow (Y-axis) since the dissipation rate decreases. However, as expected, the decrease of the Kolmogorov scale is much smaller than the dissipation rate. Looking at the highest flow rate, 49 L/hr., on Figure 4.12 (b), the Kolmogorov scale range was between 0.1 – 0.3 mm. while the Kolmogorov scale range of 19 L/hr. and 11 L/hr. were 150 μm. – 500 μm. and 200 μm. – 700 μm., respectively. It is apparent that the Kolmogorov scale increased when the flow rate decreased. The Kolmogorov scale (η) depends on turbulence kinetic energy dissipation rate (ε) (see Equation A.11 on Appendix A).
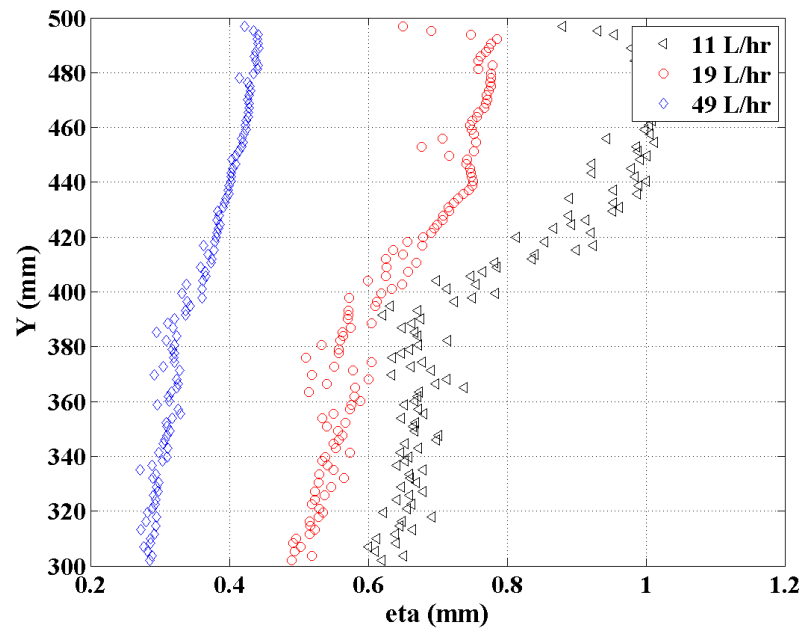
a) Upper part of flocculation zone (field 1)
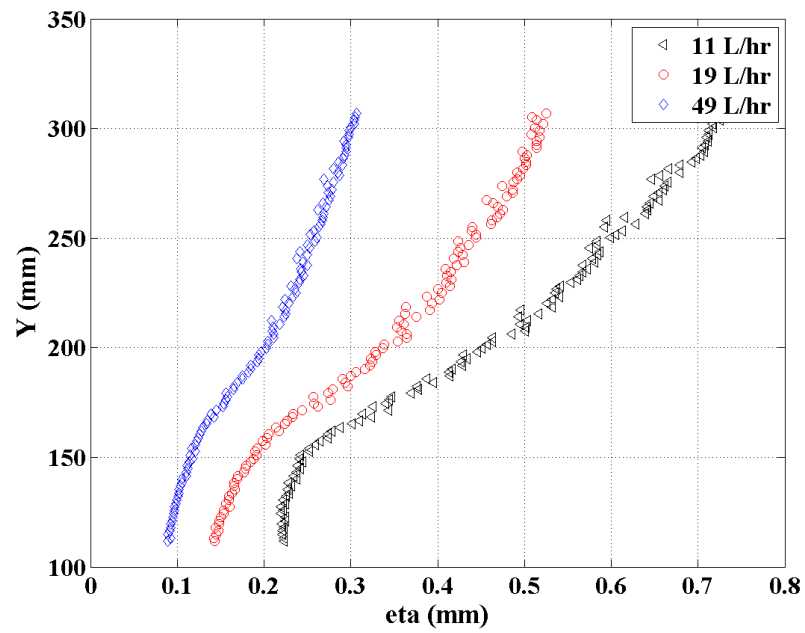
b) Lower part of the flocculation zone (field 2)

Figure 4.12 The vertical profile of Kolmogorov (η)
of 11 L/hr., 19 L/hr., and 49 L/hr. flow rates on a) field 1 and b) field 2

Table 4.5 summarizes the range of η for the 3 flow rates; the value of the global Kolmogorov scale ($<\eta>$) computed from the supplied power by Equation 2.13 (See Table 4.6) and the ratio of PIV filters. Here again, the local Kolmogorov scale in the upper part is close to the global estimation. The comparison to the PIV filter shows value much less than 10, confirming that the estimation of both dissipation rate of TKE and Kolmogorov scale are reliable.

Table 4.5 Kolmogorov scale of the jet flow

Flow rate (L/hr.)	Global Kolmogorov scale (µm)	Kolmogorov scale range (µm)		Ratio of PIV filter	
		Field 1	Field 2	Field 1	Field 2
11	700	700 – 1050	200 – 700	1.5 – 2	2
19	460	500 – 800	150 – 500	2 – 3	3
49	260	300 – 450	100 – 300	3 – 5	6

4.1.5 Velocity gradient (G)

4.1.5.1 Vertical Profiles of Velocity Gradient (G)

After estimation of the local viscous dissipation rate of turbulent kinetic energy, local velocity gradient G is estimated, based on the local dissipation rate of total kinetic energy by the following equation:

$$G = \dot{\gamma} = \sqrt{\frac{1}{2}tr(\overline{S^2})} = \sqrt{\frac{1}{2}tr(\bar{S}^2) + \frac{1}{2}tr(\overline{s'^2})} \qquad \text{Equation 4.3}$$

Where S is the symmetric part of the velocity gradient tensor. Here, $tr(\overline{S^2})$ is an invariant.

Figure 4.13 shows the vertical profiles of the velocity gradient for the 3 flow rates (Q = 11, 19, and 49 L/hr.). As expected, the velocity gradient along the axis of the jet decreases with distance to the nozzle. The ratio between position X = 100 mm. and X = 300 mm. is now 10 (square root of 100 for dissipation rate ratio).
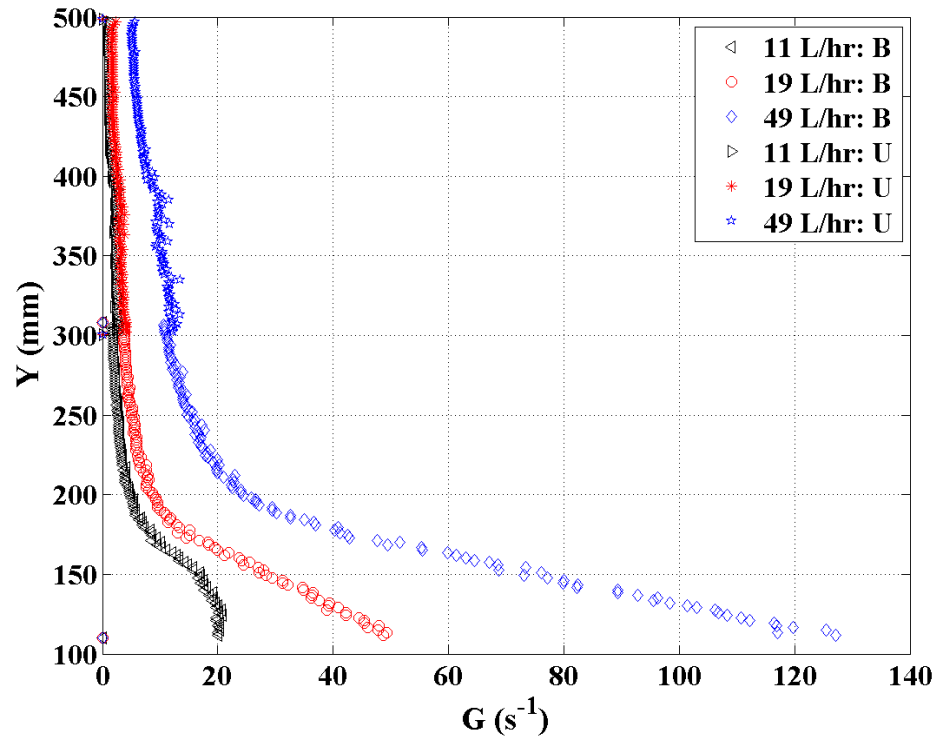
Figure 4.13 The vertical profile of velocity gradient (G)

of 11 L/hr., 19 L/hr., and 49 L/hr. flow rates

The range of the local velocity gradient and the average velocity gradient (average of local values along the horizontal axis) are summarized in Table 4.6 including the global velocity gradient (refer to Table 2.6). Here again, there is consistency between local values obtained by PIV data post-processing and global values presented in Chapter 2. In particular, the horizontal averages of local velocity gradients in the lower and upper parts of the flocculation zone surround the global values.

Table 4.6 Local and global velocity gradient of three flow rates

Flow rate (L/hr.)	Global velocity gradient (s^{-1})	Velocity gradient range (s^{-1})		Average velocity gradient $(G(< \varepsilon_{\text{Floc\_zone}} >)) \; (s^{-1})$	
		Field 1	Field 2	Field 1	Field 2
11	2.1	1 – 3	2 – 20	1.3	4.1
19	4.7	1.5 – 4.5	5 – 50	2	7.1
49	14.3	5 – 15	10 – 130	6	17.2

The vertical profiles of velocity gradient (G) divided by the inlet velocity ($U_{\text{injection}}$) are shown in Figure 4.14. Interestingly, the three profiles are superimposed, which confirm that the velocity gradient of the Q2D jet clarifier depends on the inlet velocity.
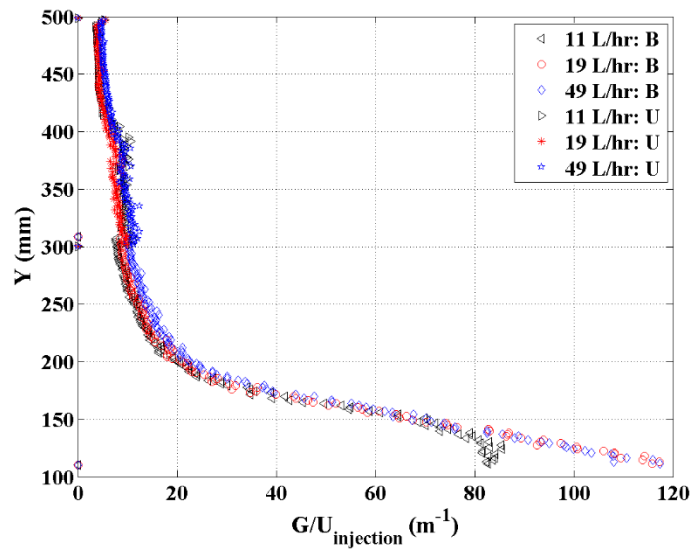
Figure 4.14 The vertical profile of velocity gradient (G) divided by the inlet velocity ($U_{\text{injection}}$) of 11 L/hr., 19 L/hr., and 49 L/hr. flow rates

4.1.5.2 Horizontal Profiles of Velocity Gradient (G)

Horizontal profiles of local velocity gradients are plotted on Figure 4.15. Their analysis is close to the comments given on the horizontal profiles of the dissipation rate of TKE.
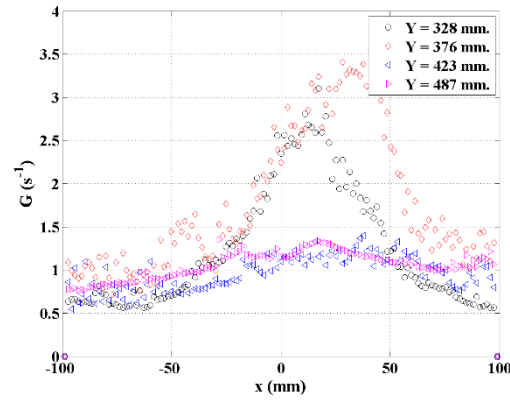
a) Field 1, 11 L/hr.
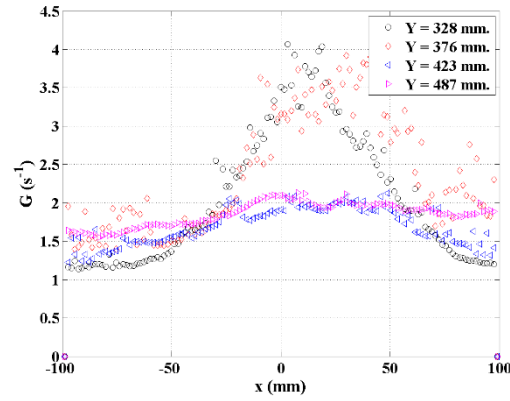
b) Field 1, 19 L/hr.
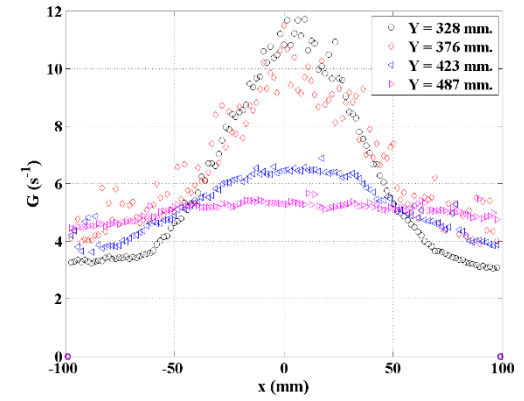
c) Field 1, 49 L/hr.
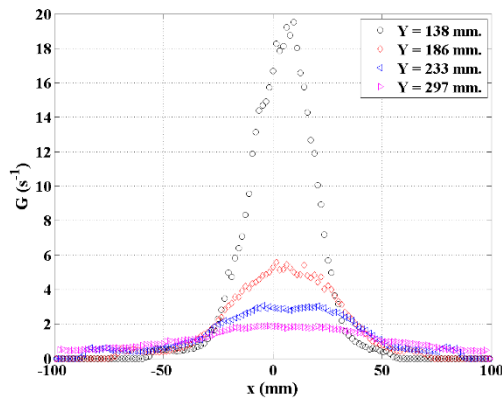
d) Field 2, 11 L/hr.
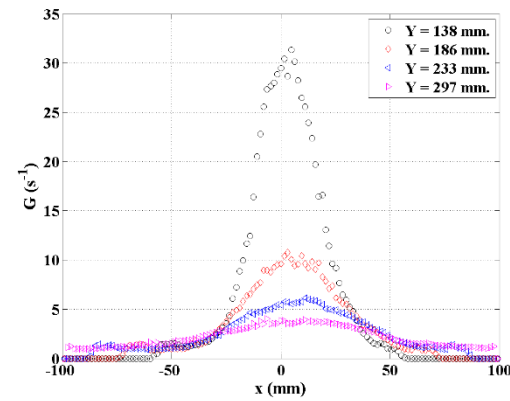
e) Field 2, 19 L/hr.
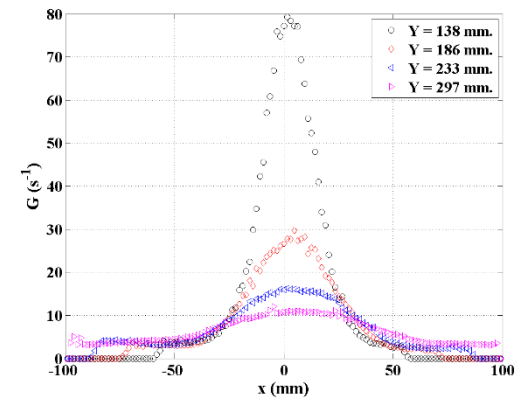
f) Field 2, 49 L/hr.

Figure 4.15 Horizontal profile of velocity gradient (G)

4.1.6 Discussion on Hydrodynamics

In the previous sections, both local and global (time and space averaged) velocity gradients were addressed. On Figure 4.16, the vertical profiles of four characteristic variables are plotted: the local mean vertical velocity, the viscous dissipation rate of kinetic energy, the Kolmogorov scale and the local velocity gradient (shear rate).

Figure 4.16 (a) corresponds to the vertical profile of mean velocity along the axis (X = 0), normalised by the inlet velocity. Clearly, the profiles are identical, except in the lower zone, closer to the injection nozzle, where the circulation around the internal baffle should modify the total flow rate that enters the flocculation zone. This plot confirms that the global hydrodynamics induced by the jet is similar for the three flow rates and the mean vertical velocity is simply proportional to the injected flow rate.

Figure 4.16 (b) presents the vertical profiles of the horizontal averaged (along the width of the divergent) value of the viscous dissipation rate of total (mean flow + turbulent flow) kinetic energy.

Figure 4.16 (c) presents the vertical profile of the horizontal averaged (along the width of the divergent) value of the Kolmogorov scale, based on the local viscous dissipation rate of the turbulent kinetic energy.

Figure 4.16 (d) presents the vertical profile of the horizontal average of the local velocity gradient <G>, multiplied by the depth of the pilot (h = 100 mm.) and divided by the inlet velocity. The choice of inlet velocity as velocity scale is straightforward, but the choice of pilot thickness as length scale is arbitrary. It leads to non-dimensional velocity gradients close to unity. Distinctly, the three curves of such normalised velocity gradients are identical, indicating that the velocity gradient is proportional to the inlet velocity.
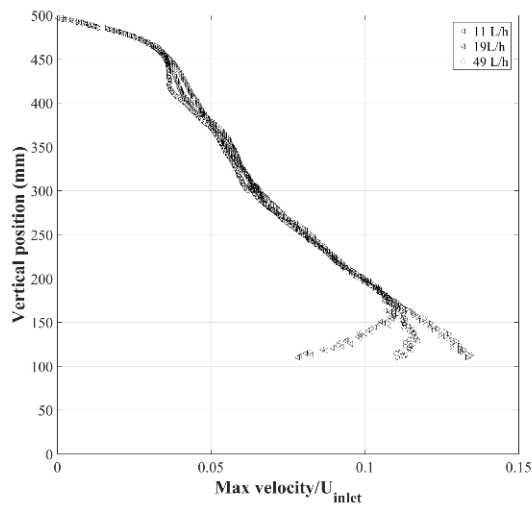
a) normalized mean velocity components
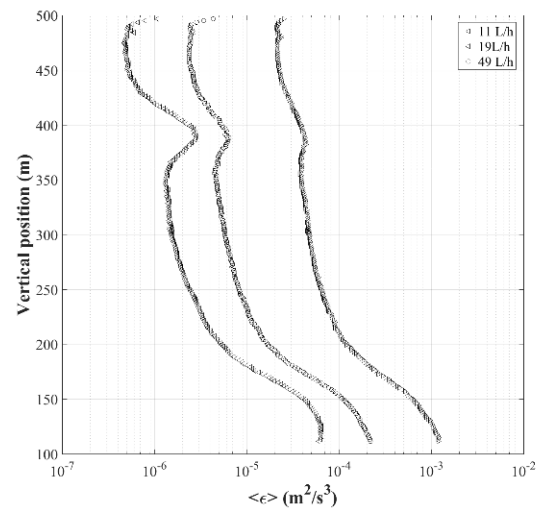
b) horizontal averaged viscous dissipation rates of mean and turbulent kinetic energy
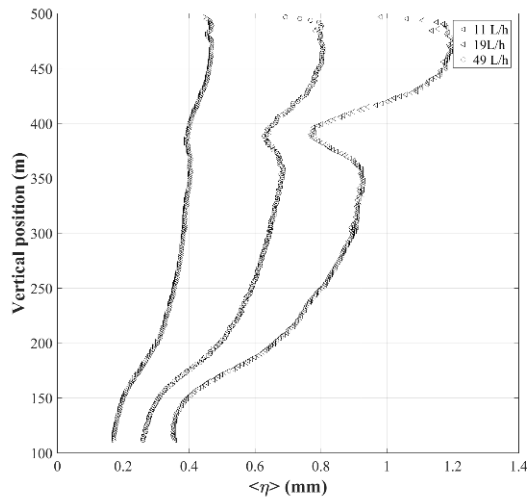
c) horizontal averaged Kolmogorov scale
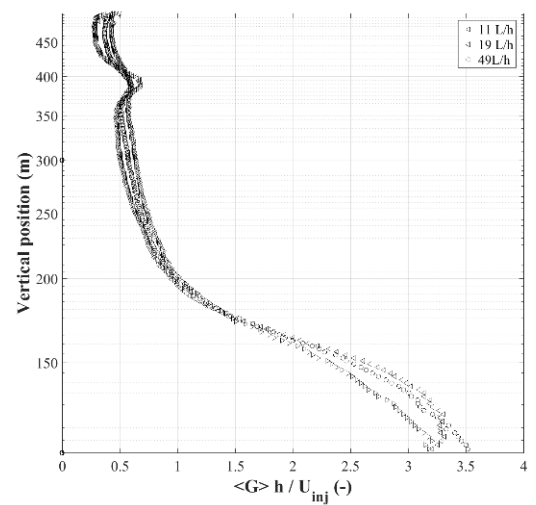
d) normalised total velocity gradients

Figure 4.16 Vertical profiles of a) mean velocity components along the jet axis (X = 0 mm), b) viscous dissipation rates of mean and turbulent kinetic energy, c) and d) mean flow and total turbulent gradients for the three flow rates (< 11 L/h, o 19 L/H, > 49 L/hr.)

After estimation of the local viscous dissipation rate of turbulent kinetic energy, local velocity gradient G was estimated, based on the local dissipation rate of total kinetic energy. These local values of viscous dissipation have been averaged in space along the width of the divergent; afterwards, they have been averaged along Y-axis (vertical average); thus, the horizontal averaged of the velocity gradients were estimated (Figure 4.16 (d)), and the global velocity gradients in the flocculation zone (Table 4.7). A first warning lies in the fact that the global value is defined as: $G(\langle\varepsilon\rangle) = \sqrt{\frac{\langle\varepsilon\rangle}{\nu}} \neq \langle G \rangle = \langle \sqrt{\frac{\varepsilon}{\nu}} \rangle$.

The different results are given in Table 4.7. The flow rates, inlet velocities and residence times in the flocculation zone are recalled. Then the viscous dissipation rate of total kinetic energy is averaged in the plane of measurement in both horizontal and vertical directions. It can be noticed that the viscous dissipation rate is 10 times higher close to the jet inlet thus the velocity gradients are stronger in this zone. The associated global velocity gradients are estimated and are $\sqrt{10}$ times greater in the bottom field and are proportional to the flow rate. Then, the velocity gradient averaged over the whole flocculation zone (once again in the vertical plane of PIV measurement) is calculated. $G(< \varepsilon_{Floc\_zone} >)$ ranges between 3 and 13 s^{-1}, whereas the global values estimated initially (Table 2.6) were in the range 2-14 s^{-1}. If we multiply these velocity gradients averaged over the whole flocculation zone by the residence time in the flocculation zone $G(< \varepsilon_c >) \times t_{RE}$, we obtain an almost constant value close to 7000 for the three flow rates.

Table 4.7 Estimation of global velocity gradients in flocculation zone, based on PIV data processing

Abbreviations	Parameters	Flow rate (Q) (L/hr.)		
		11	19	49
U (m/s)	Injection velocity	0.24	0.42	1.08
t_{RF} (hr.)	Residence time in flocculation zone	0.636	0.368	0.143
$< \varepsilon_{Field\_1} >$ (m^2/s^3)	Average ε in field 1 zone	1.8×10^{-6}	4.0×10^{-6}	3.6×10^{-5}
$G(< \varepsilon_{Field\_1}>)$ (s^{-1})	Velocity gradient in field 1 zone	1.34	2	6
$< \varepsilon_{Field\_2}>$ (m^2/s^3)	Average ε in field 2 zone	1.7×10^{-5}	5×10^{-5}	3×10^{-4}
$G(< \varepsilon_{Field\_2}>)$ (s^{-1})	Velocity gradient in field 2 zone	4.1	7.1	17.2
$< \varepsilon_{Floc\_zone}>$ (m^2/s^3)	Average ε in flocculation zone	9.3×10^{-6}	2.7×10^{-5}	1.7×10^{-4}
$G(< \varepsilon_{Floc\_zone} >)$ (s^{-1})	Velocity gradient in flocculation zone	3.06	5.2	12.9
$G(< \varepsilon_c>) \times t_{RE}$ (-)	First non-dimensional velocity gradient	7010	6890	6640
$G(< \varepsilon_c>) / (U/hr.)$	Second non-dimensional velocity gradient	1.28	1.24	1.19

As shown in the last lines of Table 4.7, two non-dimensional velocity gradients are defined: (1) global G (square root of space average dissipation divided by the viscosity) times flocculation zone residence time or (2) global G (square root of space average dissipation divided by the viscosity) times (depth/U injection); whatever the definition, the non-dimensional global velocity gradient give constant values for the different flow rates. Since the velocity gradients in the flocculation zone evolve always more or less linearly

with the inlet flow, as the residence time is inversely proportional to the flow rate, the Camp and Stein criteria *Gt* parameter recommended to achieve efficient flocculation will be almost constant.

Finally, the results on velocity gradients are summarized in Table 4.8 for the whole jet clarifier. Initially, global estimations of velocity gradients were obtained from global analysis where the total dissipation rate is calculated from a balance with the supplied power at the injection. In Table 4.8, they are compared to the PIV measured velocity gradients, averaged over the 4 PIV planes and derived from the local estimation of the shear rate (in terms of the local viscous dissipation rate of kinetic energy, given by the sum of Equation 4.1 and Equation 4.2). On the whole jet tank again, the global velocity gradient increases linearly with the jet flow rate whereas the residence time decreases linearly. Consequently, the product *Gt* remains constant close to 30,000 for the PIV fields whereas it was close to 7,000 for the first two fields near in the flocculation zone. At the same time, the residence time increased 6 times (the ratio of the total volume divided by the flocculation volume), which means that the average velocity gradient decreases rapidly around 60% between the two first fields and the two followings (comparison between Table 4.7 and Table 4.8).

Table 4.8 Values of velocity gradients in the whole jet clarifier

Parameters	Injected flow rate (L/hr.)		
	11	19	49
$\langle G \rangle$ (s^{-1})	2.1	4.7	14.3
<G> PIV planes (s^{-1})	2.18	3.74	9.4
Residence time t_{res} (hr.)	3.82	2.21	0.86
$\langle G \rangle$ global $\times$ t_{res}	28,500	37,500	44,150
<G> PIV plane $\times$ t_{res}	29,980	29,760	29,100

This is a very interesting result that will be exploited to explain the efficiency of such a jet clarifier in terms of flocculation. Recall that during the residence time in the flocculation zone, there is a loop of circulation with a circulation time 10 times smaller than the flocculation residence time. The flocculation zone is thus a mixing zone very efficient to perform floc aggregation, followed by a clarification zone where the velocity gradient decrease progressively and the residence time increase linearly with the velocity reduction due to the geometrical enlargement.

4.1.7 Summary

In order to understand the good efficiency of a jet clarifier, a hydrodynamic study was performed. To use the PIV technique for local analysis, a quasi-bidimensional (Q2D) pilot was designed. Three flow rates were investigated which correspond to residence time from 1 hr. to 4 hr. Results concerning the hydrodynamics of the flocculation zone reveal that the velocity fields exhibit a large circulation loop (Figure 4.2). Circulation flow rates are estimated as well as circulation time that is 10 times larger at least than the residence time in this zone. The characteristic shape of the jet is also investigated in terms of the vertical distribution of its width. Then, the outflow is analysed, and the outward flow rate is shown to be close to the inlet flow rate. These features are similar for the three flow rates. The plot of the vertical distributions of the jet plume width (Figure 4.6 (b)), the vertical profiles of vertical velocity divided by the inlet velocity are also superimposed (Figure 4.16 (a)), confirming that the velocity field in the flocculation zone only depends on the inlet velocity. The flow structures (circulation) are similar, and the amplitude of the velocities are proportional to the inlet (jet) velocity. During the residence time in the flocculation zone, there is a loop of circulation with a circulation time 10 times smaller than the residence time. The mixing in the flocculation zone is thus very efficient.

In the discussion, both local and global (time and space averaged) velocity gradients were addressed. First local viscous dissipation rates of turbulent kinetic energy were derived from PIV data; thus, the local velocity gradients (G) were estimated. Then, these local values of dissipation rate have been averaged in space along the width of the

divergent; afterwards, they have been averaged along Y-axis (vertical average); thus, the horizontal average of velocity gradients G (horizontal average, Figure 4.16 (d)) and their global averages were estimated (Table 4.7), in order to get global velocity gradients. The vertical profiles of horizontal average velocity gradients normalised by the inlet velocity are superimposed. Finally, the velocity gradients averaged over the whole flocculation zone were calculated. They range between 3 and 13 s^{-1} (Table 4.7), whereas the global values estimated initially (Table 2.6) were in the range 2-14 s^{-1}. Increasing the inlet jet flow rate, the global velocity gradients increase linearly with the jet flow rate whereas the residence time decreases linearly. Consequently, the global product *Gt* remains constant in this region where 10 loops are followed during the flocculation process. This very interesting result will be exploited to explain the efficiency of such a jet clarifier in terms of flocculation.

4.2 Analysis of Aggregates Properties in the Flocculation Zone

To understand flocculation in the jet clarifier, which is a free jet flow and complex system due to a combination of flocculation and settling process in a single unit, the relation between the aggregate size distribution and the hydrodynamics in the flocculation zone of the jet clarifier, is examined. The methodology of the experiments have been presented in the topic of 2.2.2.2 and is recalled briefly as follows: the bentonite suspension is prepared and coagulated in a tank. At the same time, the jet clarifier is filled with clear water. The experiences begin with the injection of the coagulated bentonite suspension in the jet clarifier full of tap water at rest and are continued until the steady state is reached. The number of flocs, the mean floc size diameter, and floc size distribution were monitored with shadowgraphy at two positions along the jet. Position 1 is situated 15 cm. above the injection nozzle, and Position 2 is located 41.5 cm. above the nozzle near the free surface as shown in Figure 2.14. The relation between the floc properties (number, mean diameter, size distribution) and the liquid flow inside the flocculation zone are analyzed in detail. Finally, the connection between the floc size distributions and the Camp Number ($G \cdot t_{cont}$) is discussed.

4.2.1 Number of Flocs and Mean Diameter

The time evolution of the number of flocs in Position 1 that is close to the nozzle (see Figure 2.14) is presented in Figure 4.17 (a). Each point corresponds to a set of 1000 images that were acquired in 200 s.
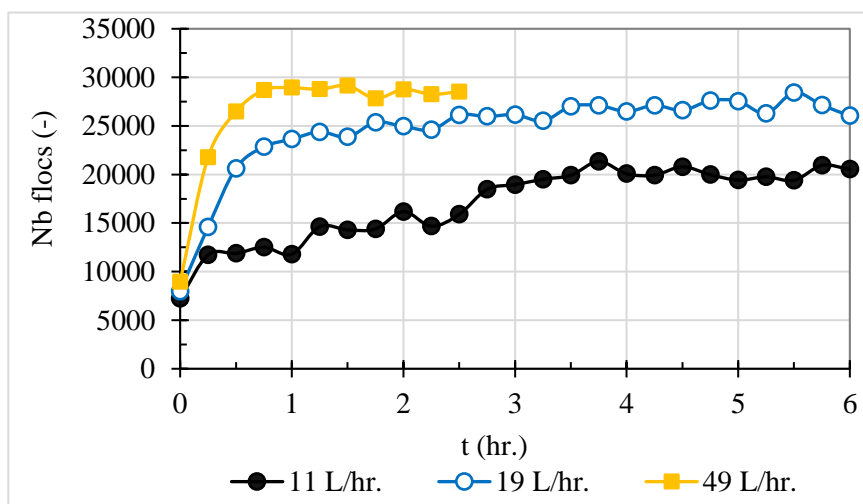
a)
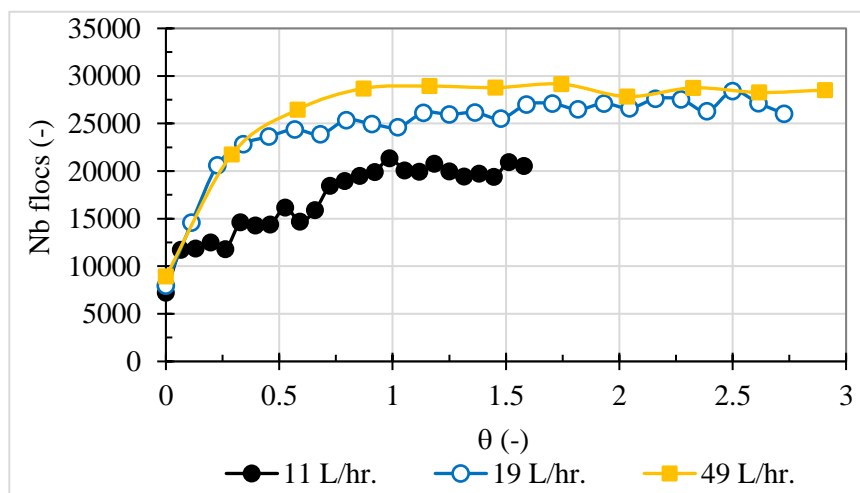
b)

Figure 4.17 Time evolutions of the number of flocs for each flow rate in Position 1

As the Q2D jet clarifier tank only contained clear tap water at rest at the beginning of the experiments and as the concentration of the inlet suspension was the same for all the experiments, the total number of flocs passing through Position 1 was thus directly proportional to the injected flow rate (Q). That is why the data at t = 0 s were not superimposed. As time goes on, the number of flocs increased. This increase is all the more important as the flow rate is high. The time required to reach a steady state depends on the flow rate as can be seen in Figure 4.17 (a). For the low flow rate, 11 L/hr., the number of flocs passing through Position 1 is stable when time (t) is almost equal to 4 hours. For the medium flow rate, 19 L/hr., it needs about 2 hours to stabilize whereas for the highest flow rate, 49 L/hr., the steady state seems to be reached 1 hour after the beginning of the experiment. Thus, it could be deduced that time needed to reach the steady state is related to the flow rate. The Figure 4.17 (b) has thus been plotted versus a non-dimensional time (θ) defined as the ratio of t and the theoretical residence time ($\tau = \frac{Volume}{Flow\ rate}$). Whatever the injected flow rate, the number of flocs was stable once $t/\tau = 1$ suggesting that τ is the characteristic time scale for the dynamics of the number of aggregates.

Looking at the time evolution of the mean diameter (D_{mean}) Figure 4.18 (a), it can be seen that the steady state was also reached for values of t close to those of τ. Here again, as pictured in Figure 4.18 (d), the global residence time τ seems to be the correct characteristic time. Conversely to the number of flocs, the mean diameter of the flocs does not seem to be particularly sensitive to injected flow rate (Q), as whatever the flow rate, the mean diameter stabilizes at steady state around 80 – 100 µm.
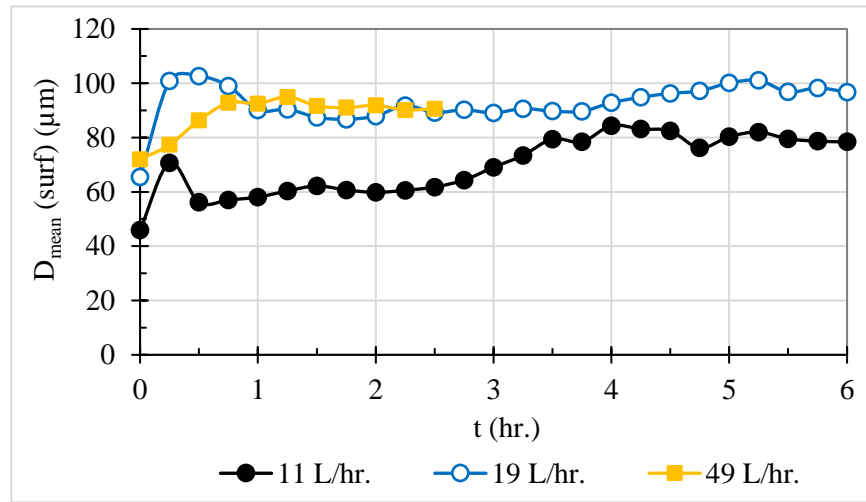
a)
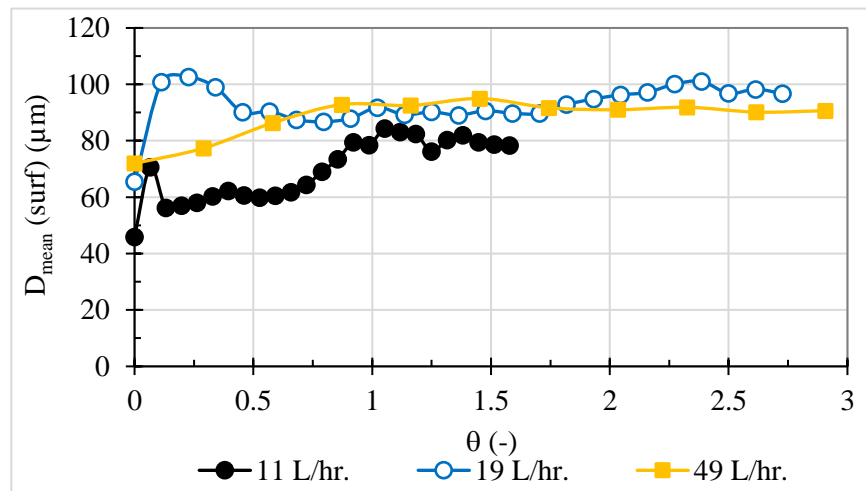
b)

Figure 4.18 D_{mean} of flocs for each flow rate in Position 1

Regarding to Position 2, the dynamics of the number of flocs and the evolution of the mean diameter are plotted on Figure 4.19 (a) and Figure 4.19 (b), respectively versus dimensional time and non-dimensional time. It can be noticed that the number of flocs as the mean diameter were roughly the same at steady state whatever flow rate. At the same time, the number of flocs in Position 2 was higher than those in Position 1.
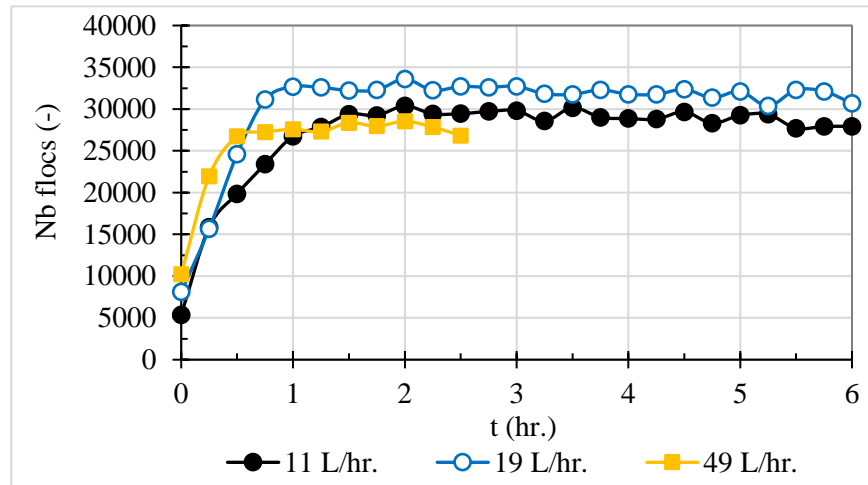
a)
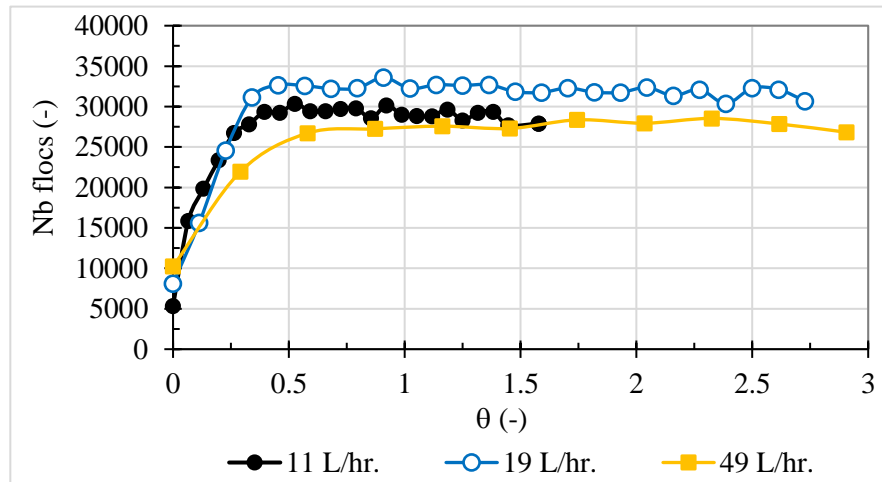
b)

Figure 4.19 Time evolutions of the number of flocs for each flow rate in Position 2

For the low flow rate, 11 L/hr., the number of flocs passing through Position 1 is stable when t is almost equal to 2 hours. For the medium flow rate, 19 L/hr., it needs about 1 hour to stabilize whereas for the highest flow rate, 49 L/hr., the steady state seems to be reached 1 hour from the experiment started. Thus, it could be deduced that time needed to reach the steady state is related to the flow rate similarly to what has been seen for the Position 1. It could be seen that the number of flocs is stable when $\theta = 1$.

The time evolution of the mean diameter (D_{mean}) in Position 2 over time and the non-dimensional time are shown respectively on (Figure 4.20 (a)) and (Figure 4.20 (b)). Again, the time required to reach a steady state in Position 2 also depends on the flow rate as can be seen in Figure 4.20 (a). At this position, it was clear that the number of flocs and the mean diameter of the flocs (D_{mean}) were not particularly sensitive to injected flow rate (Q), as whatever is the flow rate, the mean diameter stabilizes around $80 - 100\ \mu m$.
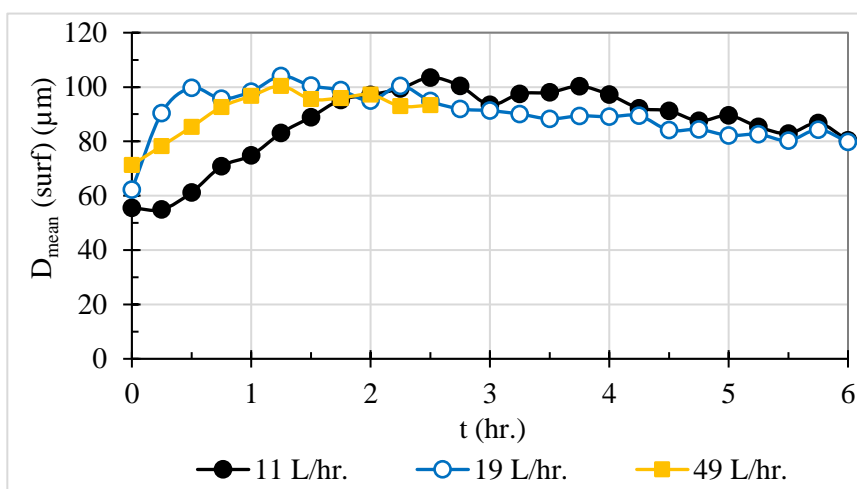
a)
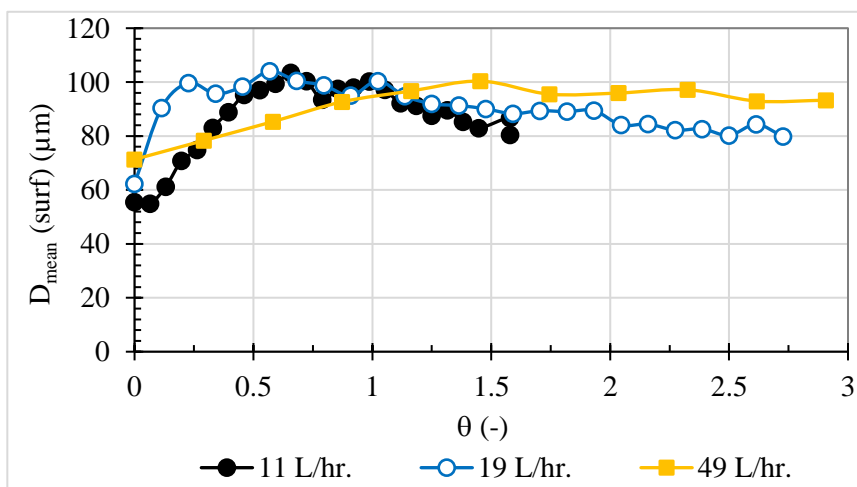
b)

Figure 4.20 D_{mean} of flocs for each flow rate in Position 2

The mean diameter (D_{mean}) in Position 2 is then compared to those in Position 1, as shown in Figure 4.21. For all flow rates, there is an increase in the mean diameter before reaching the steady state. Once the steady state has been reached, for the lowest and highest flow rates the D_{mean} in Position 2 is slightly higher than in Position 1. Whatever the flow rate, the D_{mean} is rather close to 80-100 µm.

The fact that the average diameter does not seem to be particularly dependent on flow rate is a rather unexpected result. Indeed, many studies in the literature mention that there is a direct relationship between aggregate size and flow rate. In order to refine this result, the following paragraph presents the size distributions of the aggregates allowing a better understanding of the floc population as a whole.
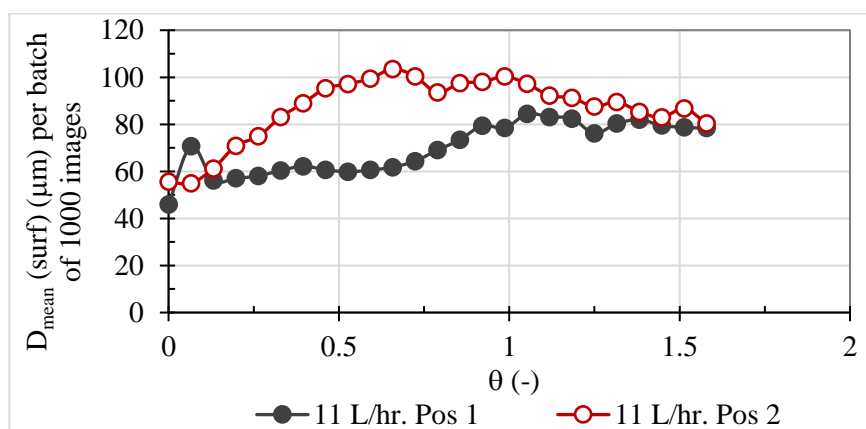
a) 11 L/hr.
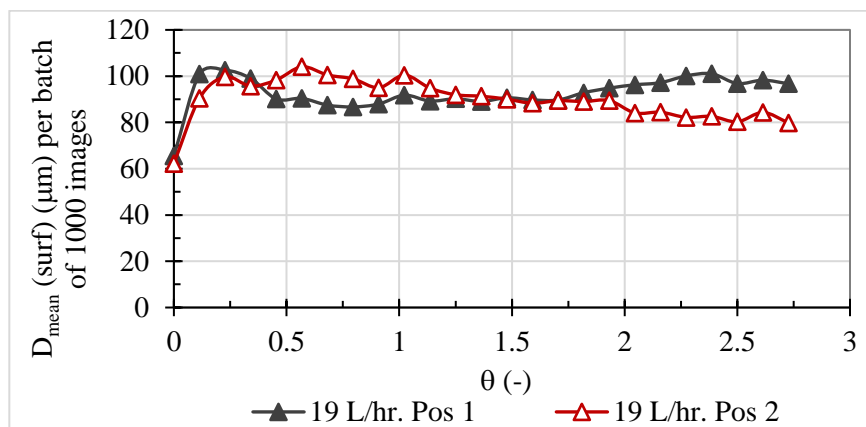
b) 19 L/hr.
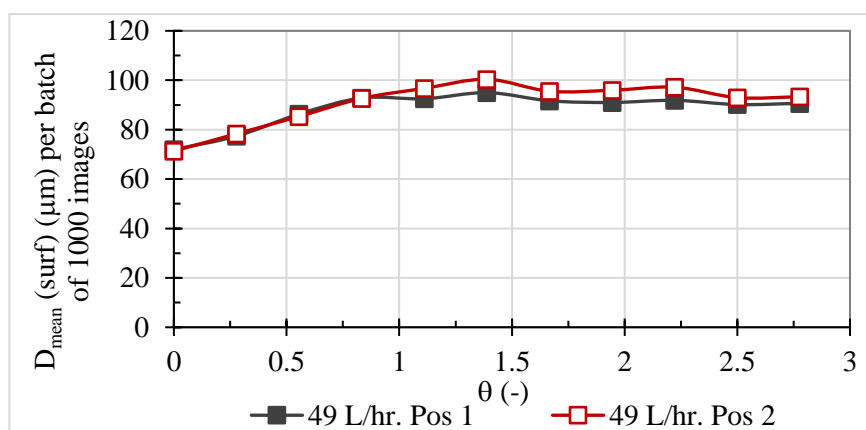
c) 49 L/hr.

Figure 4.21 Comparison of D_{mean} Position 1 and Position 2 along time of (a) 11 L/hr., (b) 19 L/hr., and (c) 49 L/hr. flow rate

4.2.2 Floc Size Distributions in Position 1

The floc size distributions weighted by surface are presented in Figure 4.22 at four different instants t = 70 s, t = 200 s, t = 1020 s, and t = τ. The transient size distributions (t = 70 s, t = 200 s, t = 1020 s) come from the data analysis of 50 images corresponding to at least 500 flocs, whereas those at steady state (t = τ) have been calculated with a set of 1000 images.

For the low flow rate (Figure 4.22 (a)), it can be noticed that the distribution at t = 70 s is quite spread. The mode is situated around 40 µm and the peak around 15 µm can certainly be attributed to primary particles that have not been yet aggregated (cf. Figure 2.5). As time goes on, the distribution tightens, and its mode shifts progressively from 50 µm. at 200 s toward 100 µm when t = τ. At steady state, the maximum floc size is around 250 µm.

For the medium flow rate in Figure 4.22 (b), the distributions are narrower than those for low flow rate, meaning that there are less small flocs (d < 40 µm). It also can be underlined that at t = 1020 s, the distribution is quite close to those at steady state for which the mode of the distribution is 100 µm. In the case of the highest flow rate (in Figure 4.22 (c)), the dynamics is even faster as the mode of the distribution is close to 80 µm only 70 s after the beginning of the experiment.
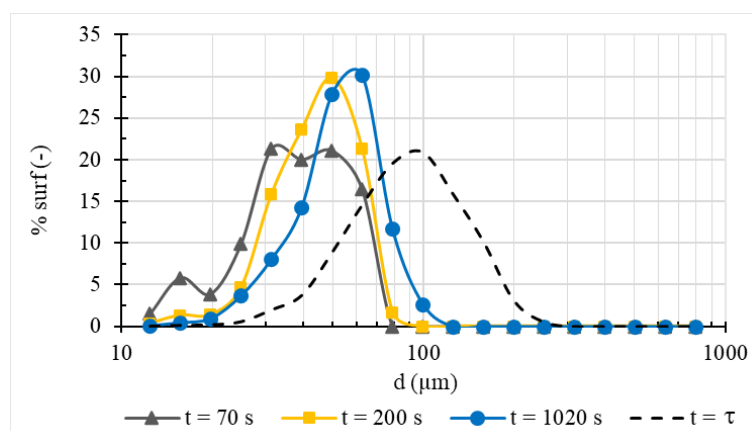
a) 11 L/hr.
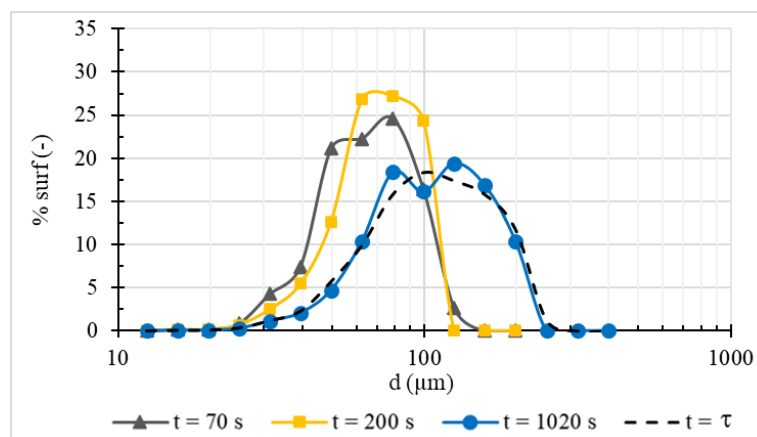
b) 19 L/hr.
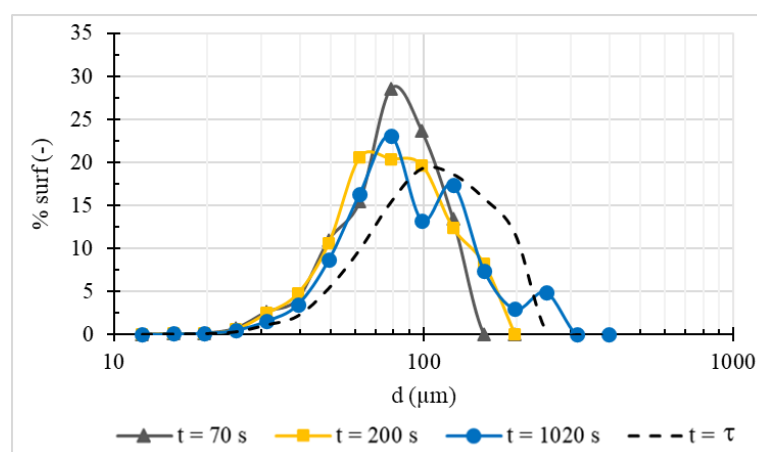
c) 49 L/hr.

Figure 4.22 Time evolution of size distributions in Position 1 of (a) 11 L/hr.,

(b) 19 L/hr., and (c) 49 L/hr. flow rate

Another way to analyze these data is to compare the distributions at a given time for the different flows. This is what is proposed on the Figure 4.23.

For t = 70 s (Figure 4.23 (a)), the distributions are shifted more towards the larger sizes as the flow rate increases. At intermediates times (t = 200 s and 1020 s - Figure 4.23 (b) and (c)), size distributions for the medium and high flow rates are quite close while those of the low flowrate slightly move towards larger sizes. At steady state (Figure 4.23 (d)), whatever the flow rate, the size distributions are almost superimposed.

a) t = 70 s

b) t = 200 s

c) t = 1020 s

d) t = τ
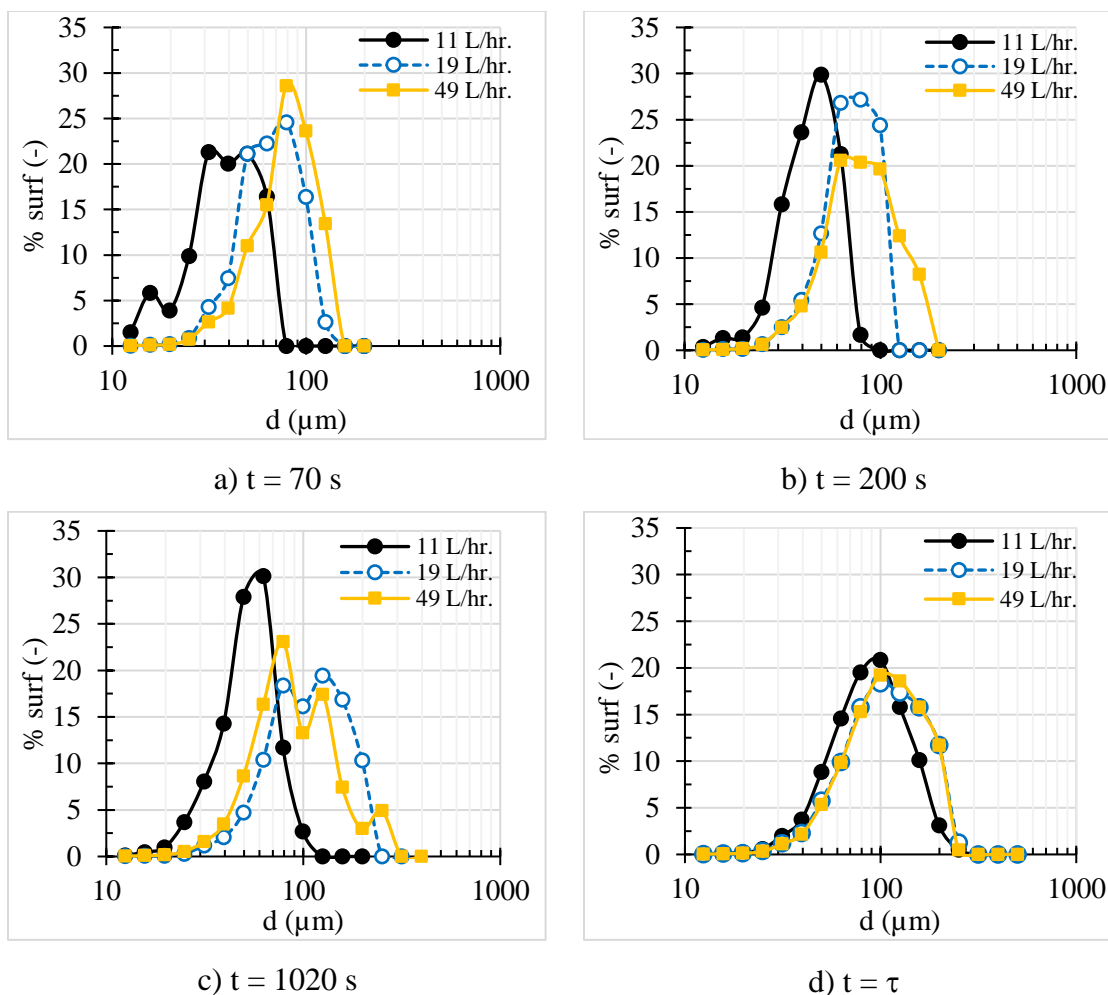
Figure 4.23 Size distribution in Position 1 at (a) 70 s (b) 200 s (c) 1020 s, and (d) τ for each flow rate

The dynamics of the evolution of size distributions thus appear to be closely related to flow rate. In order to better understand these dynamics, it is necessary to relate them to the circulation times (t_c) that have been determined experimentally and are presented in the Table 4.2.

For the lowest flow rate, $t_c = 153$ s, thus when t = 70 s, the aggregates have not yet had time to follow one circulation loop in its entirety, whereas, for the highest flow, they have almost completed 2 circulation loops ($t_c = 40$ s). The size distribution for the highest flow is clearly shifted towards the larger sizes compared to the case of the smaller flow rates, this indicates that aggregation phenomena have therefore taken place within these circulation loops. These aggregation phenomena are therefore all the faster as the flow is high.

The next section will be devoted to the description of the results in terms of flocs size distributions in Position 2.

4.2.3 Floc Size Distributions in Position 2

The dynamics of flocculation in Position 2 (Figure 4.24 and Figure 4.25) is presented as it has been done for Position 1. For the lowest flow rate (Figure 4.24 (a)), as time increases, the size of flocs increases as the mode of the distributions is about 50 µm when t = 70 s, 60 µm. when t = 200 s. At t = 1020 s, it can be seen that the mode is still near 60 µm, but the distribution is bi-modal with a population of larger aggregates whose size is about 100 µm. At steady state, the size distribution is rather spread, the most probable floc size being around 80 µm and the maximum floc size is 250 µm.

For the medium and high flow rates (Figure 4.24 (b) and (c)), the dynamics is even faster. Indeed, as early as 70 seconds the distributions are already shifted towards the large sizes (the modes are beyond 70 µm), and approach more rapidly those of the steady state.
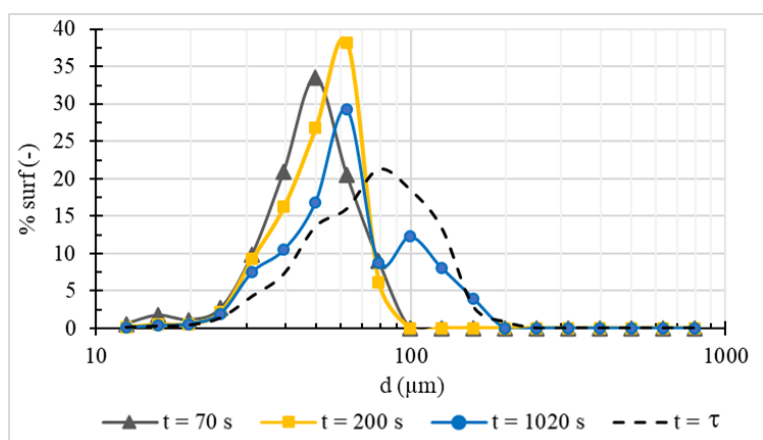
a) 11 L/hr.
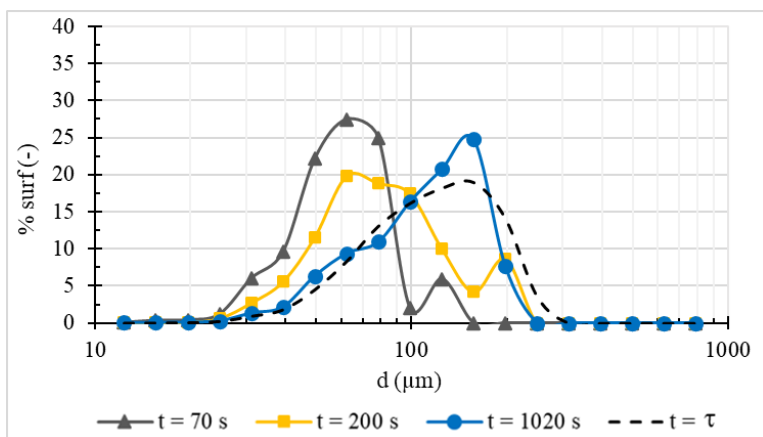
b) 19 L/hr.
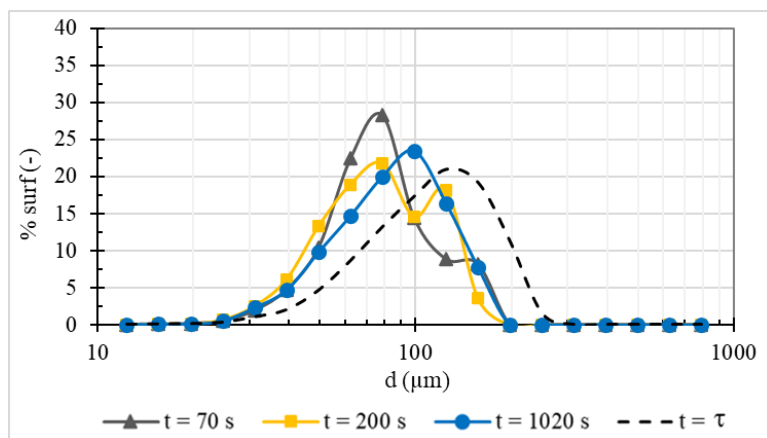
c) 49 L/hr.

Figure 4.24 Time evolution of size distributions in Position 2 of (a) 11 L/hr.,

(b) 19 L/hr., and (c) 49 L/hr. flow rate

Looking at the Figure 4.25 (a), for the medium flow rate and the high flow rate when t = 70 s, there are fewer small flocs than for the low flow rate. The size distributions for the medium and high flowrates are quite close whatever the time. At steady state, the mode of the distributions is about 120 µm and the maximal floc size is about 250 µm.

a) t = 70 s

b) t = 200 s

c) t = 1020 s

d) t = τ
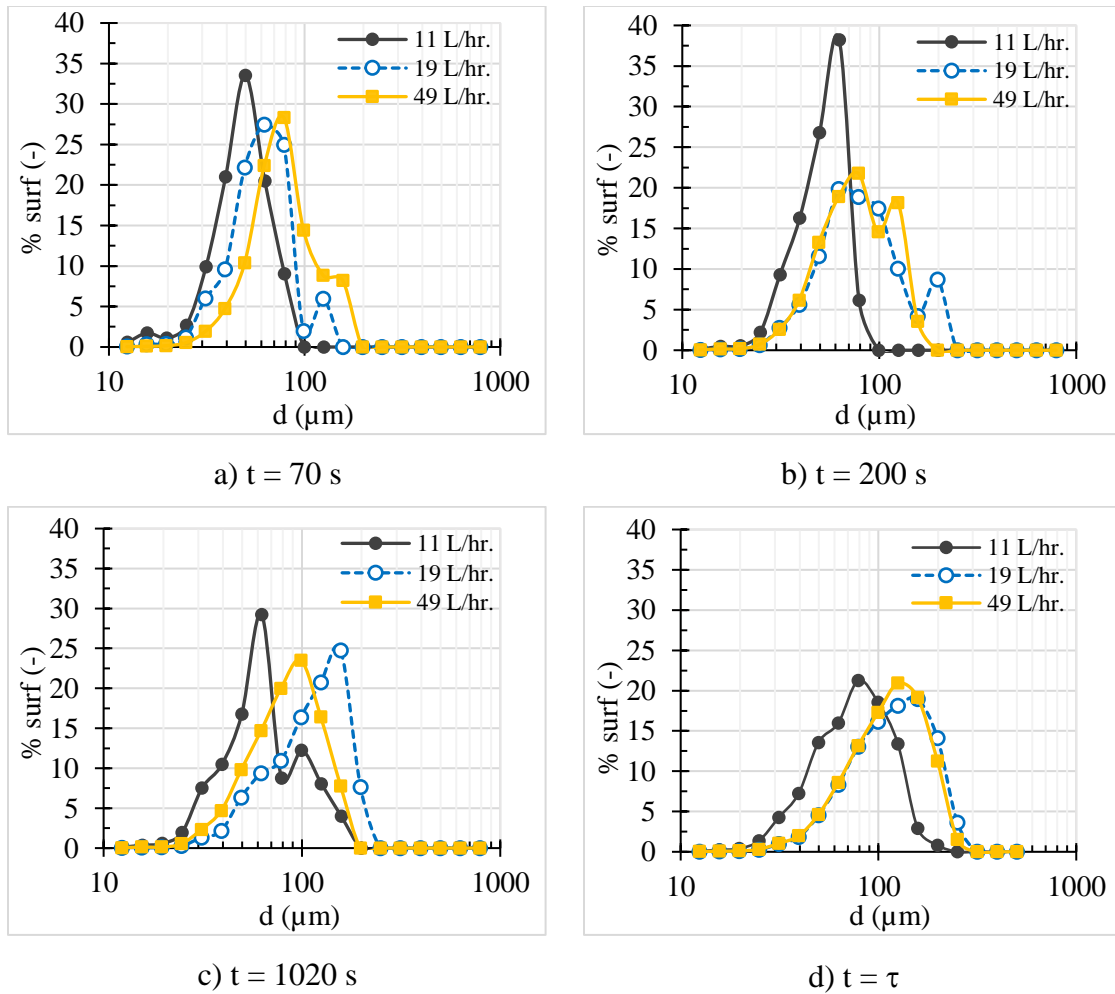
Figure 4.25 Size distribution in Position 2 at (a) 70 s (b) 200 s (c) 1020 s, and (d) τ for each flow rate

The analysis that was carried out with regard to the circulation times in the case of the results obtained in Position 1, still seems valid in the case of the results obtained in Position 2. On a global point of view, the evolution of the size distribution is faster the

higher the flow rate is. At steady state, the Figure 4.23 (d) and Figure 4.25 (d) show that the flocs size distributions and the mean diameter for each position were roughly the same. The analysis results thus lead to the comparison of the floc size distributions between both positions at steady state, which is described in the next section.

4.2.4 Comparison of Floc Size Distributions Between Position 1 and Position 2 at Steady State

On Figure 4.26 the floc size distributions at steady state for both positions and the three flow rates are plotted. It could be obviously seen that whatever the flow rate, the size distribution shifts towards slightly bigger sizes between Position 1 and Position 2. Revealing that some agglomeration phenomena take place within the jet. Nevertheless, the shifts between the two positions were limited and the size distributions for medium flow rate (19 L/hr.) and high flow rate (49 L/hr.) could be seen as almost superimposed.
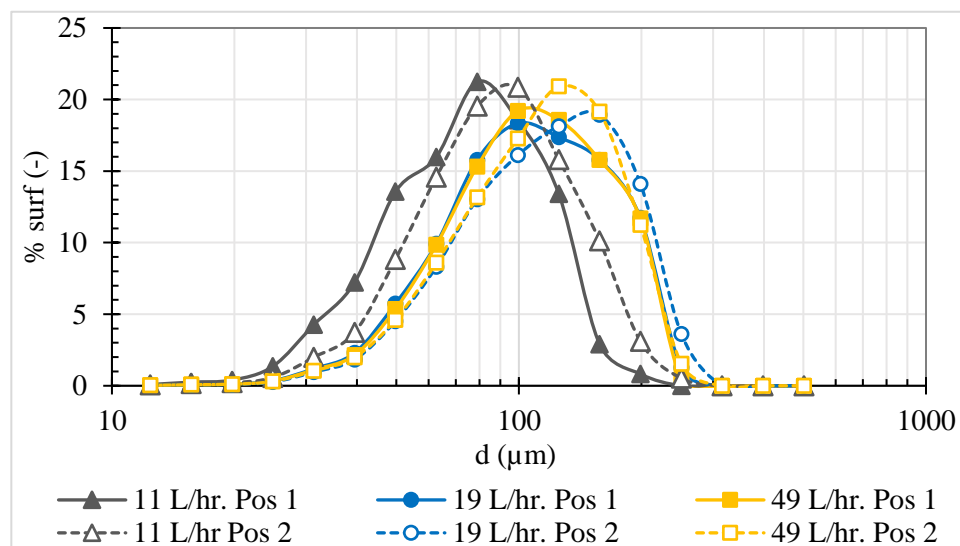
Figure 4.26 Steady state floc size distributions in position 1 and position 2
for the 3 flow rates and inlet injection of 50 NTU

In conclusion, the results show that the size distributions seem almost not influenced by the flow rate. Compared to previous studies in mixing tanks where the floc size was closely related to the maximum local dissipation rate (Bouyer et al., 2004; C.

Coufort et al., 2005; Kilander et al., 2006; T. Kramer and Clark, 1997a; Pougatch et al., 2021); the results obtained in this study were unexpected. To confirm this result, experiments were performed with a much higher concentration of bentonite. The following paragraph presents the results obtained in the case of the intermediate flow rate.

4.2.5 Influence of Inlet Concentration

Increasing the inlet concentration modifies the number of flocs injected into the apparatus. According to the theoretical analysis, this would have an influence on the flocculation (see the topic of 1.4.1). For this new set of experiences, the inlet concentration of bentonite has been multiplied by 5 (1,100 mg/L) corresponding to turbidity equal to 250±1 NTU.

On Figure 4.27, the size distributions for the medium flow rate (19 L/hr.) are shown for both positions. When comparing these results to those obtained for inlet turbidity of 50 NTU, it must be pointed out that once again, whatever the concentration of the inlet suspension, the size distribution seems to little evolve. These results go beyond previous reports, showing that the range of concentration in this study does not affect floc size distribution.
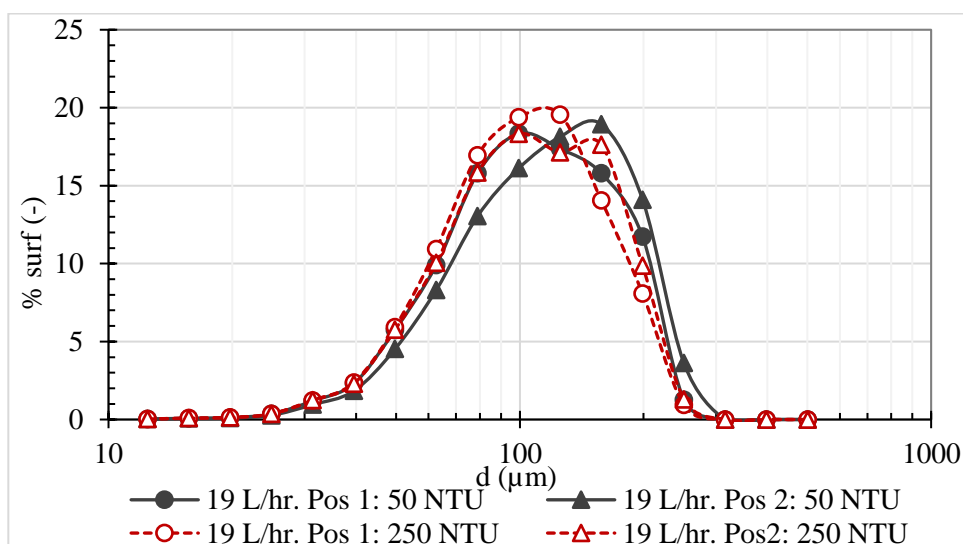
Figure 4.27 Steady state floc size distributions in position 1 and position 2
for the medium flow rate (19 L/hr.) and inlet injection of 50 and 250 NTU

From the results presented so far, the size distribution of the aggregates at steady state seems not to depend on the flow rate nor on the concentration. The analysis of the transient phase, both on the evolution of the number of aggregates and on the size distributions, showed that the circulation loop plays a particular role in the course of the flocculation in the clarifier. Therefore, the link between the flow characteristics in the flocculation zone and the number of flocs will be focused.

4.2.6 Number of Flocs and Circulation

The transient evolution of the number of flocs between Position 1 and Position 2 has been presented in Figure 4.17 (b) and Figure 4.19 (b). It was pointed out that for the lowest Position, the number of flocs depends on the flow rate, whereas for the Position 2, the number of flocs seems not to be affected by the flow rate.

This finding could be emphasized by plotting the ratio of the number of flocs between Position 1 and Position 2, as done in Figure 4.28. The number of flocs was reasonably constant for the high flow rate (49 L/hr.) because the ratio is close to 1, whereas the number of flocs increases between Position 1 and Position 2 for the low flow rate (11 L/hr.) and the medium flow rate (19 L/hr.), which the values were about 0.7 and 0.8, respectively. The increase was all the more significant as the flow rate is low.

To better understand these results, a connection with the hydrodynamics in the flocculation zone is necessary. The experimental study of the local hydrodynamics in the jet clarifier (see topic 4.1.1) pointed out that a circulation loop was present as shown by the velocity fields of Figure 4.29 for all flow rates, where the locations of Positions 1 and 2 have also been reported as red squares. The recirculation loop is present on the entire height of the flocculation zone and its main characteristic values are reported in Table 4.9.
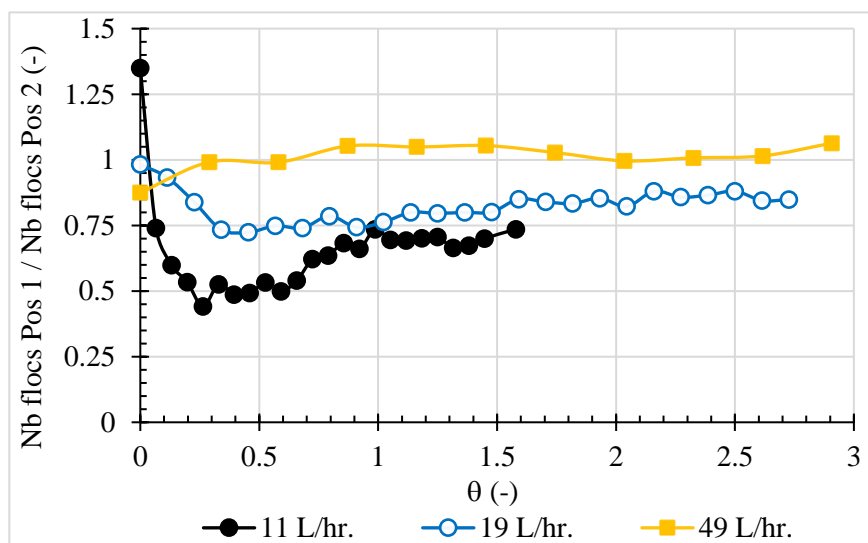
Figure 4.28 Ratio between the number of flocs in Position 1

and the number of flocs in Position 2 versus θ

Table 4.9 Hydrodynamic characteristics of circulation in the flocculation zone (cone) of
the clarifier

Parameters	Inlet flow rate (Q) (L/hr.)		
	11	19	49
Circulation time: t_C (s)	153	110	40
Ratio: $Q_c/Q_{inlet} = t_C/\tau$	15	12	13
Residence time in the flocculation zone (cone): $\tau_{FZ} = V_{cone}/Q$ (s)	2290	1325	514
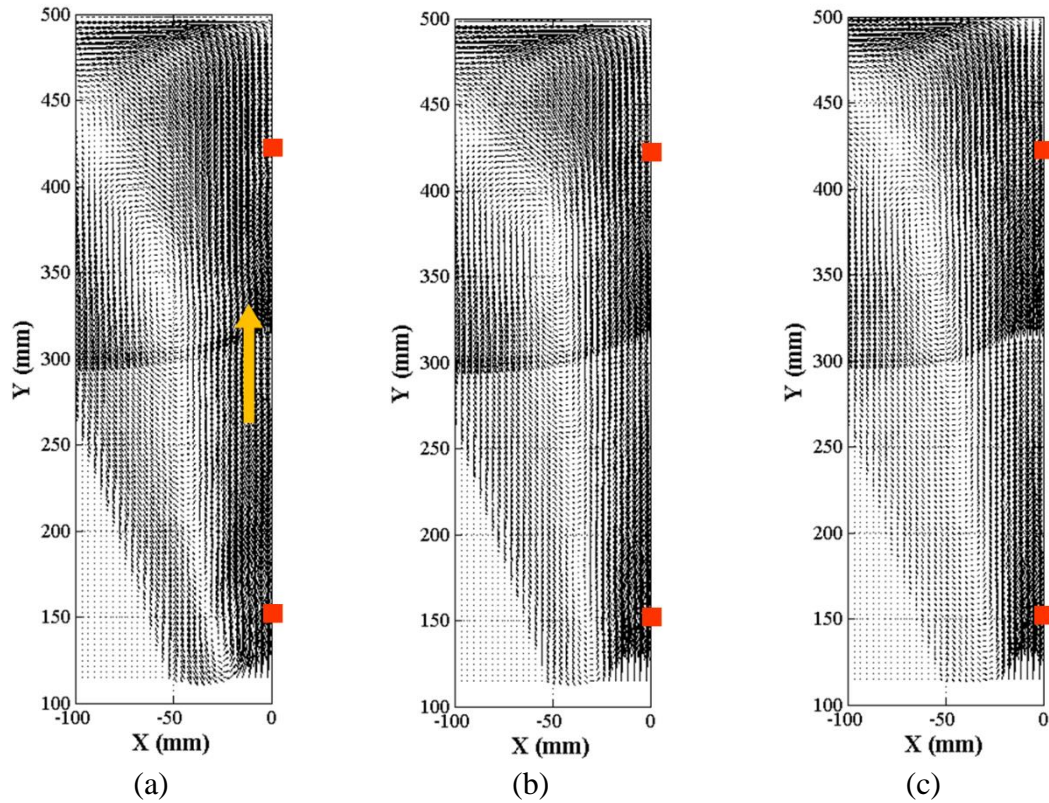
Figure 4.29 Mean velocity field in the flocculation zone
of (a) 11 L/hr. (b) 19 L/hr., and (c) 49 L/hr. flow rate.

The flow rate trapped within the recirculation loop (Q_c) is relatively large compared to the injected one (Q) as the ratio is in the range of 12 – 15. There is no doubt that this recirculation carries flocs as those latter have a density close to the water. To assess the impact of this recirculation on a local hydrodynamic point of view, the evolution of the upward mass flux can be evaluated from PIV data and a Non-Dimensional Mass Flux (NDMF) can be estimated. The NDMF corresponds to the ratio between the upward mass flux (right part of the picture Figure 4.29 (a) to (c) and represented by a yellow arrow on Figure 4.29 (a) and the injected flow rate (Q). The NDMF has thus been estimated according to Equation 4.4 as shown below:

$$NDMF = \frac{\frac{h}{2} \int_{x_{min}}^{x_{max}} V(x)dx}{Q} \qquad \text{Equation 4.4}$$

Where x_{min} and x_{max} are the boundaries of positive axial velocity V (the jet) and h is the depth of the pilot. PIV measurements being limited in a single plane of symmetry of the pilot and Reynolds numbers at the outlet of the flocculation zone ranging from 100 to 150 (see Table 4.3), the factor ½ corresponds to the ratio between mean velocity and maximum velocity in laminar flow. The axial profile of NDMF was plotted for each flow rate on Figure 4.30. The NDMF value was in abscissa and the ordinate corresponds to the height in the flocculation zone. The Position 1 where the images of flocs have been acquired was also mentioned (Y = 150 mm).

◁ : LFR   ○ : MFR   ▷ : HFR
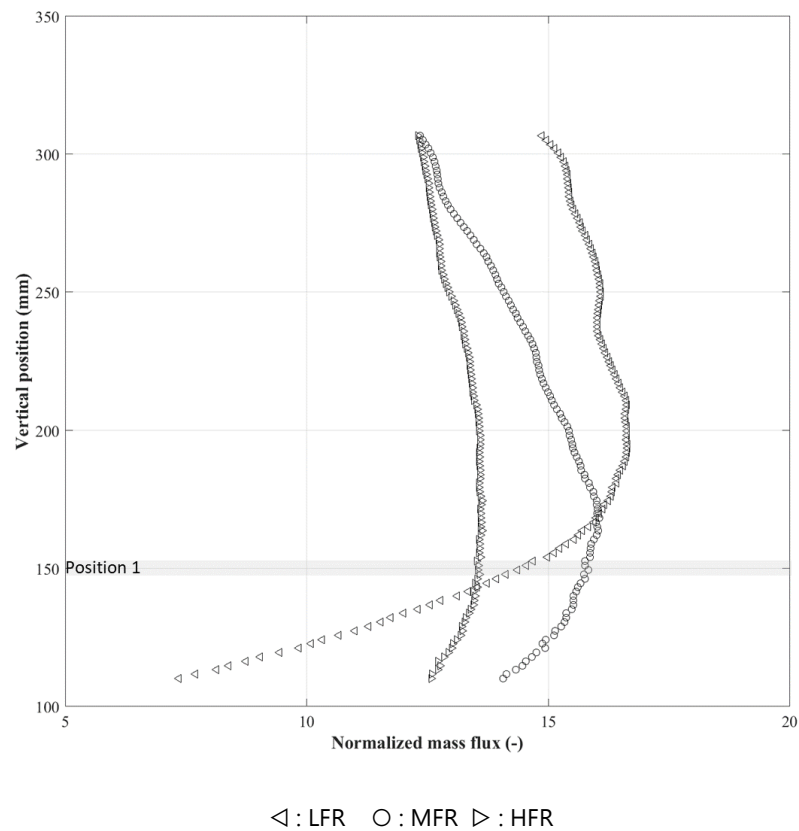
Figure 4.30 Axial profile of the Non-Dimensional upward Mass Flux (NDMF) for each flow rate

For the high flow rate (49 L/hr.), the NDMF was almost constant (12.5 – 13) along the vertical axis and close to the ratio Q_c/Q (yellow value of 13 see Table 4.9) meaning that the entire recirculation flow rate arrives below the Position 1 where the images have been

acquired. This signifies that most of the flocs trapped in the circulation loop meet those of the injection below the Position 1. The numbers of flocs in Position 1 and Position 2 are thus quite similar, which can explain the rather flat profile and the value of almost 1 for the high flow rate in Figure 4.28.

In comparison, the NDMF profile for the low flow rate (11 L/hr.) was different. Indeed, below the Position 1 (Y < 150 mm), the NDMF increases continuously from 6 to 14. Above the Position 1, the NDMF was still increasing meaning that some flocs join the upward flux. It could be noticed that for vertical position greater than 175 mm, the value of the NDMF for the low flow rate was higher than for the medium flow rate and high flow rate. This means that only a part of the circulation loop carries the aggregates below the Position 1, the rest of the aggregates arriving between Position 1 and Position 2. A scheme of how the flocs is carried out in the upward flux can be suggested in Figure 4.31. For pedagogic purposes, the recirculation has been divided into two parts: Recirculation 1 is the part arriving below the Position 1 where the size distributions have been acquired; Recirculation 2 is the part arriving above Position 1. The intensity of the grey color represents the intensity of the recirculation rate and therefore of the number of carried aggregates.
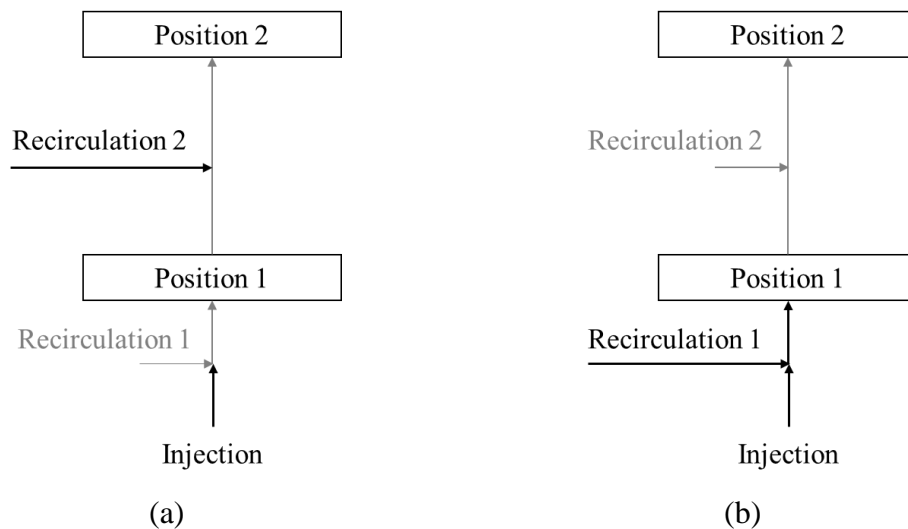
Figure 4.31 Diagram of the global hydraulic view for
(a) the low flow rate, and (b) the high flow rate

To assess this hypothesis, a global hydraulic view of flow transport, not taking into account agglomeration, breakup, and settling could be established based on the previous figure. This global hydraulic view was based on the following assumptions: (1) the flocs that are detected in Position 1 come from the injection and the bottom recirculation (Recirculation 1); (2) the flocs detected in Position 2 come from the Position 1 and from the upper part of the recirculation (Recirculation 2). Then the number of flocs carried out by both Recirculation 1 and 2 and the total recirculation (Recirculation 1 + Recirculation 2) could be estimated through the following equations (Equation 4.5, Equation 4.6, and Equation 4.7).

$$\text{Recirculation 1} = \text{Position 1 - Injection} \qquad \text{Equation 4.5}$$

$$\text{Recirculation 2} = \text{Position 2 - Position 1} \qquad \text{Equation 4.6}$$

$$\text{Total Recirculation} = \text{Recirculation 2} + \text{Recirculation 1} \qquad \text{Equation 4.7}$$

The calculations for Recirculation 1, Recirculation 2 and Total Recirculation have been performed with the experimental results acquired all along the experience. The number of flocs per unit time that were injected in the pilot (called Injection in Equation 4.5) has been estimated from the data acquired at the beginning of each experiment. Indeed, at t = 0 s, the pilot is full of clear tap water at rest and the injection of the bentonite suspension is started. The 100 images acquired during the first 20 seconds of the experiments thus corresponds to the flocs that are only due to the injection as the circulation loop has not yet had time to set up. Indeed, as mentioned in Table 4.9, the circulation time is at least 40 s for the highest flow rate.

Once those calculations are completed, the ratio between the number of flocs in the total recirculation (Recirculation) and the number of flocs injected (Injection) can be plotted and is presented in the Figure 4.32.
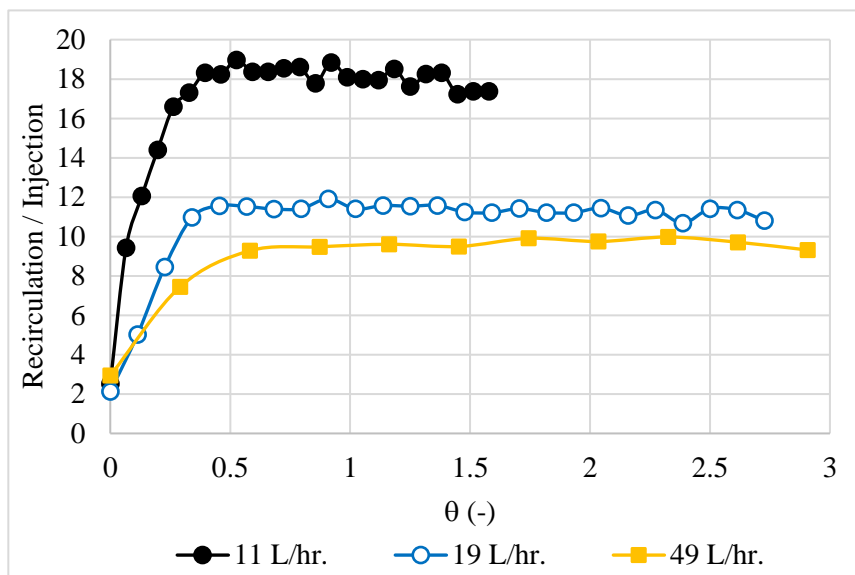
Figure 4.32 Ratio between the number of flocs in the total recirculation
and the number of flocs injected.

At steady state, these ratios were quite important. For example, for the lowest flow rate (11 L/hr.), the number of flocs transported by the circulation loop is 18 times higher than the number of flocs injected. These values were of the same order of magnitude as the ones of the ratio Q_c/Q that are shown in Table 4.9. These values were not exactly the same because the global hydraulic view does not take into account some physical phenomena undergone by the flocs such as settling, agglomeration or rupture.

On a practical point of view, this result indicates:

- that the circulation loop is most significant as the flow rate is low.
- that the size distributions measured are mainly those of flocs that were in the flocculation zone since a certain amount of time. This was directly linked to the efficient mixing of the jet clarifier that was highlighted in the study of local hydrodynamic as discussed in the topic of 0.

On an industrial point of view, the interest of such a circulation loop lies in the fact that it highly increases the number of aggregates inside the flocculation zone and, by the

way, the number of collisions (cf. Equation 1.21). The flocculation takes thus place at a particle concentration greater than those of the injection.

4.2.7 Maximal Size, Size Distributions, and Camp Number

The main result of the Figure 4.29 was that the floc size distributions seemed to be independent on the flow rate. This finding was rather discordant with most of the works of the literature that stated a direct relationship between the size of the aggregates and the dissipation rate of the total kinetic energy (ε), velocity gradient (G) such as mentioned in the Equation 1.30 or the Kolmogorov microscale (η). Nevertheless, one can notice that the maximal size reached by the flocs is around $250 - 300\,\mu$m whatever the flow rate. Looking at the vertical profile of the horizontal average Kolmogorov scale plotted in the Figure 4.16 (c) near the Position 1 (Vertical position ≈ 150 mm), the order of magnitude of η is close to $200 - 300\,\mu$m. This would tend to indicate that the stresses exerted by the fluid on the flocs near the outlet of the nozzle tend to limit their maximal size, at least in the vicinity of Position 1.

Looking at the size distributions themselves, the slight shift towards bigger sizes between Positions 1 and 2 (cf. Figure 4.22) can certainly be attributed to the rather short time of circulation ($t_c < 160$ s (See Table 4.9)) in the flocculation zone limiting the number of agglomeration phenomena even if the residence time in this zone is high ($\tau_{FZ} > 500$ s). However, in light of the theoretical model of flocculation described in the Chapter 1, the almost superimposed distributions can certainly be associated to the values of the Camp Number ($G{\cdot}t_{cont}$). Based on PIV data processing, estimated local and instantaneous shear rates, presented the analysis of the space averaged velocity gradient (G) and deduced the parameter $G{\cdot}t_{cont}$ for the three flow rates. The main values were summarized in Table 4.10. It must be noticed that the value of the Camp Number was based on the residence time in the flocculation zone where the flocculation takes place.

Table 4.10 Global hydrodynamic parameters in the flocculation zone

Parameters	Injected flow rate (Q) (L/hr.)		
	11	19	49
Space averaged value of the viscous dissipation rate of the kinetic energy in the flocculation zone $<\varepsilon>$ (m²/s^{-3})	9.3×10^{-6}	2.7×10^{-5}	1.7×10^{-4}
Global velocity gradient in the flocculation zone (cone): $G(<\varepsilon>)$ (s^{-1})	3.06	5.2	12.9
Camp Number of the flocculation zone: $G(<\varepsilon>).\tau_{FZ}$	7010	6890	6640

Whatever the flow rates, the values of the Camp Number were almost constant. Indeed, increasing the flow rate, the global velocity gradient increases linearly whereas the residence time decreases giving a nearly constant value for the Camp Number in the flocculation zone where the flocculation takes place. In this study, a factor of almost 5 on the flow rate does not seem to have a great impact on the floc size distribution at steady state as shown in Figure 4.22. Thus, the Camp Number, based on the values of the residence time τ_{FZ} and on $<\varepsilon>$ in the flocculation zone seems thus a rather reliable criteria for the design of such apparatus.

These results can explain some findings of previous works such as (Sobrinho et al., 1996) and some other authors that mentioned the relative insignificance of the flow rate on the turbidity removal in the case of submerged jet flocculators. Indeed, if the floc size distribution is roughly the same, whatever the flow rates, the ability of the formed aggregates towards settling is certainly similar and so on for the turbidity removal. This means that despite load variations in terms of flow rate or concentration, the size distribution does not change in the flocculation zone which seems of significant industrial interest in representations of operability.

4.3 Conclusion

The aim of this part of the thesis was to better understand the relationship between flocculation and hydrodynamics in the jet clarifier. To that end, flocculation experiments have been performed in a quasi-two-dimensional jet clarifier (Q2D jet clarifier). The hydrodynamics of the pilot has before been experimentally studied with PIV. A strong recirculation is induced by the jet in the divergent zone, promoting long residence times and efficient mixing. Using Image analysis, the aggregates size distributions have been measured over time for two different positions of the flocculation zone of the Q2D jet clarifier. The Position 1 was 15 cm above the injection and the Position 2 was 41.5 cm above the injection, which was the top of the flocculation zone. Three flow rates were investigated, with a ratio of almost 5 between the smallest and the highest flow rate.

The time evolutions of the mean diameter and of the number of flocs in both positions revealed that the global residence time τ was the right characteristic time scale (Figure 4.17 to Figure 4.20). The number of flocs near the injection (Position 1) and at the top of the flocculation zone (Position 2) do not seem to have the same dependance on the flow rate (Figure 4.17 to Figure 4.20). The time evolutions of floc size distributions in both positions are presented on Figure 4.22 and confirm that the steady state is all the more quickly reached that the flow rate is high. At steady state, Figure 4.27 exhibits a relative insignificance of the flow rate and of the inlet concentration on the floc size distributions.

In the discussion, a global hydraulic view performed between Position 1 and Position 2 suggests that most of the measured aggregates are trapped in the circulation loop that was present in the flocculation zone. Indeed, the recirculation loop carries between 10 and 18 times more flocs than the injection. A connection with the circulation flow rates issuing from the hydrodynamic study of the apparatus was established. A vertical profile of the Non-Dimensional upward Mass Flux (Figure 4.30) was further used to understand the way the flocs were trapped in the circulation loop. If for the medium and high flow rates the NDMF was almost constant, its profile for the lowest flow rate was linearly increasing in the bottom part if the flocculation zone explaining the lower number of flocs in Position 1. At least, the relative independence of the flow rate on the floc size

distributions was discussed in the light of the Camp number, which remained constant in the apparatus and can thus explain the efficiency of the jet clarifier in terms of flocculation.

Recall first that now to examine the parameter that might affect the performance of the small scale prototype (SSP) and the large scale prototype (LSP) jet clarifiers such as the effect of the reactor's configuration, the appearance of sludge and flow rates. Concurrently, the global fluid flow has been investigated through the residence time distribution (RTD). Then, the Q2D jet clarifier was conducted to examine the local hydrodynamics and its effects on the floc size distributions in relation with a Camp Number based on $G(<\varepsilon>).\tau_{FZ}$. The next chapter will be dedicated to:

- the simulation of the hydrodynamics in the SSP clarifier with a particular attention to the residence time distribution and Camp number
- how the scale-up of such devices could be considered using Computational Fluid Dynamics.

CHAPTER 5

COMPUTATIONAL FLUID DYNAMIC (CFD)

This chapter details the CFD program is used to numerically simulate with study cases carried out in the small scale prototype (SSP) of this study to reproduce hydrodynamic phenomena of SSP in order to consider upscaling based on CFD. This chapter begins with the theory behind the methods employed in this part and the details of study conditions (section 5.1), which were conducted to verify and applied the modelling methods, standard k-ε and Detached Eddy Simulation (DES), were used in the simulation to account for the turbulence effect. They feature comparisons with numerical data and experimental results by the residence time distribution method (RTD) data. The results of both RTD measurement and simulation, and CFD prediction would be presented in the 5.2 sections.

5.1 Computational Fluid Dynamic (CFD)

In recent years, computational fluid dynamics (CFD) has become an essential/key tool in the reactor design and provides useful and detailed information prevailing in the reactors, such as velocity field and concentration distribution (Salem et al., 2011; Yáñez-Varela et al., 2018; T. Zhou et al., 2014). Indeed, the basic knowledge of the process itself and of fluid dynamics was required for selecting the suitable CFD model to solve the equations. This section thus describes the theory behind the methods employed in this thesis. It covers the main CFD methods focusing on the RANS, standard k-ε model as well as Detached Eddy Simulation (DES) model. The section also concludes with descriptions of the passive scalar transport for RTD-numerical and the species transport for internal age distribution simulation. The CFD simulation was performed with ANSYS Fluent version 16.2 in this study.

5.1.1 Governing Equation

The Computational Fluid Dynamics (CFD) provided an efficient approach to study fluid flow inside reactors. The resulting prediction accuracy depends on physical properties of fluid such as velocity, pressure, temperature, density, viscosity and geometry of reactors. CFD modelling is based on the Reynolds Averaged Navier–Stokes (RANS) equations that consist of the fundamental mass and momentum balance equations using numerical techniques. The governing equations of mass and momentum equations for incompressible fluid were defined as Equation 5.1 to Equation 5.4 (O. Reynolds, 1883). Equation 5.1 is the mass conservation, Equation 5.2 is the momentum conservation, and Equation 5.3 and Equation 5.4 describe the viscous stress and turbulent stress tensor, respectively.

$$\vec{\nabla} \cdot \vec{U} = 0 \qquad\qquad\qquad \text{Equation 5.1}$$

$$\frac{\partial(\rho\vec{U})}{\partial t} + \vec{\nabla}\cdot(\rho\vec{U}\otimes\vec{U}) = -\vec{\nabla}p + \vec{\nabla}\cdot(\tau_{lam} + \tau_{turb}) + \rho\vec{g} \qquad \text{Equation 5.2}$$

$$\tau_{lam} = \mu\left(\nabla\otimes\vec{U} + \nabla\otimes\vec{U}^{T}\right) \qquad\qquad \text{Equation 5.3}$$

$$\tau_{turb} = \mu_{t}\left[\left(\nabla\otimes\vec{U} + \nabla\otimes\vec{U}^{T}\right)\right] - \frac{2}{3}\rho\,k\,I \qquad \text{Equation 5.4}$$

Where $\vec{U}$ is the mean velocity vector, ρ is the liquid density, t is time, p is the mean pressure, τ is the mean viscous stress tensor, $\rho\vec{g}$ is the gravitational body force, μ is the viscosity, k is the turbulent kinetic energy, and μ_{t} is the dynamic turbulent viscosity.

The turbulent stress tensor represents the effect of turbulence on the mean flow. For the turbulent flow, which is characterized by irregular fluctuations of velocity, it is conceivable to model turbulent flow within CFD without any adjustments to the NS-equations that is known as direct numerical simulation (DNS) and is exceptionally computationally extravagant. Nevertheless, CFD simulations can be solved by focusing on the mean properties of the flow due to its simplicity and less computationally intensive; thus, it is saved computer costs and required time to solve the equations. For this reason,

the Reynolds-Averaged Navier–Stokes (RANS) equation is the advantageous equation to solve the in any cases. These equations contain correlation of Reynolds stress, that is the fluctuating of velocity components $\overline{u_i' u_j'}$. For the turbulent field, other models are required to think about a possibility and make a decision about the effect of the turbulent fluctuations because no turbulent model is universally accepted to be appropriate for all conditions so that many turbulent models have been developed; they are known as Standard k-ε (S k-ε), Realisable k-ε (R k-ε), Renormalisation Group k-ε (RNG k-ε), and Reynolds stress model (RSM). The selection of an appropriate turbulence model is a great important considering. Among all, the Standard k-ε model is the most widely used model (Guillas et al., 2014; Phuan et al., 2017).

5.1.2 The Standard k-ε Model

The Standard k-ε turbulence model is a primary practical engineering tool for flow calculation, and it is a popular choice of the RANS model to simulate mean flow characteristics for turbulent flow conditions. Thus, the Standard k-ε model for an incompressible fluid was selected to investigate the hydrodynamic phenomena of the jet clarifier. Turbulence kinetic energy (k) and dissipation rate (ε) are the critical parameters for the accurate prediction of momentum diffusion. In the case of the standard k-ε model, Equation 5.5 is used to calculate the turbulent viscosity, μ_t.

$$\mu_t = C_\mu \, \rho \, \frac{k^2}{\varepsilon} \qquad \qquad \text{Equation 5.5}$$

Where C_μ is a model constant (Jones and Launder, 1972).

The values of k and ε in the standard k-ε model can be estimated by Equation 5.6 and Equation 5.7, respectively (Grotjans and Menter, 1998; Wilcox, 1998).

$$\frac{\partial(\rho k)}{\partial t} + \nabla \cdot (\rho U k) = P_k - \rho \varepsilon + \nabla \cdot \left(\mu + \frac{\mu_t}{\sigma_k} \nabla k \right) \qquad \qquad \text{Equation 5.6}$$

$$\frac{\partial(\rho\varepsilon)}{\partial t} + \nabla\cdot(\rho U\varepsilon) = \frac{\varepsilon}{k}(C_{\varepsilon1}P_k - C_{\varepsilon2}\rho\varepsilon) + \nabla\cdot\left(\mu+\frac{\mu_t}{\sigma_\varepsilon}\nabla\varepsilon\right)$$
<div align="right">Equation 5.7</div>

Where P_k is the production rate of turbulence. And the set of the standard k-ε model constants is $C_\mu = 0.09$, $C_{\varepsilon1} = 1.256$, $C_{\varepsilon2} = 1.92$, $\sigma_k = 0.9$, and $\sigma_\varepsilon = 1.3$ that they are all empirical model constants. To solve the equations, they must be solved over many small control volumes (the computational mesh). For determination of the flow field these simulations require input of geometry, boundary conditions and fluid properties (Brannock et al., 2010).

5.1.3 Detached Eddy Simulation (DES)

Detached-Eddy Simulation (DES) is among the more well-known and actively applied hybrid Reynolds-averaged Navier-Stokes and Large Eddy Simulation (RANS-LES) strategies. The method was proposed by Spalart in 1997 as a numerically feasible and plausibly accurate approach for the prediction of massively separated flows, which must be addressed in such fields as hydrodynamic as well as aerospace or atmospheric studies (P. Spalart et al., 1997). The DES formulation is based on a modification to the Spalart-Allmaras (S–A RANS) that is a one-equation model that solves a modeled transport equation for the kinematic eddy turbulent viscosity (Kotapati-Apparao et al., 2003; P. Spalart and Allmaras, 1992). The S-A RANS model is summarized below along with issues related to the DES formulation. Additional discussion can be found in (P. Spalart and Allmaras, 1992), (P. R. Spalart, 2000), and (Strelets, 2001). In the S-A RANS model, a transport equation is used to compute a working variable used to form the turbulent eddy viscosity is given by Equation 5.8.

$$\frac{\partial\tilde{v}}{\partial t} = c_{b1}[1 - f_{t2}]\tilde{S}\,\tilde{v} - \left[c_{\omega1}f_\omega - \frac{c_{b1}}{K^2}f_{t2}\right]\left[\frac{\tilde{v}}{d}\right]^2$$
$$+ \frac{1}{\sigma}\left[\nabla\cdot\left((v + \tilde{v})\nabla\tilde{v}\right) + c_{b2}(\nabla\tilde{v})^2\right] + f_{t1}\Delta U^2$$
<div align="right">Equation 5.8</div>

Where $\tilde{v}$ is a viscosity-like variable. And the turbulent eddy viscosity (μ_t) is computed from:

$$\mu_t = \rho\tilde{v}f_{v1} \qquad \text{Equation 5.9}$$

Where $f_{v1} = \dfrac{\chi^3}{\chi^3 + c_{v1}^3}$, $\chi = \dfrac{\tilde{v}}{v}$, and ρ is the density, $v = \mu/\rho$ is the molecular kinematic viscosity, and μ is the molecular dynamic viscosity. The production term is expressed as,

$$\tilde{S} \equiv f_{v3}S + \frac{\tilde{v}}{\mathcal{K}^2 d^2}f_{v2} \quad ; \quad f_{v2} = 1 - \frac{\chi^3}{1 + \chi f_{v2}} \qquad \text{Equation 5.10}$$

Where S is the magnitude of the vorticity. The function f_w is given as Equation 5.11.

$$f_\omega = g\left[\frac{1 + c_{\omega3}^6}{g^6 + c_{\omega3}^6}\right]^{1/6} \qquad \text{Equation 5.11}$$

Where $g = r + c_{\omega2}(r^6 - r)$, while $r = min\left[\dfrac{\tilde{v}}{\tilde{S}\mathcal{K}^2 d^2}, 10\right]$.

The function f_{t2} is defined as,

$$f_{t2} = c_{t3}exp(-c_{t4}\chi^2) \qquad \text{Equation 5.12}$$

The trip function f_{t1} is specified in terms of the distance d_t from the field point to the trip, the wall vorticity w_t at the trip, and ΔU which is the difference between the velocity at the field point and that at the trip,

$$f_{t1} = c_{t1}g_t exp\left(-c_{t2}\frac{\omega_t^2}{\Delta U^2}[d^2 + g_t^2 d_t^2]\right) \qquad \text{Equation 5.13}$$

Where $g_t = min\,(0.1, \Delta U/\omega_t\,\Delta\mathcal{X})$. The solid wall boundary condition is $\tilde{v} = 0$ and the constant are $c_{b1} = 0.1355$, $\sigma = 2/3$, $c_{b2} = 0.622$, $K = 0.41$, $c_{\omega 1} = c_{b1}/K^2 + (1+ c_{b2})/\sigma$, $c_{\omega 2} = 0.3$, $c_{\omega 3} = 2$, $c_{v1} = 7.1$, $c_{v2} = 5$, $c_{t1} = 1$, $c_{t2} = 2$, $c_{t3} = 1.1$, and $c_{t4} = 2$.

The DES formulation is obtained by replacing in the S-A RANS model the distance to the nearest wall, d, by $\tilde{d}$, where $\tilde{d}$ is defined as Equation 5.14.

$$\tilde{d} = min\,[d, c_{DES}\Delta]$$ Equation 5.14

Where $c_{DES} = 0.65$ in the homogeneous turbulence (Shur et al., 1999) and Δ is the largest distance between the cell center under consideration and the cell center of the neighbors (i.e., those cells sharing a face with the cell in question). While, the production and destruction terms of the model are balanced, the length scale $\tilde{d} = min\,[d, c_{DES}\Delta]$ in the LES region yields a Smagorinsky-like eddy viscosity ($\tilde{v} \propto S\Delta^2$). Analogous to classical LES, linking the eddy viscosity to Δ allows an energy cascade down to the grid size.

As of now, there has been a range of flows predicted using DES. These investigations have been broadly successful, yielding predictions superior to those obtained using RANS approaches while resolving three-dimensional, time-dependent features because of the LES treatment of separated regions (Squires et al., 2004). Many previous pieces of research suggested that the DES approach may be used with any turbulence model that has a judiciously defined turbulence length scale and is a sufficiently localized model (Kotapati-Apparao et al., 2003; Philippe R. Spalart, 2009; Tucker and Liu, 2005). Meanwhile, (Forbes et al., 2014) proposed that The deficiencies of using a steady state RANS methodology for an inherently unsteady flow are highlighted by inaccuracies in the base surface pressures and locations of the wake vortex structures. Time dependent DES approaches present the closest match to the experimental data, but these methods come with the highest cost. Afterward, (Vocciante et al., 2018) evaluated the performance of turbulence models, including RANS, DES, LES by comparing the resulting base on the experiment, since using an appropriate turbulence model is necessary for obtaining reliable results. The result was summarized that DES seems to be an optimal approach: it provides

the best agreement with experiments over the entire range of Reynolds numbers is 3000 – 8000, has lower computational costs and is easier to configure compared to LES simulation and best fit shows a relative error around 5%. For this reason, several models were used to test on studied cases.

5.1.4 Passive Scalar Transport for RTD-numerical

As explained in the RTD topic (section 1.6.1.4), the residence time of the reactor refers to the time of material flowing through reactors. For simulation, the tracer method is the most classical method to determine the RTD. In the RTD-numerical technique, there are two steps to be involved in the RTD investigation. The first step is to determine accurately the velocity fields and kinetic energy inside the reactor with the Eulerian–Eulerian method with the model is performed. The second one is to simulate the virtual tracer experiment, in which a non-reacting tracer transport equation is solved by using the previously obtained flow field. To set the physical properties of the virtual tracer in the RTD-numerical be set the same as the simulated physical material, thus the flow field would not be disturbed by the injected tracer and the flow field of virtual tracer is represent the physical flow inside the reactor. In order to figure out the RTD function, it is imperative to solve a transient species transportation equation of the tracer in the simulation. Based on the conservation equations for chemical species, the virtual tracer is used to detect the global and local mass fraction of the virtual tracer, C, on the continuous phase to predict the flow phenomena of the reactor. The conservation equation is taken following general as Equation 5.15.

$$\frac{\partial C_t}{\partial t} + \nabla \cdot \left(\vec{U_i}\, C \right) = \nabla \cdot (D_{ef}\, \nabla C) \qquad \text{Equation 5.15}$$

where D_{ef} is the effective diffusivity, the sum of molecular diffusion (laminar diffusivity), and turbulent diffusivity. The velocity and turbulent viscosity used in the transport equation are taken from fluid dynamic simulation.

5.1.5 Species Transport for Internal Age Distribution Simulation

Ordinarily, the residence time represents the time that a molecule exits the reactor. It means that the elapsed time since they entered. Therefore, the age of a molecule equals to its residence time, which is the concept of internal age distribution described by Danckwerts (Danckwerts, 1981). Likewise, the mean age distribution as a function of spatial position was proved by Lui (M. Liu and Tilton, 2010) that is A($\mathbf{x}$), as shown in Equation 5.16. The field variable A($\mathbf{x}$) is referred to as the mean age distribution.

$$A(\mathbf{x}) = \frac{\int_0^\infty t\, C_{(\mathbf{x},t)}\, dt}{\int_0^\infty C_{(\mathbf{x},t)}\, dt} \qquad \text{Equation 5.16}$$

Furthermore, a mixing cup (flow-weighted) average equation was applied and proved in order to figure out the relationship between internal age distribution and residence time distribution by Lui (M. Liu and Tilton, 2010). From this research, it can be concluded that the mean age distribution at the exit and mean residence time are identical. More precisely, the mean age distribution was calculated from the mixing cup average equation, from this concept, the concentration of the mixing cup equation can be calculated from Equation 5.17 which is considered both concentration and velocity field.

$$C_{out}(t) = \frac{\int_0^\infty U\, C_{(\mathbf{x}.t)}\, ds}{\int_o^\infty U\, ds} \qquad \text{Equation 5.17}$$

Therefore, it can be demonstrated that the functions of residence time distribution with mixing cup average equation is able to apply locally to any position in the reactor, to use local tracer concentration measurement to display spatially resolved distribution function. For more details about these settings can be found in the 5.1.10 topic.

Flow patterns in continuous systems are usually too complex to be experimentally measured while theoretically predicted from solutions of the Navier–Stokes equation or statistical mechanical considerations. The residence time of an element of fluid is defined

as the time elapsed from its entry into the system until it reaches the exit (Villermaux, 1995). The simulation is able to be applied to determine the flow field of the jet clarifier, but the model must be validated to make sure that it is correct as of the actual flow field.

To simulate numerically the flow field in the small scale prototype (SSP), a model based on the finite element method was developed using commercial CFD software, ANSYS Fluent version 16.2. The numerical technique was applied to determine the time that molecules remain in the actual flocculation zone. In this step, the case that was focused is only on the simulated liquid phase was pure water within the SSP without sludge case because of the reason of work limitations. Several models are available, and those used for our case are presented in the following section. At this point, the purpose finds out the model that fits the reality flow phenomenon of the reactor. Consequently, to solve either RTD-numerical simulation or the internal age distributions are need to be validated the model, which can be compared with the RTD-experiment (section 3.2) thus that experiments are still imperative in order to validate simulations (Furman and Stegowski, 2011; Klusener et al., 2007).

In all study cases, hydrodynamic solutions must be obtained from the first step, then the RTD-numerical and internal age distribution techniques would be solved. Both techniques are thus solved based on the stationary hydrodynamic; for the time solver settings that contain controls relating to solver settings (steady and transient). The steady means specifies that a steady flow is being solved while the meaning of transient is enabling a time-dependent solution, which can see performing time-dependent calculations for details. On the part of the transient cases, the hydrodynamic would be fixed to solve either scalar or internal age distribution when the physical time of any solving cases starting reached half of the theoretical mean residence time (0.5τ) and again three times theoretical mean residence time (3τ). Furthermore, the internal age distribution technique was used to figure out the local residence time and it was described in the species transport which was expressed in section 5.1.4.

5.1.6 Governing Equations and Boundary Conditions

In order to characterize numerically the reactor flow and to be able to estimate the fluid residence time distribution, Navier Stokes equations were solved under boundary conditions related to fluid domain, wall, and reactor's configuration, which describe the present working conditions:

- The 2D axisymmetric simulation focused on half of the jet clarifier of small size without sludge and the flow field was assumed to be symmetric due to the benefit of technical cost as shown in Figure 5.1 that was duplicated another side to show the whole reactor in order to be better visualizing.

- The inlet tube diameter was 0.39 cm., which was equal to the inlet diameter of the small size reactor while the width of the outlet was set as 0.65 cm., but for the actual experiment was free overflow. Hence, positions of injection and tracer detection are at moderately different positions between experiments and numerical simulations methods. All of the positions were shown in Figure 5.1. The different color lines were set to show the surface types of the numerical simulation case. At the same time, in the RTD experiment, the injection position was at a Y-connector installed before inlet tube of the jet clarifier while the injection position for numerical simulation was at an inlet tube of jet clarifier. Besides, tracer concentration detection position was an outlet of the reactor while in case of experiments the tracer concentration was detected at exit position at a drain tube of the reactor (see Figure 3.9) which was used to collect overflow fluid for the sake of detecting all of the tracer concentration;

- Velocity vectors on all the walls, including (1) the surface of the flocculation section, and (2) the surface dividing sedimentation section from the whole reactor, and (3) the surrounding wall (Figure 5.1, wall ①-③), were imposed to 0 m/s considering no-slip boundary conditions at the fluid-solid interface;
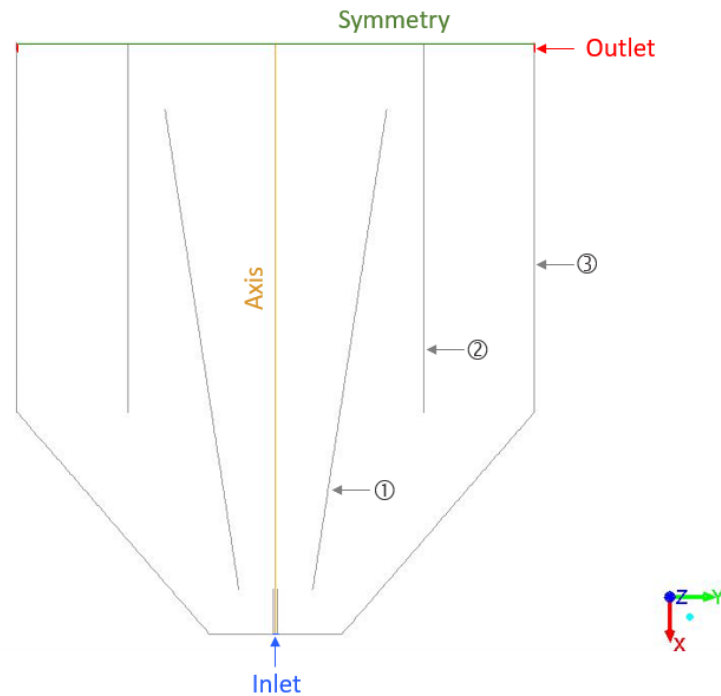
Figure 5.1 Geometry of the jet clarifier; ① the internal wall of flocculation,
② the internal wall of sedimentation, and ③ the surrounding wall of the jet clarifier

5.1.7 Numerical Method and Calculation Mesh

Equation 5.1 and Equation 5.2, which are mass and momentum balances were governed by the Navier Stokes equations were solved by the Fluent 16.2, which were both time-dependent (transient) and stationary (steady) phases. Mesh sizing was a compromise between accuracy and reduction of the calculation time. For the simulations dealing with several models due to the flow regimes to work out precisely the hydrodynamic. Figure 5.2 shows mesh was set in various sizes, which was depending on the geometry of the jet clarifier; the finest mesh size was located at the inlet tube and the largest mesh size was located at the sedimentation zone with the numbers of nodes and elements were 19,241 and 18,900, respectively.
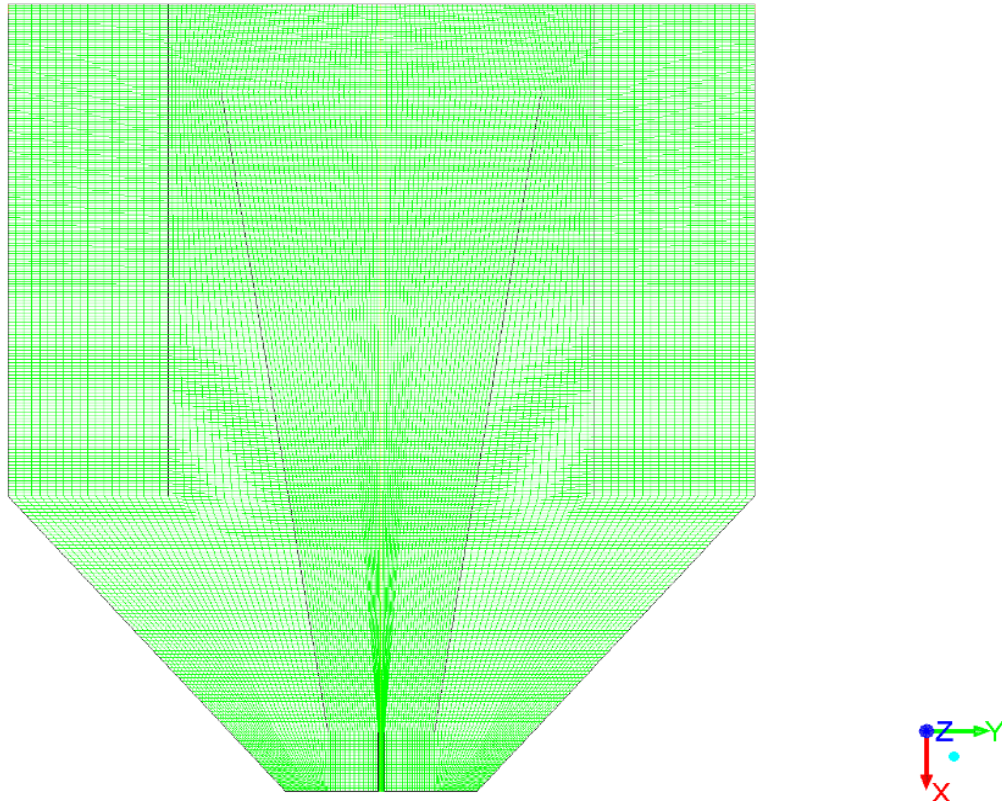
Figure 5.2 Mesh size of the jet clarifier

5.1.8 Operating Conditions

For CFD simulation, the water in the liquid phase was used as the material in case studies. The properties of water were set as density is 998.2 kg/m^3 and viscosity is 1.003×10^{-3} kg/m-s, which was assumed to be incompressible and independent of temperature in agreement with test fluid for PIV measurements (20ºC). Simulation conditions were imposed with various flow rates equal to 11, 19, and 49 L/hr. performing to realize the impact of flow rate on the flow field. Since the diameter of the inlet tube was 0.39 cm; consequently, the velocity magnitudes were set as 0.2554, 0.4467, and 1.1489 m/s for the lowest flow rate to the highest flow rate.

5.1.9 Simulating the Transport of a Passive Scalar for Numerical Residence Time Distribution (RTD-numerical)

In this study, the water in the liquid phase was used as the material. A scalar is an entity that is transported by the flow. For a fluid element, the amount of the scalar time variation is the amount transported by convection, molecular diffusion, and turbulent diffusivity directly added by a scalar source, which was explained by Equation 5.15 in section 5.1.4. The D_{ef} as was mentioned as the effective diffusivity, the sum of molecular diffusion (laminar diffusivity) and turbulent diffusivity. The velocity and turbulent viscosity used in the transport equation are taken from the fluid dynamic simulation.

In the case where the flow regime is turbulent, the Reynolds decomposition is made:

$$C = \overline{C} + c \qquad\qquad \text{Equation 5.18}$$

Again, where C is scalar concentration.

The resulting terms are applied to the transport equation, Equation 5.15. It appears then a new term that is related to the random turbulence fluctuation $\left(\overline{u_j c}\right)$.

$$\frac{\partial \overline{C}}{\partial t} + \nabla\cdot\left(\overrightarrow{U_i}\,\overline{C}\right) = \nabla\cdot\left(D_{ef}\,\nabla\overline{C} - \overline{u_j c}\right) \qquad\qquad \text{Equation 5.19}$$

To complete the system of equations, a model for the new term is needed. This model makes appear the turbulent diffusivity (D_t) that depends on the turbulent viscosity (ν_t) and the turbulent Schmidt number.

$$\overline{u_j c} = -D_t\frac{\partial \overline{C}}{\partial x_j} \;\;,\; D_t = \frac{\nu_t}{Sc} \qquad\qquad \text{Equation 5.20}$$

The turbulent Schmidt number is quite variable. It depends on the distance between the studied zone and the fluid jet or the wall. Several studies have found it to be a sensitive

parameter and have estimated different values that fit well the simulation and the experimental results. (Tominaga and Stathopoulos, 2007) had made a review of several research works and results obtained regarding the influence of the *Sc* number in the scalars transportation; generally, a value of 0.7 is taken.

Focusing on the validating model, the pulse input technique was used on the RTD-numerical simulation; at the inlet, the tracer was set to inject only in 0.5 seconds with a specified scalar value of 1000 (equivalent to a Dirac pulse). The details of time size and the number of time steps were shown in Table E.1 (see Appendix E). The concentration of the virtual tracer at the outlet was monitored and plot versus various times from the beginning of the tracer injection until the virtual tracer concentration reach 10^{-6}.

5.1.10 Species Transport for Internal Age Distribution Simulation

The transport or conservation equation for mean internal age distribution was derived from Equation 5.15 and Equation 5.17 shows in Equation 5.21 that is the same as the conservative forms as the steady transport equations in energy, momentum, and species, and it can be solved with the Fluent program with a source term function which was applied to the classical equation of transport in order to model the variation of age as Equation 5.21 that shows the mean age, that is the first moment, is distributed. This steady transport equation can be solved by CFD after the steady flow solution is obtained.

$$\nabla \cdot \left(\vec{U_i} A \right) = \nabla \cdot (D_{ef} \nabla A) + 1 \qquad \text{Equation 5.21}$$

Furthermore, the spatial of variance (σ^2) of mean age distribution and skewness (s^3) that are the second and the third moment of the origin can be determined. The equation for the n-th moment is Equation 5.22.

$$\nabla \cdot \left(\vec{U_i} M_n \right) = \nabla \cdot (D_{ef} \nabla M_n) + n M_{n-1} \qquad \text{Equation 5.22}$$

where M_n is n-th moment ($M_1 = A$). Thus, the equation for the second moment and third moment are Equation 5.23 and Equation 5.24, respectively.

$$\nabla \cdot \left(\overrightarrow{U_i} \, M_2\right) = \nabla \cdot (D_{ef}\nabla M_2) + 2A \qquad \text{Equation 5.23}$$

$$\nabla \cdot \left(\overrightarrow{U_i} \, M_3\right) = \nabla \cdot (D_{ef}\nabla M_3) + 3\sigma^2 \qquad \text{Equation 5.24}$$

Indeed, the equation to solve variance (σ^2) and skewness (s^3) are shown as Equation 5.25 and Equation 5.26, respectively.

$$\sigma^2 = M_2 - \tau^2 \qquad \text{Equation 5.25}$$

$$s^3 = M_3 - 2\tau^2 - 3\tau M_2 \qquad \text{Equation 5.26}$$

In summary, the work of this study is based on the flow characterization by CFD. The results provide a basis for the RTD-numerical simulation was done by Fluent 16.2 and they were validated by the RTD-experiments at the outlet position. Then, the internal age method was proposed to figure out the internal age distribution of the flocculation zone inside the jet clarifier. So, it is such a parallel step to work with the experiment of mean residence time distribution to examine the hydrodynamic.

5.2 Velocity Flow Field

The flow velocity field of the SSP could be characterized using the velocity field extracted from the CFD model output. The initial study undertaken on the SSP was to examine the complex hydrodynamic for only one phase; no sludge and particle were incorporated in the liquid flow except seeding. Flow behavior has a dominant influence on the mean residence time distribution that occurs within the SSP since the hydrodynamic of the SSP was induced by flow velocity and the mixing level is determined by turbulence. Figure 5.3 shows the hydrodynamic (velocity field) behavior of the fluid at steady state inside the SSP at the flow rate of 11 L/hr. of three models (laminar, standard k-ε, and DES. It is essential to mention that the flow maps of the model each are similar for all flow rates

studied except for only the velocity field magnitude. The multicolor bars located beside the image represent the magnitude of the velocity field, the dark blue color represents the lowest velocities, and the red color represents the highest velocities set at 0.4 m/s. The arrow and color represent the direction and velocity of the flow, respectively.

a) Laminar model   b) Standard k-ε model
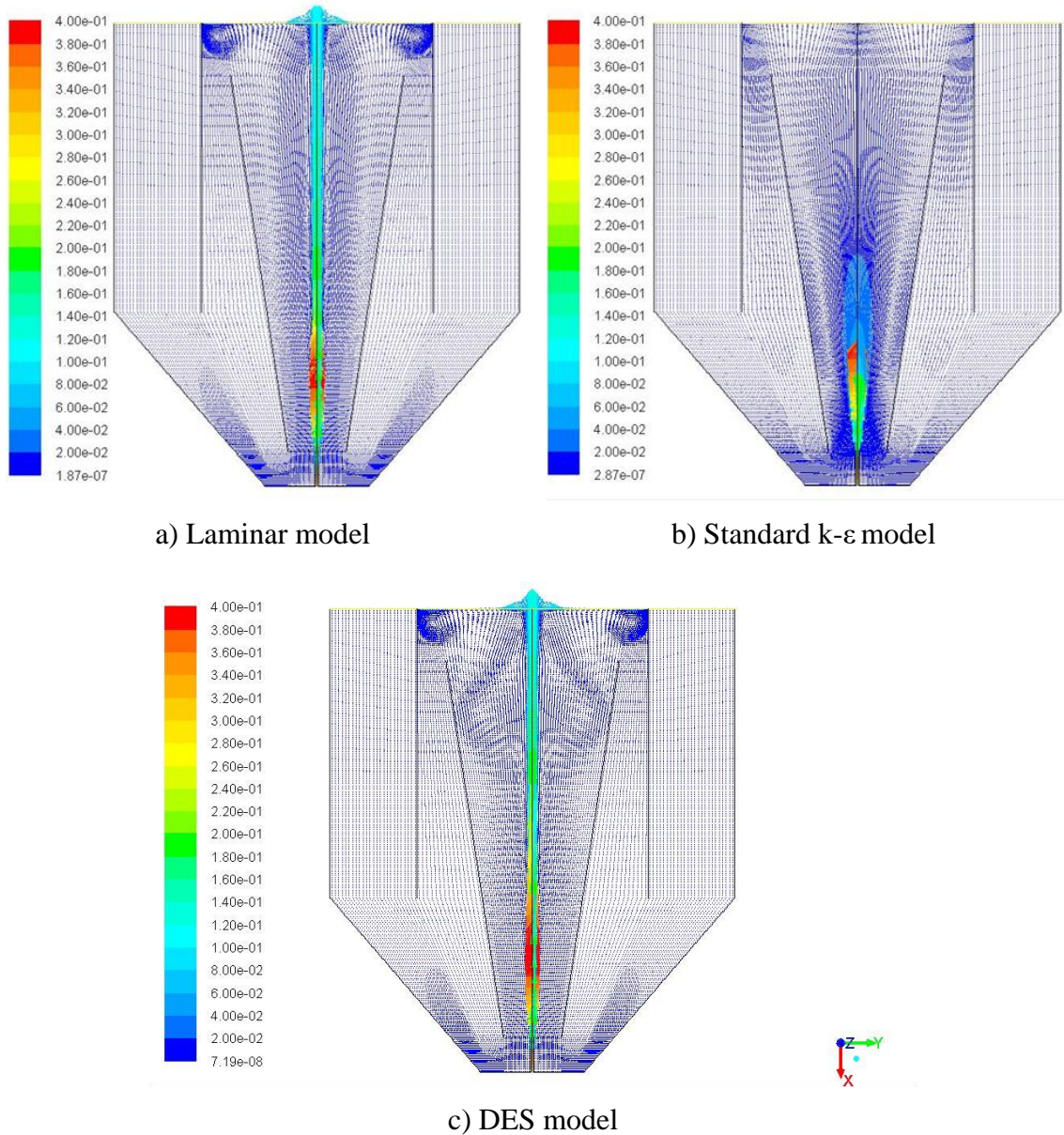
c) DES model

Figure 5.3 Velocity flow field obtained from DES hydrodynamic study for SSP (flow rate of 11 L/hr.) of (a) Lamina model (b) Standard k-ε model, and (c) DES model

The flow rate in the SSP could be calculated to verify the mass conversion of the measured flow field. The flow maps of all models were shown in Figure 5.3 (a – c) of low flow rate (11 L/hr.). It could be seen that two flow velocity zones were identified; high velocity zone was identified by red color and there were always located at the inlet, and then it reduced along the flow stream, which was the direction of fluid flowing from the inlet to free surface within the flocculation zone, and low velocity zone (stagnant zone) identified by dark blue color presented in a high proportion of the reactor volume, and it seems to be homogeneous, which was the direction moving down to the bottom of the tank before upflowing to the free surface at the outlet.

Figure 5.3 (a) presents the flow pattern by solving the laminar model. It was apparent to be seen that the flow pattern was an ideal laminar flow pattern; the velocity profile was infinitesimal parallel layers with no disruption between them. In laminar flows, fluid layers slide in parallel, with no eddies, swirls, or currents normal to the flow itself in the flocculation zone. Furthermore, there were small swirls flows at the edge of the SSP, which could be indicated that there was recirculation flows in the jet clarifier.

Figure 5.3 (b) shows the velocity vectors of the realizable standard k-ε model. As can be seen from the figure, the flow velocity vectors seem to spread along the flow direction where the maximum velocity occurs. It was noticeable that there also were circular motions inside the SSP, especially on the flocculation zone.

As can be observed in Figure 5.3 (c), the solution clearly illustrates the recirculation regions and the high velocity path generated by the jet. There was a recirculation region in the flocculation zone as same as the hydrodynamic results discussed in the topic of 4.1.6 (Hydrodynamic of flocculation investigated by PIV). From the results, it could be stated that the velocity flow fields of the flocculation zone were involved by two main velocity flow paths; the first one is the straight direction fluid flowing from the inlet to the free surface within the zone and recirculation flow. Moreover, the velocity vectors of the model studied were almost the same form, indicating the recirculation path (circular motion).

5.3 Comparison between RTD-experimental and RTD-numerical

This section of the work focuses on the results obtained from both the experimental data and simulations at the outlet position in order to validate the model with 3 flow rates. The residence time curves plotting the exit age distribution of the tracer against time for each condition from the RTD-numerical and RTD-experimental results for the SSP are presented in Figure 5.4. Note that the data were acquired at the outlet position of numerical methods comparing with the RTD curve at the drain tube of the experiment. The response concentration curves were distinguished. The curves in Figure 5.4 display the expected deviations that the peak of the RTD function for numerical technique is far higher than of the experiment.

For validating the RTD curves, the results were focused on the beginning of the experiment (10% of tracer concentration, t_{10}) and the mean residence time (t_m) were given from the experiment and simulation results according to Equation 2.3 and Equation 2.2, respectively. The comparisons were listed in Table 5.1. The results of the numerical methods were based on the standard k-ε model, Detached Eddy Simulation (DES), and laminar model to find out the model that given a good agreement with the RTD curves of the experiments. Figure 5.4 (a) shows a disapprobation between the result from the numerical method, which consisted of the DES and laminar models, and experimental results of low flow rate (11 L/hr.). It could be observed that the trend of numerical results was close to each other, although there were two peaks of the curve of the laminar model while the DES result established only one peak and a smoother curve. Furthermore, the remarkable shifted-left RTD curves can be seen in the experimental.
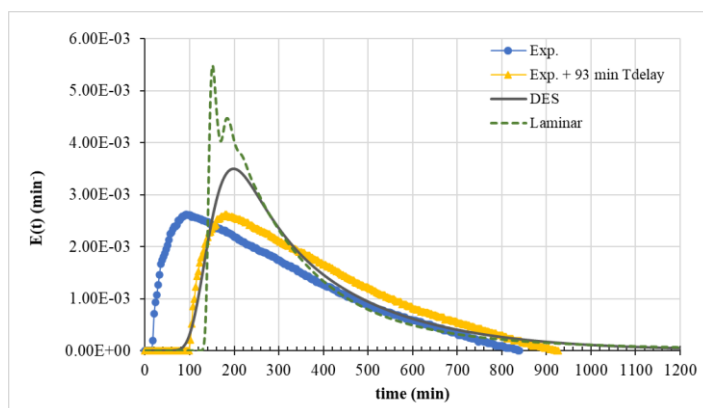
a) 11 L/hr.
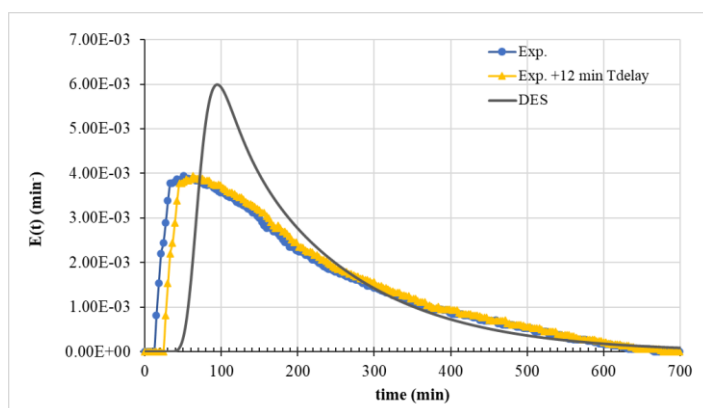
b) 19 L/hr.
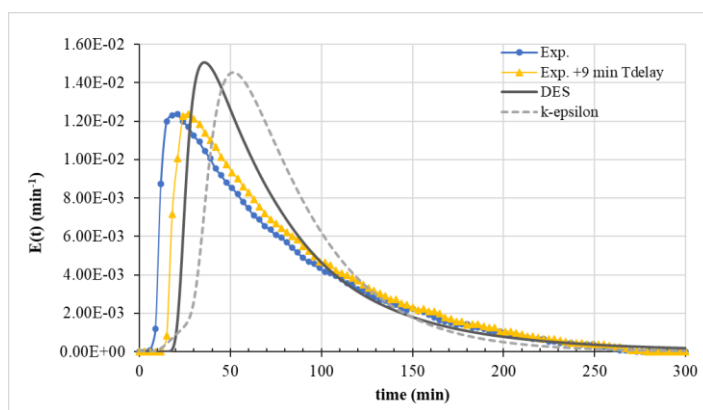
c) 49 L/hr.

Figure 5.4 RTD curves of experimental and numerical methods for the SSP

of (a) 11 L/hr., (b) 19 L/hr., and (c) 49 L/hr. flow rates

Then adjusting the experimental result thus was considered by adding 93 minutes (stand for T_{delay} on the Figure 5.4) at the beginning of the curve of the experiment result. The result adjusted was a better agreement with the DES model. Indeed, the curve's trend after the peak of the experimental result was a downward linear slope, while the shapes of both simulation models were downward exponential slopes. The results of the medium flow rate (19 L/hr.) are shown in Figure 5.4 (b), which was a comparison of only the result from the DES model and experiment. Again, the tracer signal of the experiment was very early detected if compared to the result of the DES model; thus that the 12 minutes delay time was also added at the beginning of the RTD curve. For the high flow rate (49 L/hr.) (see Figure 5.4 (c)), the curve of the experiment was compared with numerical curves from the standard k-ε model and DES since the standard k-ε model generally used to simulate the turbulent flow. The agreement between the experimental data and the result of the DES simulation model was more similar than the result from the standard k-ε model since the tracer's signal at the beginning and the peak of the curve were close to the experimental data. However, the 9 minutes delay still needs to be added to shift the trends signal curve of the experiment result getting closer to the RTD curve of the DES.

Comparing the agreement trend of the RTD experiment curves with the curves of numerical methods, it could be seen that if the flow rate increase, the trend of the RTD curve is closer to the simulation's results. For example, looking at Figure 5.4, the shape of the RTD experimental curve of the high flow rate (49 L/hr.) was the most similar to the model curve except for the early tracer's signal detected. In contrast, the shape of the RTD experimental curve of low flow rate (11 L/hr.) was quite a low-quality agreement due to the downward linear slope and also early tracer's signal detected. This illustrated that the simulated hydrodynamic was closer to the ideal flow more than the experiments; that was because there were more conditions in the experiment that affected the ideal state. For example, due to the action of recirculation loops, a part of the fluid that stayed around the wall caused the circular flow at the experiment or short circuit flow.

Notwithstanding, the analyzed data from the RTD curves are shown in Table 5.1. From the result, the numbers of time escape 10% of tracer throughout the outlet position,

mean residence time (t_m), and standard deviation (σ) of RTD-experiment adjusted and RTD-numerical were acceptable with maximum errors of 17%, 5%, and 6%, respectively. The trend of t_m examined values were likewise the general cases that t_m based on the experiment is less than the value of numerical prediction (S. Chen et al., 2019). Similarly, the skewness (s^3) values from RTD-experiment adjusted, and RTD-numerical were also acceptable with a maximum error of 15%. The results of skewness (s^3) were positive values in all cases; it means that the shapes of the RTD curves were in form skewed to the right or positively skewed, as shown in Figure 5.4. That was because there were long tails in the positive direction on time (x-axis). Besides, the skewness represents the deviation from the symmetry axis for the experiment is significantly less than that of simulation. Hence, the results derived from CFD simulation accord with the theoretical situation that seems to be more advisable. For these reasons, in the end, the mean residence time (t_m) values of the RTD experiment were approximately close to the calculated mean residence time values for the DES model with errors of 4.6%, 1.4%, and 1.9% of 11 L/hr., 19 L/hr, and 49 L/hr. flow rates, respectively. It could be attributed to the apparent effect of the beginning time deviation in the experiment, which is shown in Figure 5.4.

Table 5.1 Mean residence time distribution of the SSP from numerical and adjusted experimental data

Flow rate (L/hr.)	Method	t_{10} (min)	t_m (min)	Std. Deviation, σ (min)	Skewness, s^3 (-)
11	Experiment	159	365	180	0.71
	Numerical (DES model)	163	334	164	0.97
19	Experiment	60	210	139	0.91
	Numerical (DES model)	85	204	123	1.28
49	Experiment	27	81	54	1.10
	Numerical (DES model)	32	78	48	1.45

With the application of the pulse input method, the tracer injection technique took only a few seconds to perform smoothly injected tracer. More importantly, the time-step size was rather longer than the time-step size in CFD simulation; thus, the sampling quantity was limited to several dozens. Because of the complex fluidity of fluid, the initial sample in the outlet would inevitably experience the process of dissolution and dilution before the measurement of tracer is detected. In the process of metastasis, the error would be increased inadvertently.

In order to verify if the Navier-Stoke equation for DES flow solved represents the actual hydrodynamic profile and transport of a passive scalar of the SSP, the adjusted experimental RTD curves were compared with those obtained by Fluent 16.2. The RTD curves obtained were in agreement with experimental RTD curves (see Figure 5.4 and Table 5.1). It seemed that the difference in t_m between experiment and numerical technique was already within the acceptable range, with just a few exceptions that t_{10} is over 10%. Thus, the transport of a passive scalar described reasonably correctly the RTD curves in all cases. The value of t_m of DES showed an error lower than 5% respecting to t_m value obtained experimentally indicating that good fitting results (S. Chen et al., 2019; Plascencia-Jatomea et al., 2015). It was also worth noting that the s^3 obtained via numerical method increased with the long-tail curve, which is quite contrary to the value obtained via the experiment.

5.4 Precision Verification by Mean Residence Time

To examine the accuracy of the species transport for the internal age distribution method, the results from the internal age method have to be verified with the results of the RTD-numerical method with the adjusted delay conditions. In this step, the mean residence time from both numerical methods (RTD-numerical, and internal age) and the theoretical residence time were shown in Table 5.2 to compare and verify the data accuracy. The mean residence time from both methods should be either equal or close to theoretical residence time as long as the tracer has been carried out for a long enough time for all the tracer material to exit. The results show that the mean residence time distributions (t_m) from RTD-

numerical were close to the theoretical residence time with a maximum difference of 4.4% for the low flow rate (11 L/hr.) while the medium flow rate (19 L/hr.) and high flow rate (49 L/hr.) gave the difference of 1.2% and 1.9%, respectively. Again, the value of t_m of DES taken an error lower than 5% respecting to theoretical residence time (τ) that good fitting results (S. Chen et al., 2019; Plascencia-Jatomea et al., 2015).

The results from the internal age distribution method were also validated by comparing with the theoretical residence time (τ) in the first place. Then, they would be compared with the RTD-numerical results on several parameters that included mean residence time, standard deviation, and skewness to validate and check the accuracy of the data. For the first parameter or the first moment, that is mean residence time distribution; all of the results from internal age distribution were very close to RTD-numerical results with a maximum error of 4.3%. Furthermore, the results from the internal age method seemed to be more accurate than the RTD-numerical results if compared with the theoretical residence time (τ) since there were given maximum errors of 0.27%. It could be concluded that the results from the internal age distribution method can be accepted at this accuracy.

Table 5.2 Mean residence time of SSP by DES model

Theoretical residence time (min)	Mean residence time distribution (min)		Std. deviation, σ (min)		Skewness, s^3 (-)	
	Simulation method		Simulation method		Simulation method	
	RTD-numerical	Internal age distribution	RTD-numerical	Internal age distribution	RTD-numerical	Internal age distribution
365	334	364	164	222	0.97	1.69
209	204	209	123	146	1.28	1.96
81	78	81	48	53	1.45	2.89

The second moment that is the standard deviation (σ) of RTD, has been used in the literature to classify the flow of the reactors. For an ideal flow, the standard deviation of a

plug flow reactor is equal to 0. In case of comparison the standard deviation of non-ideal flow to the ideal flow, and standard deviation of non-ideal reactor can be exposed some kinds of flow characteristic. If a reactor has some features of a short-circuiting or some death zone, the residence time distribution tends to carry a narrow distribution because some tracer will leave the system earlier than the ideal flow. On the other hand, if a reactor has recirculation, the residence time distribution tends to carry a wide distribution because some tracer will be left in the system in the extended time. Therefore, the exit ages distribution will be a broader distribution with a larger standard than the ideal mix (Fu et al., 2018; Furman and Stegowski, 2011; Guo et al., 2018; Salem et al., 2011). For all the cases discussed in this article, the standard deviation values are widely due to recirculation in the flocculation zone.

Moreover, by comparing the standard deviation of different numerical methods that were reasonably well reported with errors of 15%, 8.6%, and 5% for 11 L/hr., 19 L/hr., and 49 L/hr., respectively. The reason for the range of error value of numerical methods is the errors caused by cutting the RTD curve tail too early or later. If it is too much greater, it is the magnifying effect of mean residence time. In contrast, if it is cut too early, it will be lost some portion of the mean residence time (M. Liu and Tilton, 2010). In this study, the tails of the RTD curve of numerical were cut at the precision were 10^{-6}.

The third moment is skewness (s^3) that is a measure of the asymmetry of the distribution. Positive skewness signifies that the long-age tail is larger than the small-age tail. For the large positive skewness of all cases were obtained at all the test point, caused by the long tail. The results reported that skewness received by the RTD-numerical method were less than the internal age method for all flow rate studied. To compare the third moment, the results from RTD-numerical methods could be agreed to the results from internal age, with just a few exceptions that the error is about 30%. This significant difference in value might be due to the effect of cutting the tail of the RTD curves of the RTD numerical method. It should be noted that the difference of t_m between RTD numerical prediction and internal age method was satisfactorily less than 5% for a wide

range of fluid flow, as listed in Table 5.2, which validates the dependability of mean residence time (t_m) results from both numerical methods.

From the data in Table 5.1 and Table 5.2, it can be seen that the results of CFD simulation (RTD-numerical and internal age) are basically consistent with the experimental results, which verifies the reliability of the present investigation. Thus, local contact time (t_{cont}) would be evaluated for the only flocculation zone, which was described in the next topic.

5.5 Spatial Distribution of Mean Age Distribution in Jet Clarifier

The spatial distribution of mean age and higher moment are obtained by solving by Equation 5.21 and Equation 5.22 with user-defined scalars in the Fluent program after the velocity field has been accessible. Contour plots of age are across a cross-section of the reactor. Figure 5.5 (a – c) shows independently the age distribution for the jet clarifier in the case of the SSP within various flow rates studied. The color shades are represented the internal age in seconds; the blue color represents the area that was the shortest time escape while the red one representing the longest time zone of the reactor. The character of the contour of an internal age whatever flow rate was quite similar except the time scale since there were the same hydrodynamic as described in the 5.3 section. Then, the Figure 5.5 (d – f) has thus been plotted the non-dimensional time (θ) defined as the ratio of t and the theoretical residence time, which were 365, 209, and 81 minutes for 11 L/hr., 19 L/hr., and 49 L/hr., flow rate, respectively. Again, the blue color represents the area that was the shortest time escape while the red one representing the longest time zone of the reactor. Hence, all figures of the non-dimensional time (θ) the maximum values of θ equal to 1. It meant that the mean resident time solved by CFD was equal to the theoretical mean residence time, which could be referred to the Table 5.1.
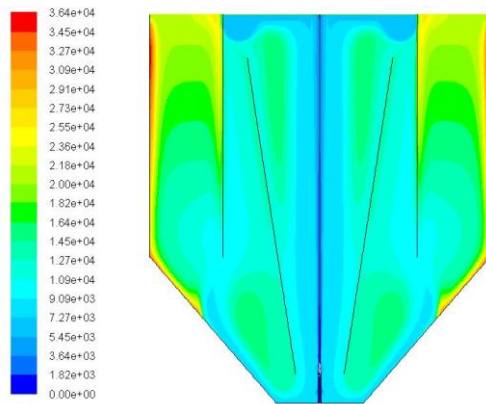
a) time (s), 11 L/hr.
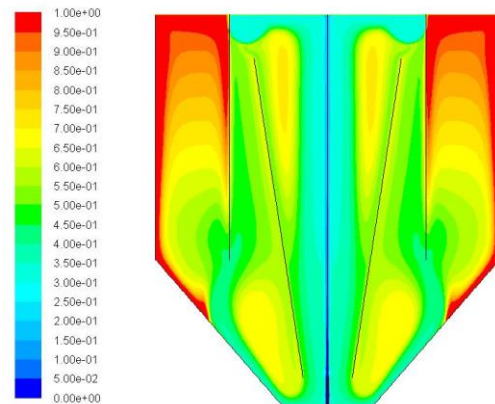
d) non-dimensional time (θ), 11 L/hr.
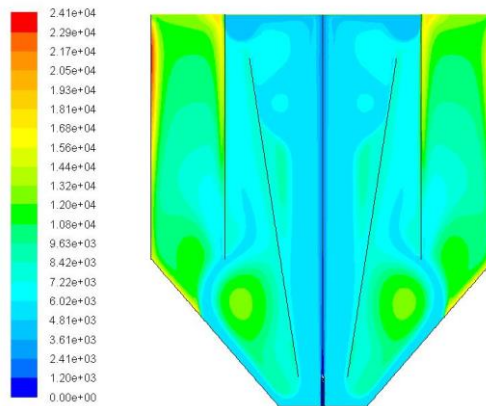
b) time (s), 19 L/hr.
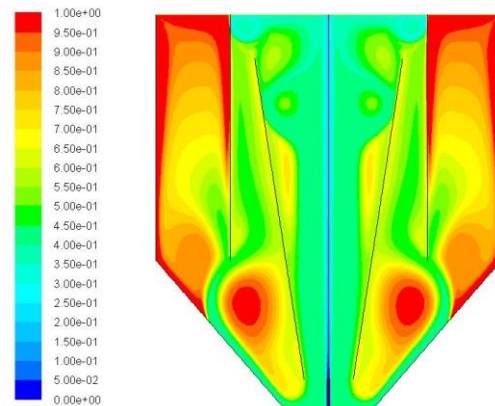
e) non-dimensional time (θ), 19 L/hr.
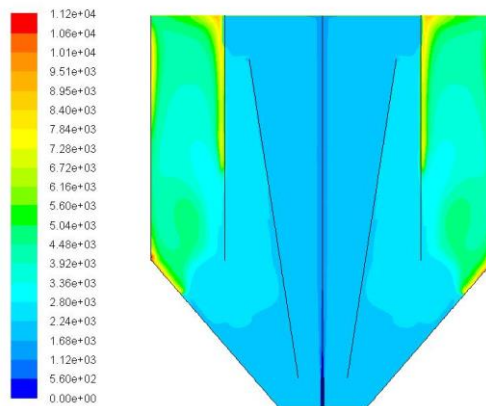
c) time (s), 49 L/hr.
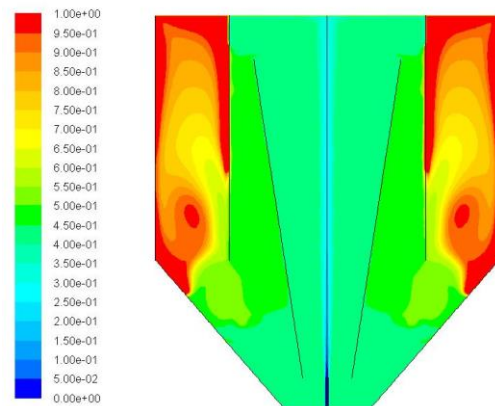
f) non-dimensional time (θ), 49 L/hr.

Figure 5.5 Contour of age distribution

Focusing on the flocculation zone, the mean residence time was estimated as the ratio of the volume of this zone (estimated to 6 liters) divided by the injected flow rate (Q). The residence times were thus equal to 33.2, 19.0, and 7.4 minutes, which were reported in Table 5.3 with the flocculation time by the internal method. It could be noticed that the values of resident time exported from the internal age method were larger than the theoretical residence time about 6 times of flow rate studied each since there were the recirculation loops within this zone. Moreover, the ratio of time from internal age divided by injected flow rate could be presented as the contour of the non-dimensional time (θ) as Figure 5.6. Again, the blue color represents the area that was the shortest time escape while the red one represents the longest time zone of the reactor. Hence, all figures of the non-dimensional time (θ) the maximum values of θ equal to 10 (the red position) while the most area of flocculation zone was about 6. It means that the resident time of some local positions was up to 10 times the mean theoretical residence time, while most of the flocculation areas were about 6 times theoretical residence time. Comparing Figure 5.6 to Figure 5.3, the positions were shown the area of high resident time, which were the circulation path in the flocculation zone and the circle or eye of the recirculation was created the results likewise PIV's results. Thereby, the number of recirculation loops within the flocculation zone could be estimated by the recirculation flow rate as described in the next paragraph.

Table 5.3 The residence time of flocculation zone by species transport for internal age distribution simulation

Injected flow rate (L/hr.)	The mean resident time of flocculation zone (min)		Standard deviation (σ) (min)	Ratio of Internal age/ Theoretical time
	Theoretical time (τ)	Internal age		
11	33.2	204	205	6
19	19.0	118	124	6
49	7.4	40	40	6

a) 11 L/hr.

b) 19 L/hr.

c) 49 L/hr.

Figure 5.6 Contour of the internal age distribution of flocculation zone

with non-dimensional time (θ)

The second moment (standard deviation (σ)) was also shown in Table 5.3. As expected, that their spatial distribution pattern was found to be the same as that of mean age; the more mean age value is, the large spatial distribution spread. The distribution of the normalized variance (CoV=$\sqrt{\sigma^2/\tau^2}$) was found to be the same. The contour plot of the normalized variance is shown in Figure 5.7. It meant that the character of the flow pattern of the SSP was perfectly mixed flow (CoV = 1) following by plug flow (CoV = 0) for all flow rates studied. In the flocculation zone, it can be noticed that the internal age is close to the standard deviation which is characteristic of an exponential distribution for the residence times and confirms again the perfectly mixed behavior of this zone.

In addition, it was reasonable evidence if compare the flow characteristic with both PIV results and the mixing results by solving velocity gradient (it can be seen in the following topic). The total area of the flocculation zone was indicated as a mixing area and follow by the plug flow of the settling zone.

a) 11 L/hr.

b) 19 L/hr.

c) 49 L/hr.
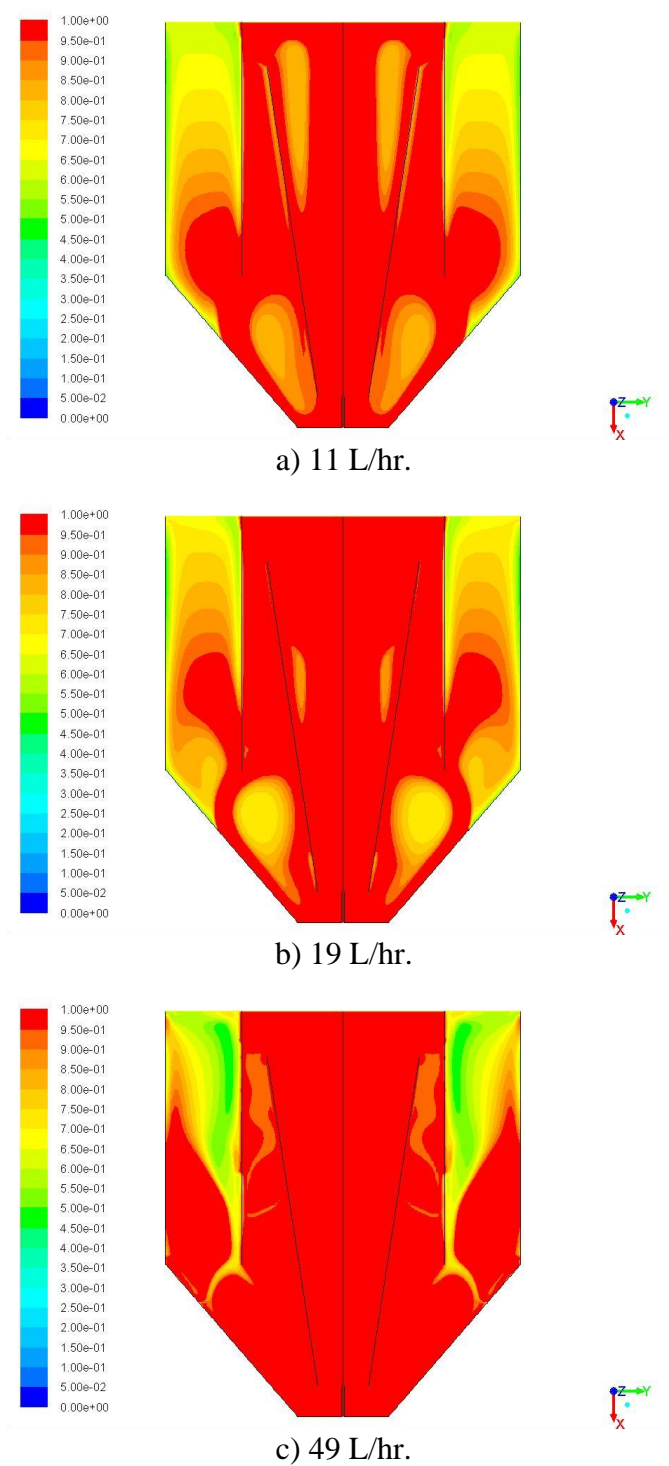
Figure 5.7 Contour of normalized variance of the SSP

The number of recirculation loops within the flocculation zone of the SSP could be estimated by Equation 5.27, while the flow rates of upward vertical of whatever injected flow rates could be determined by using Equation 5.28. The results were given in Table 5.4.

$$\text{Number of recirculation loop} = \frac{\text{Flow rate of upward of flocculation zone}}{\text{Injected flow rate}} \qquad \text{Equation 5.27}$$

$$\text{Flow rate} = \text{Velocity} \times \text{Area} \qquad \text{Equation 5.28}$$

Referred to Figure 5.3 in the topic of 5.2 there were the recirculation regions and the high velocity path generated by the jet at the center of the SSP, which could be reported the axial velocity at Y-axis = 328 mm. (middle range of Y-axis) versus the X-axis as shown in Figure 5.8. It could be seen that whatever flow rate, the radius of upward flow was about 0.01 m. At the same time, the axial velocities were proportional to the injected flow rate with the maximum at 1.48×10^{-1} m/s, 2.32×10^{-1} m/s, and 5.20×10^{-1} m/s for 11 L/hr., 19 L/hr., and 49 L/hr. flow rate, respectively.
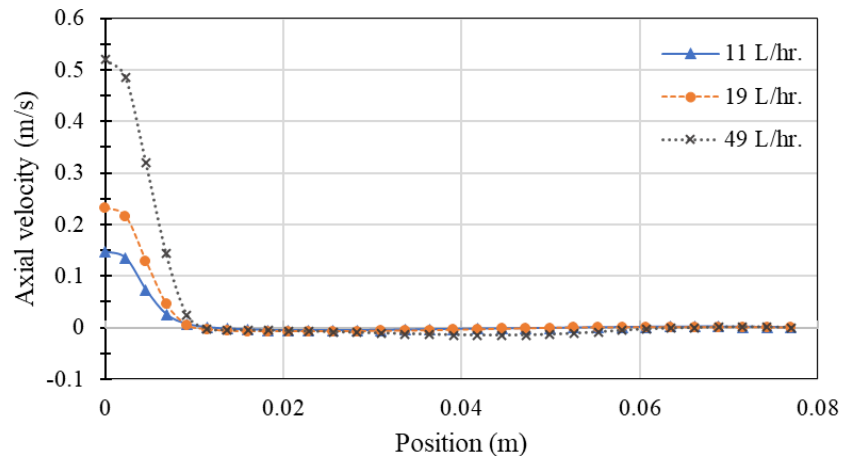
Figure 5.8 Axial velocity of jet flow of the SSP at Y-axis = 328 mm.

From Figure 5.8 could be implied that the radius of the jet plume was close to 10 mm. since the edges of the positive value of vertical velocity were located there, an axisymmetric jet could be assumed. As a result, it was possible to determine the upward vertical flow rate, which would be considered as circulating flow rate (Qc), by using the average values of the upward vertical velocity multiply by the area of the jet at the center of the SSP (cf. Figure 5.3). The results were given in Table 5.4. They range about 7 times the injected flow rates, indicating entrainment and a powerful recirculation in the flocculation zone.

Table 5.4 Estimation of the number of recirculation loops of SSP (from CFD)

Injected flow rate (L/hr.)	Axial velocity (m/s)		Upward flow rate (L/hr.)	The number of recirculation loops.
	Max	Average		
11	1.48×10^{-1}	6.46×10^{-2}	73	7
19	2.32×10^{-1}	1.25×10^{-2}	141	7
49	5.20×10^{-1}	2.99×10^{-2}	338	7

To compare the results between residence time of flocculation zone by species transport for internal age distribution simulation and the number of recirculation loops of SSP, the number of recirculation loops was very close to the ratio of the spatial distribution of mean age and theoretical residence time. The results thus could be satisfied with this validation. Characteristic time scales of the circulation thus have been summarized in Table 5.5.

Table 5.5 Processed hydrodynamic characteristics for the 3 flow rates of the SSP

Abbreviations	Parameters	Injected flow rate (Q) (L/hr.)		
		11	19	49
U (m/s)	Injection velocity	0.24	0.42	1.08
t_{RF} (min)	Residence time in flocculation zone	204	118	40
Q_c (L/hr.)	Circulation flow rate	73	141	338
Q_c/Q	Ratio of circulation flow rate and injected flow rate	7	7	7
t_c (min)	Circulation time	29.1	16.9	5.7

In conclusion, the results of Fluent showed the circulation loops inside the flocculation zone (see Figure 5.4), which were induced by jet flow. Whatever the flow rate, the number of recirculation loops was 7 with similar circulation patterns. The number of recirculation loops of the SSP was lower than the loops from the PIV results (15 loops) since it was in a quasi 2D geometry, whereas both results show that the numbers were constant with varying flowrates. Thus, the difference in the number of the recirculation loop is due to the geometry of the reactor (3D and Q2D jet clarifier). Then, the next step is to investigate the distribution of velocity gradients G.

5.6 Viscous Dissipation Rate of Turbulent Kinetic Energy (ε)

The contour of the viscous dissipation rate of TKE (Turbulent Kinetic Energy) in the whole volume of the reactor is shown in Figure 5.9. The maximum value of the color scale was set as 1×10^{-5} m^2/s^3, which was represented as red color and the minimum value was set as 0. It could be seen that the viscous dissipation rate of TKE occurs in the position near the inlet, the jet pathway at the middle of the SSP, and the located position of recirculation, where more turbulence flow takes place.
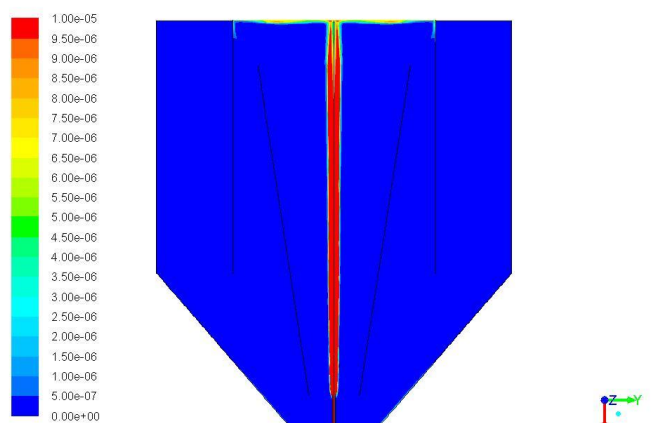
a) 11 L/hr.
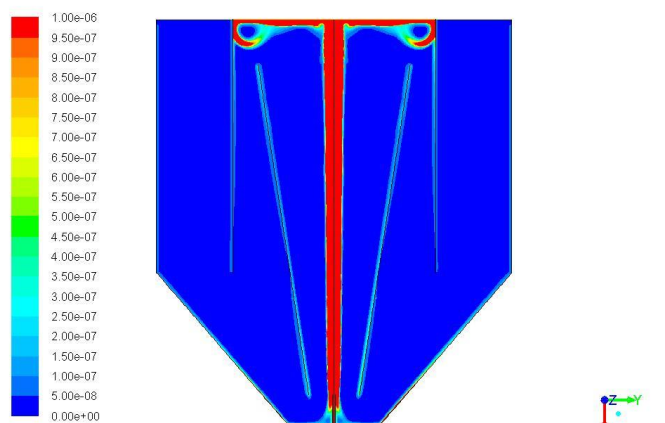
b) 19 L/hr.
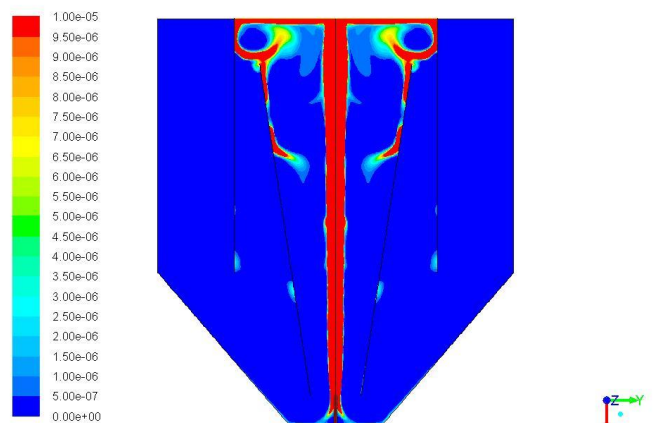
c) 49 L/hr.

Figure 5.9 The viscous dissipation rate of TKE of the SSP

Figure 5.9 presents the viscous dissipation rate of TKE in the flocculation of the SSP. Following the jet flow assumption, the viscous dissipation rate of TKE was decreasing along the liquid flow moving range. These results corresponded to the trend of the vertical velocity (V) profiles as seen in Figure 5.3. Thus, the viscous dissipation rate of TKE was highest at the position that was close to the injected nozzle. The minimum value of viscous dissipation rate of TKE on Y = 100 mm and Y = 300 mm could be seen in Table 5.6. It could be noticed that the ratio of the viscous dissipation rate of TKE at Y = 100 mm. of three flow rates is constant and, which is equal to 10 while the ratio at Y = 300 mm. is close to unity; the trend of the result was as same as the result of PIV experiment (cf. topic of 4.1.3) as well; whereas, the volume average values of the global viscous dissipation rate of TKE of the simulation were lower than the result of PIV about 10 times in a quasi 2D geometry.

Table 5.6 Viscous dissipation rate of TKE of the SSP

Flow rate (L/hr.)	Averaged turbulence kinetic energy dissipation rates (m^2/s^3)	The value of turbulence kinetic energy dissipation rates (m^2/s^3)	
		Y = 100 mm.	Y = 300 mm.
11	1.6×10^{-5}	2.3×10^{-4}	4.5×10^{-5}
19	2.3×10^{-4}	3.8×10^{-3}	2.6×10^{-4}
49	3.8×10^{-3}	6.0×10^{-2}	9.1×10^{-3}

Regarding the velocity gradient of the flocculation zone, it could be calculated based on the viscous dissipation rate of TKE recently presented. Thus, the next topic would present the local velocity gradient and the Camp number, product of velocity gradient, and contact time.

5.7 Velocity gradient (G) and Camp Number

Equation 5.29 describes the local velocity gradient (G) estimated based on the shear rate that can be defined in laminar flow and in turbulent flow, which was described in Equation 1.17 and Equation 1.19, could be simplified as Equation 5.30 and Equation 5.31, respectively. The average values of velocity gradient and their details are listed in Table 5.7.

$$G = \sqrt{\bar{\dot{\gamma}}^2 + \frac{\varepsilon'}{\nu}}$$ Equation 5.29

$$G_{\text{lam}} = \sqrt{\bar{\dot{\gamma}}^2}$$ Equation 5.30

$$G_{\text{turb}} = \sqrt{\frac{\varepsilon'}{\nu}}$$ Equation 5.31

The contour plots of G_{lam} and G_{turb} were presented in Figure 5.10 (a – b) and Figure 5.10 (c – d), respectively, for three flow rates (11, 19, and 49 L/hr.) and the contour plots of G would be shown in Figure 5.11. The shades of color represent the velocity gradient with the s^{-1} unit; the blue one represents the area that was zero to low-velocity gradient, while the red one represents the high velocity area located with a maximum of 5 s^{-1} of the reactor. As expected, the plot clearly shows the location of the height velocity gradient where the high velocity is located (at the symmetry axis).

a) G_{lam} (s^{-1}) of 11 L/hr.

d) G_{turb} (s^{-1}) of 11 L/hr.

b) G_{lam} (s^{-1}) of 19 L/hr.

e) G_{turb} (s^{-1}) of 19 L/hr.

c) G_{lam} (s^{-1}) of 49 L/hr.

f) G_{turb} (s^{-1}) of 49 L/hr.
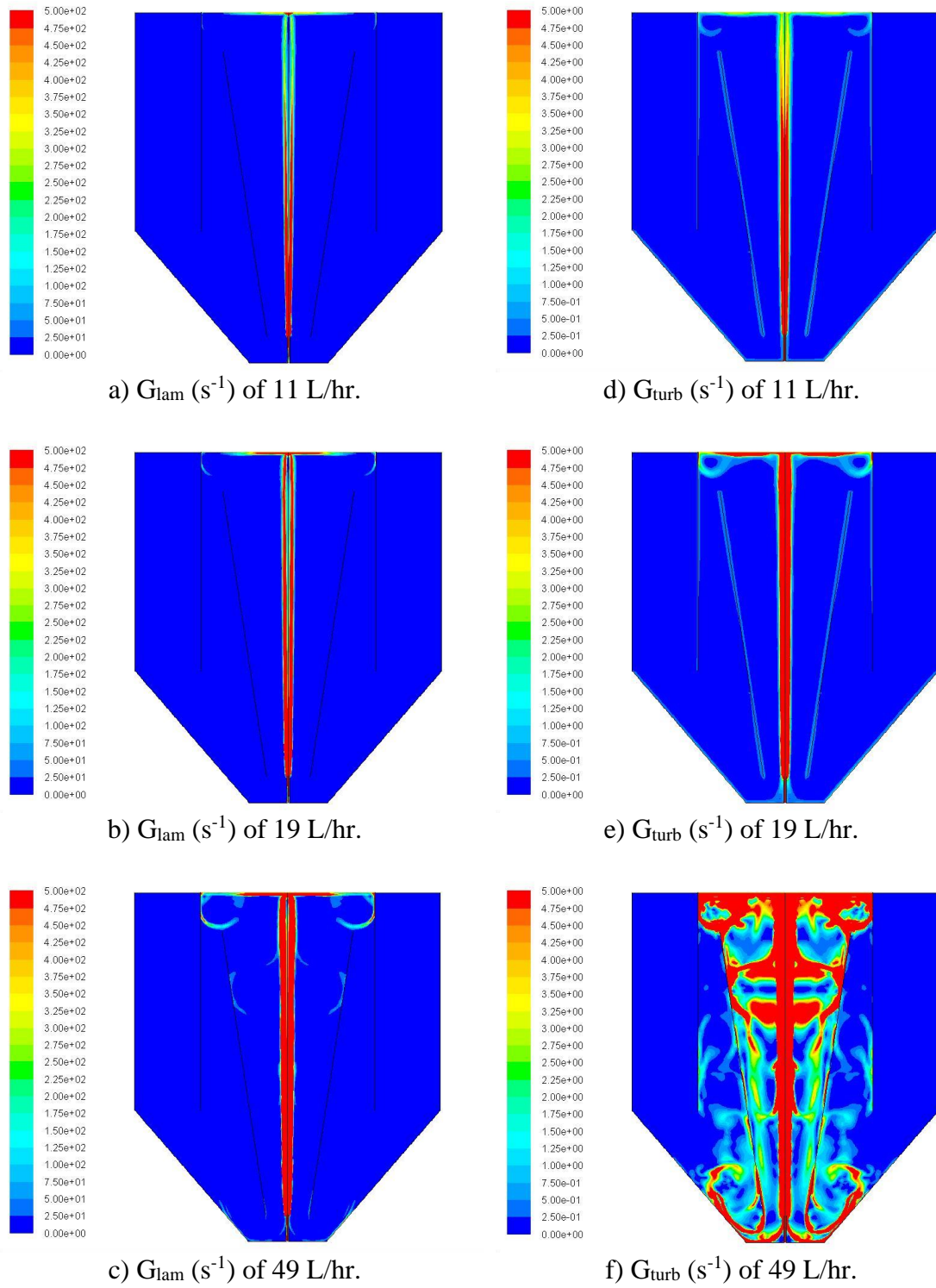
Figure 5.10 Contours of G_{lam} and G_{turb} of the SSP

a) velocity gradient (s^{-1}) of 11 L/hr.

d) Camp number of 11 L/hr.

b) velocity gradient (s^{-1}) of 19 L/hr.

e) Camp number of 19 L/hr.

c) velocity gradient (s^{-1}) of 49 L/hr.

f) Camp number of 49 L/hr.
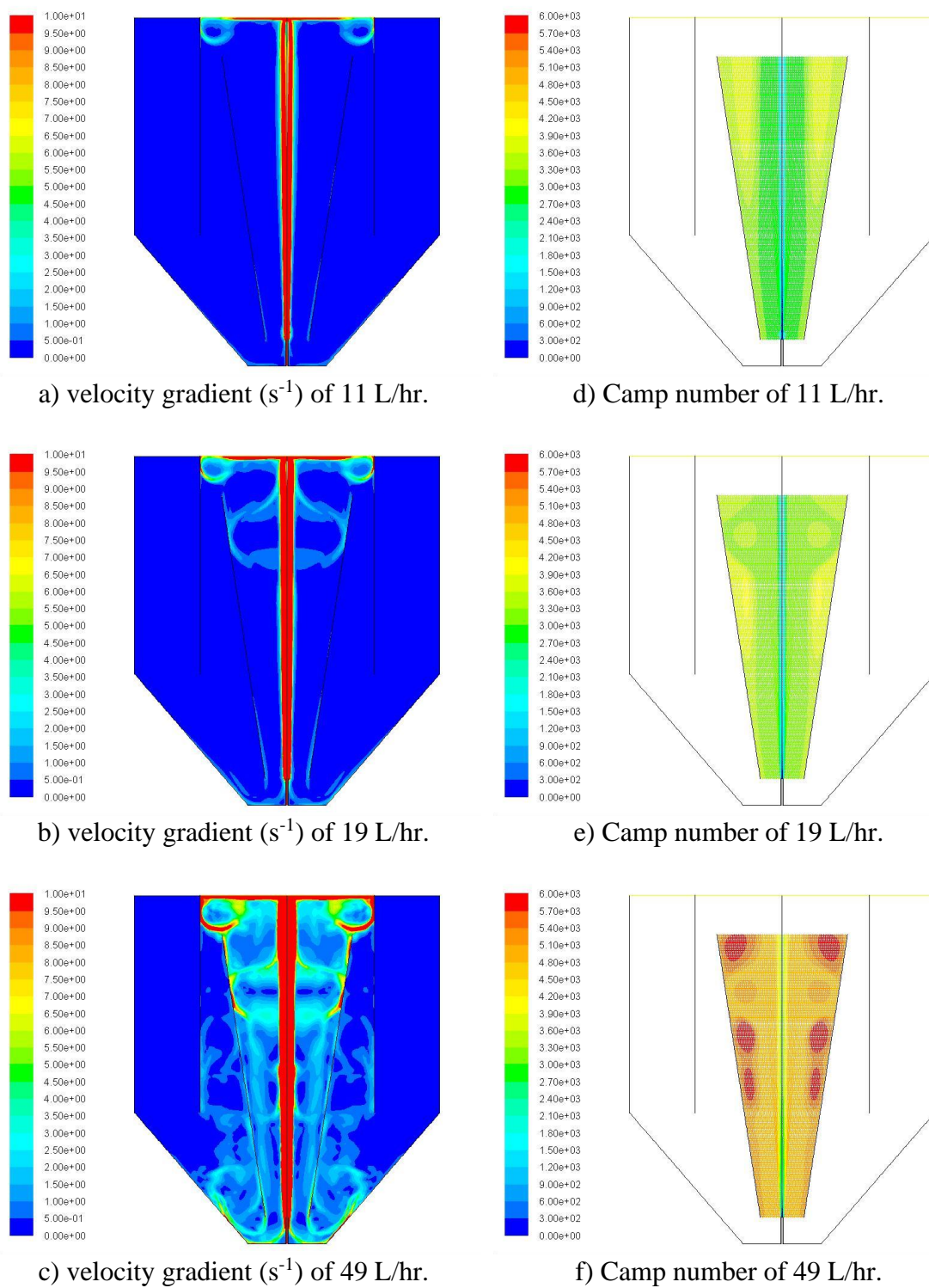
Figure 5.11 Contours of velocity gradient and Camp number of the SSP

Figure 5.11 (a – c) illustrates the contour of the velocity gradient. Once again, the shades of color are represented the velocity gradient; the blue one represents the area that was zero to low-velocity gradient while the red one representing the high velocity area with a maximum of 10 s^{-1} of the reactor. It could be seen that the character of the contour of the velocity gradient was the same trend as the viscous dissipation rate of TKE (cf. Figure 5.9). From the theory of the free jet, it is known that most of the kinetic energy of the jet be dissipated within a distance of 40 – 45 times to the diameter of the inlet tube (Pani and Patil, 2007). However, there was the recirculation within the flocculation zone as the results the characteristic of average velocity gradient (G) shown in the figure indicating high-velocity gradient zone in the recirculation pathway.

Table 5.7 Estimation of mixing parameter in flocculation zone of SSP, based on Fluent

Abbreviations	Parameters	Injected flow rate (Q) (L/hr.)		
		11	19	49
t_{AF} (min)	Internal age in flocculation zone	204	118	40
G_{lam} (s^{-1})	Average value of velocity gradient calculated by shear rate	0.61	1.12	3.45
G_{turb} (s^{-1})	Average value of velocity gradient calculated by dissipation rate of total kinetic energy	0.33	0.88	4.46
G (s^{-1})	Average value of velocity gradient	0.73	1.55	6.21
<Gt> (-)	Accumulative of Gt	3288	3390	5277
Gt (-)	Camp Number	4210	4851	7390

One was observed that as long as the camp number of the flocculation process lay in the range of 10,000 – 150,000 the performance of the flocculation zone has remained no effect (Qasim et al., 2000b). That is a vast range for a simple guideline to design the reactors. In this case, the usage of the camp number parameter, thought simple, cannot

explain the actual performance of the flocculation process. For instance, the performance of the jet clarifier had been estimated and reported. Concisely, turbidity removal efficiency of the jet clarifier at lowest and middle flow rate cases were very similar at approximately $80 \pm 3\%$ (referred topic of 3.1.1.2(v)). Although, the camp numbers of flocculation zone were less than the design criteria approximately 3 times. That is an interesting thing and perspective to investigate the cause of the performance of jet clarifiers in the future.

Finally, the results of the global parameter estimation for the whole jet clarifier solved by Fluent were summarized in Table 5.8. The global velocity gradients of the whole reactor were estimated and listed to compare to the estimation results of the velocity gradient of only the flocculation zone. It could be noticed that whatever flow rate the global velocity gradients of the whole reactor increased 4 times (the mean velocity gradient of the flocculation zone divided by the whole reactor). Again, the global velocity gradient on the whole jet clarifier tank seems to increase linearly with the jet flow rate, whereas the residence time decreases slightly linearly. Consequently, the Camp number remains 16000 – 30000 for the whole reactor, and it was in the range of 4,000 – 7,000 for the flocculation zone, whereas the Camp number of the Q2D jet clarifier shows the constant values in the result of PIV (the Camp numbers of the Q2D jet clarifier are approximately 29,000 and 7,000 of the whole reactor, and flocculation zone, respectively). However, the Camp number is meaningful only for the flocculation zone, but not for the whole reactor due to including the sedimentation zone.

In order to compare the Camp number of the flocculation zone between the SSP and the Q2D, the Camp number of the Q2D jet clarifier was higher about 2 times than the results of the SSP (cf. Table 4.7 and Table 5.7). It might be an effect of the geometry of the reactor (Q2D and 3D) since the volume of the flocculation zone was kept the same volume. Concurrently, the internal age of the SSP was larger than the mean residence time of the Q2D due to the total volume of the reactor, 67 and 42 litres of the SSP and the Q2D jet clarifier; respectively, it directly caused disparate mean resident time on the same flow rate operated.

Table 5.8 Values of velocity gradients in the whole jet clarifier, based on Fluent

Parameters	Injected flow rate (Q) (L/hr.)		
	11	19	49
$<G>$ (s^{-1}) of whole jet clarifier	0.24	0.43	1.58
$<G_{local}>$ of flocculation zone (s^{-1})	0.73	1.55	6.21
Mean residence time (τ) (min)	364	209	81
$<G_{local}> \times \tau$ (-)	15,943	19,437	30,181

In conclusion, the estimated parameter obtained in the SSP (3D-jet clarifier) used the axisymmetric simulation to describe the crucial parameters (velocity gradient, mean resident time, and Camp number). These are consistent with the PIV results in the Q2D reactor. For instance, there is a circulation loop with a circulation time during the residence time in the flocculation zone. The flocculation zone is thus a mixing zone very efficient to perform floc aggregation, followed by a clarification zone where the velocity gradient decrease progressively, and the residence time increase linearly with the velocity reduction due to the geometrical enlargement.

5.8 Summary

In this chapter, a Fluent-based 2D axisymmetric numerical model is used to analyze the hydrodynamics, such as velocity flow field, mean resident time or mean age distribution, velocity gradient, and camp number in order to understand the hydrodynamics cause the high efficiency of the jet clarifier. The initial study undertaken on the small scale prototype (SSP) was a simple case to examine the complex hydrodynamic for only one phase; no sludge and particle were incorporated in the liquid flow. Three flow rates were investigated which correspond to residence time from 1 to 6 hours. The mean resident time distribution (RTD) method was validated model first. Then, the local hydrodynamic analysis was evaluated, and the results were discussed separately into two parts including the flocculation zone, and the whole reactor. In the present work, numerical simulations with three advanced models (laminar, standard k-ε, and DES) were performed to study the

RTD-numerical of the SSP on flow rates and operation parameters. Also, the predictions of the SSP were compared to PIV results.

For the case studied, the results showed clearly behaviors of the liquid flow characteristic of the SSP. First, the result of residence time distribution, especially the RTD curves were used to validate the model. The time escape of molecule of 10% of tracer throughout the outlet position (t_{10}), mean residence time (t_m), and standard deviation (σ) of RTD-experiment and RTD-numerical were acceptable with maximum errors of 17%, 5%, and 6%, respectively. Meanwhile, the mean residence time (t_m) values of the RTD experiment were approximately close to the calculated mean residence time values for the DES model with errors of 4.6%, 1.4%, and 1.9% of 11 L/hr., 19 L/hr, and 49 L/hr. flow rates, respectively. The comparisons of RTD-experimental, that have been adjusted time delay at the beginning of the curves due to the difficulty calculates the mean residence time of the very low flow rate and the dilution of the tracer, and RTD-numerical curves were listed in Table 5.1.

Second, the velocity flow field indicated a large circulation loop (Figure 5.3). Whatever flow rates, the internal age of flocculation was 6 times the theoretical residence time of the flocculation zone, which was close to the number of recirculation flow rates within the flocculation zone. The flow structures (circulation) are similar, and the amplitude of the velocities are proportional to the inlet (jet) velocity as the PIV results. During the residence time in the flocculation zone, there is a loop of circulation with a circulation time 7 times smaller than the residence time. The flocculation zone of the SSP was thus a mixing zone very efficient to perform floc aggregation.

Finally, the velocity gradient and the mean residence time of both the flocculation zone and the whole reactor were estimated. For the flocculation zone, the range of the total velocity gradients (G) was about $1 - 6$ s^{-1} (Table 5.7) with turbulent contribution representing close to 40% of the total. Furthermore, the global velocity gradient of the whole reactor was in the range between $0.24 - 1.58$ s^{-1} (Table 5.8). Increasing the inlet jet flow rate, the global velocity gradients increase linearly with the jet flow rate, whereas the residence time decreases linearly; this trend was similar to the PIV result except for the

highest liquid flow rate. Consequently, the Camp number remains constant in this region where 7 loops are followed during the flocculation process; such circulation may contribute to the strength of the flocs. This result would be used to describe the efficiency of a jet clarifier related to floc aggregation during the flocculation process.

CHAPTER 6

CONCLUSION AND PERSPECTIVE

In this closing chapter, the general contexts and scientific actions of this work are briefly recapped. A final part opens a discussion on the scientific perspectives and future works by considering the methodology, the CFD simulations, and the application to industrial water treatment plants.

6.1 Conclusion

Among the various existing technologies for water treatment, the jet clarifier, that couples flocculation and clarification in a single unit, is considered as an effective and compact system. The reactor consists of two sections, corresponding to mixing (flocculation) and settling (clarification) zones. Upstream injection in the jet clarifier, the raw water is mixed with coagulants. It is injected at the inlet of the clarifier as a jet; the water thus flows through the mixing zone. In this zone, the flocculation occurs as destabilized particles aggregate into flocs. The flocs are then transported outside the mixing zone to the settling zone where they form a sludge blanket. If this blanket is thick enough, it may contribute too to floc separation. Reviewing the literature, hydrodynamic behaviours of such flocculators has received little interest. Most of the researchers were focusing on global performances (efficiency, producing rate, and concentrate of settled sludge, etc.). However, understanding local phenomena is necessary to optimize the overall performances of the jet clarifier.

In the first chapter, a literature review enabled to describe different aspects of water treatment, in particular related to flocculation and clarification. A key parameter characterizing the clarifiers is the Camp number. It is defined as the product of the velocity gradient and the residence time.

In the second chapter, material and methods are presented.

In the third chapter, the first series of experiments were conducted in Thailand, on two sizes of 3D jet clarifiers. The efficiency of such a geometry was assessed in terms of turbidity removal. Different geometrical parameters were investigated and their sensitivity to global parameters such as residence time was analysed. Furthermore, the reactor configuration (diameters of the truncated cone base) does not much affect the global hydrodynamics of the jet clarifier since the performance is stable even when changing the diameter of the truncated cone base. The appropriate conditions in terms of turbidity removal efficiency of the jet clarifier depend on several impact parameters, which can be divided into two sets.

- First, the liquid flow rates and the sludge blanket are the high impact factors of the design and operation due to their effects on efficiency.
- Second, sludge blanket's characteristics, tank's configuration, and water characteristics have less impact on the turbidity removal efficiency.

In the fourth chapter, the second series of experiments was conducted in Toulouse, on a quasi-2D jet clarifier. Such a geometry enables optical measurements in terms of velocity fields (based on PIV) and floc size distributions (based on floc image analysis). This chapter reveals a large circulation loop generated by the jet in the flocculation zone. This loop enables to understand the evolution of floc size inside this zone. The analysis of space averaged velocity gradient (G) and residence time in the flocculation zone are determined, enabling to revisit the parameter Gt, Camp number. In conclusion, the relative independence of the floc size distributions on the flow rate is discussed in the light of the Camp number which remained constant in the apparatus and can thus explain the efficiency of the jet clarifier in terms of flocculation. The advantage of this result (constant Gt for different flow rates) is an original and interesting finding since the jet clarifier is an efficient technology to remove turbidity of raw waters.

The last chapter is dedicated to CFD. CFD simulations are performed on the 3D jet clarifier. Such simulations are shown to be difficult to perform, but interesting results are obtained and discussed. From the hydrodynamic point of view, in general, the RTD results of the experiments and simulations were in good agreement, although there are some small

differences remaining between experiments and simulation. In particular, the delay time at the beginning of the RTD curves is not well predicted; however, it is not an important parameter on the jet and it might be the most tricky parameter to reproduce by numerical technique (CFD) because it is very challenging to get the delay when the flow rates are very low and the velocities at the outlet of jet clarifier are extremely small. Anyway, simulations reproduce the shape of experimental RTD curves, which is essential to perform scale-up/down based on the CFD.

6.2 Perspectives

Based on the present results, the first perspective may be to develop population balance modeling. It may be developed in terms of global hydrodynamic parameters or in terms of coupling with local CFD. In this second approach, settling of flocs could be considered in the CFD.

A second perspective could be to simulate the hydrodynamics of the jet clarifier using advanced model of turbulence, such as Large Eddy Simulation, for example.

In terms of industrial application, several issues are still open: impact of sludge blanket on both hydrodynamic and separation may be investigated; reshape the overflow in order to improve the operation of the jet clarifier.

REFERENCES

Aboubaraka, A. E., Aboelfetoh, E. F., and Ebeid, E.-Z. M. (2017). Coagulation effectiveness of graphene oxide for the removal of turbidity from raw surface water. *Chemosphere,* 181, 738-746. doi:https://doi.org/10.1016/j.chemosphere.2017.04.137

Adair, J. H., Suvaci, E., and Sindel, J. (2001). Surface and Colloid Chemistry. In K. H. J. Buschow, R. W. Cahn, M. C. Flemings, B. Ilschner, E. J. Kramer, S. Mahajan, & P. Veyssière (Eds.), *Encyclopedia of Materials: Science and Technology* (pp. 1-10). Oxford: Elsevier.

Adler, P. M. (1981). Streamlines in and around porous particles. *Journal of colloid and interface science,* 81(2), 531-535. doi:https://doi.org/10.1016/0021-9797(81)90434-3

Adrian, R. (1991). *Particle-Imaging Techniques For Experimental Fluid-Mechanics* (Vol. 23).

Al-Husseini, T. R., Ghawi, A. H., and Ali, A. H. (2019). Performance of hydraulic jump rapid mixing for enhancement of turbidity removal from synthetic wastewater: A comparative study. *Journal of Water Process Engineering,* 30, 100590. doi:https://doi.org/10.1016/j.jwpe.2018.03.005

Alkhaddar, R. M., Higgins, P. R., Phipps, D. A., and Andoh, R. Y. G. (2001). Residence time distribution of a model hydrodynamic vortex separator. *Urban Water,* 3(1), 17-24. doi:https://doi.org/10.1016/S1462-0758(01)00015-2

Alshikh, O. (2007). *Parameters affecting coagulation/flocculation of drinking water under cold temperatures*.

American Water Works, A. (1999). *Water quality and treatment: a handbook of community water supplies* (R. D. Letterman Ed. 5 ed.): McGraw-Hill.

Angeloudis, A., Stoesser, T., Gualtieri, C., and Falconer, R. A. (2016). Contact Tank Design Impact on Process Performance. *Environmental Modeling & Assessment,* 21(5), 563-576. doi:10.1007/s10666-016-9502-x

Baik, M. H., and Lee, S. Y. (2010). Colloidal stability of bentonite clay considering surface charge properties as a function of pH and ionic strength. *Journal of Industrial and Engineering Chemistry,* 16(5), 837-841. doi:https://doi.org/10.1016/j.jiec.2010.05.002

Bałdyga, J., and Bourne, J., R. . (1999). *Turbulent Mixing and Chemical Reactions*. Chichester, UK: John Wiley and Sons Ltd.

Barbot, E., Dussouillez, P., Bottero, J. Y., and Moulin, P. (2010). Coagulation of bentonite suspension by polyelectrolytes or ferric chloride: Floc breakage and reformation. *Chemical Engineering Journal,* 156(1), 83-91. doi:https://doi.org/10.1016/j.cej.2009.10.001

Bates, R. L., Fondy, P. L., and Corpstein, R. R. (1963). Examination of Some Geometric Parameters of Impeller Power. *Industrial & Engineering Chemistry Process Design and Development,* 2(4), 310-314. doi:10.1021/i260008a011

Bickley, W. (1937). The plane jet. *London Edinburgh Dublin Philos, Mag. J. Sci.,* 23(7), 727–731. doi:https://doi.org/10.1080/14786443708561847

Bittante, A., García-Serna, J., Biasi, P., Sobrón, F., and Salmi, T. (2014). Residence time and axial dispersion of liquids in Trickle Bed Reactors at laboratory scale. *Chemical Engineering Journal,* 250, 99-111. doi:https://doi.org/10.1016/j.cej.2014.03.062

Boadway, J. D. (1978). Dynamics of Growth and Breakage of Alum Floc in Presence of Fluid Shear. *Journal of the Environmental Engineering Division,* 104(5), 901-915. doi:doi:10.1061/JEEGAV.0000826

Boer, G. B. J., Weerd, C., Thoenes, D., and Goossens, H. W. J. (1987). Laser Diffraction Spectrometry: Fraunhofer Diffraction Versus Mie Scattering. *Particle & Particle Systems Characterization,* 4(1-4), 14-19. doi:https://doi.org/10.1002/ppsc.19870040104

Bohren, C. F., and Huffman, D. R. (1983). *Absorption and scattering of light by small particles*. New York: John Wiley & Sons.

Bouyer, D., Coufort, C., Liné, A., and Do-Quang, Z. (2005). Experimental analysis of floc size distributions in a 1-L jar under different hydrodynamics and physicochemical conditions. *Journal of colloid and interface science,* 292(2), 413-428. doi:https://doi.org/10.1016/j.jcis.2005.06.011

Bouyer, D., Escudié, R., and Liné, A. (2005). Experimental Analysis of Hydrodynamics in a Jar-test. *Process Safety and Environmental Protection,* 83(1), 22-30. doi:https://doi.org/10.1205/psep.03109

Bouyer, D., Liné, A., and Do-Quang, Z. (2004). Experimental analysis of floc size distribution under different hydrodynamics in a mixing tank. *AIChE Journal,* 50(9), 2064-2081. doi:doi:10.1002/aic.10242

Brandt, M. J., Johnson, K. M., Elphinston, A. J., and Ratnayaka, D. D. (2017). Chapter 8 - Storage, Clarification and Chemical Treatment. In M. J. Brandt, K. M. Johnson, A. J. Elphinston, & D. D. Ratnayaka (Eds.), *Twort's Water Supply (Seventh Edition)* (pp. 323-366). Boston: Butterworth-Heinemann.

Brannock, M., Wang, Y., and Leslie, G. (2010). Mixing characterisation of full-scale membrane bioreactors: CFD modelling with experimental validation. *Water Research,* 44(10), 3181-3191. doi:https://doi.org/10.1016/j.watres.2010.02.029

Bratby, J. (2016). *Coagulation and Flocculation in Water and Wastewater Treatment* (3 ed.). London, UK: IWA Publishing.

Camp, T. R. (1955). Flocculation and Flocculation Basins. *Transactions of the American Society of Civil Engineers,* 120(1), 1-16. doi:doi:10.1061/TACEAT.0007139

Camp, T. R., and Stein, P. C. (1943). Velocity gradients and internal work in fluid motion. *Boston Society of Civil Engineering,* 30, 219-237.

Cao, B., Gao, B., Xu, C., Fu, Y., and Liu, X. (2010). Effects of pH on coagulation behavior and floc properties in Yellow River water treatment using ferric based coagulants. *Chinese Science Bulletin,* 55(14), 1382-1387. doi:10.1007/s11434-010-0087-5

Chassaing, P. (2000). *Turbulence en Mécanique des Fluides; Analyse du phénomène en vue de sa modélisation à l'usage de l'ingénieur* (3 ed.): Polytech

Chen, S., Zhang, L., Wang, Y., Zhang, X., and Chen, W. (2019). Residence time distribution of high viscosity fluids falling film flow down outside of industrial-scale vertical wavy wall: Experimental investigation and CFD prediction. *Chinese Journal of Chemical Engineering,* 27(7), 1586-1594. doi:https://doi.org/10.1016/j.cjche.2018.12.022

Chen, W. F., and Liew, J. Y. R. (2002). *The Civil Engineering Handbook (2nd ed.)*: CRC Press.

Chu, V. H., and Lee, J. H. W. (1996). General Integral Formulation of Turbulent Buoyant Jets in Cross-Flow. *Journal of Hydraulic Engineering,* 122(1), 27-34. doi:doi:10.1061/(ASCE)0733-9429(1996)122:1(27)

Clark, M. (1985). Critique of Camp and Stein's RMS Velocity Gradient. *Journal of Environmental Engineering,* 111, 741-754.

Cleasby, J. L. (1984). Is Velocity Gradient a Valid Turbulent Flocculation Parameter. *Journal of Environmental Engineering,* 110, 875-897.

Coufort - Saudejaud, C., Bouyer, D., and Line, A. (2005). Flocculation related to local hydrodynamics in a Taylor–Couette reactor and in a jar. *Chemical Engineering Science - CHEM ENG SCI,* 60, 2179-2192. doi:10.1016/j.ces.2004.10.038

Coufort, C., Bouyer, D., and Liné, A. (2005). Flocculation related to local hydrodynamics in a Taylor–Couette reactor and in a jar. *Chemical Engineering Science,* 60(8), 2179-2192. doi:https://doi.org/10.1016/j.ces.2004.10.038

Coufort, C., Dumas, C., Bouyer, D., and Liné, A. (2008). Analysis of floc size distributions in a mixing tank. *Chemical Engineering and Processing: Process Intensification,* 47(3), 287-294. doi:https://doi.org/10.1016/j.cep.2007.01.009

Danckwerts, P. V. (1981). D2 - Local residence-times in continuous-flow systems. In P. V. Danckwerts (Ed.), *Insights Into Chemical Engineering* (pp. 229-230). Amsterdam: Pergamon.

DeCarlo, P. F., Slowik, J. G., Worsnop, D. R., Davidovits, P., and Jimenez, J. L. (2004). Particle Morphology and Density Characterization by Combined Mobility and Aerodynamic Diameter Measurements. Part 1: Theory. *Aerosol Science and Technology,* 38(12), 1185-1205. doi:10.1080/027868290903907

Degremont, S. A. (2007). *Water treatment handbook* (6 ed.). Paris: Degrémont : distributed by Lavoisier Publishing.

Deininger, A., Günthert, F. W., and Wilderer, P. A. (1996). The influence of currents on circular secondary clarifier performance and design. *Water Science and Technology,* 34(3), 405-412. doi:https://doi.org/10.1016/0273-1223(96)00605-1

Delichatsios, M. A., and Probstein, R. F. (1976). The Effect of Coalescence on the Average Drop Size in Liquid-Liquid Dispersions. *Industrial & Engineering Chemistry Fundamentals,* 15(2), 134-138. doi:10.1021/i160058a010

Dentel, S. K., Resta, J. J., Shetty, P. V., and Bober, T. A. (1988). Selecting Coagulant, Filtration, and Sludge-Conditioning Aids. *Journal (American Water Works Association),* 80(1), 72-84.

Duan, J., and Gregory, J. (2003). Coagulation by hydrolysing metal salts. *Advances in Colloid and Interface Science,* 100-102, 475-502. doi:https://doi.org/10.1016/S0001-8686(02)00067-2

Ducoste, J., and Clark, M. (1998). The Influence of Tank Size and Impeller Geometry on Turbulent Flocculation: I. Experimental. *Environmental Engineering Science - ENVIRON ENG SCI,* 15, 215-224. doi:10.1089/ees.1998.15.215

Ducoste, J. J., Clark, M. M., and Weetman, R. J. (1997). Turbulence in flocculators: Effects of tank size and impeller type. *AIChE Journal,* 43(2), 328-338. doi:10.1002/aic.690430206

Eaton, A. D., Clesceri, L. S., Franson, M. A. H., Association, A. P. H., Rice, E. W., Greenberg, A. E., . . . Federation, W. E. (2005). *Standard Methods for the Examination of Water & Wastewater*: American Public Health Association.

Eisma, D., and Kalf, J. (1996). In situ particle (floc) size measurements with the Nioz in situ camera system. *Journal of Sea Research,* 36(1), 49-53. doi:https://doi.org/10.1016/S1385-1101(96)90770-4

El Korchi, K., Alami, R., Saadaoui, A., Mimount, S., and Chaouch, A. (2019). Residence time distribution studies using radiotracers in a lab-scale distillation column: Experiments and modeling. *Applied Radiation and Isotopes,* 154, 108889. doi:https://doi.org/10.1016/j.apradiso.2019.108889

Elson, T. (2007). Chapter 6 Scale-Up in Chemical Engineering. In *Concepts of Chemical Engineering* 4 *Chemists* (pp. 171-202): The Royal Society of Chemistry.

EPA. (2019). Conventional Treatment. Retrieved August 10, 2019, from Drinking Water Treatability Database https://iaspub.epa.gov/tdb/pages/treatment/treatmentOverview.do

Eppler, B., Neis, U., and Hahn, H. H. (1975). Engineering Aspect of the Coagulation of colloidal Particles in Natural Water. *Progress in Water Technology, Pergamon press,,* 7(2), 207-216.

Escudié, R., and Liné, A. (2003). Experimental analysis of hydrodynamics in a radially agitated tank. *AIChE Journal,* 49(3), 585-603. doi:10.1002/aic.690490306

Essadki, A. H., Gourich, B., Vial, C., and Delmas, H. (2011). Residence time distribution measurements in an external-loop airlift reactor: Study of the hydrodynamics of the liquid circulation induced by the hydrogen bubbles. *Chemical Engineering Science,* 66(14), 3125-3132. doi:https://doi.org/10.1016/j.ces.2011.02.063

Fazli-Abukheyli, R., and Darvishi, P. (2019). Combination of axial dispersion and velocity profile in parallel tanks-in-series compartment model for prediction of residence time distribution in a wide range of non-ideal laminar flow regimes. *Chemical Engineering Science,* 195, 531-540. doi:https://doi.org/10.1016/j.ces.2018.09.052

Federico, M. (2005). *Flocculation dynamics of cohesive sediment.* (the degree of doctor), Delft University of Technology (TU Delft),

Fernandes del Pozo, D., Line, A., Van Geem, K., and Nopens, I. (2020). Experimental analysis of hydrodynamics induced by an axial impeller in a non-Newtonian fluid at different flow regimes. *AIChE Journal,* 66.

Fogler, H. S. (2006). *Elements of Chemical Reaction Engineering*: Prentice Hall PTR.

Forbes, D. C., Page, G. J., Passmore, M. A., and Gaylard, A. P. (2014). Computational study of wake structure and base pressure on a generic SUV model. In H. Park (Ed.), *The International Vehicle Aerodynamics Conference* (pp. 67-77). Oxford: Woodhead Publishing.

Fossett, H. (1951). The action of free jets in mixing of fluids. *Trans. Inst. Chem. Eng,* 29, 322 - 332.

Fossett, H., and Prosser, L. E. (1949). The Application of Free Jets to the Mixing of Fluids in Bulk. *Proceedings of the Institution of Mechanical Engineers,* 160(1), 224-232. doi:10.1243/pime_proc_1949_160_024_02

Fox, E. A., and Gex, V. E. (1956). Single-phase blending of liquids. *AIChE Journal,* 2(4), 539-544. doi:https://doi.org/10.1002/aic.690020422

François, R. J. (1987). Strength of aluminium hydroxide flocs. *Water Research,* 21(9), 1023-1030. doi:https://doi.org/10.1016/0043-1354(87)90023-6

Fu, H., Ma, L., and Wang, H. (2018). Experimental and numerical studies of residence time in SK direct contact heat exchanger for heat pump. *Chemical Engineering Research and Design,* 135, 94-102. doi:https://doi.org/10.1016/j.cherd.2018.05.013

Furman, L., and Stegowski, Z. (2011). CFD models of jet mixing and their validation by tracer experiments. *Chemical Engineering and Processing: Process Intensification,* 50(3), 300-304. doi:https://doi.org/10.1016/j.cep.2011.01.007

Gabelle, J.-C., Morchain, J., Anne-Archard, D., Augier, F., and Liné, A. (2013). Experimental determination of the shear rate in a stirred tank with a non-

newtonian fluid: Carbopol. *AIChE Journal,* 59(6), 2251-2266. doi:https://doi.org/10.1002/aic.13973

Gao, Y., Muzzio, F. J., and Ierapetritou, M. G. (2012). A review of the Residence Time Distribution (RTD) applications in solid unit operations. *Powder Technology,* 228, 416-423. doi:https://doi.org/10.1016/j.powtec.2012.05.060

Garland, C., Weber-Shirk, M., and Lion, L. W. (2017). Revisiting Hydraulic Flocculator Design for Use in Water Treatment Systems with Fluidized Floc Beds. *Environmental Engineering Science,* 34(2), 122-129. doi:10.1089/ees.2016.0174

Ghafari, S., Aziz, H. A., Isa, M. H., and Zinatizadeh, A. A. (2009). Application of response surface methodology (RSM) to optimize coagulation–flocculation treatment of leachate using poly-aluminum chloride (PAC) and alum. *Journal of Hazardous Materials,* 163(2), 650-656. doi:https://doi.org/10.1016/j.jhazmat.2008.07.090

Ghawi, A. H., and Abudi, Z. N. (2012). Improving the Performance of Conventional Wastewater Treatment Plants. *Iraqi Journal of Civil Engineering,* 8(1), 62-73.

Ghernaout, D., and Ghernaout, B. (2012). Sweep Flocculation as a Second Form of Charge Neutralisation-A Review. *Desalination and Water Treatment,* 44, 15-28. doi:10.1080/19443994.2012.691699

Ghernaout, D., Naceur, M. W., and Ghernaout, B. (2011). A review of electrocoagulation as a promising coagulation process for improved organic and inorganic matters removal by electrophoresis and electroflotation. *Desalination and Water Treatment,* 28(1-3), 287-320. doi:10.5004/dwt.2011.1493

González-Neria, I., Alonzo-Garcia, A., Martínez-Delgadillo, S. A., Mendoza-Escamilla, V. X., Yáñez-Varela, J. A., Verdin, P. G., and Rivadeneyra-Romero, G. (2019). PIV and dynamic LES of the turbulent stream and mixing induced by a V-grooved blade axial agitator. *Chemical Engineering Journal,* 374, 1138-1152. doi:https://doi.org/10.1016/j.cej.2019.06.033

Gregory, J. (1997). The density of particle aggregates. *Water Science and Technology,* 36(4), 1-13. doi:https://doi.org/10.1016/S0273-1223(97)00452-6

Gregory, J. (2006a). Chapter 3 - Floc formation and floc structure. In G. Newcombe & D. Dixon (Eds.), *Interface Science and Technology* (Vol. 10, pp. 25-43): Elsevier.

Gregory, J. (2006b). *Particles in Water: Properties and Processes*. Florida, USA.: CRC Press and Taylor & Francis Group.

Gregory, J. (2013). Flocculation Fundamentals. In T. Tadros (Ed.), *Encyclopedia of Colloid and Interface Science* (pp. 459-491). Berlin, Heidelberg: Springer Berlin Heidelberg.

Gregory, J. (2016). *Coagulation and Flocculation in Water and Wastewater Treatment*. London, UK: IWA Publishing.

Gregory, J., and Duan, J. (2001). Hydrolyzing metal salts as coagulants. *Pure and Applied Chemistry - PURE APPL CHEM,* 73, 2017-2026. doi:10.1351/pac200173122017

Grenville, R. K., and Tilton, J. N. (1996). A New Theory Improves the Correlation of Blend Time Data from Turbulent Jet Mixed Vessels. *Chem. Eng. Res. Des.,* 74, 390 - 396.

Grenville, R. K., and Tilton, J. N. (1997). Turbulence of flow as a predictor of blend time in turbulent jet mixed vessels. *Proceedings of* 9*th European Conference on Mixing*, 67 - 74

Grenville, R. K., and Tilton, J. N. (2011). Jet mixing in tall tanks: Comparison of methods for predicting blend times. *Chemical Engineering Research and Design,* 89(12), 2501-2506. doi:https://doi.org/10.1016/j.cherd.2011.05.014

Grotjans, H., and Menter, F. R. (1998). *Wall Functions for General Application CFD Codes.* Paper presented at the Proceedings of the Fourth EuropeanComputation Fluid Dynamics Conference, Chichester.

Guillas, S., Glover, N., and Malki-Epshtein, L. (2014). Bayesian calibration of the constants of the k–ε turbulence model for a CFD model of street canyon flow. *Computer Methods in Applied Mechanics and Engineering,* 279, 536-553. doi:https://doi.org/10.1016/j.cma.2014.06.008

Guo, X., Fan, Y., and Luo, L. (2018). Residence time distribution on flow characterisation of multichannel systems: Modelling and experimentation. *Experimental Thermal and Fluid Science,* 99, 407-419. doi:https://doi.org/10.1016/j.expthermflusci.2018.08.016

Hackley, V., Lum, L.-S., Gintautas, V., and Ferraris, C. (2004). Particle Size Analysis by Laser Diffraction Spectrometry: Application to Cementitious Powders. *NISTIR* 7097.

Ham, J.-H., and Platzer, B. (2004). Semi-Empirical Equations for the Residence Time Distributions in Disperse Systems – Part 1: Continuous Phase. *Chemical Engineering & Technology,* 27(11), 1172-1178. doi:10.1002/ceat.200407038

Han, M., and Lawler, D. F. (1992). The (Relative) Insignificance of G in Flocculation. *American Water Works Association,* 84(10), 79-91.

Hariganesh, S., Vadivel, S., Maruthamani, D., and Rangabhashiyam, S. (2020). Chapter 12 - Disinfection by-products in drinking water: detection and treatment methods. In M. N. V. Prasad (Ed.), *Disinfection By-products in Drinking Water* (pp. 279-304): Butterworth-Heinemann.

Harris, A. T., Davidson, J. F., and Thorpe, R. (2003). Particle residence time distributions in circulating fluidised beds. *Chemical Engineering Science,* 58, 2181-2202. doi:10.1016/S0009-2509(03)00082-4

Hassanien, W. A. M. (2004). *Physico-chemical Pre-treatment for Drinking Water.* (The Degree Of Doctor Of Philosophy In Chemistry), University of Khartoum,

He, W., Zhao, Z., Nan, J., Xie, Z., and Lu, W. (2018). The role of mixing hydrodynamics on floc growth in unbaffled square stirred-tank reactors for flocculation. *Journal of Environmental Chemical Engineering,* 6(2), 3041-3053. doi:10.1016/j.jece.2018.04.055

Hiby, J. W., and Modigell, M. (1978). *Experiments on jet agitation.* Paper presented at the 6th CHISA congress, Prague.

Hill, C. G., and Root, T. W. (2014). *Introduction to Chemical Engineering Kinetics and Reactor Design Charles* (2 ed.). New Jersey: John Wiley & Sons.

Honkanen, M., Eloranta, H., and Saarenrinne, P. (2010). Digital imaging measurement of dense multiphase flows in industrial processes. *Flow Measurement and Instrumentation,* 21(1), 25-32. doi:https://doi.org/10.1016/j.flowmeasinst.2009.11.001

Hsu, J.-P., and Liu, B.-T. (1998). Effect of Particle Size on Critical Coagulation Concentration. *Journal of colloid and interface science,* 198(1), 186-189. doi:https://doi.org/10.1006/jcis.1997.5275

Huang, M., Wang, Y., Cai, J., Bai, J., Yang, H., and Li, A. (2016). Preparation of dual-function starch-based flocculants for the simultaneous removal of turbidity and inhibition of Escherichia coli in water. *Water Research,* 98, 128-137. doi:https://doi.org/10.1016/j.watres.2016.04.009

Hughes, M. A. (2001). 4 - Coagulation and flocculation: Part I. In L. Svarovsky (Ed.), *Solid-Liquid Separation (Fourth Edition)* (pp. 104-129). Oxford: Butterworth-Heinemann.

Hunt, J. R. (1980). Prediction of Oceanic Particle Size Distributions from Coagulation and Sedimentation Mechanisms. In *Particulates in Water* (Vol. 189, pp. 243-257): AMERICAN CHEMICAL SOCIETY.

Hunter, R. J. (2001). *Foundations of colloid science* (2 ed.). Oxford ; New York: Oxford University Press.

Jarvis, P., Jefferson, B., Gregory, J., and Parsons, S. A. (2005). A review of floc strength and breakage. *Water Research,* 39(14), 3121-3137. doi:https://doi.org/10.1016/j.watres.2005.05.022

Jarvis, P., Jefferson, B., and Parsons, S. A. (2005). Breakage, Regrowth, and Fractal Nature of Natural Organic Matter Flocs. *Environmental Science & Technology,* 39(7), 2307-2314. doi:10.1021/es048854x

Jayanti, S. (2001). Hydrodynamics of jet mixing in vessels. *Chemical Engineering Science,* 56(1), 193-210. doi:https://doi.org/10.1016/S0009-2509(99)00588-6

Jones, W. P., and Launder, B. E. (1972). The prediction of laminarization with a two-equation model of turbulence. *International Journal of Heat and Mass Transfer,* 15(2), 301-314. doi:https://doi.org/10.1016/0017-9310(72)90076-2

Karimi, L., and Salem, A. (2011). The role of bentonite particle size distribution on kinetic of cation exchange capacity. *Journal of Industrial and Engineering Chemistry,* 17(1), 90-95. doi:https://doi.org/10.1016/j.jiec.2010.12.002

Kawamura, S. (2000). *Integrated Design and Operation of Water Treatment Facilities*: Wiley.

Kennedy, S., Bhattacharjee, P. K., Bhattacharya, S. N., Eshtiaghi, N., and Parthasarathy, R. (2018). Control of the mixing time in vessels agitated by submerged recirculating jets. *Royal Society Open Science,* 5(1), 171037. doi:doi:10.1098/rsos.171037

Kerker, M. (1969). The Scattering of Light and Other Electromagnetic Radiation *Academic Press*.

Kilander, J., Blomström, S., and Rasmuson, A. (2006). Spatial and temporal evolution of floc size distribution in a stirred square tank investigated using PIV and image analysis. *Chemical Engineering Science,* 61(23), 7651-7667. doi:https://doi.org/10.1016/j.ces.2006.09.001

Kim, H. S., Lamarche, C., and Verdier, A. (1982). Flocculation of Bentonite by non Ionic Polyelectrolyte: Influence of Cations. In L. Pawlowski (Ed.), *Studies in Environmental Science* (Vol. 19, pp. 101-113): Elsevier.

Kinoshita, T., Nakaishi, K., and Kuroda, Y. (2017). Determination of kaolinite floc size and structure using interface settling velocity. *Applied Clay Science,* 148, 11-16. doi:https://doi.org/10.1016/j.clay.2017.07.024

Klusener, P. A. A., Jonkers, G., During, F., Hollander, E. D., Schellekens, C. J., Ploemen, I. H. J., . . . Bos, A. N. R. (2007). Horizontal cross-flow bubble column reactors: CFD and validation by plant scale tracer experiments. *Chemical Engineering Science,* 62(18), 5495-5502. doi:https://doi.org/10.1016/j.ces.2007.03.044

Koohestanian, A., Hosseini, M., and Abbasian, Z. (2008). The Separation Method for Removing of Colloidal Particles from Raw Water. *Am.-Euras. J. Agric. & Environ. Sci.,* 4.

Kopeliovich, D. (2019). Stabilization of colloids. Retrieved August 23, 2019 http://www.substech.com/dokuwiki/doku.php?id=stabilization_of_colloids

Kotapati-Apparao, R., Forsythe, J., and Squires, K. (2003). Computation of the Flow Over a Maneuvering Spheroid. In 41*st Aerospace Sciences Meeting and Exhibit*: American Institute of Aeronautics and Astronautics.

Kramer, T., and Clark, M. (1997a). Influence of Strain-Rate on Coagulation Kinetics. *Journal of Environmental Engineering-asce - J ENVIRON ENG-ASCE,* 123. doi:10.1061/(ASCE)0733-9372(1997)123:5(444)

Kramer, T., and Clark, M. (1997b). Influence of Strain-Rate on Coagulation Kinetics. *Journal of Environmental Engineering,* 123(5), 444-452. doi:10.1061/(ASCE)0733-9372(1997)123:5(444)

Kramer, T. A., and Clark, M. M. (1999). Incorporation of Aggregate Breakup in the Simulation of Orthokinetic Coagulation. *Journal of colloid and interface science,* 216(1), 116-126. doi:https://doi.org/10.1006/jcis.1999.6305

Kretzschmar, R. (2005). Colloid-Facilitated Sorption and Transport In D. Hillel (Ed.), *Encyclopedia of Soils in the Environment* (pp. 276-284). Oxford: Elsevier.

Kundu, P. K. (1990). *Fluid Mechanics*. San Diego: Academic Press.

Kusters, K. A., Wijers, J. G., and Thoenes, D. (1997). Aggregation kinetics of small particles in agitated vessels. *Chemical Engineering Science,* 52(1), 107-121. doi:https://doi.org/10.1016/S0009-2509(96)00375-2

L. Marchisio, D., Dennis Vigil, R., and O. Fox, R. (2003). Implementation of the quadrature method of moments in CFD codes for aggregation–breakage problems. *Chemical Engineering Science,* 58(15), 3337-3351. doi:https://doi.org/10.1016/S0009-2509(03)00211-2

Lane, A. G. C., and Rice, P. (1981). An experimental investigation of jet mixing employing a vertical submerged jet. *International Chemical Engineering Symposium Series* 64:*K*1.

Lane, A. G. C., and Rice, P. (1982). An experimental investigation of jet mixing employing an inclined side entry jet. *Transaction of the Institution of Chemical Engineers,* 60, 171 - 176.

Laupsien, D., Cockx, A., and Line, A. (2021). The Organized Flow Structure of an Oscillating Bubble Plume. *AIChE Journal*. doi:10.1002/aic.17334

Laupsien, D., Men, C. L., Cockx, A., and Liné, A. (2019). Image processing for bubble morphology characteristics in diluted bubble swarms. *Physics of Fluids,* 31, 053306.

Lee, E. (2019). Chapter 1 - Electrophoresis of a Single Rigid Particle. In E. Lee (Ed.), *Interface Science and Technology* (Vol. 26, pp. 3-45): Elsevier.

Lee, H., and Hwang, W. (2019). Error quantification of 3D homogeneous and isotropic turbulence measurements using 2D PIV. *International Journal of Heat and Fluid Flow,* 78, 108431. doi:https://doi.org/10.1016/j.ijheatfluidflow.2019.108431

Levenspiel, O. (1999). *Chemical reaction engineering*: Wiley.

Levenspiel, O. (2013). *Chemical Reactor Omnibook*: Lulu.com.

Liu, M. (2012). Age distribution and the degree of mixing in continuous flow stirred tank reactors. *Chemical Engineering Science,* 69(1), 382-393. doi:https://doi.org/10.1016/j.ces.2011.10.062

Liu, M., and Tilton, J. N. (2010). Spatial distributions of mean age and higher moments in steady continuous flows. *AIChE Journal, 56*(10), 2561-2572. doi:10.1002/aic.12151

López-Jiménez, P. A., Escudero-González, J., Montoya Martínez, T., Fajardo Montañana, V., and Gualtieri, C. (2015). Application of CFD methods to an anaerobic digester: The case of Ontinyent WWTP, Valencia, Spain. *Journal of Water Process Engineering, 7*, 131-140. doi:https://doi.org/10.1016/j.jwpe.2015.05.006

Luckham, P. F., and Rossi, S. (1999). The colloidal and rheological properties of bentonite suspensions. *Advances in Colloid and Interface Science, 82*(1), 43-92. doi:https://doi.org/10.1016/S0001-8686(99)00005-6

Ma, J., Fu, K., Jiang, L., Ding, L., Guan, Q., Zhang, S., . . . Fu, X. (2017). Flocculation performance of cationic polyacrylamide with high cationic degree in humic acid synthetic water treatment and effect of kaolin particles. *Separation and Purification Technology, 181*, 201-212. doi:https://doi.org/10.1016/j.seppur.2017.03.027

Mackenzie L. Davis. (2010). *Water and Wastewater Engineering: Design Principles and Practice*. New York: McGraw-Hill Education.

Maggi, F., Manning, A. J., and Winterwerp, J. C. (2006). Image separation and geometric characterisation of mud flocs. *Journal of Hydrology, 326*(1), 325-348. doi:https://doi.org/10.1016/j.jhydrol.2005.11.005

Marques, R. D. O., and Ferreira, S. S. F. (2017). Flocculation kinetics of low-turbidity raw water and the irreversible floc breakup process. *Environmental Technology, 38*(7), 901-910. doi:10.1080/09593330.2016.1236149

Maruyama, T., Ban, Y., and Mizushin, T. (1981). Jet Mixing of Fluids in Tanks. *Chemical Engineering of Japan, 15*, 342-348.

Maruyama, T., Kamishima, N., and Mizushina, T. (1984). An investigation of bubble plume mixing by comparison with liquid jet mixing. *Journal of Chemical Engineering of Japan, 17*(2), 120 - 126 doi:https://doi.org/10.1252/jcej.17.120

Metcalf, Eddy, I., Tchobanoglous, G., Burton, F., and Stensel, H. D. (2002). *Wastewater Engineering: Treatment and Reuse*: McGraw-Hill Education.

Miljojkovic, D., Trepsic, I., and Milovancevic, M. (2019). Assessment of physical and chemical indicators on water turbidity. *Physica A: Statistical Mechanics and its Applications, 527*, 121171. doi:https://doi.org/10.1016/j.physa.2019.121171

Miller, D. R., and Comings, E. W. (1957). Static pressure distribution in a free turbulent jet. *Journal of Fluid Mechanics 3*, 1 - 16. doi:https://doi.org/10.1021/ie50570a029

MJ van der Zande, WMGT van den Broek, JH Muntinga, and KR van Heuven. (2001). *Droplet break-up in turbulent oil-in-water flow through restrictions in a pipe.* Paper presented at the 10th International Conference Multiphase, Cannes, France.

Mohammed, T. J., and Shakir, E. (2018). Effect of settling time, velocity gradient, and camp number on turbidity removal for oilfield produced water. *Egyptian Journal of Petroleum,* 27(1), 31-36. doi:https://doi.org/10.1016/j.ejpe.2016.12.006

Mollendorf, J., and Gebhart, B. (1973). An experimental and numerical study of the viscous stability of a round laminar vertical jet with and without thermal buoyancy for symmetric and asymmetric disturbances. *Journal of Fluid Mechanics,* 61(2), 367-399. doi:doi:10.1017/S0022112073000765

Moran, S. (2018). Chapter 7 - Clean water unit operation design: Physical processes. In S. Moran (Ed.), *An Applied Guide to Water and Effluent Treatment Plant Design* (pp. 69-100): Butterworth-Heinemann.

Mullen, K. (2020). Information on Earth's Water. from The Groundwater Association https://www.ngwa.org/what-is-groundwater/About-groundwater/information-on-earths-water

MWA. (2019). *Statistic of water quality*. bangkok, Thailand: Metropolitan Waterworks Authority.

Naceradska, J., Pivokonska, L., and Pivokonsky, M. (2019). On the importance of pH value in coagulation. *Journal of Water Supply: Research and Technology-Aqua,* 68(3), 222-230. doi:10.2166/aqua.2019.155

National Research Council (US) Safe Drinking Water Committee. (1977). Drinking Water and Health, Solid Particles in Suspension. Retrieved August 10, 2019, from National Academies Press (US) https://www.ncbi.nlm.nih.gov/books/NBK234169/

Nauman, E. B., and Buffham, B. A. (1983). *Mixing in Continuous Flow Systems*. New York: John Wiley & Sons Inc.

O'Kennedy, R., Murphy, C., and Lysakova-Devine, T. (2016). Technology advancements in antibody purification. *Antibody Technology Journal, Volume* 6, 17-32. doi:10.2147/ANTI.S64762

O'Melia, C. R. (1978). Coagulation in Wastewater Treatment. In K. J. Ives (Ed.), *The Scientific Basis of Flocculation* (pp. 219-268). Dordrecht: Springer Netherlands.

Ogedengbe, O. (1984). Alkalinity Consumption during Water Coagulation. *Journal of Environmental Engineering,* 110(1), 290-295. doi:doi:10.1061/(ASCE)0733-9372(1984)110:1(290)

Ohshima, H. (2014). Chapter 1 - Interaction of colloidal particles. In H. Ohshima & K. Makino (Eds.), *Colloid and Interface Science in Pharmaceutical Research and Development* (pp. 1-28). Amsterdam: Elsevier.

Oyegbile, B., Ay, P., and Narra, S. (2016). Flocculation kinetics and hydrodynamic interactions in natural and engineered flow systems: A review. *Environmental Engineering Research,* 21, 1-14. doi:10.4491/eer.2015.086

Palacios, Ò. C. (2010). *IN THE WAKE OF BUBBLES: VELOCITY FIELD MEASUREMENT BY PIV TECHNIQUE.* (Master's Thesis), INSA Toulouse,

Pani, B. S., and Patil, L. G. (2007). Single-basin jet flocculators. *Journal of Hydro-environment Research,* 1(1), 20-29. doi:10.1016/j.jher.2007.04.002

Pant, H. J., Sharma, V. K., Shenoy, K. T., and Sreenivas, T. (2015). Measurements of liquid phase residence time distributions in a pilot-scale continuous leaching reactor using radiotracer technique. *Applied Radiation and Isotopes,* 97, 40-46. doi:https://doi.org/10.1016/j.apradiso.2014.12.010

Parker, D. S., Kaufman, W. J., and Jenkins, D. (1972). Floc Breakup in Turbulent Flocculation Processes. *Journal of the Sanitary Engineering Division,* 98(1), 79-99. doi:doi:10.1061/JSEDAI.0001389

Patel, H., and Vashi, R. T. (2015). Chapter 2 - Characterization of Textile Wastewater. In H. Patel & R. T. Vashi (Eds.), *Characterization and Treatment of Textile Wastewater* (pp. 21-71). Boston: Elsevier.

Pearce, A. F. (1965). *Reynolds Number effects in submerged jets.* (M.Sc.), University of Natal,

Pedocchi, F., and Piedra-Cueva, I. (2005). Camp and Stein's Velocity Gradient Formalization. *Journal of Environmental Engineering,* 131, 1369-1376. doi:10.1061/(ASCE)0733-9372(2005)131:10(1369)

Perumal, R., and Saravanan, K. (2012). Experimental Investigation on Mixing time Analysis of Jet Mixer. *Research Journal of Engineering Sciences,* 1(5), 7-11.

Phuan, Y. W., Ismail, H. M., Garcia-Segura, S., and Chong, M. N. (2017). Design and CFD modelling of the anodic chamber of a continuous PhotoFuelCell reactor for water treatment. *Process Safety and Environmental Protection,* 111, 449-461. doi:https://doi.org/10.1016/j.psep.2017.08.019

Plascencia-Jatomea, R., Almazán-Ruiz, F. J., Gómez, J., Rivero, E. P., Monroy, O., and González, I. (2015). Hydrodynamic study of a novel membrane aerated biofilm reactor (MABR): Tracer experiments and CFD simulation. *Chemical Engineering Science,* 138, 324-332. doi:https://doi.org/10.1016/j.ces.2015.08.004

Pougatch, K., Delfel, S., Hosseini, M., Moyls, B., Sadighian, A., and Revington, A. (2021). Population balance modelling of dense clay slurries flocculation. *Chemical Engineering Science,* 231, 116260. doi:https://doi.org/10.1016/j.ces.2020.116260

Qasim, S. R., Motley, E. M., and Zhu, G. (2000a). Coagulation, Flocculation and precipitation. In *Water Works Engineering: Planning, Design, and Operation* (pp. 229 - 230). New Jersey, USA Prentice Hall PTR.

Qasim, S. R., Motley, E. M., and Zhu, G. (2000b). *Water Works Engineering: Planning, Design, and Operation*: Prentice Hall PTR.

Ramphal, S., and Sibiya, M. (2014). Optimization of coagulation-flocculation parameters using a photometric dispersion analyser. *Drinking Water Engineering and Science Discussions,* 7, 95-120. doi:10.5194/dwesd-7-95-2014

Randive, P. S., Singh, D. P., Varghese, V., and Badar, A. M. (2018). Study of Jet Mixing in Flocculation Process. *International Journal of Innovative Research in Engineering & Multidisciplinary Physical Sciences,* 6(4), 76-85.

Ratnayaka, D. D., Brandt, M. J., and Johnson, K. M. (2009). CHAPTER 7 - Storage, Clarification and Chemical Treatment. In D. D. Ratnayaka, M. J. Brandt, & K. M. Johnson (Eds.), *Water Supply (Sixth Edition)* (pp. 267-314). Boston: Butterworth-Heinemann.

Rattanakawin, C. (2005). Aggregate size distributions in sweep flocculation. *Songklanakarin Journal of Science and Technology,* 27.

Ravi, R., Vinu, R., and Gummadi, S. N. (2017). *Coulson and Richardson's Chemical Engineering* (Vol. 3A: Chemical and Biochemical Reactors and Reaction Engineering): Elsevier Science.

Ravina, L. (1993). *Everything You Want to Know about Coagulation & Flocculation*. Virginia: Zeta-Meter, Inc.

Ren, P., Nan, J., Zhang, X., and Zheng, K. (2017). Analysis of floc morphology in a continuous-flow flocculation and sedimentation reactor. *Journal of Environmental Sciences,* 52, 268-275. doi:https://doi.org/10.1016/j.jes.2016.04.007

Reynolds, O. (1883). An experimental investigation of the circumstances which determine whether the motion of water shall be direct or sinuous, and of the law of resistance in parallel channels. *Philosophical Transactions of the Royal Society of London,* 174, 935-982. doi:https://doi.org/10.1098/rstl.1883.0029

Reynolds, T. D., and Richards, P. A. (1996). *Unit Operations and Processes in Environmental Engineering*: PWS Publishing Company.

Romphophak, P. (2013). *Turbidity Removal by Solid Contact Clarifier with Sludge Recirculation.* (Master of Engineering Program in Environomental Engineering), Chulalongkorn University, Thailand.

Romphophak, P., Wongwailikhit, K., Chawaloesphonsiya, N., Samornkraisorakit, P., and Painmanakul, P. (2016). Study of Flow Pattern in Jet Clarifier for Removal of Turbidity by Residence Time Distribution Approach. *Engineering Journal,* 20(2), 17-27. doi:10.4186/ej.2016.20.2.17

Saarenrinne, P., and Piirto, M. (2000). Turbulent kinetic energy dissipation rate estimation from PIV velocity vector fields. *Experiments in Fluids,* 29(1), S300-S307. doi:10.1007/s003480070032

Saffman, P. G., and Turner, J. S. (1956a). On the collision of drops in turbulent clouds. *Journal of Fluid Mechanics,* 1, 16-30.

Saffman, P. G., and Turner, J. S. (1956b). On the collision of drops in turbulent clouds. *Journal of Fluid Mechanics,* 1(1), 16-30. doi:10.1017/S0022112056000020

Sahu, O. P., and Chaudhari, P. K. (2013). Review on Chemical treatment of Industrial Waste Water. *Journal of Applied Sciences and Environmental Management,* 17. doi:10.4314/jasem.v17i2.8

Salem, A. I., Okoth, G., and Thöming, J. (2011). An approach to improve the separation of solid–liquid suspensions in inclined plate settlers: CFD simulation and experimental validation. *Water Research,* 45(11), 3541-3549. doi:https://doi.org/10.1016/j.watres.2011.04.019

Sano, M., Kamino, A., and Shinkai, S. (2000). Critical Coagulation of Langmuir Monolayers: 2D Schulze−Hardy Rule. *The Journal of Physical Chemistry B,* 104(44), 10339-10347. doi:10.1021/jp002387y

Saritha, V., Karnena, M. K., and Dwarapureddi, B. K. (2019). "Exploring natural coagulants as impending alternatives towards sustainable water clarification" – A comparative studies of natural coagulants with alum. *Journal of Water Process Engineering,* 32, 100982. doi:https://doi.org/10.1016/j.jwpe.2019.100982

Sarpola, A., Hellman, H., Hietapelto, V., Jalonen, J., Jokela, J., Rämö, J., and Saukkoriipi, J. (2007). Hydrolysis products of water treatment chemical aluminium sulfate octadecahydrate by electrospray ionization mass spectrometry. *Polyhedron,* 26(12), 2851-2858. doi:https://doi.org/10.1016/j.poly.2007.01.035

Saxena, K., Brighu, U., and Choudhary, A. (2018). Parameters affecting enhanced coagulation: a review. *Environmental Technology Reviews,* 7(1), 156-176. doi:10.1080/21622515.2018.1478456

Scharnowski, S., Grayson, K., de Silva, C. M., Hutchins, N., Marusic, I., and Kähler, C. J. (2017). Generalization of the PIV loss-of-correlation formula introduced by Keane and Adrian. *Experiments in Fluids,* 58(10), 150. doi:10.1007/s00348-017-2431-x

Schiestel, R. (1993). *Modélisation et simulation des écoulements turbulents.* Paris: Hermes Science Publications.

Schlichting, H. (1979). *Boundary Layer Theory* (7 ed.). New York McGraw-Hill.

Selomulya, C., Amal, R., Bushell, G., and Waite, T. D. (2001). Evidence of Shear Rate Dependence on Restructuring and Breakup of Latex Aggregates. *Journal of colloid and interface science,* 236(1), 67-77. doi:https://doi.org/10.1006/jcis.2000.7372

Selomulya, C., Bushell, G., Amal, R., and Waite, T. D. (2003). Understanding the role of restructuring in flocculation: The application of a population balance model. *Chemical Engineering Science,* 58(2), 327-338. doi:https://doi.org/10.1016/S0009-2509(02)00523-7

Shah, M. T., Parmar, H. B., Rhyne, L. D., Kalli, C., Utikar, R. P., and Pareek, V. K. (2019). A novel settling tank for produced water treatment: CFD simulations and PIV experiments. *Journal of Petroleum Science and Engineering,* 182, 106352. doi:https://doi.org/10.1016/j.petrol.2019.106352

Shaikh, S. M. R., Nasser, M. S., Hussein, I. A., and Benamor, A. (2017). Investigation of the effect of polyelectrolyte structure and type on the electrokinetics and flocculation behavior of bentonite dispersions. *Chemical Engineering Journal,* 311, 265-276. doi:https://doi.org/10.1016/j.cej.2016.11.098

Shammas, N. (2007). Coagulation and Flocculation. In L. K. Wang, Y. Hung, & N. K. Shammas (Eds.), *Physicochemical Treatment Processes* (Vol. 3, pp. 103-139): Humana Press.

Shen, X., and Maa, J. P. Y. (2016). A camera and image processing system for floc size distributions of suspended particles. *Marine Geology,* 376, 132-146. doi:https://doi.org/10.1016/j.margeo.2016.03.009

Shur, M., Spalart, P. R., Strelets, M., and Travin, A. (1999). Detached-eddy simulation of an airfoil at high angle of attack. In W. Rodi & D. Laurence (Eds.), *Engineering Turbulence Modelling and Experiments* 4 (pp. 669-678). Oxford: Elsevier Science Ltd.

Simons, S. (2016). *Concepts of Chemical Engineering for Chemists (Second Edition)*: Royal Society of Chemistry.

Singh, A. K., and Dara, S. S. (2004). *Basic of Engineering Chemistry* New-Delhi: S. Chand Limited.

Snoeyink, V. L., and Jenkins, D. (1980). *Water Chemistry*. New York: John Wiley & Sons.

Sobrinho, J. A. H., Thiem, L. T., and Alkhatib, E. A. (1996). Optimizing submerged jet flocculator performance. *Journal American Water Works Association,* 88(8), 81-92. doi:https://doi.org/10.1002/j.1551-8833.1996.tb06602.x

Sohrabi, Y., Nafez, A., Mirzaei, N., Bagheri, A., Ghadiri, K., Rezaei, S., and Charganeh, S. S. (2018). Chemical coagulation efficiency in removal of water turbidity. *International Journal of Pharmaceutical Research,* 10, 188-194.

Sonin, A. (2019). Basics of Turbulent Flow Retrieved October 09, 2019, from Massachusetts Institute of Technology http://www.mit.edu/course/1/1.061/www/dream/SEVEN/SEVENTHEORY.PDF

Soros, A., Amburgey, J. E., Stauber, C. E., Sobsey, M. D., and Casanova, L. M. (2019). Turbidity reduction in drinking water by coagulation-flocculation with chitosan polymers. *Journal of Water and Health,* 17(2), 204-218. doi:10.2166/wh.2019.114

Spalart, P., and Allmaras, S. (1992). A One-Equation Turbulence Model for Aerodynamic Flows. *AIAA,* 439. doi:10.2514/6.1992-439

Spalart, P., Jou, W. H., Strelets, M., and Allmaras, S. (1997). *Comments on the Feasibility of LES for Wings, and on a Hybrid RANS/LES Approach*, Louisiana, USA.

Spalart, P. R. (2000). Strategies for turbulence modelling and simulations. *International Journal of Heat and Fluid Flow,* 21(3), 252-263. doi:https://doi.org/10.1016/S0142-727X(00)00007-2

Spalart, P. R. (2009). Detached-Eddy Simulation. *Annual Review of Fluid Mechanics,* 41(1), 181-202. doi:10.1146/annurev.fluid.010908.165130

Spicer, P. T., and Pratsinis, S. E. (1996). Shear-induced flocculation: The evolution of floc structure and the shape of the size distribution at steady state. *Water Research,* 30(5), 1049-1056. doi:https://doi.org/10.1016/0043-1354(95)00253-7

Squires, K., Forsythe, J., and Kotapati-Apparao, R. (2004). Prediction of the Flow over an Airfoil at Maximum Lift. In 42*nd AIAA Aerospace Sciences Meeting and Exhibit*.

Strelets, M. (2001). Detached eddy simulation of massively separated flows. *AIAA J*, 1-18.

Suopajärvi, T. (2015). *Functionalized Nanocelluloses in Wastewater Treatment Applications.*

Svarovsky, L. (2000). *Solid-Liquid Separation* (4 ed.): Elsevier Science.

Syvitski, J. P. M., and Hutton, E. W. H. (1996). In situ characteristics of suspended particles as determined by the floc camera assembly FCA. *Journal of Sea Research,* 36(1), 131-142. doi:https://doi.org/10.1016/S1385-1101(96)90783-2

Tennekes, H., and Lumley, J. L. (1972). *A First Course in Turbulence*. Cambridge, MA: MIT press.

Thomas, D. G. (1964). Turbulent disruption of flocs in small particle size suspensions. *AIChE Journal,* 10(4), 517-523. doi:https://doi.org/10.1002/aic.690100420

Tominaga, Y., and Stathopoulos, T. (2007). Turbulent Schmidt numbers for CFD analysis with various types of flowfield. *Atmospheric Environment,* 41(37), 8091-8099. doi:https://doi.org/10.1016/j.atmosenv.2007.06.054

Torres, F. E., Russel, W. B., and Schowalter, W. R. (1991). Simulations of coagulation in viscous flows. *Journal of colloid and interface science,* 145(1), 51-73. doi:https://doi.org/10.1016/0021-9797(91)90099-T

Tse, I. C., Swetland, K., Weber-Shirk, M. L., and Lion, L. W. (2011). Fluid shear influences on the performance of hydraulic flocculation systems. *Water Research,* 45(17), 5412-5418. doi:https://doi.org/10.1016/j.watres.2011.07.040

Tucker, P. G., and Liu, Y. (2005). Application of Zonal Les/Iles Approaches to an Unsteady Complex Geometry Flow. In W. Rodi & M. Mulas (Eds.), *Engineering*

Turbulence Modelling and Experiments 6 (pp. 339-348). Amsterdam: Elsevier Science B.V.

Vallero, D. (2014). *Findamentals od Air Pollution*. USA: Academic Press.

Villermaux, J. (1995). *Génie de la réaction chimique: Conception et fonctionnement des réacteurs* (2 ed.). Paris, France: Tec & Doc-Lavoisier.

Vlieghe, M., Coufort-Saudejaud, C., Frances, C., and Liné, A. (2014). In situ characterization of floc morphology by image analysis in a turbulent Taylor–Couette reactor. *AIChE Journal,* 60(7), 2389-2403. doi:doi:10.1002/aic.14431

Vlieghe, M., Coufort-Saudejaud, C., Liné, A., and Frances, C. (2016). QMOM-based population balance model involving a fractal dimension for the flocculation of latex particles. *Chemical Engineering Science,* 155, 65-82. doi:https://doi.org/10.1016/j.ces.2016.07.044

Vocciante, M., Piper, M., Zibart, A., and Kenig, E. Y. (2018). Numerical Evaluation of Different Turbulence Models for Single-Phase Flow in the Outer Pillow-Plate Channel. In A. Friedl, J. J. Klemeš, S. Radl, P. S. Varbanov, & T. Wallek (Eds.), *Computer Aided Chemical Engineering* (Vol. 43, pp. 397-402): Elsevier.

Wang, L., Marchisio, D. L., Vigil, R. D., and Fox, R. O. (2005). CFD simulation of aggregation and breakage processes in laminar Taylor–Couette flow. *Journal of colloid and interface science,* 282(2), 380-396. doi:https://doi.org/10.1016/j.jcis.2004.08.127

Wasewar, K. L. (2006). A design of jet mixed tank. *Chemical & Biochemical Engineering Quarterly,* 20(1), 31-46.

White, F. M. (2011). *Fluid Mechanics* (7 ed.). New York, USA: McGraw-Hill.

WHO. (2017). Water safety in distribution systems. Retrieved 27 June 2021, from World Health Organization http://www.who.int/water_sanitation_health/publications/water-safety-indistribution-system/en/

Wilcox, D. C. (1998). *Turbulence Modeling for CFD* (2 ed.). Canada, California: DCW Industries

Wilkinson, N., Metaxas, A., Quinney, C., Wickramaratne, S., Reineke, T. M., and Dutcher, C. S. (2018). pH dependence of bentonite aggregate size and morphology on polymer-clay flocculation. *Colloids and Surfaces A: Physicochemical and Engineering Aspects,* 537, 281-286. doi:https://doi.org/10.1016/j.colsurfa.2017.10.007

Xu, D., and Chen, J. (2013). Accurate estimate of turbulent dissipation rate using PIV data. *Experimental Thermal and Fluid Science,* 44, 662-672. doi:https://doi.org/10.1016/j.expthermflusci.2012.09.006

Yáñez-Varela, J. A., Mendoza-Escamilla, V. X., Alonzo-Garcia, A., Martinez-Delgadillo, S. A., Gonzalez-Neria, I., and Gutiérrez-Torres, C. (2018). CFD and experimental

validation of an electrochemical reactor electrode design for Cr(VI) removal. *Chemical Engineering Journal,* 349, 119-128. doi:https://doi.org/10.1016/j.cej.2018.05.067

Yang, R., Li, H., Huang, M., Yang, H., and Li, A. (2016). A review on chitosan-based flocculants and their applications in water treatment. *Water Research,* 95, 59-89. doi:https://doi.org/10.1016/j.watres.2016.02.068

Ye, C., Wang, D., Shi, B., Yu, J., Qu, J., Edwards, M., and Tang, H. (2007). Alkalinity effect of coagulation with polyaluminum chlorides: Role of electrostatic patch. *Colloids and Surfaces A: Physicochemical and Engineering Aspects,* 294(1), 163-173. doi:https://doi.org/10.1016/j.colsurfa.2006.08.005

Zhao, C., Zhou, J., Yan, Y., Yang, L., Xing, G., Li, H., . . . Zheng, H. (2021). Application of coagulation/flocculation in oily wastewater treatment: A review. *Science of The Total Environment,* 765, 142795. doi:https://doi.org/10.1016/j.scitotenv.2020.142795

Zheng, M. X., Wang, K. J., Zuo, J. E., Yan, Z., Fang, H., and Yu, J. W. (2012). Flow pattern analysis of a full-scale expanded granular sludge bed-type reactor under different organic loading rates. *Bioresource Technology,* 107, 33-40. doi:https://doi.org/10.1016/j.biortech.2011.11.102

Zhou, D., Dong, S., Gao, L., Ju, R., and Niu, S. (2012). Effect of double-stage velocity gradients on abatement and morphology characteristics of flocs in a conical fluidized-bed flocculator. *Separation and Purification Technology,* 98, 383-388. doi:https://doi.org/10.1016/j.seppur.2012.07.016

Zhou, T., Li, M., Li, Q.-l., Lei, B., Chenn, Q.-z., and Zhou, J.-m. (2014). Numerical simulation of flow regions in red mud separation thickener's feedwell by analysis of residence-time distribution. *Transactions of Nonferrous Metals Society of China,* 24(4), 1117-1124. doi:https://doi.org/10.1016/S1003-6326(14)63170-8

APPENDIX

Appendix A
Local Analysis of the Hydrodynamic

Local Analysis of the Hydrodynamic

In water treatment plants, the flocculation process is carried out in large flocculation tanks. Turbulent flow is a majority regime of the tank while in the jet clarifier, which is a complex reactor; the turbulent flow regime is only in the flocculation zone. Thus, it seems necessary to give a short description of the fundamental of turbulence, besides, to characterize the scales of length and velocity as well as the term of viscous dissipation of kinetic energy.

1. Turbulence Features

Turbulence is a natural phenomenon. Its manifestations are extremely diverse and easily observable. However, despite the obviousness of the phenomenon, its understanding remains problematic and complex (Chassaing, 2000). From the first studies conducted by Osborne and Reynolds in 1883 to the most recent works, many authors have succeeded one another to understand, characterize and define turbulence.

At the present time, there is no unique definition of turbulence (Chassaing, 2000; Schiestel, 1993). Turbulence is a property of the flow and not of the fluid itself. These flows nevertheless have a number of common features highlighted below.

1.1 Irregularity of the Phenomenon and Mean Flow

As discussed above, the flow regime (laminar, transition, or turbulent) depends on the Reynolds number, which is the ratio between inertial and viscous forces. Figure A.1 shows the characters of flow regime by tracking dye trace (O. Reynolds, 1883). In laminar flow, there is a linear dye trace since particles follow the streamlines that are straight. In turbulent flow, there are eddies of various sizes that overlap the mean flow. When the dye trace enters the turbulent region, it traces a path governed by both the mean flow (streamlines) and the eddies. Large eddies carry the dye towards the side across

streamlines. Smaller eddies create smaller-scale stirring that causes the dye filament to spread (diffuse).
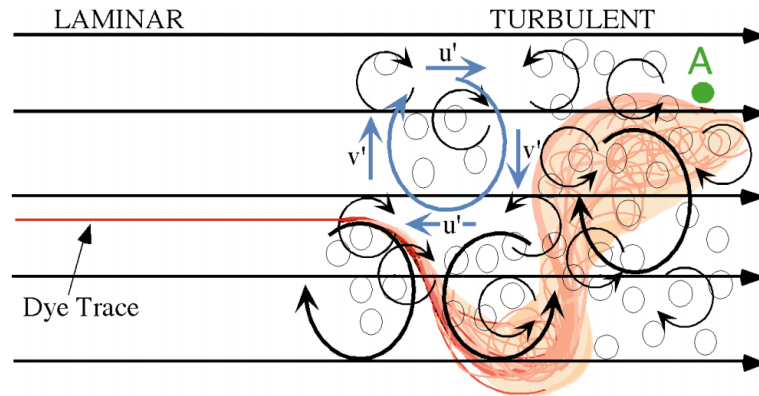
Figure A.1 Tracer transport in laminar and turbulent flow (Sonin, 2019)

If both the longitudinal (u) and vertical (v) velocity are measured at point A in Figure A.1, in the case of laminar at steady state, $u = \bar{u}$ and $v = \bar{v}$, where the overbar denotes a time average value. In the case of turbulent flow, the time evolution of both velocities is characterized by fluctuations as shown in Figure A.2.
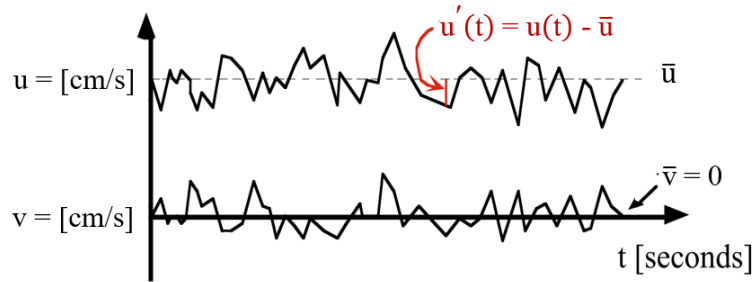
Figure A.2 Velocity recorded at point A in Figure A.1 (Sonin, 2019)

Those fluctuations are due to the eddies and are one of the features of turbulence. Reynolds suggested to decompose the instantaneous velocity into its time-averaged and fluctuating components (Equation A.1 and Equation A.2):

$$u(t) \ = \ \bar{u} \ + \ u'(t) \qquad\qquad \text{Equation A.1}$$

$$v(t) = \ \bar{v} \ + \ v'(t) \qquad\qquad \text{Equation A.2}$$

$$\text{mean} \qquad \text{turbulent fluctuation}$$

Based on the theory, the velocity is continuous, and the mean can be evaluated through integration as suggested on the left part of Equation A.3 where t represents a time much longer than any turbulence time scale. Nevertheless, technically the velocity records (u_i) are a series of N discrete points. The mean velocity can thus be derived from the right part of Equation A.3 and the fluctuating velocity by Equation A.4 and Equation A.5.

Mean velocity:

$$\bar{u} \ = \ \int_{t}^{t+T} u(t)\,dt \ = \ \frac{1}{N}\sum_{i=1}^{N} u_i \qquad \text{Equation A.3}$$

$$\text{continuous record} \quad \text{discrete, equi-spaced pts.}$$

Turbulent fluctuation: (continuous record) $\qquad u'(t) = u(t) - \bar{u} \qquad$ Equation A.4

(discrete points) $\qquad u_i' = u_i - \bar{u} \qquad$ Equation A.5

Turbulence strength:

$$u_{rms} \ = \ \sqrt{\overline{u'(t)^2}} \ = \ \sqrt{\frac{1}{N}\sum_{i=1}^{N}(u_i')^2} \qquad \text{Equation A.6}$$

$$\text{continuous record} \quad \text{discrete, equi-spaced pts.}$$

Turbulence Intensity: $\qquad u_{rms}/\bar{u} \qquad$ Equation A.7

Where the subscript "rms" stands for root-mean-square.

The definition of u_{rms} given in Equation A.6 means that the standard deviation of a set of "random" velocity fluctuations, u_i'. A large u_{rms} illustrates a higher level of turbulence. In Figure A.3, both records have the same mean velocity, but the record on the left has a higher level of turbulence.
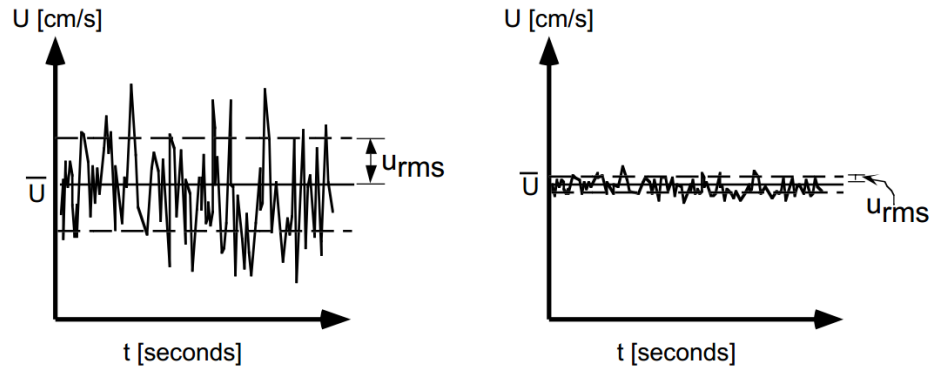
Figure A.3 The number of u_{rms} versus mean flow

The example above has been given for longitudinal velocity but similar definitions apply for the other components of the velocity, v(t) and w(t) or for the pressure or the concentration.

1.2 Turbulent Reynold Number

The flow becomes turbulent for high Reynolds numbers (Bałdyga and Bourne, 1999; Tennekes and Lumley, 1972). Opposing the laminar regime to the turbulent regime, they state that instabilities appear in the flow. These instabilities are related to nonlinear terms in the Navier-Stokes momentum equation.

For its part, Chassaing (2000) shows that turbulent phenomena can exist in the case of fluids at rest. Grid turbulence is a good example: a grid is set in periodic motion in a fluid at rest; turbulent fluctuations appear which can be characterized. In this case, there is no average flow; the Reynolds number based on the average speed loses its meaning. Thus, then leads to expressing the Reynolds number by quantities different from the average speed or the diameter of the stirrer:

$$Re_\lambda = \frac{u_{rms}\,\lambda}{\nu} \qquad\qquad \text{Equation A.8}$$

Where $u_{rms} = \sqrt{\overline{u'^2}}$ and λ is the Taylor micro-scale, which will be defined in section Appendix A 2.2.

1.3 Diffusivity of Turbulence

One of the main characteristics of turbulence is its ability to diffuse any transportable quantity, such as the concentration of the solid particles or the temperature, much more efficiently than the molecular diffusion. The turbulent diffusion results from advection phenomena at the level of the flow structures. In other words, the quantities are transported by the proper movement of the eddies.

1.4 Three-dimensional Structure

In the vast majority of cases, the structure of turbulence is three-dimensional. However, this three-dimensional character does not mean that the turbulence is isotropic in all cases.

1.5 Wide Range of Length Scales

Turbulence, represented by the Kolmogorov energy cascade, has a wide range of length scales; the largest ones represent the largest energy eddies while the smaller ones represent the smallest Kolmogorov dissipative eddies. Big swirls absorb the energy from the mean flow and transmit it to smaller eddies. The commonly accepted transfer mechanism is vortex stretching. This transfer of energy from large eddies to smaller ones known as the Kolmogorov eddies that dissipate the kinetic energy by viscous friction. A very broad spectrum of vortices exists therefore in turbulent regime.

1.6 Viscous Dissipation of Turbulent Kinetic Energy

The turbulent motion contributes very largely to the dissipation of kinetic energy, even if the other motions (mean and periodic) also participate. Chassaing (2000) noted that the viscous dissipation of kinetic energy is a scalar quantity, the total sum being the sum of the contributions of all the vorticity classes present in the flow. Theoretically, the dissipation can be defined in terms of spectrum. However, it shows that only eddies with

significant strain rates have a significant spectral contribution, these vortices being none other than the Kolmogorov vortices.

Express the local viscous dissipation rate of TKE and relate it to the local turbulent shear rate.

2. Length Scales

In each point, three scales are particularly important for characterizing hydrodynamics; ranked in descending order of size, they are:

- Taylor Macroscale (Λ)
- Taylor Microscale (λ)
- Kolmogorov (η)

2.1 The Spatial Macro-scale of Taylor (Λ)

The macro-scale of Taylor (Λ) corresponds locally to the size of the most energetic turbulent structure. It can be spatial or temporal. In the first case, it defines the distance over which the speed is correlated with itself. In the second case, it corresponds to the time at the end of which, at a point of measurement, the speed is again correlated with itself. Taylor's spatial macro-scale can be determined directly using PIV (Particle Image Velocimetry), which provides spatial information (Escudié and Liné, 2003). Under certain assumptions (steady flow, homogeneous, negligible transportation, and isotropic turbulence), an estimate of the dissipation rate (ε) involving the Taylor macro-scale (Λ), as well as the turbulent kinetic energy (k), can be given as:

$$\Lambda = \frac{k^{3/2}}{\varepsilon} \qquad\qquad \text{Equation A.9}$$

Where k is the local turbulent kinetic energy and ε is the local viscous dissipation rate of turbulent kinetic energy. It is important to recall that the Taylor macro-scales are

related to the dimensions of the system, the size of the largest eddies being limited by the size of the pilot. This scale is a characteristic scale of macro-mixing, close to the turbulent viscosity.

2.2 The Spatial Micro-scale of Taylor (λ)

The size of the Taylor microscale (λ) can be characterized by the smallest energetic structures. In the case of isotropic turbulence, the Taylor microscale can be expressed in terms of dissipation rate of kinetic energy (ε) and turbulent kinetic energy (k).

$$\lambda = \sqrt{\frac{15\, \nu\, \overline{u'^2}}{\varepsilon}} = \sqrt{\frac{10\, \nu\, k}{\varepsilon}} \qquad \text{Equation A.10}$$

Where $\overline{u'^2}$ is mean value of turbulent velocity fluctuations [m^2/s^2].

Thus that the Reynold number of Taylor can be describe as:

$$Re_\lambda = \sqrt{\frac{10}{C_\mu}} \sqrt{\frac{\nu_t}{\nu}} = \sqrt{10} \sqrt{\frac{k^2}{\nu\, \varepsilon}} \qquad \text{Equation A.11}$$

Where Re_λ is local turbulent Re number. This size corresponds to the smallest eddies contributing significantly to the turbulent kinetic energy. Consequently, the PIV filter should be smaller than this Taylor microscale. Similarly, in Large Eddy Simulation, the mesh size should be smaller than this Taylor microscale.

2.3 Kolmogorov microscale (η)

In the energy-cascade theory, the smallest turbulent structures are called Kolmogorov scale, denoted by η. At this scale, the turbulent kinetic energy is dissipated by molecular viscosity. Kolmogorov stated that since the phenomena arising at this scale are controlled by the kinematic viscosity of the fluid (m^2/s) and the dissipation rate (m^2/s^3),

a dimensional analysis leads to the following expression. The scale η can be expressed in terms of the dissipation rate of turbulent kinetic energy (ε), and kinematic viscosity (ν) as shown in Equation A.12.

$$\eta = \left(\frac{\nu}{\varepsilon}\right)^{1/4}$$

Equation A.12

3. Velocity Scale

Turbulence is a movement of eddies, which is at high Reynolds numbers, has a large size range. The always rotational movement can be conceived as an entanglement of eddy structures, whose rotational vectors are oriented in all directions and are strongly unsteady. It is generally considered that turbulent flows are formed by a cascade of eddies of increasingly smaller scales. Large vortices are formed by the mean flow; their larger dimension is of the order of magnitude of the domain. They are mainly the ones who carry the energy from the mean flow to the turbulence. In the process of the energy cascade, the small vortices tend to free themselves from the anisotropic characteristics of larger ones. This is called local isotropy.

At each size of eddies (λ), we can associate a turbulent Reynolds number; this number, therefore, decreases with the size.

$$Re_\lambda = \frac{u'(\lambda)\lambda}{\nu}$$

Equation A.13

Where λ is the length scale considered (m), $u'(\lambda)$ is the speed of eddy (m/s), and ν is kinematic viscosity.

Finally, there is a scale below which there are no more eddies. Indeed, when these are small, one approaches the laminar conditions (small Reynolds number). Viscous forces then dissipate the energy. This final scale leading to $Re_\lambda = 1$ is called the Kolmogorov scale (η) as shown in Equation A.14.

$$\mathrm{Re}_\lambda = \frac{u^{'}(\eta)\eta}{\nu} = 1 \qquad \text{Equation A.14}$$

Thanks to a dimensional analysis, it is possible to show that the following relation gives the Kolmogorov scale fluctuation.

$$u^{'}(\eta) = (\nu\varepsilon)^{1/4} \qquad \text{Equation A.15}$$

Two scales can be associated:

- The time scale

$$\frac{\eta}{u^{'}(\eta)} = \left(\frac{\varepsilon}{\nu}\right)^{1/2} \qquad \text{Equation A.16}$$

- The frequency scale

$$\frac{u^{'}(\eta)}{\eta} = \left(\frac{\nu}{\varepsilon}\right)^{1/2} \qquad \text{Equation A.17}$$

Thus, in the case of isotropic turbulence, can be rewritten as:

$$\eta = \left(\frac{\nu^3}{\varepsilon}\right)^{1/4} \qquad \text{Equation A.18}$$

Therefore, the "cascade" consists of the size of eddies between Λ (Taylor's macro-scale or scale of the largest vortices) and η. Different size domains can then be distinguished.

3.1 λ ≈ Λ: Zone of Production of Turbulent Kinetic Energy

This zone corresponds to a large size of eddies Λ which are created by the mean velocity field. This is where the turbulent kinetic energy k is produced. In this zone, the hypothesis of isotropy of turbulence can be questioned.

3.2 Universal Equilibrium Zone

When the Reynolds number is large enough, there can be a wide spectrum of intermediate-sized vortices: this is the universal equilibrium zone.

3.2.1 Λ >> λ >> η : Zone of Inertia

In this zone, the size of eddies are large enough for Re_λ to be large ($Re_\lambda > 1$). In other words, the energy transfer by inertia is the dominant process and the effect of the viscosity is negligible. This zone is all the greater as the number of turbulent Reynolds is high.

3.2.2 λ < η : Zone of Viscous dissipation

Finally, for the size of eddies close to η, the turbulent Reynolds number becomes very small. This means that viscous forces are important at this scale and dissipate the energy carried by the vortices into heat.

4. Viscous Dissipation Rate of Turbulent Kinetic Energy

The expression of the viscous dissipation rate of the turbulent kinetic energy is given by Equation A.19.

$$\varepsilon = 2\, \nu\, s_{ij}^{'}\, s_{ij}^{'} \qquad\qquad \text{Equation A.19}$$

$s_{ij}^{'}$ being the symmetrical part of the strain rate tensor:

$$s'_{ij} = \frac{1}{2}\left(\frac{\partial u'_i}{\partial x_j} + \frac{\partial u'_j}{\partial x_i}\right)$$ Equation A.20

In turbulent flow, the shear rate can be estimated by Equation 1.19.

The experimental determination of ε requires to be able to estimate with precision, at each point of the considered domain, all the local gradients of the fluctuating speeds. The smallest structures (Kolmogorov vortices) must not be filtered because it is at their scale that most of the dissipation of the kinetic energy in viscous form is carried out. Moreover, the difficulty of making direct measurements using PIV was showed and mentioned in many pieces of research (González-Neria et al., 2019; Kilander et al., 2006; Saarenrinne and Piirto, 2000; Shah et al., 2019; Xu and Chen, 2013). In addition, Escudié (2003) estimated the value of the viscous dissipation rate of turbulent kinetic energy through a turbulent kinetic energy balance.

Indeed, the work of Camp and Stein has been revisited by many workers (among them (Clark, 1985; Cleasby, 1984; T. Kramer and Clark, 1997a). It is now accepted that the velocity gradient is defined as the square root of the viscous dissipation rate of kinetic energy (W/kg) divided by the kinematic viscosity. It is thus identical to the local shear rate and is defined as:

$$G = \dot{\gamma} = \sqrt{\frac{1}{2}tr(\overline{S^2})} = \sqrt{\frac{1}{2}tr(\bar{S}^2) + \frac{1}{2}tr(\overline{s'^2})}$$ Equation A.21

Where S is the symmetric part of the velocity gradient tensor. Here, $tr(\overline{S^2})$ is an invariant. The first term on the r.h.s. is related to the square of mean velocity gradients whereas the second one stands for the average of the square of the fluctuating (turbulent) velocity gradients. These two terms are respectively related to the viscous dissipation of the mean flow kinetic energy and to the viscous dissipation of the turbulent kinetic energy. In turbulent flow, the first one is negligible compared to the viscous dissipation of the

turbulent kinetic energy. Averaged over the whole tank or clarifier, the dissipated power is equal to the power input.

Appendix B

Reactor Design

Reactor Design

A chemical reactor is an enclosed volume in which a chemical reaction takes place. In chemical engineering, it is broadly understood to be a tank that is used to hold liquid used to carry out a chemical reaction, which is one of the classic unit operations in chemical process analysis (Levenspiel, 1999; Simons, 2016). The design of a chemical reactor deals with numerous aspects of chemical engineering. The reactors are designed to maximize net present value for the given reaction with the optimum condition, which is the highest efficiency towards the desired output product, producing the highest yield of the product while requiring the least amount of money to purchase and operate. The idealized models are used to design reactors consist of batch reactor, plug flow reactor (PFR), and completely stirred tank reactor (CSTR), or mixed flow and the most simple basic types of chemical reactors are tanks (Hill and Root, 2014).

Batch reactor is the simplest type of reactor. Materials are loaded into a batch reactor, and the reaction proceeds with time; thus, the batch reactor does not reach a steady state, and control of temperature, pressure, and volume is often necessary. In a CSTR, one or more chemical solutions are fed into a tank reactor, which is regularly stirred with an impeller to ensure proper mixing of the chemical solutions while the reactor effluent is removed. The concentration of the chemical solution is assumed to be homogenous throughout the reactor when the chemical reactions reach steady state, and the mass flow rate in must equal the mass flow rate out. To calculate the time required to process one reactor volume of fluid can be dividing the volume of the tank by the average volumetric flow rate through the tank. To operate several CSTRs in series is often to be used to operate for economically beneficial since the first CSTR to operate at a higher chemical solution concentration, it means that its reaction occurring in higher reaction rate. Thus, the sizes of the reactors may be varied in order to minimize the total investment required to achieve the process. Moreover, it can be demonstrated that an infinite number of infinitely small CSTRs operating in series would be equivalent to a PFR (Ravi et al., 2017). In a PFR, one

or more chemical solution is fed through a pipe or the channel like a tube. In this type of reactor, the rate of reaction changes along the X-axis; at the inlet of PFR, the rate is very high, but as the concentrations of the chemical solution decrease and the concentration of the products increases the reaction rate slows. The idealized PFR model assumes that no axial mixing in the reactor, so any element of fluid travelling through the reactor does not mix with fluid upstream or downstream from it so that it is impliedly the term of "plug flow".

Therefore, the chemical reaction and aspects of reactors are required for reactor design to achieve a goal of the reactor. Many cases, reactors were designed and investigated the efficiency of the reactors in lab-scale to find optimum conditions of each reactor purpose. Then, the reactors are enlarged the full scale to use in industrial processes. For increasing or reducing the size of reactor, scale method is widely used to actualize their potential. Thus, scale is described briefly in the next section.

1. Scale-up/down and Process Design

Generally, apparatuses of engineering research are necessary to work from small scale or pilot scale models to large scale to complete studies. Even though there are many available reactors that can use in factories, experimental results are still necessary to investigate and verify it since theories are invariably based on assumptions that may not be completely satisfied in the real systems. A reduction in unit cost and improved quality are also desired in factories. Scale model, which is the various design methods, that enlarge the small equipment to a large-scale equipment, called scale-up is used. Similar approach, in this case, scale model is used to reduce a large-scale equipment to a small scale, called scale down. The objective of scale-down is to make small quantities of materials having the same or similar properties that were made on a large scale, or real system. The benefit of a small scale is easily investigating the phenomena of the reactor.

Taking all of the different types of physical quantities into account figuring in a system, the physical similarity is observed that it is very difficult to attain and to ensure. For this reason, dimensionless groups/numbers are used for scale-up/down. The

dimensionless group is obtained by dimensional analysis in order to reduce the number of parameters needed to describe a system without destroying the generality of the relationship (Elson, 2007). Moreover, Engineering data and most of the literature or correlation are often presented using dimensionless.

Scale method which bases on physical similarity. It respects to certain specified physical quantities when the ratio of corresponding magnitudes of these quantities between the two systems are the same. There is a lot of systems aligning the physical similarity and it can be shown in Table B.1.

Table B.1 List the type of physical similarity

Type	Physical quantity	Example system
Geometric	Lengths	Stirred tank
Kinematic	Lengths + time intervals, or velocities	Planetarium, tidal models
Dynamic	Forces	Flow models, wind tunnel
Thermal	Temperature differences	Pilot-plant heat exchanger
Chemical	Concentration differences	Bench-scale reactor

Two types of physical similarities were focused on this research, that is geometric similarity and dynamic similarity. The methods of two types of physical similarities approach as follows.

1.1 Geometric Similarity

Geometric similarity, which is the similarity of shape, is the most accessible specification in a model system designed to equalize to a given prototype system. Two systems are geometrically similar when the ratio of any length of reactor between two systems is everywhere the same. The example of geometric similarity is schematically depicted in Figure B.1.

(a) model   (b) prototype
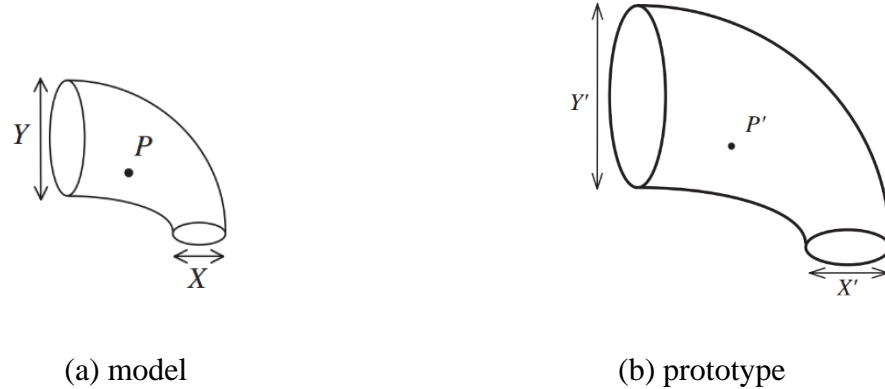
Figure B.1 Geometric similarity (Simons, 2016)

Figure B.1 represents two objects which have similar geometric. Here P and P' are known as corresponding points. Moreover, X and X', Y and Y' are known as corresponding lengths. The ratio of corresponding lengths is known as the scale factor:

$$\text{Scale factor} = \frac{X}{X'} = \frac{Y}{Y'} \qquad\qquad \text{Equation B.1}$$

For instance, If the scale factor is equal to 2, the prototype is enlarged, so its dimensions are twice the model. While the scale factor is equal to 0.5, the prototype is reduced, with its dimensions are half of the model and the scale factor is equal to 1, the prototype is exactly the same size as the model.

Perfect geometric similarity is not always easy to achieve, and difficulties can happen due to (1) scaling of surface roughness or finish, (2) scaling of surface tension (e.g., scale-down of a river will result in a thin water layer where surface tension effects will be more important than in the river). So, this study will be done the experiment to confirm that if the geometric similarity between the model and the prototype, the performance of the reactors to remove the turbidity is not different.

1.2 Dynamic Similarity

Dynamic similarity means similarity of forces. Forces of the same kind, e.g., gravitation, viscous, centripetal, etc., acting at corresponding points at corresponding times are corresponding forces. Many forces that might be involved in the reactor system are below:

- viscous forces – due to the fluid's viscosity;
- inertial forces – due to its density and velocity;
- pressure forces – due to pressure difference acting over an area of fluid;
- body forces, e.g., gravitational – due to earth's gravitational field;
- surface tension forces – due to the presence of interfaces;
- boundary forces, e.g., forces imparted by a moving boundary, a rotating impeller.

The dynamic similarity is especially crucial in fluid flow systems, which normally determined by the forces acting on the fluid elements. The net force acting on a fluid element gives the acceleration of that element and, hence, determines its motion. If the net forces on corresponding fluid elements at corresponding times are similar, then their motion will be similar. Based on the theory, a prototype, and model are dynamically similar when all forces acting at corresponding points, on fluid elements or corresponding boundaries, form a constant ratio between model and prototype. In contrast, there are many reactors or systems which were scaled-up/down having not exactly the same of dynamic similarity, but they can operate and give the same result, or they have the same efficiency. This is an interesting thing and a gap of the research because in the realistic it is very difficult to do the scale-up/down to get exactly the same dynamic similarity, but in the reactor designs field, they are accepted, and the design criteria can be suggested.

Thus, this research focuses on scale-down the reactor by using the geometric similarity method because the jet clarifier is a reactor that consists of coagulation, flocculation, and sedimentation process. The flocculation process is an important process because it influences floc growth and floc size. The properties of floc are a key-parameter to achieve the most efficient separation from the water. Previously, the flocculation process

was studied in jar test method for bench scale or stirred tank for pilot-tank. Several parameters were investigated such as pH, velocity gradient, chemical type, and dose. Then, they were adapted using in the reactors. Moreover, the geometric similarity is an uncomplicated system because it has only one implicated physical quantity. So, it can be used easily to scale at the beginning of the first stage. For these reasons, the geometric similarity was selected to scale-down the reactor in this research. Moreover, the dynamic similarity and reactor performance would be investigated in the second step.

Appendix C
Static Mixer

The details of the static mixer

The static mixer is a unique standstill pipe. Liquid that enters the mixer is sequentially mixed and stirred by elements. The length and diameter pipe used in the experiment were 500 mm. and 12.5 mm, respectively. Six elements, installed rectangular plate twisted 180 degrees, in the pipe were shown in Figure C.1. Moreover, as mention above, the global velocity gradient (G) and contact time are the key parameters in the mixing conditions. Thus, the calculation of them was briefly described in the next paragraph.

1st element, 2nd element, 3rd element, . . . , 6th element
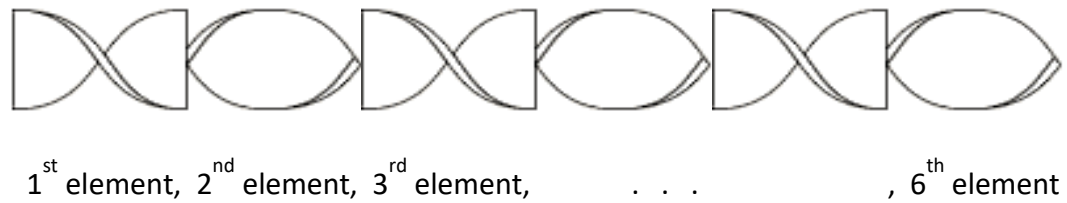
Figure C.1 The geometry of Static Mixer Elements (adapted from Noritake®)

The global velocity gradient (G) can be calculated by the pressure drop since it is due to the dissipation that takes place when a large velocity gradient is presented in the flow. By applying the laws of conservation in the integral format to a suitable control volume, Kundu (1990) derived that in a duct flow the energy dissipation rate as the Equation C.1 (Kundu, 1990).

$$E \ = \ \Delta P_{perm} \ \times \ Q \qquad\qquad \text{Equation C.1}$$

Where E = energy dissipation rate [W], ΔP_{perm} = permanent pressure drop [N/m^2] and Q = volumatic flow rate [m^3/s]. Since most of the energy dissipation ensues where large velocity gradients are present, the description of turbulent flow is repeatedly simplified by

using the mean energy dissipation rate per unit mass. The mass of the fluid in the dissipation zone is given by $\rho_c \times V_{dis}$. In consequence, the mean energy dissipation rate per unit mass can be calculated by using Equation C.2 (MJ van der Zande et al., 2001).

$$\varepsilon \;=\; \frac{E}{\rho_c \times V_{dis}} = \frac{\Delta P_{perm} \times Q}{\rho_c \times V_{dis}} \;=\; \frac{\Delta P_{perm}}{\rho_c \times t_{res}} \qquad \text{Equation C.2}$$

Where ρ_c = density of the continuous phase [kg/m^3], V_{dis} = volume used for energy dissipation rate [m^3] and t_{res} = mean residence time of the dissipation take places.

The details of the static mixer used in the experimental conditions were shown in Table C.1.

Table C.1 Summarization of key parameters of the static mixer used in the experiment

Flow rate (LPH)	t_{design} (s)	Δmm H$_2$O (mm.)	Pressure loss (N/m^2)	ε (m^3/s^2)	G (s^{-1})	Camp No. (-)
40	5.55	2	19.62	3.55×10^{-3}	62.97	349.51
70	3.16	5	49.05	1.56×10^{-2}	131.96	416.99
180	1.23	18	176.58	1.44×10^{-1}	401.31	493.61

The RTD experiment on the static mixer

The total volume of the static mixer was 6.14×10^{-2} L with the specific dimension were 500 mm., and 12.5 mm. of length and diameter, respectively. The static mixer was constructed to be the pilot plant. It was designed explicitly for investigating residence time distribution and a process flow diagram of the experimental set-up and hydrodynamic scheme diagram were shown in Figure C.2. The experiment was carried out under three different flow rates as same as it was done in the RTD experiment of jet clarifier, which was 40, 70, and 180 L/hr. Before the inlet, a Y-type connector was installed for tracer injection. In order to obtain the signal of the tracer, a conductivity probe (HACH, USA)

was placed in the reactor at an outlet every second to detect the amount of tracer concentration, which could be represented by conductivity. The 200 g. analytical chemical-grade Sodium chloride (NaCl) from KemAus, Australia mixed with 1 L. demineralized water to be used as the tracer solution. The volume of tracer solution used in the experiments was 13 mL.
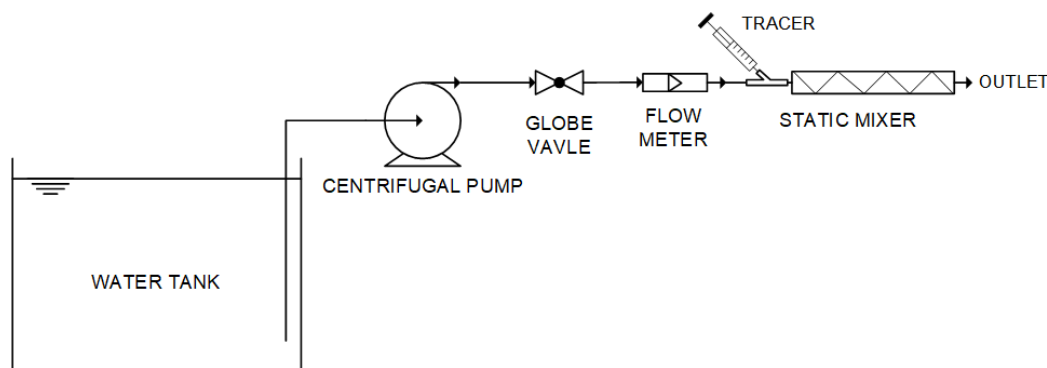

Figure C.2 A process flow diagram of the experiment for static mixer

The experiment had been performed 3 trials for flow rate each. Plots of the RTD curves, *E(t)* versus sampling time (t), were plotted with the average curve as shown in Figure C.3 in order to determine to mean residence time distribution, and Figure C.4 was the average plot of flow rate each to compare the curves. The mean residence time (t_m), standard deviation (σ), and Peclet number with the theoretical residence time was reported in Table C.2 to check the validity of data.

There is variance present presented in Figure C.3, but all the curves have nearly identical shapes to their curves with different peak values depending on flow rates. The *E(t)* of varying flow rates follow the same general flow pattern, but the t values of *E(t)* function and sampling time were different. There was the highest value from the high flow rate since the tracer was transported by convection more than diffusion and dispersion, which could be indicated by the shape of the RTD curve; the high flow rate causes height and narrow shape than lower flow rate. The peak's sharps were directly relevant to the flow rate examined, which were around at 9, 15, and 26 seconds for low, medium, and high flow rates, respectively.
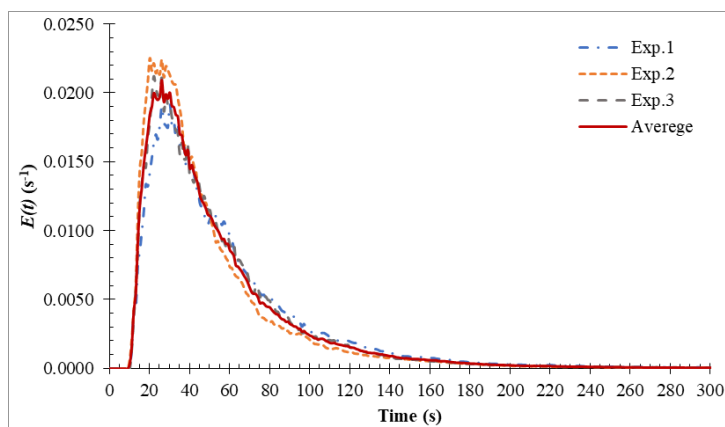
a) 40 L/hr.
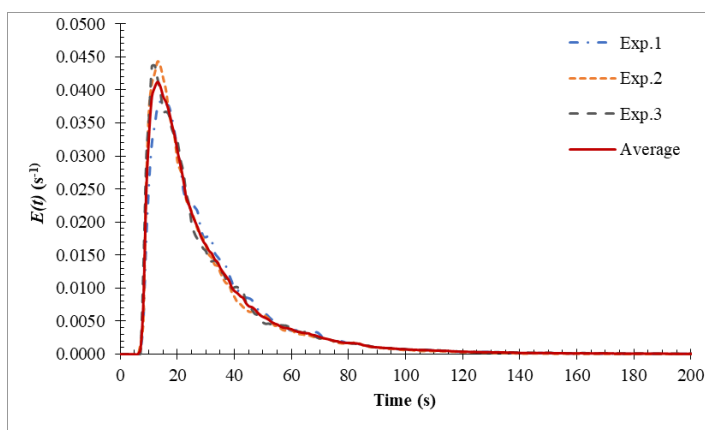
b) 70 L/hr.
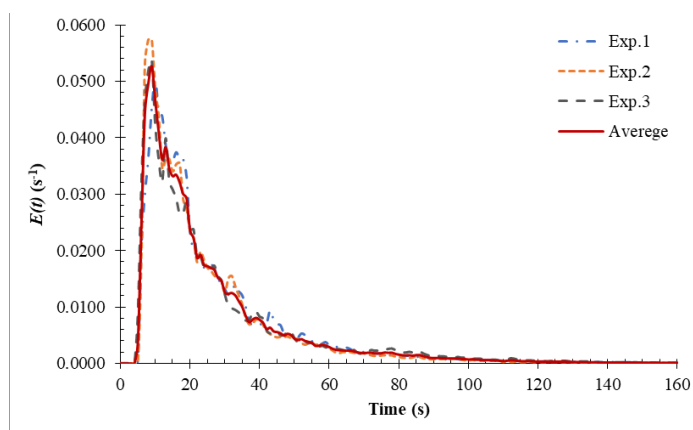
c) 180 L/hr.

Figure C.3 $E(t)$ experimental data curve of static mixer of

(a) 40 L/hr., (b) 70 L/hr., and (c) 180 L/hr.
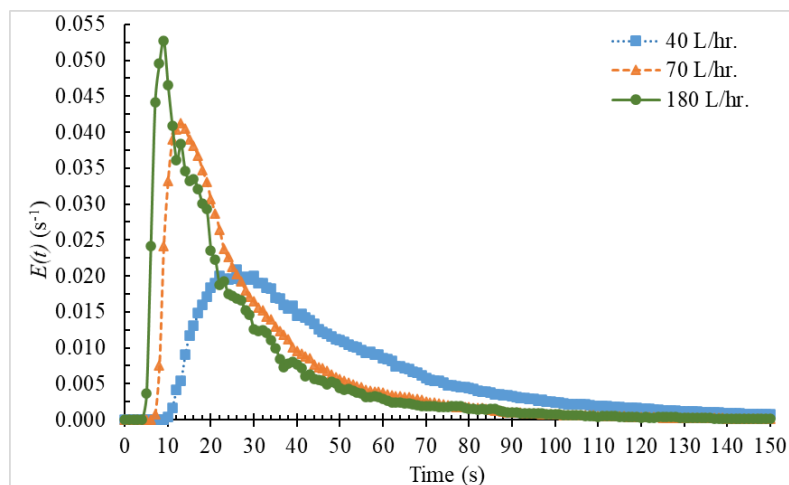
Figure C.4 *E(t)* experimental data curve of static mixer in various flow rate

From the results shown in Figure C.3 – C.4 and Table C.2, it is clear that the RTD of the static mixer is varied responsively to change in flow rate and the average values of the three trials were forthright. The trend of the RTD curve and t_m values were then subjected to flow rate. Still, it is essential to note that the present evidence relies on the practical limit, which could be described by t_m comparison with hydraulic retention time (HRT) in the next paragraph.

Table C.2 Analysis data of the static mixer

Flow rate (L/hr.)	Experiment	Hydraulic retention time (s)	t_m (s)	σ (-)	$\dfrac{D}{uL}$	Peclet Number (-)
40	1		61.37	53.38	0.21	4.83
	2	5.55	52.43	49.43	0.23	4.33
	3		55.72	46.35	0.19	5.14
70	1		32.42	27.41	0.20	5.02
	2	3.16	31.13	29.77	0.24	4.25
	3		31.01	28.14	0.22	4.56
180	1		26.95	23.18	0.20	4.91
	2	1.23	24.70	21.43	0.21	4.85
	3		27.72	26.23	0.23	4.31
40		5.55	56.37	50.10	0.21	4.69
70	Average	3.16	31.50	28.48	0.22	4.58
180		1.23	26.49	23.91	0.22	4.59

From Table C.2, it could be see that the t_m values were 56.37, 31.50, and 26.49 seconds, while the HRT or designing time was 5.55, 3.16, and 1.23 seconds for 40, 70, and 180 L/hr., respectively. It was noticeable that t_m were larger than hydraulic retention time (HRT) about 10 times for 40 L/hr., and 70 L/hr. flow rate, and about 20 times for 180 L/hr. It could be explained that the injection time impacted the results since the pulse input technique requires the shortest injection time as much as possible, while in practice were spent time lager than the HRT, especially on the 180 L/hr. flow rate the HRT was only a second. Thus, the effect of injection time impacted on t_m of height flow rate than low flow rate. This may raise concerns about the tracer injection technique which should be addressed. For all this reason, the results of the RTD study on the effect of flow rate of the static mixer turned out that it is sufficiently inaccurate for very speedy like the static mixer; therefore, the RTD study on the effect of flow rate of static mixer required more pulse input technique accurate.

Appendix D

Mean Residence Time Distribution of Small Scale Prototype (SSP)

The RTD results of SSP in the case of without porous zone with various inlet flow rate
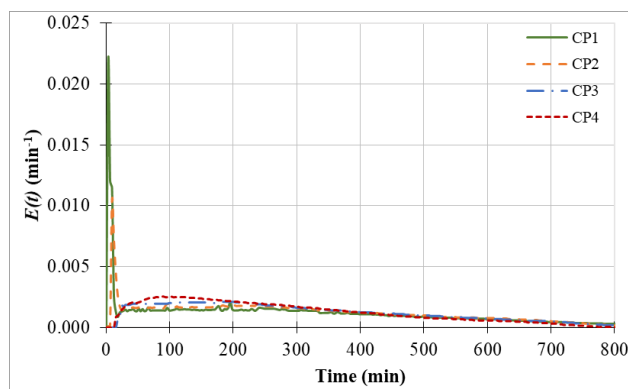
a) 11 L/hr.

b) 19 L/hr.

c) 49 L/hr.

Figure D.1 $E(t)$ experimental data curve for various tracer detection positions of
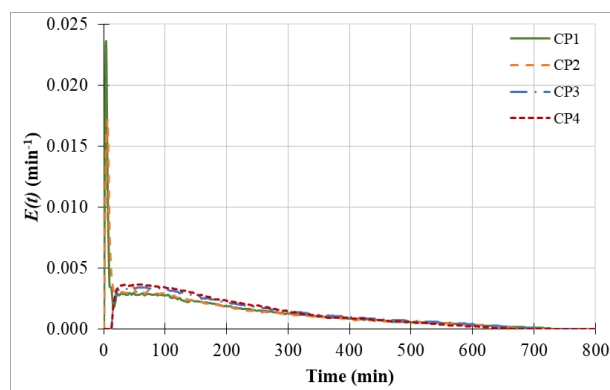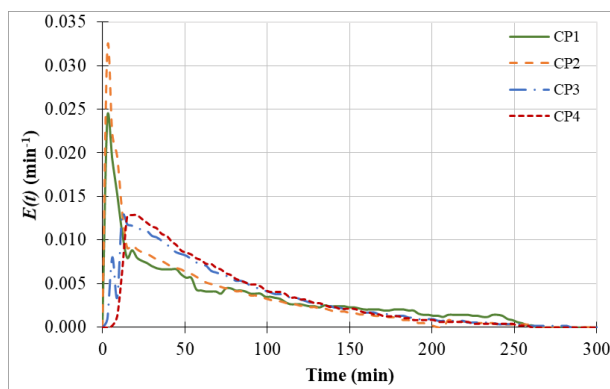(a) 11 L/hr., (b) 19 L/hr., and (c) 49 L/hr.

Table D.1 Water characteristic and treatment efficiency of small size jet clarifier

Porous zone	Truncated cone's base diameter	Flow rate (L/hr.)	Water characteristic						Efficiency (%)
			Initial			Effluent			
			Turbidity (NTU)	pH	ALK (mg/L as $CaCO_3$)	Turbidity (NTU)	pH	ALK (mg/L as $CaCO_3$)	
without	3.25	11	-	-	-	-	-	-	-
		19	50.20	7.67	82.20	17.70	7.54	99.20	65.02
		49	-	-	-	-	-	-	-
	6.50	11	50.10	7.69	80.60	12.10	7.37	74.80	76.04
		19	50.00	7.62	85.70	12.50	7.10	73.40	75.20
		49	49.80	7.85	82.80	18.60	7.33	70.80	62.65
	9.75	11	-	-	-	-	-	-	-
		19	49.90	7.45	85.20	18.90	7.31	77.20	61.97
		49	-	-	-	-	-	-	-
with	3.25	11	50.20	7.62	81.6	10.5	7.42	76.6	79.33
		19	50.00	7.69	83.00	8.20	7.46	75.20	83.60
		49	50.00	7.56	85.40	15.50	7.33	73.20	69.00
	6.50	11	49.80	7.85	92.00	8.13	7.73	78.60	83.64
		19	49.80	7.66	80.10	8.95	7.35	77.80	81.99
		49	49.90	7.68	80.10	14.60	7.21	70.40	70.74
	9.75	11	49.80	7.63	86.80	9.61	7.48	79.00	80.59
		19	50.20	7.68	88.00	8.14	7.52	80.00	83.78
		49	50.20	7.62	83.20	14.30	7.21	73.20	71.63

Table D.2 Water characteristic and treatment efficiency of large size jet clarifier

Porous zone	Truncated cone's base diameter	Flow rate (L/hr.)	Water characteristic						Efficiency (%)
			Initial			Effluent			
			Turbidity (NTU)	pH	ALK (mg/L as CaCO₃)	Turbidity (NTU)	pH	ALK (mg/L as CaCO₃)	
without	5	40	-	-	-	-	-	-	-
		70	50.10	7.69	81.2	17.8	7.69	75.6	64.54
		180	-	-	-	-	-	-	-
	10	40	50.20	7.70	85.60	13.10	7.41	81.20	74.11
		70	50.20	7.76	89.60	14.90	7.24	85.40	70.32
		180	49.90	7.77	90.40	16.10	7.42	80.10	68.06
	15	40	-	-	-	-	-	-	-
		70	49.80	7.85	83.5	14.5	75.4	74.6	70.88
		180	-	-	-	-	-	-	-
with	5	40	49.80	7.65	82.3	9.5	7.2	76.5	80.92
		70	49.90	7.8	82.8	10.2	7.45	74.6	79.44
		180	50.10	7.88	90.43	14.32	7.5	80.6	71.42
	10	40	50.20	7.64	79.20	8.64	7.49	73.00	82.96
		70	50.10	7.71	85.40	10.50	7.43	76.80	79.13
		180	49.90	7.67	81.20	13.50	7.33	71.00	72.84
	15	40	50.20	7.68	81.3	8.64	7.35	76.8	82.82
		70	50.10	7.58	80	10.2	7.52	72.4	79.92
		180	50.20	7.67	80.4	14.22	7.35	70.3	71.67

Table D.3 Surface raw water characteristic and treatment efficiency of simulated water treatment plant system.

Types of water	Flow rate (L/hr.)	Water characteristic						Efficiency (%)
		Initial			Effluent			
		Turbidity (NTU)	pH	ALK (mg/L as CaCO₃)	Turbidity (NTU)	pH	ALK (mg/L as CaCO₃)	
Raw water	11	60.00	7.01	81.60	10.22	6.87	78.60	82.97
	19	58.00	7.25	90.10	10.68	7.20	77.80	81.59
	49	62.00	7.36	85.30	19.22	7.12	70.40	69.00
Synthesis water	11	49.70	7.85	92.00	8.13	7.73	78.60	83.64
	19	49.70	7.66	80.10	8.95	7.35	77.80	81.99
	49	49.90	7.68	80.10	14.60	7.21	70.40	70.74

Appendix E

Setting of Numerical Methods

Table E.1 The Setting of Transient Solving for RTD-numerical

Scalar Value	Time step size	Number of time step	Δt (s)	Cumulative Δt (s)
1000	0.01	50	0.5	0.5
0	0.01	50	0.5	1
0	0.1	500	50	51
0	0.5	500	250	301
0	1	500	500	801
0	2	500	1000	1801
0	5	500	2500	4301
0	10	4500	45000	49301
0	20	4000	80000	129301
0	40	2000	80000	209301